Holographic Jet Quenching

Andrej Ficnar

Submitted in partial fulfillment of the

requirements for the degree of

Doctor of Philosophy

in the Graduate School of Arts and Sciences

COLUMBIA UNIVERSITY

2014

Abstract

Holographic Jet Quenching

Andrej Ficnar

In this dissertation we study the phenomenon of jet quenching in quark-gluon plasma using the AdS/CFT correspondence.

We start with a weakly coupled, perturbative QCD approach to energy loss, and present a Monte Carlo code for computation of the DGLV radiative energy loss of quarks and gluons at an arbitrary order in opacity. We use the code to compute the radiated gluon distribution up to $n = 9$ order in opacity, and compare it to the thin plasma ($n = 1$) and the multiple soft scattering ($n = \infty$) approximations. We furthermore show that the gluon distribution at finite opacity depends in detail on the screening mass μ and the mean free path λ.

In the next part, we turn to the studies of how heavy quarks, represented as "trailing strings" in AdS/CFT, lose energy in a strongly coupled plasma. We study how the heavy quark energy loss gets modified in a "bottom-up" non-conformal holographic model, constructed to reproduce some properties of QCD at finite temperature and constrained by fitting the lattice gauge theory results. The energy loss of heavy quarks is found to be strongly sensitive to the medium properties. We use this model to compute the nuclear modification factor R_{AA} of charm and bottom quarks in an expanding plasma with Glauber initial conditions, and comment on the range of validity of the model.

The central part of this thesis is the energy loss of light quarks in a strongly coupled plasma. Using the standard model of "falling strings", we present an analytic derivation of the stopping distance of light quarks, previously available only through numerical sim-

ulations, and also apply it to the case of Gauss-Bonnet higher derivative gravity. We then present a general formula for computing the instantaneous energy loss in non-stationary string configurations. Application of this formula to the case of falling strings reveals interesting phenomenology, including a modified Bragg-like peak at late times and an approximately linear path dependence. Based on these results, we develop a phenomenological model of light quark energy loss and use it compute the nuclear modification factor R_{AA} of light quarks in an expanding plasma. Comparison with the LHC pion suppression data shows that, although R_{AA} has the right qualitative structure, the overall magnitude is too low, indicating that the predicted jet quenching is too strong.

In the last part of the thesis we consider a novel idea of introducing finite momentum at endpoints of classical (bosonic and supersymmetric) strings, and the phenomenological consequences of this proposal on the energy loss of light quarks. We show that in a general curved background, finite momentum endpoints must propagate along null geodesics and that the distance they travel in an AdS_5-Schwarzschild background is greater than in the previous treatments of falling strings. We also argue that this leads to a more realistic description of energetic quarks, allowing for an unambiguous way of distinguishing between the energy in the dual hard probe and the energy in the color fields surrounding it. This proposal also naturally allows for a clear and simple definition of the instantaneous energy loss. Using this definition and the "shooting string" initial conditions, we develope a new formula for light quark energy loss. Finally, we apply this formula to compute the nuclear modification factor R_{AA} of light hadrons at RHIC and LHC, which, after the inclusion of the Gauss-Bonnet quadratic curvature corrections to the AdS_5 geometry, shows a reasonably good agreement with the recent data.

Contents

List of Figures

Acknowledgements

I would like to thank my advisor Miklos Gyulassy for his guidance and support, for inspiring me, and for challenging me to become a better physicist. It is hard to imagine the chaotic transition from being a student to becoming a researcher without Miklos' invaluable help, his broad knowledge, and his constant encouragement to interact with the rest of the scientific community, as well as the stimulating and supportive research environment of our group. Through his example, Miklos showed me the perseverance, enthusiasm, and intellectual curiosity a scientist needs to have, and for this I am tremendously grateful.

I am deeply indebted to Jorge Noronha and Steve Gubser, with whom I successfully collaborated over the past years and from whom I have learned so much. Jorge was there in the very beginning of my PhD, teaching me and helping me in my first steps towards real research and, after years of encouragement and genuine support in my career, I am happy that I can call him my friend. Steve showed me a new level of thinking about physics and approaching problems; this, together with his inspirational creativity and extensive knowledge make him the kind of scientist I aspire to be.

I am thankful to my friends and colleagues Giorgio Torrieri, Mohammed Mia, Barbara Betz, and Jiechen Xu, whose worldline has passed through the nuclear theory group at Columbia over the past several years. Their friendship and fruitful discussions created an enjoyable working atmosphere and made doing physics even more fun.

I would also like to thank the members of my thesis examination committee: Brian

Cole, Adrian Dumitru, John Harris and Erick Weinberg, for reading this dissertation, offering their recommendations and asking stimulating questions.

My time in New York would not feel complete without the amazing people I met along the way; they made it an exciting and unforgettable adventure, and some of the best years of my life. I feel both lucky and privileged to call Alexander Stoffers, Nikiforos Nikiforou, Solomon Endlich, Niamh Sweeney, Chris Gutiérrez, Filippo Ferraris, Yuliya Tarasava, Valentina Doro and especially Alessandro Buzzatti my close friends. You guys have been there for me when I needed a friend, support, or just to have a good time, making New York feel like home. It's been quite a ride! I will miss all of you, and even though we might be oceans apart, I know I can count on you any time.

Living far away from home has its own downsides, and I am grateful to my Croatian friends, Filip Kiš, Goran Nikšić, and Mihael Grbić, for being the reliable and familiar pillars of support and friendship during all these years, always being there for me, and always making me feel welcome back home.

I owe my sincere gratitude to my family: my mom, my aunt, my uncle, my brother and my grandpa. Even though we've been apart for so long, they have been an incredible team that always had my back, always there to turn to, and always there to offer their advice, encouragement, unconditional love and infinite support.

And finally, as lucky as I feel for having Miklos as my mentor, I feel even luckier because, thanks to him, I met Kamilla. I don't know how we managed to find each other in the vastness of New York, but her support, endless care, understanding, and love made my last couple of years in New York truly wonderful. And this is just the beginning.

Introduction

Gauge field theories, such as Quantum Chromodynamics (QCD) and Quantum Electrodynamics (QED) have been very successful in describing the world around us down to very small scales. However, the tractability of many calculations is restricted to the case of small coupling constants, that is, to the regime where the relevant interactions are weak. When interactions become strong, the usual field theoretical methods break down, and, apart from the computationally demanding lattice gauge theory techniques, one is left without the much needed tools to cope with various important questions in strongly coupled physics. Examples of these include the meson spectra and phase transition in QCD, transport properties of strongly coupled plasmas, certain properties of superfluids and superconductors, and many other. These are precisely the questions that, in principle, gauge/gravity duality can address: there, the strongly coupled processes in the gauge theory are mapped to significantly simpler problems in the appropriate classical gravity theory.

Gauge/gravity dualities are a general set of ideas that claim gauge field theories in four dimensions in flat space should be dual to gravity theories in curved space with one extra dimension [1, 2]; this is also the reason why this framework is often referred to as holography. The Anti-de Sitter / Conformal Field Theory (AdS/CFT) correspondence [3–5] is a particular case of gauge/gravity dualities, and, since its advent in the late nineties, it has become one of the most actively studied areas in theoretical high energy physics. The AdS/CFT correspondence is a conjectured duality between two seemingly very different physical theories: one is a particular gauge field theory ($\mathcal{N} = 4$ super-Yang-Mills (SYM) in flat (3+1) dimensions), and the other a particular string theory (type IIB string theory on $AdS_5 \times S^5$ background). In the limit of large number of colors, the correspondence allows us to study strongly coupled processes on the gauge theory side through classical (super)gravity calculations on the string theory side.

This important aspect makes the AdS/CFT correspondence a very useful and powerful tool that can help us gain more insight into the properties of a variety of interesting strongly coupled systems, ranging from strongly coupled non-Abelian plasmas to exotic states of matter such as superconductors and superfluids. One of the most important applications of the correspondence is the study of properties of the quark-gluon plasma created [6–10] in ultra-relativistic heavy ion collisions at the Relativistic Heavy Ion Collider (RHIC) at BNL and the Large Hadron Collider (LHC) at CERN. Quark-gluon plasma, a hot and dense soup of asymptotically free quarks and gluons, is a deconfined phase of QCD and also one of the early stages of the universe, and hence represents an interesting and important system to study. After many indications that the quark-gluon plasma created in heavy ion collisions is a strongly coupled, near-perfect fluid [6, 11], the gauge/gravity duality became an important and promising approach towards a better understanding of the plasma and its properties.

A great way to learn about the properties of the quark-gluon plasma is through the study of high momentum particles. These particles originate from energetic partons, whose production is well described by perturbative QCD, and hence the interactions of these "hard probes" with the medium serve as a good probe of its properties. One of the important aspects of these medium-parton interactions is energy loss, which will result in the attenuation of the momentum distributions of the observed hadrons, with respect to what we would expect from analogous proton-proton collisions. This is the phenomenon of jet quenching [12–14], best studied through the nuclear modification factor R_{AA}, a ratio of the observed particle distribution in a heavy collision and a distribution that we would expect if there was no medium created.

A standard and highly developed approach of studying the energy loss in the quark-gluon plasma, based on an assumption of weak coupling between the energetic parton and the medium, is the perturbative QCD [15–18]. In this picture, energetic partons propagate through the medium eikonally and lose most of their energy through medium-induced radiation of gluons. Although pQCD has been largely successful in describing the heavy ion suppression data, some puzzles still remain; for example, a consistent theoretical description that can account simultaneously for the dependence of certain hard probe observables on beam energy and centrality still seems to be challenging. We will see that some of these puzzles hint at possible strong coupling effects. In this thesis we will take this complementary approach, assume that the coupling between the medium and the parton is strong and study jet quenching using the gauge/gravity duality.

In AdS/CFT, the energetic partons are naturally represented by classical strings, and their energy loss by the flux of the momentum down the string, see Fig. 1 for illustration. The endpoints of these strings are generally attached to a "flavor" D-brane (necessary for introduction of quarks to the theory [19]), while the bulk of the string extends in the extra-dimensional Anti-de Sitter space with a black hole (necessary to study the theory at a finite temperature [20, 21]). For heavy quarks, the "bottom" of the flavor D-brane turns out to be close to the boundary of Anti-de Sitter space, where one generally imagines the gauge theory to be living on. A standard way to study the energy loss of heavy quarks is by considering the string endpoint being dragged at a constant velocity along the bottom of the flavor brane, while the rest of the string trails behind it, the so-called "trailing" strings [22, 23]. For light quarks, the flavor D-brane fills the entire available geometry, and one generally studies their energy loss using strings whose endpoints are free to fly apart and fall towards the black hole, the so-called "falling" strings [24, 25].

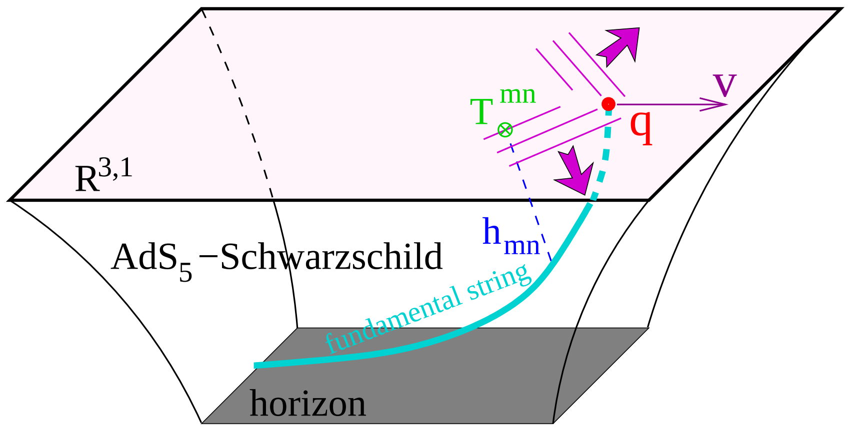

Figure 1: *Illustration of jet quenching in gauge/gravity duality (in particular, for heavy quarks). The heavy quark moving at a constant velocity in the "boundary" gauge theory is represented by a classical string that trails behind it in the five dimensional Anti-de Sitter spacetime with a black hole, which encodes the physics of a strongly coupled $\mathcal{N} = 4$ SYM plasma at a finite temperature. (Taken from [26].)*

In standard AdS/CFT, the arena in which processes dual to classical string dynamics take place is the $\mathcal{N} = 4$ SYM gauge theory, and this theory is somewhat different from QCD. It is therefore important to consider the extensions of the duality to include gauge theories that resemble QCD more, either through a theoretically more rigorous "top-down" approach [27, 28], or through a more phenomenologically driven "bottom-up" approach [29–32]. Luckily, modeling of the medium (the plasma) and modeling of the processes in it are two almost unrelated problems in AdS/CFT: the properties of the medium are encoded in the background metric of its dual string theory (AdS_5 in case of $\mathcal{N} = 4$ SYM) and the various dynamical processes in it are encoded in the classical dynamics of strings in that background.

One of the main challenges in successful applications of AdS/CFT to the quark-gluon plasma is the construction of realistic holographic models that would resemble as close as possible both the plasma and the interactions of quarks and gluons with it. This thesis will follow this path, by focusing on the quantitative analysis of jet quenching in gauge/gravity duality, with special emphasis on light quarks [33–36], and confronting these calculations with the heavy ion experimental data from RHIC and LHC. Our goal is to use the powerful theoretical tools of holography to gain a unique insight on how hard probes lose energy in a strongly coupled medium, an important piece of non-equilibrium physics inaccessible with conventional lattice or perturbative QCD techniques, and, in this way, ultimately learn more about the quark-gluon plasma produced at RHIC and LHC.

Chapter 1

Quark-gluon plasma and heavy ion collisions

We start this thesis with a somewhat introductory chapter, where we will not only give a brief overview of the main properties of the quark-gluon plasma and the phenomenology of heavy ion collisions, but also set some theoretical basis on how we will model the plasma and compute the jet quenching observables.

We start with Section 1.1, a brief overview of quantum chromodynamics and how, based on studies of its properties, we expect to see a deconfined quark-gluon plasma phase at high enough temperatures. In Section 1.2, building on the theory from the previous section, we describe how can the quark-gluon plasma be created in heavy ion collisions, and what does the vast amount of experimental data teach us about this hot and dense system. After these introductory sections, we move to Section 1.3, where we set up a simple model of the plasma to describe its non-trivial geometry and spacetime evolution, which we will use in our computations of jet quenching observables. Finally, in Section 1.4 we describe the nuclear modification factor, the observable of our main interest, and how we will calculate it, starting from some (holographic) energy loss model.

1.1 Quantum chromodynamics and its phases

The topic of this thesis is the holographic treatment of energy loss of quarks and gluons in the quark-gluon plasma, so it is only fair that we start this project with a short introduction and reminder on the main properties of the most successful theory of strong interactions, quantum chromodynamics (QCD).

The immense success of QCD is reflected in its explanation of various properties of hadrons, as well as its extensive experimental validation through processes hadrons are involved in. Origins of QCD go back to 1960s, when it was proposed that hadrons are made of quarks [37, 38] and gluons [39], which was motivated by the succesful explanation of the hadron classification through the eightfold way [40] and the existence of the Ω^- hyperon [41]. These proposals were later confirmed by numerous experiments, starting from the deep inelastic scattering (DIS) experiments at the SLAC collider [42, 43] and three jet events at the PETRA collider [44], respectively. Subsequent experimental verification, including observations of the running coupling, Bjorken scaling violations in DIS [45], and vector boson production [46] firmly established QCD as the fundamental theory of strong interactions.

1.1.1 Quantum chromodynamics at zero temperature

Quantum chromodynamics is a non-Abelian (Yang-Mills) $SU(3)$ gauge theory, coupled to $N_f = 6$ spin-1/2 matter fermions in the fundamental representation of the gauge group. The gauge group is also historically called the color group (with 3 being the number of colors), the $3^2 - 1 = 8$ gauge bosons are called gluons, the matter fermions are called quarks and the six families they come in are called flavors. The first three families (up, down and strange) are often regarded as the "light quarks" and the other three families (charm, bottom and top) as the "heavy quarks"[1]. We will often, for various reasons, keep the number of colors N and the number of flavors N_f general.

QCD is a renormalizable quantum field theory and its coupling g will for this reason in general "run", i.e. it will be a function of the energy scale μ, which is often expressed in terms of the renormalization group beta function, $\beta(g) \equiv \partial g/\partial \log \mu$. Beta function of QCD with N colors and N_f flavors was almost simultaneously calculated in [47, 48] and [49] to be (to the one-loop order)

$$\beta(g) = -\left(\frac{11}{3}N - \frac{2}{3}N_f\right)\frac{g^3}{16\pi^2}\,. \tag{1.1}$$

Hence, for $N = 3$, if $N_f \leq 16$, the coupling will decrease as we increase the energy scale (or decrease the length scale), which is the famous phenomenon of asymptotic freedom. This means that we can use the standard perturbation theory for calculating various processes at high energies, or, more precisely, high momentum transfers Q^2, also called "hard" processes. This has given rise to phenomenologically very successful methods of perturbative QCD (pQCD), that have been experimentally thoroughly verified in many processes, such as the aforementioned deep inelastic scattering experiments. At asymptotically high energies, both the coupling and the beta function of QCD vanish, the theory reaches a (trivial) ultraviolet fixed point and QCD becomes conformal.

Equation (1.1) also indicates that at low energies (large distances) the coupling increases and at some point we will not be able to use perturbation theory any more, and QCD will become strongly coupled, i.e. non-perturbative. This means that low-Q^2, or "soft", processes and low energy properties of hadrons cannot be treated perturbatively

[1]This division of course depends on the relevant scales in the system under consideration, such as the temperature. For the case of the quark-gluon plasma created at RHIC and LHC this division makes sense (especially for up and down quarks), as the temperature of the medium will be on the order of 200-300 MeV. We will also sometimes approximate the up and down quarks as massless, as their mass is on the order of a few MeV.

and one has to rely on less analytic and more approximate methods. This mainly includes the low energy effective models which incorporate certain features of QCD (e.g. the effective chiral Lagrangian [50]) and the numerical simulations of lattice QCD, a computationally demanding approach based on a discretized version of the QCD Lagrangian, which will be discussed more in Section 1.1.3. As we will see later, the AdS/CFT correspondence provides an important analytical insight into certain strongly coupled field theories that are more or less similar to QCD.

The Lagrangian of QCD without quarks (or, as a first approximation, setting the masses of light quarks to zero and masses of heavy quarks to be infinite) has only one parameter, the coupling constant g. Since the coupling constant is dimensionless and it runs according to (1.1), one needs to have an additional, dimensionful parameter: this is $\Lambda_{\rm QCD}$ which is introduced as the solution of (1.1), $g^2 \propto 1/\log(\mu^2/\Lambda_{\rm QCD}^2)$, and essentially is a scale at which the theory becomes non-perturbative. To be more precise, $\Lambda_{\rm QCD}$ is not really a parameter, it simply reflects our choice of units: in standard units $\Lambda_{\rm QCD} \approx 200$ MeV or ≈ 1 fm^{-1}[2].

QCD has a large amount of symmetries. Being a Yang-Mills theory, the Lagrangian is invariant under local $SU(3)$ gauge transformations. In addition to these, we also have various global symmetries associated with the quarks. Neglecting the heavy quarks and assuming that the masses of light quarks are the same, $m_u = m_d = m_s$, QCD is invariant under global $SU(3)$ transformations of quarks: this is the well known flavor symmetry of strong interactions. Assuming that the quark masses vanish, this symmetry is enlarged as we can independently perform flavor transformations of left and right handed quark fields, $\psi_{L,R} = \frac{1}{2}(1 \pm \gamma_5)\psi$, and one has an $SU(3)_L \times SU(3)_R$ global symmetry, called

[2] In this thesis, as is standard in particle physics, we will employ the system of natural units in which $\hbar = c = k_B = 1$. All quantities can be hence expressed in terms of energy units, which will often be MeV's or GeV's. The length units will often be fm's, and we can easily transform to and from the energy units using $\hbar c = 0.197$ GeV$\cdot$fm, so for example 1 fm $= 1$ fm$/(\hbar c) \approx 5$ GeV^{-1}.

the chiral symmetry. Of course, these are only approximate symmetries as the quarks are not really massless, but because of the hierarchy $m_u, m_d \ll m_s < \Lambda_{QCD}$, they are good approximations, especially for up and down quarks. Finally, we also have two $U(1)$ symmetries: $U(1)_B$ which rotates both left and right quark fields by the same angle, and the axial $U(1)_A$ which rotates them by opposite angles, and which is anomalously broken, i.e. $\partial^\mu j^5_\mu \neq 0$.

The ground state of QCD breaks the chiral symmetry in two ways. The first is the non-perturbative, spontaneous breaking by a quark-anti-quark ($\bar{q}q$) condensate $\langle\bar{\psi}\psi\rangle$, which in the QCD vacuum is non-zero, and which breaks $SU(2)_L \times SU(2)_R \to SU(2)_V$ (considering only up and down quarks), a vector-like symmetry called the isospin. Spontaneous symmetry breaking also involves generation of massless Goldstone bosons, three of them in our case - the pions. In addition to the spontaneous breaking, the chiral symmetry is explicitly broken by finite quark masses, which gives mass to the pions:

$$m_\pi^2 = (m_u + m_d)\frac{\langle\bar{\psi}\psi\rangle}{f_\pi^2}\,. \tag{1.2}$$

Since the mass of the pions is about 140 MeV and the masses of up and down quarks are only several MeV, we see that most of the pion mass comes from chiral symmetry breaking. If the up and down quarks were massless, one would still have $\langle\bar{\psi}\psi\rangle \neq 0$, but the pions, now true Goldstone bosons, would be massless.

Another important feature of QCD is the phenomenon of color confinement, which states that only color neutral objects are observable, that is, quarks and gluons are confined in hadrons. Although there is no analytic proof that QCD should be confining, most qualitative, phenomenologically successful ideas about the nature of confinement are based on quarks being bound by "strings" [51] or tubes of color flux. This is based on the fact that the QCD vacuum is a condensate of gluons (and quarks),

$$\left\langle 0 \left| \frac{\alpha_s}{\pi} \mathrm{Tr} F^2 \right| 0 \right\rangle \approx (390 \text{ MeV})^4 \,, \tag{1.3}$$

where $\alpha_s = g^2/(4\pi)$ and $F = dA$ is the gauge field strength. This result can be obtained from QCD sum rules [52], and is also confirmed by the lattice QCD calculations. Drawing an analogy with the ground state of a superconductor consisting of a condensate of paired electrons, one expects that putting a quark and an anti-quark pair in this medium will lead to the color electric flux lines between the two being strongly localized to a tube-like region with a constant (due to translational invariance) energy density of the gluon field. Hence, the potential between the quark and an anti-quark at long distances is expected to depend linearly on the distance r between the quarks,

$$V(r) \to \sigma r \,, \tag{1.4}$$

where σ is a constant called the string tension. As we separate the quarks, at some point it becomes energetically more favorable for the string to break and create another $\bar{q}q$ pair. Estimating that this breaking happens at a typical hadronic size of ~ 1 fm and that the typical hadronic energy is about 1 GeV, we can estimate the string tension to be about $\sigma \sim 1$ GeV/fm. One of the well known successes of this string model of hadrons was the agreement with the Regge trajectories, the experimental observation that the spin J and mass M_J of hadrons (of some given internal symmetry quantum numbers) satisfy the relation [53]

$$J = \alpha_0 + \alpha' M_J^2 \,, \tag{1.5}$$

where $\alpha' \approx 1$ GeV^{-2}. In accordance with the flux tube picture, imagining that the hadrons are simply two massless quarks connected by a relativistic string (of constant energy density) and that they are rotating at the speed of light, one not only reproduces the relation (1.5) with $\sigma = 1/(2\pi\alpha')$, but also gets $\sigma \approx 0.2$ GeV^2, in accordance with our previous rough estimate.

While the potential between a quark and an anti-quark has the string form (1.4) at large distances, at small distances it exhibits a typical attractive, Coulomb-like form $\sim 1/r$. Putting these two forms together, we have the Cornell potential:

$$V_{\bar{q}q}(r) = -\frac{a}{r} + \sigma r\,, \tag{1.6}$$

where, to first loop order, $a = 4\alpha_s/3$. In general, these effective potentials are extracted from a rectangular Wilson loop,

$$W(R,T) = \mathrm{Tr}\left[\mathcal{P}\exp\left(ig\oint A^\mu dx_\mu\right)\right]\,, \tag{1.7}$$

where $\mathcal{P}$ denotes path ordering and where one integrates over a rectangular $R \times T$ region in spacetime. For $T \gg R$, the vacuum expectation value of (1.7) is dominated by the ground state, and we can extract the effective potential $V(R)$ (in the Euclidean space):

$$\langle W(R,T)\rangle \to \exp\left(-V(R)T\right)\,. \tag{1.8}$$

At small distances, we can use the perturbative methods to evaluate this expectation value, while at large distances (1.8) is well suited for implementation on the lattice, yielding the so-called area law, due to confinement.

The fact that the QCD vacuum is a gluon condensate can be used to find out its energy density ε_{vac} through the trace anomaly, the anomalous breaking of the dilatation symmetry due to the running of the coupling:

$$T^{\mu}{}_{\mu} = \frac{\beta(g)}{2g^3} \left\langle \mathrm{Tr} F^2 \right\rangle = \varepsilon_{\rm vac} g^{\mu}{}_{\mu} \,, \tag{1.9}$$

where $T^{\mu}{}_{\mu}$ is the trace of the energy-momentum tensor, $g^{\mu}{}_{\mu}$ is the trace of the metric tensor, and where Lorentz invariance dictates $T_{\mu\nu} \propto g_{\mu\nu}$. Comparing this with the result in (1.3), one can arrive at some typical values on the order of $\varepsilon_{\rm vac} \sim -0.5$ GeV/fm^3. In addition to the "true" QCD vacuum we just described, in which only color neutral objects can exist, there is also the "perturbative vacuum", an excited state with zero energy density (relative to $\varepsilon_{\rm vac}$), in which the colored quarks and gluons move freely.

Based on these considerations, it is possible to develop a simple picture of strong interactions that incorporates both the asymptotic freedom and the confinement, the so-called bag model [54–56]. In its simplest version, it consists of assuming that hadrons are "bags" of perturbative vacuum, in which massless quarks can move freely, due to the asymptotic freedom. Hadrons are placed in the confining QCD vacuum, where quarks and gluons cannot be free; they are prevented from escaping the bag by assuming that the bag has a constant energy density B, the bag constant. Therefore, the bag constant should be the energy density of the QCD vacuum, $B = -\varepsilon_{\rm vac}$. In this simple picture, the hadron energy consists of the energy associated with the creation of the finite-volume perturbative bag in a non-perturbative vacuum, and the kinetic energy of the quarks inside the bag. For simplicity, assuming that the bag is spherical with radius R and that the kinetic energy has a simple $\sim 1/R$ form coming from the uncertainty principle, the hadron energy is

$$E_H = \frac{4\pi}{3} R^3 B + \frac{C}{R} \,, \tag{1.10}$$

where C is some constant. From here, we could calculate the mass of the hadron by minimizing E_H with respect to R, but the bag model will be more useful to us in the next section, when we consider the phase transition in QCD.

1.1.2 Phase transition in QCD

In this section we will discuss what happens with the phase structure of QCD at non-zero temperature. As we increase the temperature, one would expect the melting of the gluon condensate (1.3) and hence the dissolution of the confining vacuum, leading to a phase in which quarks and gluons are deconfined. This is called the deconfinement transition and this phase is called the quark-gluon plasma phase, because, as we will see later, it will exhibit some typical plasma features. In the limit of high temperatures, the exchanged momenta in typical processes are high, leading to weak coupling, due to asymptotic freedom. And if the exchanged momenta are small, these processes will involve large distances and, as we will see later in (1.16), the quark-gluon medium screens the interaction, again leading to effectively weak coupling. So, at high temperatures, we expect to see a weakly coupled system of quarks and gluons.

Based on this discussion, we could try to roughly estimate at which temperature should this transition take place, by using some basic reasoning from thermodynamics. The phase transition we are interested in is between the hadron phase, a weakly coupled gas of hadrons, and the quark-gluon phase, a weakly coupled (at high temperatures) gas of quarks and gluons. The standard idea is to compute the pressure of the two phases as a function of temperature and find the transition temperature T_c at which these two pressures are the same. For a gas of massless bosons and fermions at zero chemical potential, we will use the results for energy density (A.4), from which we can find the pressure by using the equation of state $\varepsilon = 3P$:

$$P_b = g_b \frac{\pi^2}{90} T^4 \,, \quad P_f = g_f \frac{7\pi^2}{720} T^4 \,, \tag{1.11}$$

where g_b and g_f are the degeneracy factors. At zero chemical potential, the hadronic system will be mainly composed of pions, which, for simplicity, we will take to be massless. Hence, the degeneracy factor in the hadron phase is $g_{\text{HG}} = 3$. In the quark-gluon plasma phase, the degeneracy factor has been computed in (A.5). Now we need to include the effects of the confining medium, for which we will use the simple bag model from the previous section: as we saw in (1.9), the pressure of the vacuum is $P_{\text{vac}} = -\varepsilon_{\text{vac}} = B$, which we can add with a negative sign to the pressure of the perturbative medium of the quark-gluon plasma phase (or with a positive sign to the confining medium of the hadron phase). Finally, we have for $N_f = 2$:

$$P_{\text{HG}} = \frac{\pi^2}{30} T^4 \,, \quad P_{\text{QGP}} = \frac{37\pi^2}{90} T^4 - B \,. \tag{1.12}$$

Equating the two pressures at $T = T_c$, we get, for $B \approx 0.5$ GeV/fm^3,

$$T_c = \left(\frac{45B}{17\pi^2} \right)^{1/4} \approx 180 \text{ MeV} \,. \tag{1.13}$$

Although this was a very rough calculation, intended to illustrate some basic physics behind the deconfinement transition, it will nevertheless be in the ballpark of the actual results from lattice QCD, as we will see in the next section.

The discussion in the previous paragraph was somewhat qualitative, from the perspective of quantum field theory: although non-perturbative, how can we more precisely formulate the signature of the deconfinement transition, so that it can be calculated on the lattice? Phase transitions are usually accompanied by breaking of some symmetry, and in the case of the deconfinement transition, we can consider the Polyakov loop (really a line) as the order parameter:

$$L(\vec{x}) = \frac{1}{N}\mathrm{Tr}\left[\mathcal{P}\exp\left(ig\int\limits_0^\beta A_\tau d\tau\right)\right], \tag{1.14}$$

where the gauge fields are periodic in imaginary time τ with period $\beta = 1/T$, as appropriate in thermal field theory[3]. The reason why the Polyakov loop is useful in this context can be seen by considering an "aperiodic" gauge transformation of the form $V(\tau+\beta,\vec{x}) = z_n V(\tau,\vec{x})$, where $z_n \in Z_N = \left\{\mathbb{1}e^{2\pi i n/N} | n = 0, ..., N-1\right\}$, the center of the gauge group $SU(N)$. Under this center symmetry the gauge fields A_μ are invariant, while quarks are not, $q \to -z_n q$. However, in a pure gauge theory (or, assuming that quarks have infinite masses) in the confined phase, N external, test quarks (forming a "test baryon"), are together invariant since $z_n^N = 1$. Therefore, the center symmetry is a symmetry of the confined phase. However, the Polyakov loop is not invariant under this symmetry: $L \to z_n L$, which means that $\langle L\rangle$ must vanish in the confined phase. On the other hand, in the deconfined phase, the center symmetry is broken and $\langle L\rangle$ does not need to vanish anymore: Polyakov loop is therefore an order parameter for the symmetry. To summarize,

$$\langle L\rangle \begin{cases} = 0, & \text{confined } (T < T_c) \\ \neq 0, & \text{deconfined } (T > T_c)\,. \end{cases} \tag{1.15}$$

More physically, similar to the case of Wilson lines, the expectation value of the Polyakov

[3] In thermal field theory, by realizing that the Boltzmann operator $e^{-\beta\hat{H}}$, where $\hat{H}$ is the Hamiltonian operator, can be formally interpreted as a quantum evolution operator in imaginary time, one can express the partition function as a path integral in Euclidean space, in which one integrates over the (fermionic) bosonic fields subject to the (anti)periodicity condition in imaginary time τ, e.g. $A_\mu(\vec{x},0) = A_\mu(\vec{x},\beta)$. In this way, one can, provided the Lagrangian of a particular theory, find the partition function in terms of the path integral and then compute various thermodynamic quantities and thermal averages of operators, e.g. $\langle A\rangle_\beta = \mathrm{Tr}\left(Ae^{-\beta H}\right)/Z(\beta)$.

loop is related to the free energy of a single (heavy) quark, $\langle L \rangle \propto e^{-F_Q/T}$. Therefore, in the confined phase, since there are no free isolated quarks, the free energy should be infinite and $\langle L \rangle \to 0$. On the other hand, in the deconfined phase, the free energy is finite and hence $\langle L \rangle \neq 0$.

In addition to the gluon condensate (1.3), whose melting we just discussed and which signaled the deconfinement phase transition, there is also the non-vanishing quark condensate, $\langle \bar{\psi}\psi \rangle \neq 0$, whose melting we might also expect and which would then signal the restoration of the chiral symmetry (in the limit of vanishing quark masses). The order parameter for this transition is precisely $\langle \bar{\psi}\psi \rangle$. To summarize, $\langle L \rangle$ is the order parameter for the deconfinement transition in the pure gauge limit ($m_q \to \infty$), while $\langle \bar{\psi}\psi \rangle$ is the order parameter for chiral symmetry breaking in the chiral limit ($m_q \to 0$). Although it appears that the melting of the gluon condensate and melting of the quark condensate are in principle unrelated, the numerical simulations of lattice QCD, as we will see soon, show that they actually happen together, i.e. at the same temperature, and are signals of a single phase transition, the deconfinement / chiral transition.

In the deconfined phase, the string tension σ (eq. (1.4)) vanishes and, since, at finite temperature, the gluons acquire effective thermal masses, the Coulomb part of the $\bar{q}q$ potential (1.6) is now screened and the potential has the Yukawa form:

$$V_{\bar{q}q}(r) \approx -\frac{4\alpha_s}{3}\frac{e^{-\mu r}}{r}\,, \tag{1.16}$$

where $\mu \sim gT$ is the Debye mass. The Debye screening is common to any system of charged particles at high density and can be understood as an effective polarization of the medium around the charge, which screens it and reduces the interaction.

1.1.3 Lattice QCD

More precise statements about this non-perturbative phase transition of QCD can be given by numerical simulations in lattice QCD. Lattice QCD (a good review can be found in [57]), originally proposed in the 70s [58], has by now become a well established, non-perturbative approach to solving QCD, in situations where analytical and perturbative methods are not applicable. This includes the study of the deconfinement phase transition, thermodynamics of QCD close to the transition, various hadron spectra, and even transport coefficients. It is a discretized version of QCD, where one formulates the theory on a finite lattice of spacetime points and discretizes the fields accordingly. In non-zero temperature lattice calculations one first starts by writing the QCD partition function as a path integral in Euclidean time with suitable periodic conditions in the imaginary time. Then, at vanishing baryon chemical potential, since the partition function is given by an exponent of a real action integrated over all field configurations, one can explicitly evaluate it using Monte Carlo techniques, thanks to the discretization of the theory on the lattice. Although lattice QCD is our, in principle, only reliable tool for studying non-perturbative aspects of QCD, it is also very demanding from the technological side, as the computations, even for very modest lattice sizes, require powerful computers that run for a very long time.

Using simple estimates of the phase transition temperature T_c, such as (1.13), one could look for the phase transition in the vicinity of that estimate by calculating the pressure and energy density. In Fig. 1.1 we see these results from the HotQCD collaboration, clearly showing the expected jump in pressure and energy density, indicating that the system is now composed of more degrees of freedom. They also show that, the more degrees of freedom (flavors) one includes in the calculations, the higher the pressure and the energy density in the plasma phase, indicating that the system is indeed deconfined.

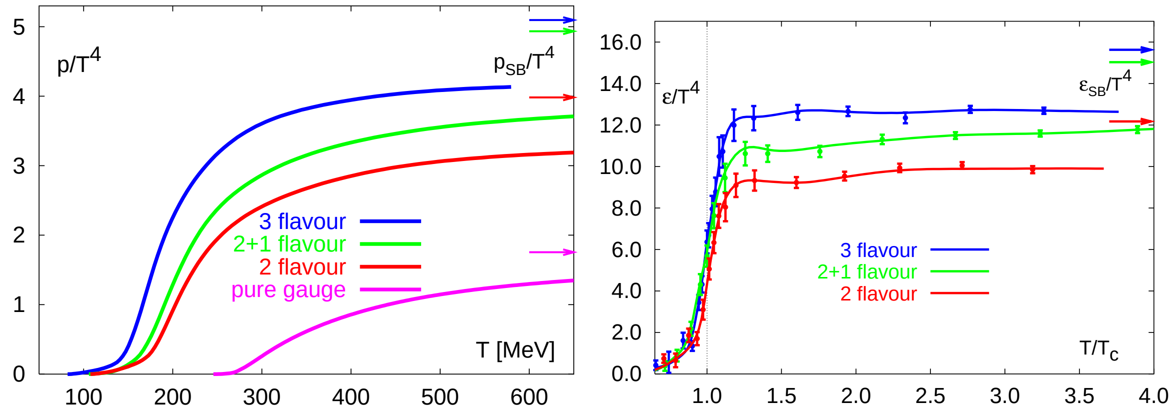

Figure 1.1: *Lattice calculations by the HotQCD collaboration [59] of the pressure and energy density in QCD with different number of degrees of freedom as a function of temperature. The curve labeled (2+1)-flavor corresponds to a calculation with two light and a four times heavier strange mass. (Taken from [59] and [57].)*

The nature of the phase transition as a function of masses of u, d and s quarks can be inferred from various universality arguments and numerical simulations. For example (see e.g. [57]), it is clear that in the pure gauge limit (when quark masses $\to \infty$) and in the chiral $SU(3) \times SU(3)$ limit (when quark masses $\to 0$) the phase transition is of first order, while for modest quark masses (including their actual physical values), the transition is a crossover, i.e. there is no discontinuity in the energy density or one of its derivatives, but a rapid change. And to convince ourselves that this transition indeed leads to deconfinement and chiral symmetry restoration, we can look at their order parameters in the pure gauge and chiral limits, the expectation values of the Polyakov loop $\langle L \rangle$ and the quark condensate $\langle \bar{\psi}\psi \rangle$, respectively. This is shown in the left plot in Fig. 1.2, where we can clearly see how these two transitions occur at the same temperature T_c. In addition to that, their susceptibilities are also plotted, the size of which indicates how rapid the change of the associated quantity is. For this reason, the peaks of the susceptibilities are usually used to define the critical transition temperature T_c: for 2-flavor QCD, $T_c \approx 173$ MeV, while for 3-flavor QCD, it is $T_c \approx 154$ MeV [60], and for pure $SU(3)$, $T_c \approx 271$

MeV [57]. All these numbers are actually in the ballpark of our previous rough estimate in (1.13).

Another interesting quantity that is often calculated on the lattice is the QCD trace anomaly, $T^{\mu}{}_{\mu} = \varepsilon - 3P$, which measures the deviation from the ideal gas limit $\varepsilon = 3P$. For this reason it is also called the interaction measure, and at leading order it is proportional to gT^4. We can see the trace anomaly in the right plot of Fig. 1.2, where the calculations from the two leading lattice collaborations, HotQCD and Wuppertal-Budapest, are compared, showing some differences due to the usage of different actions and their different technical implementation of the lattice. However, we can still clearly see that the trace anomaly peaks close to T_c and then, at both low and high temperatures tends to zero, indicating that the system is becoming more and more weakly coupled.

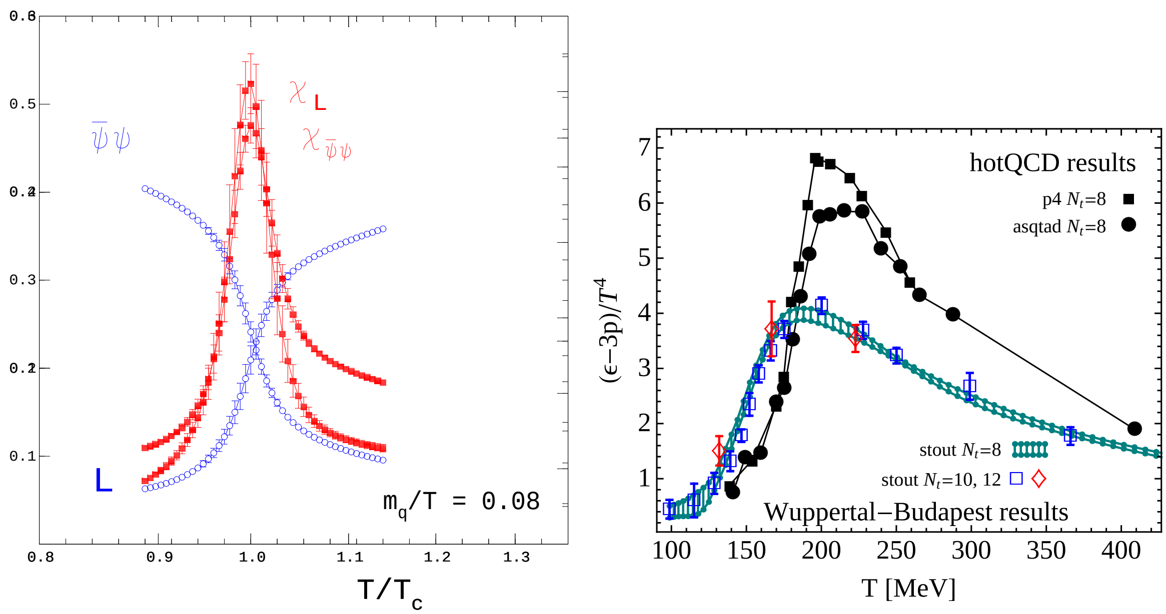

Figure 1.2: *Left: Lattice calculation by the HotQCD collaboration of the expectation values of the Polyakov loop $\langle L \rangle$ and the quark condensate $\langle \bar\psi\psi \rangle$ in 2-flavor QCD, together with their susceptibilities. (Taken from [57].) Right: Comparison of the normalized trace anomalies of the Wuppertal-Budapest [61] and the HotQCD collaborations [62, 63]. (Taken from [61].)*

Most of our analysis and discussions so far applied to the case of vanishing baryon chemical potential μ_B. Since it is difficult to perform lattice simulations at finite μ_B (due to the infamous sign problem [64]), the nature of the full phase diagram of QCD, as a function of temperature and baryon chemical potential, is a combination of lattice results, various theoretical arguments and educated guesses, and is depicted in Fig. 1.3.

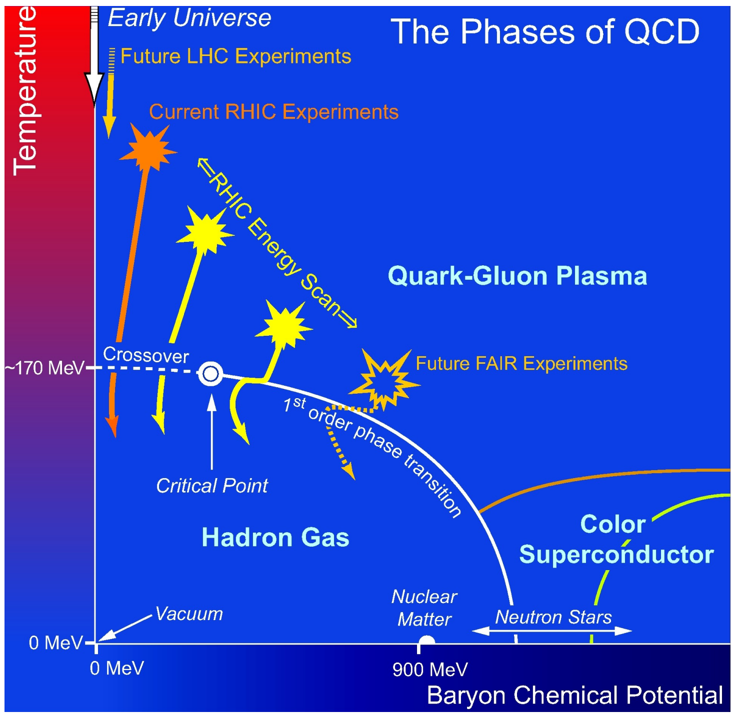

Figure 1.3: *Schematic QCD phase diagram for nuclear matter, indicating various phases, phase boundaries, the critical point, and possible trajectories for systems created in the QGP phase at different accelerators. (Taken from [65].)*

1.2 Heavy ion collisions

In the last several sections, we discussed how, at high temperatures and high densities we should expect to find the quark-gluon plasma phase of QCD, consisting of deconfined quarks and gluons. The main goal of ultra-relativistic heavy ion collisions is to create this phase experimentally, since using large nuclei allows us to create as large volume of the plasma as possible, and colliding them at high center-of-mass energy $\sqrt{s}$ allows us to generate high energy densities due to the strong Lorentz contraction in the beam direction. This goes in line with T. D. Lee's original proposal from almost 40 years ago that it would be interesting to explore new phenomena "by distributing high energy or high nucleon density over a relatively large volume" [66].

The first heavy ion collisions with the goal of creating the quark-gluon plasma started in the 1980s and 1990s at the CERN's Super Proton Synchrotron (SPS). The SPS energies reached $\sqrt{s_{NN}} \leq 20$ GeV per nucleon-nucleon pair and the data already displayed several signatures that hinted at the onset of a "new state of matter" [67]. Building upon and extending these efforts, the Relativistic Heavy Ion Collider (RHIC) at the Brookhaven National Laboratory started its heavy ion program in 2000, colliding Cu-Cu and Au-Au nuclei and reaching energies of $\sqrt{s_{NN}} = 200$ GeV. These energies are sufficient to create the QCD matter well above the deconfinement transition point and, as we will see in the coming sections, the vast experimental data (summarized in [7–10]) indeed strongly suggest that the quark-gluon plasma has been created at RHIC [6]. The experimental efforts have also started at CERN's Large Hadron Collider (LHC) in 2010, where Pb-Pb nuclei are collided at energies of up to $\sqrt{s_{NN}} = 2.76$ TeV.

1.2.1 First indications of a new state of matter

In this section we will introduce the basic heavy ion phenomenology and discuss some of the first experimental results that hinted at a creation of a non-trivial QCD medium in heavy ion collisions at RHIC.

One of the simplest measurements one can make in a heavy ion collision is to count the number of detected charged particles as a function of the polar angle θ with respect to the beam direction. This is called the multiplicity distribution and is shown in Fig. 1.4 for several beam energies at RHIC.

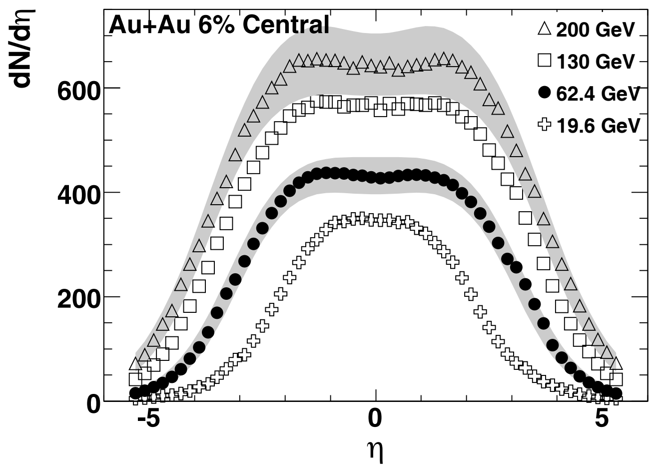

Figure 1.4: *Multiplicity distributions of charged particles as a function of pseudorapidity* (1.17)*, measured at RHIC at several different beam energies. (Taken from [68].)*

The results there are reported as a function of the pseudorapidity,

$$\eta = -\log\tan\left(\theta/2\right) \ , \tag{1.17}$$

so that $\eta = 0$ corresponds to $\theta = \pi/2$, i.e. perpendicular to the beam direction, which is also called midrapidity. A notable feature in Fig. 1.4 is the plateau around midrapidity at about $dN_{\rm ch}/d\eta \approx 700$ at $\sqrt{s_{NN}} = 200$ GeV (at LHC at $\sqrt{s_{NN}} = 2.76$ TeV, $dN_{\rm ch}/d\eta \approx 1584$ [69]). This means that the total number of charged particles is about 5000, which translates to about 8000 particles in total, approximating all the observed particles to be pions.

Fig. 1.4 is also useful for a first estimate of the energy density of the produced system, which can be done using a simple geometric method, due to Bjorken [70]. Assuming that at $\tau = 0$ the nuclei of radius R pass through each other, then at some other τ_0, the volume of the system will be roughly $2\tau_0 \pi R^2$, assuming a simple longitudinal expansion and no radial expansion. The energy contained in that system is at least $2 \cdot dE_T/d\eta|_{\eta=0}$ (making this estimate rather conservative), the total transverse energy between $\eta = -1$ and $\eta = 1$ in the plateau. Dividing these two quantities will give us the energy density of the system, which, choosing $\tau_0 = 1$ fm/c[4] turns out to be about 5 GeV/fm^3 for the most highly energetic Au-Au collisions. Although conservative, this estimate is still about five times higher than the critical energy density of about $\varepsilon_c \approx 1$ GeV/fm^3 (see Fig. 1.1), when the deconfinement transition happens, and the system undergoes a crossover from the hadronic phase to the quark-gluon plasma phase.

Of course, this is not a proof that the quark-gluon plasma has been created. The first strong indication came from the spectra of the "soft" particles (those with momenta smaller than $p_T \sim 2 - 5$ GeV), which comprise the bulk of the observed hadrons. These spectra drop exponentially with $\exp(-\sqrt{m^2 + p_T^2}/T_{\text{eff}})$, as opposed to the "hard" particles, whose spectra have a power law shape. The exponentially falling spectra show up in the case of the proton-proton (pp) collisions (which will be our standard baseline for comparison), but what is different here is that the effective temperatures T_{eff} extracted from these spectra depend strongly on particle species (see e.g. [71]). This dependence is consistent with having a system of thermally equilibrated particles that radially expands, so that all particle species have the same radial velocity (which is about $0.6c$ in central collisions [8]), but due to their different masses, that results in a different momentum boost of the final spectra.

The story from the previous paragraph indicates something that we might have expected: a (fluid) medium, where created particles explode radially, but more surprising conclusions come from a more closer look at the particle distributions in non-central

[4] At this point, this value is only a rough estimate of a typical size of the system, but, as we will soon see, the elliptic flow data in fact indicates that after about ~ 1 fm/c, the system is in thermal equilibrium.

collisions, which will be the topic of the next section.

1.2.2 Elliptic flow

In a simplistic view of a heavy ion collison, we can imagine two Lorentz-contracted "pancakes" colliding in the beam direction at some impact parameter b, see Fig. 1.5 for an illustration of this.

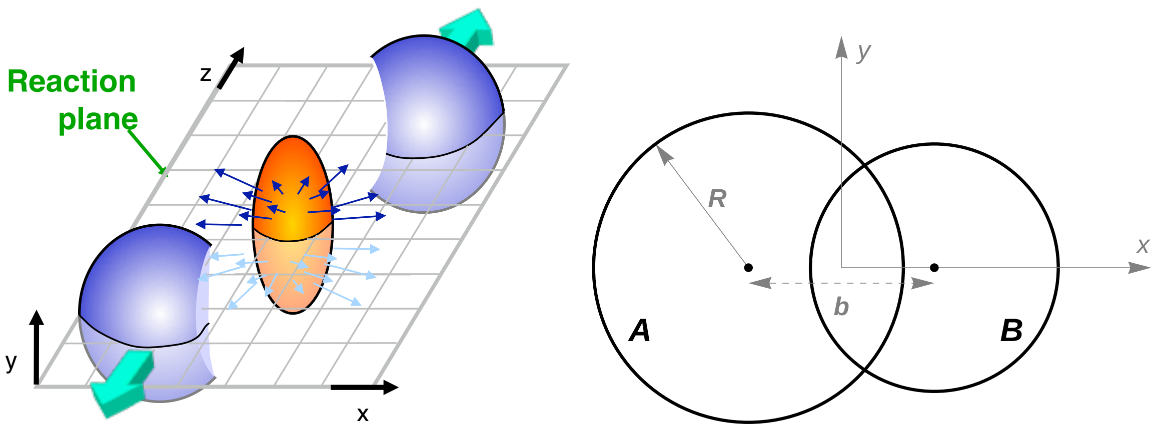

Figure 1.5: *An illustration of a non-central collision with impact parameter b of two nuclei with mass numbers A and B. (Left figure taken from [72].)*

Depending on the size of b, we have central, semi-peripheral or peripheral collisions. Of course, in an experimental setting, it is not possible to select in some way what impact parameter we are interested in; rather, one can order the events according to their multiplicities and then bin them in so-called centrality bins, so, for example, a collection of 5% of the events with highest multiplicities is then called the "0-5% centrality bin". This is possible because the smaller the impact parameter, the higher the multiplicity, and with a particular model (such as the Glauber model, which will be discussed in Section 1.3.1) it is possible to exactly quantify this.

Now let us analyze the particle spectrum in a bit more detail. In the previous section we analyzed the momentum distributions, and now we will also add the rapidity dependence.

In Eq. (1.17) we defined pseudorapidity, which is in fact closely related to the spacetime rapidity y,

$$y = \frac{1}{2}\log\left(\frac{t+z}{t-z}\right) , \tag{1.18}$$

where z is the beam direction and t is time (in the laboratory frame). Spacetime rapidity has a simple relation to the pseudorapidity:

$$y = \frac{1}{2}\log\left(\frac{E+p_z}{E-p_z}\right) = \eta - 2\frac{\cot\theta}{\sin\theta}\frac{m_\pi^2}{4p^2} , \tag{1.19}$$

where we used $p_z/p = \cos\theta$ and assumed that the observed particle is a pion. From here we get:

$$\left.\frac{d\eta}{dy}\right|_{\theta=\pi/2} = 1 + \frac{m_\pi^2}{2p^2} . \tag{1.20}$$

Hence, in general, when $p \gg m$, we can approximate $\eta \approx y$.

In addition to this, we will be also interested in the azimuthal angle ϕ dependence of the particle distributions, where ϕ is measured with respect to the x-axis in Fig. 1.5. A natural way to analyze such particle distributions is using a Fourier decomposition:

$$\frac{dN}{d^2p_T dy} = \frac{1}{2\pi p_T}\frac{dN}{dp_T dy}\left[1 + 2v_1(p_T)\cos\left(\phi - \Phi_R\right) + 2v_2(p_T)\cos\left(2(\phi - \Phi_R)\right) + ...\right] , \tag{1.21}$$

where Φ_R is the azimuthal orientation of the reaction plane (which, in accordance with Fig. 1.5 we take to be zero, but is in principle unknown) and with v_n we denote the harmonic coefficients,

$$v_n \equiv \left\langle e^{in(\phi-\Phi_R)}\right\rangle , \tag{1.22}$$

also called the "n-th order flow", for reasons that will become clear in a moment. These coefficients, as well as $dN/dp_T dy$, implicitly depend on rapidity y, as well as the impact parameter b (or the centrality bin) and the particle species. In particular, v_1 is called the directed flow, v_2 the elliptic flow, v_3 the triangular flow and so on. As it is visible from Fig. 1.5, for identical nuclei at midrapidity ($y = 0$), we expect, on average, that the odd flow coefficients vanish, $v_{2n+1} = 0$, due to the $\phi \to \phi + \pi$ symmetry of the almond-shaped region (however, event-by-event they will be in general non-zero). Hence the first (on average) non-vanishing flow coefficient in the particle distribution is the elliptic flow v_2. From its definition in (1.21) we see that it tells us about the asymmetry of the particles measured in the x-direction versus the particles measured in the y-direction in Fig. 1.5. And, as we can see from Fig. 1.6, these angular asymmetries were quite big at RHIC: for $v_2 \approx 0.15$ we see from (1.21) that this means that approximately twice as many particles have been observed going in the x-direction than in the y-direction. The angular asymmetries are similarly large at the LHC at $\sqrt{s_{NN}} = 2.76$ TeV [73–75].

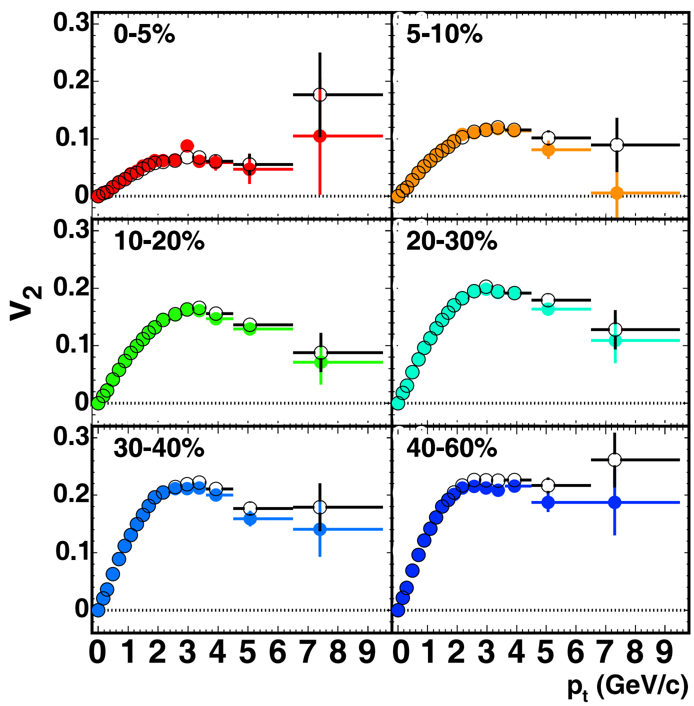

Figure 1.6: *Elliptic flow v_2 as a function of p_T for charged hadrons for different centrality bins for AuAu collisions at RHIC at $\sqrt{s_{NN}} = 200$ GeV. (Taken from [76].)*

If the observed particles came from independent pp collisions, we would get an azimuthally symmetric distribution, so obviously there must be some strong correlation effects at play. For these reasons, perhaps the next natural step is to try and use the theory of hydrodynamics to see if one can describe the data in Fig. 1.6 quantitatively. Some basic concepts and definitions in relativistic hydrodynamics are summarized in Appendix A.2. In [77] it was first shown how first order dissipative hydrodynamics can in fact successfully describe the elliptic flow data measured at RHIC, see Fig. 1.7.

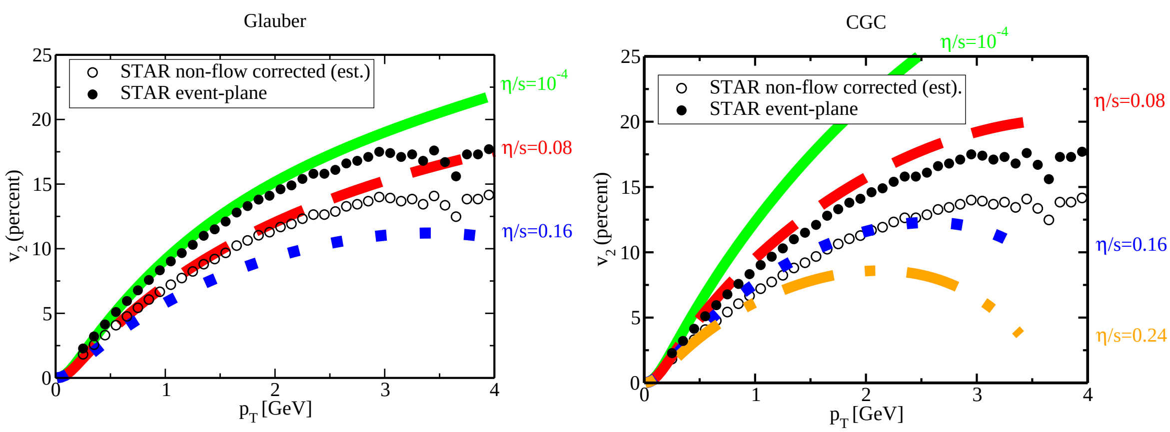

Figure 1.7: *Comparison of a conformal relativistic viscous hydrodynamic model [11] to experimental data on charged hadron minimum bias elliptic flow by STAR [77], for two different sets of initial conditions (CGC and Glauber). (Taken from [11].)*

In fact, as we can see from Fig. 1.7, the ratio of shear viscosity to entropy density needed to achieve successful fits was quite small, $\eta/s \ll 1$, implying that the medium created was in fact a near-ideal (near-perfect) liquid. This in general implies strong coupling of the underlying theory, for the following reasons. In a standard quasiparticle picture, shear viscosity is telling us how efficient the system is in transporting, say, $x-$directed momentum in the y direction. Large shear viscosity therefore means large mean free paths and hence in general implies weak coupling[5]. On the other hand, low η/s means that the

[5]Computation of the shear viscosity using the Kubo formula (which will be discussed in Section 3.2.3) shows that at high temperatures, due to asymptotic freedom, the shear viscosity in QCD diverges (see e.g. [78]). Similarly, since the low temperature hadron gas is also weakly interacting, the shear viscosity diverges in that regime as well.

momentum is not easily transported over distances of the order of $s^{-1/3}$ and, consequently, that there are no (well defined) quasiparticles with long mean free paths, which directly leads to strong coupling. As we will see in Section 3.2.3, the AdS/CFT result for η/s agrees very well with the values from Fig. 1.7. Another important conclusion is that the local equilibrium must set in very soon after the collision, since otherwise the almond shaped region in Fig. 1.5 would have time to isotropize and the angular asymmetries would not be as large as measured (Fig. 1.6). In fact, various hydrodynamic simulations imply that τ_{eq} is on the order of 1 fm/c.

We should also note that besides getting the right momentum dependence of v_2, hydrodynamic models are also successful in reproducing the centrality dependence, as well as the hadron species dependence of v_2. The model employed in [11] was based on (2+1)-dimensional relativistic viscous hydrodynamics (where the hydro fields depend on proper time τ and transverse directions $\vec{x}_\perp$) and since then there have been many improvements along these lines. These include fluctuating initial conditions, inclusion of hadronic diffusion processes, (3+1)-dimensional hydrodynamics (with additional rapidity dependence), and others. This subject is outside the scope of this thesis, but a good review can be found in [79].

The results presented lead to the following conclusion: the medium produced in ultra-relativistic heavy ion collisions at RHIC is a strongly coupled, near-perfect fluid, which reaches an approximate local thermal equilibrium within about 1 fm/c after the collision. This fluid nature easily explains the observed angular asymmetries: the spatial azimuthal anisotropy of the almond shaped region implies anisotropic pressure gradients, which then get converted into the observed asymmetry in the momentum space. The size of the elliptic flow v_2 characterizes this efficiency of translating the initial pressure gradients to the collective flow.

1.2.3 Jet quenching

From a perspective of a theoretical physicist, the term "jet quenching", in the context of heavy ion collisions, typically refers to an energetic quark or gluon that is plowing through the strongly coupled quark-gluon plasma and losing energy through the interactions with the medium. To an experimental physicist, jets are something different: they are defined as a collection of particles in the $y - \phi$ space around some energetic leading hadron, and depend on a particular jet algorithm used to define them. In this thesis, by jet quenching we will understand the energy loss of an energetic parton and its subsequent hadronization, i.e. we will focus only on single particle observables.

Jet quenching was one of the first proposed strong signals of the quark-gluon plasma formation [80]. A rather clear example of manifestation of jet quenching at RHIC are the two-particle correlations in Au-Au collisions, compared to the measurements in pp collisions at the same energy, shown in Fig. 1.8.

In these measurements, one first chooses the trigger momentum (between 4 and 6 GeV in Fig. 1.8) and some associated momentum range Δp_T: this means that, once a particle with the momentum equal to the trigger momentum is detected, we then look for other particles that have momentum within the Δp_T range and plot their azimuthal angle and pseudorapidity dependence, with respect to the trigger particle. For purposes of demonstrating the phenomenon of jet quenching, perhaps the most interesting plot in Fig. 1.8 is the lower-left one: there in the pp case we clearly see two peaks at $\Delta\phi = 0$ and $\Delta\phi = \pi$, indicating two back-to-back jets. However, in the AA case, the away-side peak ($\Delta\phi = \pi$) is missing, clearly indicating jet quenching, since the energy of the energetic parton has been transferred to the thermal constituents of the plasma, the soft particles with $p_T < 2$ GeV: this is nicely indicated in the upper left plot with the widening of the away side distribution of soft particles. The picture we have in mind is that the hard

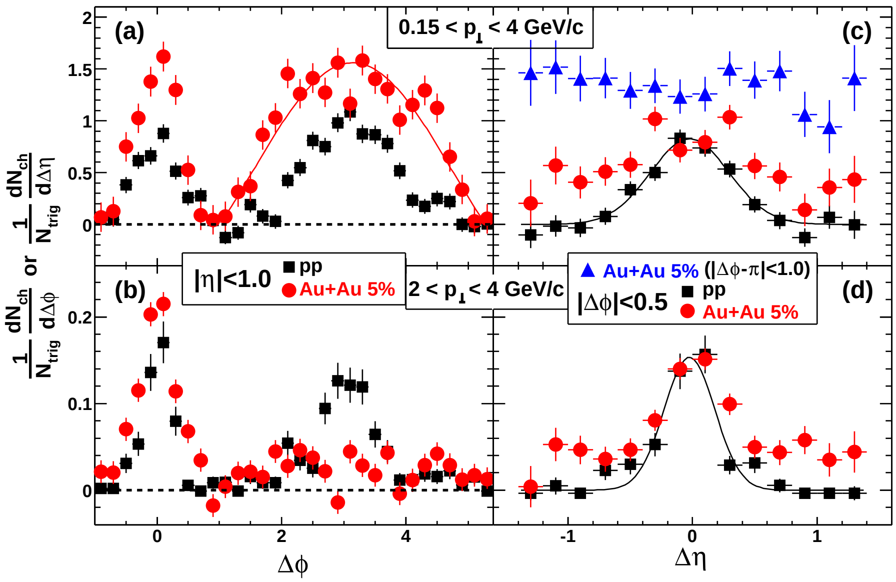

Figure 1.8: *Two-particle azimuthal $\Delta\phi$ and pseudorapidity $\Delta\eta$ correlations (with background subtracted) in central Au-Au collisons at RHIC at $\sqrt{s_{NN}} = 200$ GeV (colored dots), compared to the pp results (black dots). The trigger momentum was $4 < p_T^{\text{trig.}} < 6$ GeV and the associated momentum ranges are indicated. (Taken from [13].)*

process responsible for creating the back-to-back jet occurred close to the "edge" of the medium, so one of the partons had to traverse much larger distance in the medium and hence lose more energy than the other one; see Fig. 1.9 for an illustration of this.

Let us now try to analyze the phenomenon of jet quenching more quantitatively. We start with *pp* collisions, which is what we will compare the *AA* data to. In *pp* collisions, rarely, partons scatter with a high momentum transfer Q. These high-Q processes lead to production of highly energetic, back-to-back hadrons with p_T on the order of several GeV. At such high Q, perturbative QCD is particularly successful in calculating the rates of these processes thanks to the QCD factorization theorem (see e.g. [81] and references therein), which essentially consists in separating the soft scales from the hard

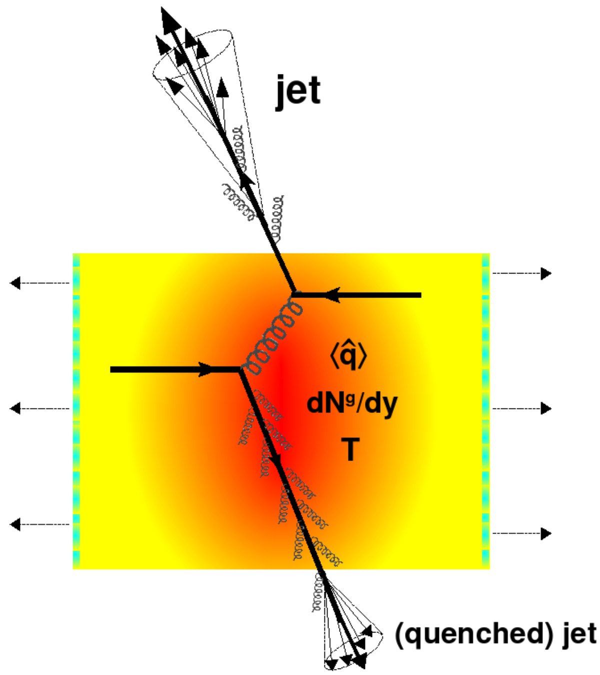

Figure 1.9: *An illustration of jet quenching in a heavy ion collision. After a hard scattering of two partons, one of them goes directly to the vacuum and hadronizes, while the other one has to plough through the strongly coupled quark-gluon plasma, where it interacts with the medium, loses energy through medium-induced gluon radiation (which will be discussed in Section 2.1.2) and finally hadronizes. (Taken from [18].)*

ones. Schematically, the cross section for production of a high-p_T hadron h is

$$d\sigma_{pp\to h}^{\mathrm{hard}} = \sum_{a,b,c} f_{a/p}(x_1, Q^2) \otimes f_{b/p}(x_2, Q^2) \otimes d\sigma_{ab\to c}^{\mathrm{hard}}(x_1, x_2, Q^2) \otimes D_{c\to h}(z, Q^2)\,. \qquad (1.23)$$

Here $f_{a/p}(x, Q^2)$ is the parton distribution function (PDF), which expresses the probability of finding the parton a with momentum fraction x inside the proton p, $D_{c\to h}(z, Q^2)$ is the fragmentation function (FF), which expresses the probability that the parton c fragments into the hadron h with fractional momentum z, and, finally, $d\sigma_{ab\to c}^{\mathrm{hard}}(x_1, x_2, Q^2)$ is a cross section for a particular (hard) process $ab \to c$, computable in perturbative QCD. Although non-perturbative, the parton distribution functions and the fragmentation functions are universal (process-independent) and hence can be measured experimentally. The factorization paradigm expressed in (1.23) therefore consists in separating the long distance interactions associated with the soft PDF's and FF's from the short distance ones associated with the hard parton-parton processes.

In passing to a collision of two heavy nuclei with mass numbers A and B, (1.23) will change:

$$d\sigma^{\rm hard}_{AB\to h} = \sum_{a,b,c} f_{a/A}(x_1, Q^2) \otimes f_{b/B}(x_2, Q^2) \otimes d\sigma^{\rm hard}_{ab\to c}(x_1, x_2, Q^2) \otimes P_c(\Delta E) \otimes D_{c\to h}(z, Q^2)\,. \tag{1.24}$$

where we now have nuclear PDFs $f_{a/A}(x_1, Q^2)$, and where $P_c(\Delta E)$ expresses the probability that the parton c will lose energy ΔE due to the interactions with the medium. Here we have assumed that the hard process $d\sigma^{\rm hard}_{ab\to c}(x_1, x_2, Q^2)$ remains unchanged, because it occurs on a scale $\sim 1/Q$, which is too short to resolve the existence of the medium. The combination $P_c \otimes D_{c\to h}$ is sometimes referred to as the modified fragmentation function. The first approximation is to approximate the nuclear PDF's with the proton PDF's, although in reality these are modified by initial-state shadowing and anti-shadowing effects [82]. If we forget, for the moment, about the medium effects in (1.24), i.e. the energy loss probability $P_c(\Delta E)$, the only difference between $d\sigma^{\rm hard}_{AB\to h}$ and $d\sigma^{\rm hard}_{pp\to h}$ in (1.23) is the effective number of inelastic binary nucleon-nucleon collisions at a given impact parameter b, $N_{\rm bin}(b)$ (which we will derive in Section 1.3.1, starting from some simple geometrical considerations). Therefore, in order to inspect the medium effects, it makes sense to take the ratio of the AA cross section, scaled by the number of binary collisions, and the pp one, or, equivalently, their corresponding particle yields:

$$R^h_{AB}(p_T; b) = \frac{\frac{dN_{AB\to h}}{dp_T d\eta}}{N_{\rm bin}(b)\frac{dN_{pp\to h}}{dp_T d\eta}}\,, \tag{1.25}$$

where $dN_{AB\to h}/dp_T d\eta$ denotes the particle yield of hadrons h as measured in a heavy ion AB collision and $dN_{pp\to h}/dp_T d\eta$ denotes the particle yield at the same momentum and same $\sqrt{s_{NN}}$, but in a proton-proton collision. Quantity R_{AB} is called the nuclear modification factor and it will be of central interest in this thesis. Of course, R_{AB} is also a function the collision energy $\sqrt{s}$ and pseudorapidity η, dependence on which we will, for simplicity, suppress. As is clear from the previous discussion, if we neglect the medium (and initial state) effects and think of the nucleus-nucleus collision as a collection of N_{bin} incoherent nucleon-nucleon collisions, R_{AB} should be approximately equal to unity. However, at highest RHIC energies, the first results [12–14] indicated very strong suppression: as we can see from Fig. 1.10, in the most central collisions at RHIC, $R_{AA} \approx 0.2$, a clear sign of significant jet quenching. The jet quenching remains strong at even higher energies, that are accessible to the LHC [83, 84].

The nuclear modification factor is, as we would expect, mainly influenced by the effects of parton energy loss in the medium, but there may be also some important initial state effects, through the modification of the parton distribution functions. For checking the importance and size of these effects, a good control experiment are the collisions of protons (whose PDF's are known) and nuclei (pA collisions), or, at RHIC, collisions of deuterons and nuclei (dA collisions). Apart from deviations from unity due to initial state effects (shadowing and Cronin [86]), $R_{dAu} \gtrsim 1$ for all transverse momenta and centralities [87, 88], indicating the absence of jet quenching and reaffirming the interpretation that the jet quenching observed in AA collisions comes from the energy loss in the medium, which is, presumably, absent in dA (pA) collisions.

As is obvious from Fig. 1.10, the nuclear modification factor shows a strong centrality dependence, in accordance to the interpretation that, at larger impact parameter, the size of the medium is smaller, and hence the jet quenching effects are not as pronounced as in the central collisions. Photons produced in the heavy ion collisions are not quenched

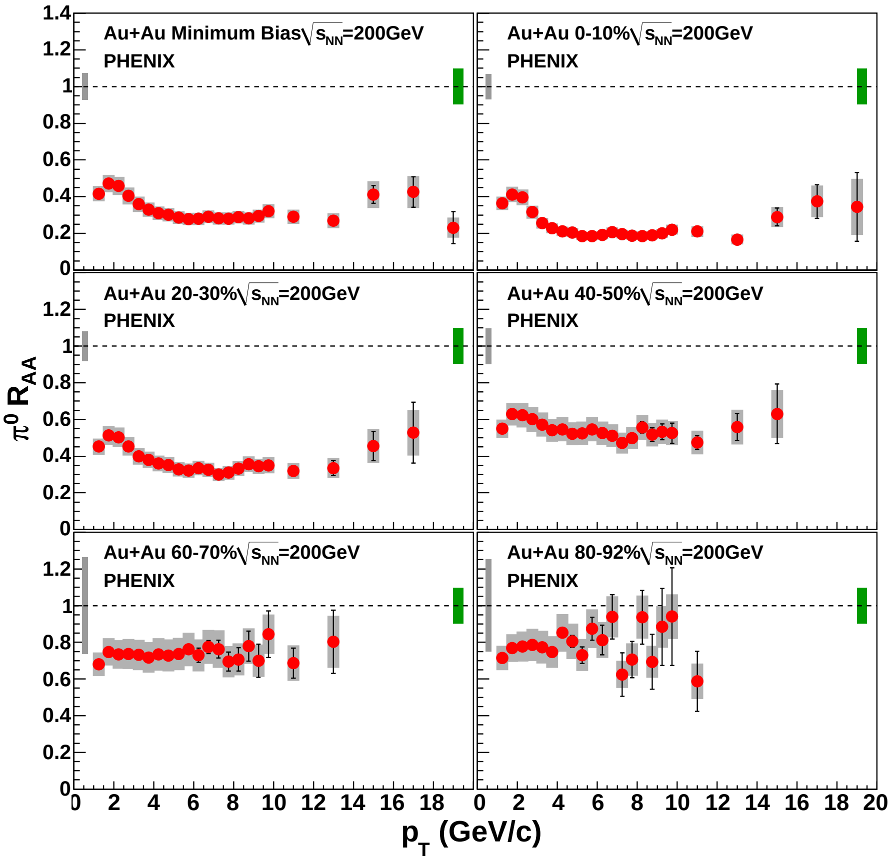

Figure 1.10: *Nuclear modification factor R_{AA} for neutral pions as a function of momentum in Au-Au collisons at RHIC at $\sqrt{s_{NN}} = 200$ GeV, for various centrality classes. (Taken from [85].)*

($R_\gamma \approx 1$) [89], providing additional evidence that jet quenching is indeed a final state effect. It is also important to notice that at high p_T, R_{AA} seems to be approximately independent of momentum and hadron species [13, 90, 91], further reaffirming the idea that it is the partons that lose energy in the medium and that the hadronization occurs outside the medium.

All these results support the interpretation that the observed nuclear suppression of various hadrons comes from jet quenching of the associated partons in the quark-gluon plasma: the interactions of the parton with the medium will affect its (transverse) momentum, and hence modify the observed p_T-spectrum of its hadron. And because the production of these hard partons is well known in pQCD, they represent well calibrated tools to probe the properties of the quark-gluon plasma. For these reasons they are often referred to as "hard probes", and this way of studying the properties of the medium is termed "tomography".

In addition to the suppression of the spectrum of the high-p_T (leading) hadron that we will be most interested in, there are many other interesting phenomenological consequences of parton energy loss. Apart from losing energy, partons experience random momentum "kicks" from the medium which can cause transverse momentum broadening and modify the jet shapes non-trivially. The medium affects the partons, but partons will also affect the medium: in addition to the simple structures on the away side as in Fig. 1.8, it is also possible to observe interesting double-peak structures, perhaps due to Mach cones [92].

1.2.4 Stages of a heavy ion collision

In the last two sections, we talked about the, for us, two most interesting phenomenological aspects of heavy ion collisions: elliptic flow, because it provides evidence that the quark-gluon plasma is strongly coupled, and jet quenching, as its observables we will try to calculate using models of (holographic) energy loss. There is, of course, much more experimental data measured by RHIC and LHC that exhibit different features with respect to the analogous pp collisions and hence provide additional evidence to support the claim that the quark-gluon plasma has been created: for example, the J/ψ suppression[6] [93]

[6] J/ψ is the lightest of the $\bar{c}c$ mesons and can be pair-produced in the initial high energy collision. Because it is composed of rather heavy quarks, we can describe it non-relativistically utilizing the idea of a $\bar{q}q$ potential (1.6) more reliably. However, in the deconfined quark-gluon plasma, this potential is replaced by the Debye-screened potential (1.16) and if the screening length $\lambda_D \sim 1/\mu$ falls below the analogue of the Bohr radius for J/ψ, we expect to see the dissociation of the meson. And because c quarks are more likely to form mesons with the lighter quarks, we expect to see fewer J/ψ in the heavy

and the strangeness enhancement[7] [94]. The vast amount of experimental data and the theory behind it have culminated in the "standard" picture of the heavy ion collision, which is illustrated in Fig. 1.11. It consists of three main stages: the initial and the pre-equilibrium stage, the quark-gluon plasma phase and its hadronization and, finally, the hadron gas phase. Let us briefly say a few words about each of these.

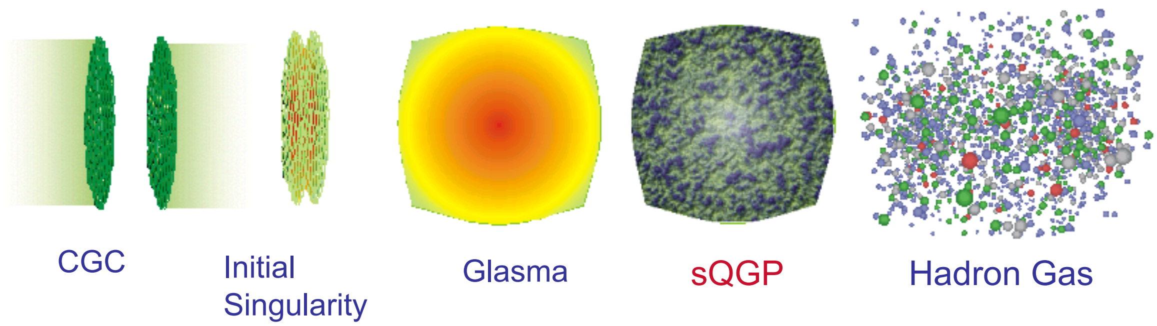

Figure 1.11: *Illustration of a relativistic heavy ion collision and the various stages that follow it, according to the "standard model" that is often used. (Taken from [95].)*

The first step is the description of the high energy nucleus. As we know from the DIS experiments [96], the density of the gluons inside the proton grows at low longitudinal momentum fraction $x = p_{\text{parton}}/p_{\text{proton}}$. Since high energies of nuclei mean small x, the ultra-relativistic nucleus is hence dominated by gluons. As the gluon density grows (at fixed Q^2), the gluons, with the transverse size on the order of $\sim 1/Q$, will eventually start to overlap in the transverse plane, i.e. the gluon density will start to saturate. At a given x, this defines the saturation momentum $Q_{\text{sat}}(x)$, which grows with the gluon density and therefore the collision energy, and at sufficiently high energies it will be much larger than Λ_{QCD}. Intuitively, because the gluons are forced at high density to occupy higher momenta, Q_{sat} becomes the relevant scale in the saturation regime, and, because at

ion collision that in the analogous (scaled) pp collisions.

[7]Strangeness enhancement means that many more hadrons containing $\bar{s}$ and s quarks are produced in heavy ion collisions than in the analogous pp collisions. One proposal to explain this is that, due to restoration of the chiral symmetry in the quark-gluon plasma and a high density of gluons, production of $\bar{s}s$ pairs through processes such as the gluon fusion $gg \to \bar{s}s$ is more likely.

high energies $Q_{\rm sat} \gg \Lambda_{\rm QCD}$, normally non-perturbative "sea gluons" can now be treated perturbatively. Also, high density of gluons means high occupation numbers and justifies a classical treatment, leading to a description of the low-x gluons by classical coherent fields: this is called the color condensate. In the language of the effective field theory, the high-x gluons act as sources for these classical, small-x gluons (i.e. one integrates out the low-x degrees of freedom to generate the sources). Now, the time evolution of these fast, high-x gluon sources is slowed down due to the time-dilation, which is then transferred to the low-x gluons as well. This means that we can approximate the low-x gluons by static classical fields, and this long time scale evolution of gluons and their sources is akin of glasses. This finally leads to the effective theory of the color glass condensate (CGC) [97–104]. A good review of CGC can be found in [105].

Therefore, we can describe the two ultra-relativistic nuclei as two colliding sheets of color glass condensate. At high energies, we expect the nuclear transparency to set in: the two colliding sheets pass through each other, carry the baryonic matter away and in the process deposit the baryon-free matter in the space between them. A possible description of how this happens is naturally extended from the concept of CGC: as the sheets collide, they become charged with color electric and color magnetic charge, which results in the creation of longitudinal color electric and color magnetic fields between the two receding nuclei, the so-called glasma [106–111] (see Fig. 1.12 for an illustration of this). Glasma eventually decays into a system of $\bar{q}q$ pairs and gluons, the quark-gluon plasma. This system then quickly thermalizes and its evolution is well described by relativistic viscous hydrodynamics, as we saw in Section 1.2.2.

As the fireball of quark-gluon plasma expands radially and longitudinally, it cools down and we expect to see the transition to the hadron gas phase. The hadronization can take place through the processes of recombination and fragmentation, depending on the p_T range of the partons. In the low to intermediate p_T range (i.e. the soft sector, up

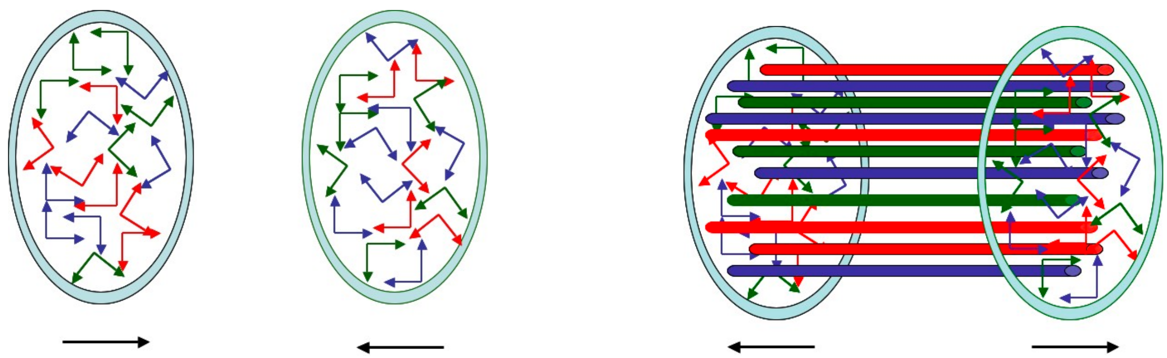

Figure 1.12: *An illustration of the colliding sheets of color glass condensate (left) and the glasma as it appears in early stages of hadronic collisions (right). (Taken from [95].)*

to about 5 GeV), the hadrons are formed by recombination (or coalescence) [112, 113] of partons that were part of the medium, i.e. thermal quarks and antiquarks. In the high p_T range (i.e. the hard sector), hadronization takes place through fragmentation that we mentioned in Section 1.2.3. After hadronization, the hadronic matter becomes more and more dilute and at some point the inelastic hadron-hadron collisions will not be able to modify the abundance ratios of hadrons anymore. The temperature at which this happens is called the chemical freeze-out temperature and is about 155-180 MeV at RHIC at $\sqrt{s_{NN}} = 200$ GeV [114]. Finally, the hadrons become dilute enough so that the interactions become negligible: the hadrons from thereon free stream and the momentum distributions do not change anymore. The temperature at which this happens is called the kinetic freeze-out temperature, which is about 90 MeV at RHIC [8]. The freeze-out processes are typically described within the Cooper-Frye formalism [115], where one defines a spacetime hypersurface $\Sigma(x^\mu)$ into which one dots the flux of the particles according to some space-momentum distribution $f(x^\mu, p^\mu)$.

1.3 Modeling the plasma

In this section we will develop a simple model of the quark-gluon plasma that we will use in the calculation of the nuclear modification factor in the coming chapters, starting with some (holographic) energy loss model. The main goal is to develop a formula for the temperature of the plasma that will take into account the non-trivial initial transverse profile of the plasma and its subsequent spacetime evolution.

1.3.1 Glauber model

The Glauber model [116] is a simple way to describe the initial conditions of the quark-gluon plasma in ultrarelativistic nucleus-nucleus collisions (another possible set of initial conditions is provided by the CGC, as denoted in Fig. 1.7 and discussed in Section 1.2.4). There are two kinds of Glauber models often used, the optical one and the Monte Carlo one (a good review of both models can be found in [117] and [118]). The main difference between the two is that the optical Glauber model assumes a continuous distribution of nucleons in the colliding nuclei, hence allowing for the development of simple and analytical formulas. Monte Carlo Glauber, on the other hand, is more advanced and treats collisions event-by-event, sampling the positions of nucleons according to some distribution. In this thesis we will use the simpler, optical Glauber model, which captures most of the phenomenological features of heavy ion collisions[8], but misses some more advanced ones (e.g. fluctuations).

The starting point in the Glauber model is the choice of a realistic function that describes the density of nucleons in a nucleus with mass number A. We will use the

[8]Since the main goal of this thesis is the application of holographic models of energy loss to quark-gluon plasma, we will focus our attention on obtaining the main phenomenological features of the relevant observables and inspecting whether or not these models can approach the experimental data without leaving the regimes of validity of various approximations in AdS/CFT. For demonstrating this, the optical Glauber model should be sufficient, while precision fits with a more realistic setting (including a better account of the plasma initial conditions) are left for the future.

standard Woods-Saxon distribution [119],

$$\rho_{WS}(\vec{r}) = \frac{\rho_0}{1 + \exp\left[(r - R)/\chi\right]}\,, \tag{1.26}$$

where R is the mean radius of the nucleus, which for our cases of Au ($A = 197$) and Pb ($A = 207$) nuclei is well described by

$$R \approx 1.1\, A^{1/3}\,\mathrm{fm}\,. \tag{1.27}$$

In (1.26) χ is the Woods-Saxon diffuseness parameter, for which the standard choice is $\chi = 0.54$ fm. Distribution (1.26) is normalized so that

$$\int d^3x\, \rho_{WS} = A\,. \tag{1.28}$$

With this normalization, ρ_{WS} tells us the number of nucleons per unit volume.

The next step is to define the nuclear thickness function:

$$T_A(\vec{x}_\perp) = \int dz\, \rho_{WS}(\vec{x}_\perp, z)\,, \tag{1.29}$$

where we take z to be the beam direction. This function gives the number of nucleons per unit transverse area. Now we consider a collision of two nuclei at an impact parameter b with coordinate system oriented as in Fig. 1.5. We will be mostly interested in a collision of two identical nuclei (AA collision), but it is easy to keep the analysis a bit more general. We will treat the nucleus-nucleus collision by building it up from individual nucleon-nucleon processes. In high energy collisions, one typically ignores diffractive and elastic processes, which makes inelastic nucleon-nucleon interactions dominant. Cross sections for those can be found in [120]:

$$\begin{aligned} \sigma_{NN}^{\text{in}} &= 42\,\text{mb} \quad \text{at} \quad \sqrt{s_{NN}} = 200\,\text{GeV}\,, \\ \sigma_{NN}^{\text{in}} &= 63\,\text{mb} \quad \text{at} \quad \sqrt{s_{NN}} = 2.76\,\text{TeV}\,. \end{aligned} \tag{1.30}$$

We will take the optical limit, in which we assume that, due to high energy, nucleon trajectories are approximately eikonal and that their distributions in the nuclei are smooth, which will allow us to develop simple analytic expressions.

In this limit, we define the number density of binary collisions:

$$T_{AB}(x, y; b) = \sigma_{NN}^{\text{in}} T_A\left(x + b/2, y\right) T_B\left(x - b/2, y\right)\,, \tag{1.31}$$

where we are assuming the geometry of Fig. 1.5, in which the left nucleus has mass number A and the right one B. For sake of simplicity we will suppress the implicit b dependence of this and all other quantities that will follow. The interpretation of (1.31) as giving the number of inelastic binary nucleon-nucleon collisions per unit transverse area comes from the following reasoning. $(T_A/A)d^2x_\perp$ is a probability of finding one nucleon in area $d^2x_\perp$ and hence $(T_A/A)(T_B/B)d^2x_\perp$ gives a joint probability per unit area for nucleons being located in their respective area elements $d^2x_\perp$. The probability of one interaction is obtained by multiplying that number by the cross section σ_{NN} and then the total number of interactions is obtained by multiplying this by the total number of nucleons, AB. The total number of binary collisions is given by

$$N_{\text{bin}} = \int d^2x_\perp\, T_{AB}(x, y)\,, \tag{1.32}$$

which will be used in calculating R_{AB} (1.25).

We can use similar logic to find the number of wounded nucleons (participants). The number of wounded nucleons per unit area in nucleus A is given by the number of nucleons per unit area T_A, times the probability P_B that one of them had at least one interaction. Probability of one interaction is $\sigma_{NN}(T_B/B)$, probability of not having that interaction is $1-\sigma_{NN}(T_B/B)$ and hence probability of not having a single interaction from B is simply that probability to the power of B (of course, there are combinatorial factors involved, but one arrives at the same expression) and so the probability of having at least one interaction is

$$P_B = 1 - \left[1 - \frac{T_B(x-b/2,y)}{B}\sigma_{NN}^{\text{in}}\right]^B . \tag{1.33}$$

If B is large enough, one can approximate this with an exponential. Multiplying (1.33) by T_A to get the number of wounded nucleons in A and then adding the analogous contribution from the other nucleus, we arrive at the Glauber participant nucleon profile density,

$$\begin{aligned}\rho_{\text{part}}(x,y) = T_A(x+b/2,y)\left[1-\exp\left(-\sigma_{NN}^{\text{in}}T_B(x-b/2,y)\right)\right] + \\ T_B(x-b/2,y)\left[1-\exp\left(-\sigma_{NN}^{\text{in}}T_A(x+b/2,y)\right)\right] .\end{aligned} \tag{1.34}$$

The total number of participants is given by

$$N_{\text{part}} = \int d^2x_\perp\, \rho_{\text{part}}(x,y)\,. \tag{1.35}$$

1.3.2 Bjorken model

One of the most important phenomenological entries for energy loss models is the evolution of the temperature of the plasma in space and time, for which we will use the standard Bjorken model [70]. Bjorken model consists in assuming a rapid thermalization of the system after the collision, following the hydrodynamic evolution in which the macroscopic degrees of freedom, such as energy density ε and pressure P, are boost invariant. This is a good approximation at high energies if we focus on the central rapidity region, since boosts are additive in rapidity and so longitudinal boosts that are much smaller than the (high) collision energy should not affect the results. This translates into the evolution of the system looking the same in all references frames near the center-of-mass frame.

A convenient set of coordinates will be the spacetime rapidity y (eq. (1.18)) and proper time τ:

$$y = \frac{1}{2}\log\left(\frac{t+z}{t-z}\right), \qquad \tau = \sqrt{t^2 - z^2}\,. \tag{1.36}$$

Boost invariance means that the energy density and pressure are functions of proper time only, $\varepsilon(\tau)$ and $P(\tau)$. We also assumed that the system is homogeneous in the transverse directions, which means that we will, for now, neglect the transverse expansion (see discussion at the end of Section 1.2.2 more realistic models that include it). For this reason, it is convenient to solve the Euler's equation (A.6) for the energy-momentum tensor,

$$\nabla_\mu T^{\mu\nu} = 0\,, \tag{1.37}$$

in the $y-\tau$ coordinates, i.e. $\tilde{x}^\mu = (\tau, \vec{x}_\perp, y)$. From (1.36) we easily get the transformation matrix $M^\mu{}_\nu = \partial\tilde{x}^\mu/\partial x^\nu$, where $x^\mu = (t, \vec{x}_\perp, z)$, from which we easily get the metric and the four-velocity:

$$\begin{aligned} \tilde{u}^\mu &= (1,0,0,0)\,, \\ \tilde{g}^{\mu\nu} &= \mathrm{diag}(-1,1,1,1/\tau^2)\,, \end{aligned} \tag{1.38}$$

where we work in the mostly positive signature. The only non-vanishing Christoffel symbols (entering the covariant derivative ∇_μ) of this metric are

$$\Gamma^y_{\tau y} = \frac{1}{\tau}, \qquad \Gamma^\tau_{yy} = \tau\,. \tag{1.39}$$

The energy momentum tensor is hence

$$\begin{aligned}\tilde{T}^{\mu\nu} &= (\varepsilon + P)\tilde{u}^{\mu}\tilde{u}^{\nu} + P\tilde{g}^{\mu\nu} \\ &= \operatorname{diag}\left(\varepsilon, P, P, \frac{P}{\tau^2}\right) .\end{aligned} \tag{1.40}$$

Plugging this in the $\nu = \tau$ component of the Euler equation (1.37), we get:

$$\frac{d\varepsilon}{d\tau} + \frac{\varepsilon + P}{\tau} = 0\,. \tag{1.41}$$

On the other hand, we know that for system at constant volume $d\varepsilon = T ds$, where s is the entropy density. Using this, together with another useful thermodynamical identity, $P + \varepsilon = Ts$, equation (1.41) becomes

$$\frac{ds}{d\tau} + \frac{s}{\tau} = 0\,, \tag{1.42}$$

which has a simple solution,

$$s(\tau)\tau = \text{const.} \tag{1.43}$$

This will be important in the next section in relating the initial state to the final one.

Let us now try and solve (1.41). First, note that:

$$\frac{d\varepsilon}{d\tau} = \frac{d\varepsilon}{dP}\frac{dP}{dT}\frac{dT}{d\tau}\,, \tag{1.44}$$

where $T(\tau)$ is the temperature, which is what we are ultimately interested in. The second term in (1.44) can be simplified by noting that, at constant volume, the identity $P+\varepsilon = Ts$ leads to $dP/dT = s$. The first term in (1.44) is just the speed of sound:

$$c_s^2(T) \equiv \frac{dP}{d\varepsilon} = \frac{s dT}{T ds} = \frac{d\log T}{d\log s}\,. \tag{1.45}$$

Using this in (1.44) and plugging it in (1.41), we can easily integrate:

$$\int_{T_0}^{T} dT' \frac{1}{T' c_s^2(T')} = \log\left(\frac{\tau_0}{\tau}\right) . \tag{1.46}$$

If we know the speed of sound as a function of temperature, this can be integrated to obtain the τ-dependence of the temperature. Speed of sound for finite temperature QCD can be obtained from lattice QCD, where the results are usually reported in the form of the trace anomaly of the energy-momentum tensor $\Theta(T) \equiv T^{\mu}{}_{\mu}$ (see Fig. 1.2),

$$\Theta(T) = \varepsilon - 3P = \frac{dP}{dT}T - 4P = \frac{d}{dT}\left(\frac{P}{T^4}\right)T^5 , \tag{1.47}$$

which can be easily integrated to obtain the pressure as a function of temperature, $P(T)$. Once that is known, one can obtain the energy density from the definition of the trace anomaly and then the speed of sound using (1.45). If, in some regime, we can approximate the speed of sound to be a constant, we can solve (1.46) exactly:

$$T(\tau) = T_0 \left(\frac{\tau_0}{\tau}\right)^{c_s^2} . \tag{1.48}$$

Furthermore, if the system is scale-invariant, the energy density must scale with T^3 and hence from (1.45) we have $c_s^2 = 1/3$, which gives the temperature evolution often referred to as the "Bjorken expansion":

$$T_{\mathrm{CFT}}(\tau) \propto \tau^{-1/3} . \tag{1.49}$$

1.3.3 Relation to the final state

We will now use the results of the previous two sections to relate the quantities from early times in the quark-gluon plasma phase to the quantities that are observable in the experiments. For that, we will first need some basic results from statistical physics, which are summarized in Appendix A.1. There, assuming that the quarks and gluons are massless, we derived the number and energy densities of the quark gluon plasma in (A.5). For a massless system, $P = \epsilon/3$ and the entropy density is simply $s = (4/3)(\epsilon/T)$. Defining the proportionality factor between s and n as

$$s = \xi n \tag{1.50}$$

we have for quark-gluon plasma

$$\xi_{\text{QGP}} = \frac{\pi^4}{45\zeta(3)} \frac{32 + 21N_f}{16 + 9N_f} \,. \tag{1.51}$$

For $N_f = 2$, $\xi_{\text{QGP}} \approx 3.92$, while for $N_f = 3$, $\xi_{\text{QGP}} \approx 3.98$. Here N_f denotes the number of "active flavors" (i.e. flavors that are considered to be part of the thermal medium), determined by the overall temperature scale. On the other hand, for a gas of massless pions we have $g_\pi = 3$ in (A.4), and hence

$$\xi_\pi = \frac{2\pi^4}{45\zeta(3)} \approx 3.6 \,. \tag{1.52}$$

The fact that $\xi_{\text{QGP}} \approx \xi_\pi$ will be useful in relating the final to the initial state.

Let us now express the entropy of the system at some time τ:

$$S(\tau) = \int d^3x \sqrt{h}\, s(\tau) = \int d^2x_\perp dy\, \tau s(\tau) \,, \tag{1.53}$$

where h is the determinant of the spatial part of metric (1.38). But, according to (1.43), $\tau s(\tau)$ is a constant, which means that the rapidity distribution of entropy is also a constant,

$$\frac{dS}{dy} = \text{const.} \tag{1.54}$$

Since entropy is proportional to the number of particles (eq. (1.50)), the Bjorken model correctly reproduces the observed rapidity plateau in the particle multiplicity (Fig. 1.4). We will use (1.54) to relate the state of the system at some τ_0 when the quark-gluon plasma has thermalized to the state at some later time τ_f, when the system has undergone the phase transition and partons have hadronized. At τ_f, if we assume that most of the multiplicity comes from the pions, we have, according to (1.50):

$$\left.\frac{dS}{dy}\right|_{\tau_f} = \xi_\pi \frac{dN_\pi}{dy} \,, \tag{1.55}$$

where dN_π/dy is the observed multiplicity of pions. At τ_0 we have:

$$\left.\frac{dS}{dy}\right|_{\tau_0} = \xi_{\mathrm{QGP}} \tau_0 \int d^2x_\perp \, n_{\mathrm{QGP}}(\tau_0, \vec{x}_\perp) \,. \tag{1.56}$$

According to (1.54), these entropies are equal and we arrive at

$$\frac{dN_\pi}{dy} f(\vec{x}_\perp) = \frac{\xi_{\mathrm{QGP}}}{\xi_\pi} \tau_0 \, n_{\mathrm{QGP}}(\tau_0, \vec{x}_\perp) \,, \tag{1.57}$$

where we have introduced a function f, normalized to unity, that describes the non-uniform transverse density profile of the medium. A reasonable choice is to use the normalized participant density (1.34),

$$f(\vec{x}_\perp) = \frac{\rho_{\mathrm{part}}(\vec{x}_\perp)}{N_{\mathrm{part}}} \,, \tag{1.58}$$

since the bulk of the plasma is soft (while the binary collision density (1.31) determines the distribution of the initial hard jet production points).

We are now in a position to express the temperature evolution of the plasma. From (A.5) we can express the temperature as a function of the entropy density and using that in (1.49) as the temperature at τ_0, we have[9]

$$T = \left[\frac{\pi^2}{\zeta(3)}\frac{1}{16+9N_f}n_{\text{QGP}}(\tau_0,\vec{x}_\perp)\frac{\tau_0}{\tau}\right]^{1/3}. \tag{1.59}$$

Plugging (1.57) here, with f given by (1.58), we finally have for the temperature profile of the plasma:

$$T_{\text{QGP}}(\vec{x}_\perp,\tau) = \left[\frac{\pi^2}{\zeta(3)}\frac{\xi_\pi}{\xi_{\text{QGP}}}\frac{1}{16+9N_f}\frac{dN_\pi}{dy}\frac{\rho_{\text{part}}(\vec{x}_\perp)}{N_{\text{part}}}\frac{1}{\tau}\right]^{1/3}. \tag{1.60}$$

As we said earlier, $\xi_\pi/\xi_{\text{QGP}} \approx 1$ for $N_f = 0,1,2,3$ and is often neglected.

In order to simulate the transverse expansion of the plasma, we will use a simple blast wave dilation factor [121, 122]:

$$r_{\text{bl}}(\tau) = \sqrt{1+\left(\frac{v_T\tau}{R}\right)^2}, \tag{1.61}$$

where R is the mean nuclear radius. We will take the transverse velocity to be $v_T = 0.6$. The effect of this dilation factor will be to replace $\rho_{\text{part}}(\vec{x}_\perp) \to \rho_{\text{part}}(\vec{x}_\perp/r_{\text{bl}})/r_{\text{bl}}^2$ in (1.60). A wide range of more realistic transverse expansion models are available, including viscous RL hydro [11, 123], VISH2+1 [124–126], and others. However, the focus in this thesis is on the development of the strong coupling methods and, for now, we will be mostly interested in the ballpark comparison with the data, for which a simple dilation factor of

[9] One might question whether it is reasonable to take the conformal proper time dependence of the temperature $T \propto \tau^{-1/3}$ when QCD close to the transition temperature seems quite non-conformal, as visible from its trace anomaly (Fig. 1.2). However, even when one takes that into account, a simple numerical calculation shows that the temperature evolution is very similar to $\sim \tau^{-1/3}$ and so, for the sake of analiticity, and also having in mind that we will be mostly interested in ballpark comparison to the data, we will work with the $\propto \tau^{-1/3}$ dependence.

(1.61) should be sufficient.

The multiplicity is usually reported as $dN_{\rm ch}/d\eta$ (Fig. 1.4), i.e. the multiplicity of all charged particles with respect to the pseudorapidity, defined in (1.17). We saw in (1.20) that the pseudorapidity differs from the spacetime rapidity up to a term of order $\mathcal{O}(m_\pi^2/p^2)$ which is negligible at high momenta, but since most of the multiplicity comes from lower energy pions, a good estimate is to take $d\eta/dy \approx 1.1$. Finally, assuming that the number of π^+, π^- and π^0 is approximately equal, we have simply:

$$\frac{dN_\pi}{dy} \approx \frac{3}{2}\frac{dN_{\rm ch}}{d\eta}\frac{d\eta}{dy}\,. \tag{1.62}$$

At the center of the plasma ($\vec{x} = 0$) at the initial time, with $\tau_0 = 1$ fm/c, $N_f = 3$ and $b = 0$ fm, formula (1.60) gives $T_{\rm RHIC,center} \approx 267$ MeV and $T_{\rm LHC,center} \approx 346$ MeV. Although these are reasonable numbers, there are certainly a lot more features that the simple formula (1.60) does not capture and that will affect the overall normalization of the temperature. However, as we will see, in many energy loss models, the temperature (to some effective power) will always be accompanied by the coupling and hence multiplying the temperature by some coefficient will be (at least roughly) equivalent to multiplying the coupling by the same coefficient (to some power). What makes formula (1.60) useful is that it tells us how these overall normalizations change relatively when we change various parameters, such as the multiplicity, formation time, impact parameter and so on.

1.4 Nuclear modification factor

In Section 1.2.3 we introduced the nuclear modification factor (1.25) and discussed how the main mechanism of such high suppression observed at high p_T is the energy loss of partons in the strongly coupled quark-gluon plasma. We also explained how such hard probes are a great tool to study the properties of the quark-gluon plasma, as their production at high Q^2 is governed by perturbative QCD. In this section, we will in detail explain how we will calculate R_{AB}, starting from the production of the parton.

1.4.1 Partonic R_{AB}

First, for the moment, we will ignore the effects of the fragmentation, and simply ask, if we were to measure the energy of the partons as they exit the plasma, what would be their (partonic) nuclear modification factor. As explained in Section 1.2.3, an equivalent (theorist's) definition of the nuclear modification (1.25) is

$$R^a_{AB}(p_T) = \frac{d\sigma_{AB\to a}/dp_T}{N_{\rm bin}\, d\sigma_{pp\to a}/dp_T}\,, \tag{1.63}$$

where we rewrote (1.25) in terms of the differential cross sections for producing the parton a in pp and AB collisions (suppressing from now on the η dependence), which are equal to the first three terms in (1.23) and first four terms in (1.24), respectively. The pp cross sections $d\sigma_{pp\to a}/dp_T$ (which we will refer to simply as the production spectra) can be obtained from pQCD calculations and are shown in Fig. 1.13. For light quarks and gluons, we use the results from a leading order pQCD CTEQ5 code [127], while for the charm and bottom quarks we use the fixed-order next-to-leading-log (FONLL) computations from [128]. Our task is to compute the analogous spectra $d\sigma_{AB\to a}/dp_T$ in the case of a heavy nuclei AB collision, using some energy loss model $dp/dx(x,T,p_0)$ which tells us how a parton with an initial momentum p_0 loses energy at some point x in the plasma with temperature T.

We imagine the parton a produced at some point $\vec{x}_\perp$ in the transverse plane of the plasma at $\tau = \tau_0$ (that is, we assume that the in-medium energy loss starts once the medium has been thermalized), moving eikonally in the $\hat{n}(\phi)$ direction, where ϕ is the

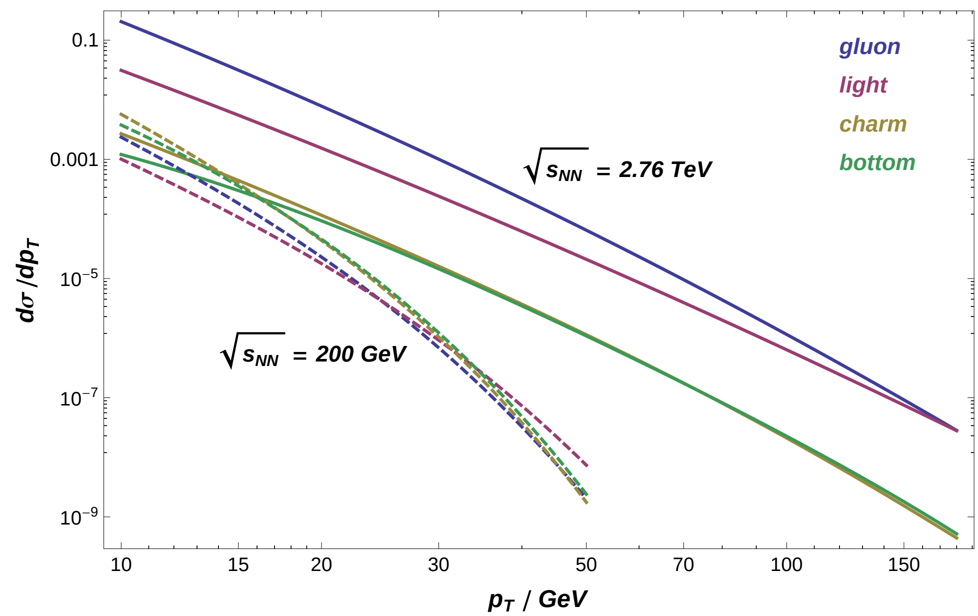

Figure 1.13: *The pp production spectra for various flavors at RHIC (dashed) and LHC (solid) from [127] and [128]. Note that although the normalizations of different spectra may be different (as they come from different calculations), this will not matter for the calculation of R_{AA}, which depends on the ratio of these spectra (Eq. (1.63)).*

azimuthal angle in the transverse plane. In order to express the temperature of the dynamic medium the partons "sees" as it moves through it, we simply replace

$$\vec{x}_\perp \quad \to \quad \vec{x}_\perp + (\tau - \tau_0)\hat{n}(\phi)\,, \tag{1.64}$$

in (1.60) and by shifting $\tau \to \tau - \tau_0$ (so that the parton energy loss starts at $\tau = 0$), we finally have

$$T_{\rm jet}(\vec{x}_\perp, \tau, \phi) = \left[\frac{\pi^2}{\zeta(3)}\frac{\xi_\pi}{\xi_{\rm QGP}}\frac{1}{16+9N_f}\frac{dN_\pi/dy}{N_{\rm part}}\frac{\rho_{\rm part}\left((\vec{x}_\perp + \tau\hat{n}(\phi))/r_{\rm bl}(\tau)\right)}{(\tau+\tau_0)r_{\rm bl}(\tau)^2}\right]^{1/3}\,. \tag{1.65}$$

As it moves through the medium, the parton is losing energy until it reaches the "end" of the medium, where the fragmentation begins. For this we will use the simplest freeze-out condition by saying that the medium "ends" when the temperature reaches some freeze-out temperature $T_{\rm fo}$ which is usually on the order of T_c in QCD:

$$T_{\rm jet}(\vec{x}_\perp, \tau_f, \phi) = T_{\rm fo}\,, \tag{1.66}$$

where we have defined the time τ_f when the energy loss stops and hadronization begins for this particular parton.

For a parton that started with some momentum p_0, let us define $P(p_f, p_0; \vec{x}_\perp, \phi)$ as the normalized ($\int dp_0 P = 1$) probability that the parton has momentum p_f when it exits the medium (i.e. P_c in (1.24)). Then, for a fixed final energy p_f, the number of partons that emerge with that p_f is given by

$$dN^a_{AB}(p_f; \vec{x}_\perp, \phi) = \int dp_0 P(p_f, p_0; \vec{x}_\perp, \phi) dN^a_{AB}(p_0) \tag{1.67}$$

where $dN^a_{AB}(p_0)$ is the initial distribution of partons. The details of the energy loss are encoded precisely in this function P, in which one can also incorporate various fluctuations effects (e.g. according to a Poisson distribution). To get $dN^a_{AB}(p_0)$ from $dN^a_{pp}(p_0)$, we multiply it by the number of binary collisions $T_{AB} d^2x_\perp$ and to get the total number of particles at some p_f, we integrate (1.67) over the transverse plane and average over ϕ:

$$\frac{d\sigma_{AB\to a}}{dp_f}(p_f) = \int d^2x_\perp\, T_{AB}(\vec{x}_\perp) \int \frac{d\phi}{2\pi} \int dp_0 \left[P(p_f, p_0; \vec{x}_\perp, \phi) \frac{d\sigma_{pp\to a}}{dp_0} \frac{dp_0}{dp_f} \right], \tag{1.68}$$

where we re-wrote (1.67) to extract the known initial pp production spectra $d\sigma_{pp\to a}/dp_0$. Plugging this in the definition of the partonic R_{AB} (1.63) we have:

$$R^a_{AB}(p_f) = \int d^2x_\perp \frac{T_{AB}(\vec{x}_\perp)}{N_{\rm bin}} \int \frac{d\phi}{2\pi} \int dp_0 \left[P(p_f, p_0; \vec{x}_\perp, \phi) \left(\frac{d\sigma_{pp\to a}/dp_0}{d\sigma_{pp\to a}/dp_f} \right) \frac{dp_0}{dp_f} \right]. \tag{1.69}$$

As we see from this expression, R_{AB} is essentially the geometrical and T_{AB}- weighted ratio of the production spectra for a given parton at initial and final energies. As mentioned earlier, one can incorporate various (realistic) fluctuation effects in P, but often in AdS calculations these are either not known or not practical to use, so we will use a simplifying assumption

$$P(p_f, p_0; \vec{x}_\perp, \phi) = \delta\left(p_0 - \tilde{p}_0(p_f; \vec{x}_\perp, \phi)\right) , \tag{1.70}$$

where $\tilde{p}_0$ is uniquely determined from the energy loss model

$$\int_0^{\tau_f} d\tau \left|\frac{dp}{dx}\right| (x = \tau, T_{\text{jet}}(\vec{x}_\perp, \tau, \phi), \tilde{p}_0) = \tilde{p}_0 - p_f , \tag{1.71}$$

where τ_f is defined by (1.66) and where we have assumed that the parton is moving close to the speed of light.

As we can see from Fig. 1.13, the pp production spectra, especially at high p_T, attain expected power-law forms. If we therefore assume that $d\sigma_{pp\to a}/dp_T \propto 1/p_T^{n_a}$, with index n_a slowly varying with p_T, and also that the relative energy loss ϵ (defined as $p_f = (1-\epsilon)p_0$) is approximately p_f-independent (which is sometimes the case in certain pQCD scenarios), we may turn (1.69) into a simple "pocket formula":

$$R^a_{AB} \approx \left\langle \int_0^1 d\epsilon \tilde{P}(\epsilon)(1-\epsilon)^{n_a - 1} \right\rangle_{(\vec{x}_\perp, \phi)} , \tag{1.72}$$

where averaging over the transverse plane and azimuthal directions is done as in (1.69). While we will in the rest of the thesis use the full production spectra as in Fig. 1.13, it is useful to have a formula like this, to motivate some simple arguments: for example, we can see that if the relative energy loss is approximately independent of the final momentum, we can expect R_{AB} to be constant at sufficiently high p_T.

1.4.2 Hadronic R_{AB}

When the partons of sufficiently high p_T reach the freezout temperature, fragmentation begins, and for this we need the fragmentation functions $D_a^h(z, Q^2)$ that we introduced in Section 1.2.3. These non-perturbative, universal objects express the probability that a parton a will fragment into a hadron h, and depend on the fraction $z = p_h/p_a$ of the hadron's momentum p_h and the factorization scale Q^2[10]. Fragmentation functions evolve with Q^2 as given by the DGLAP equations [129–131], but are generally rather simple at a fixed Q^2: for example, the KKP fragmentation functions [132], that describe the fragmentation of light quarks and gluons, can be parametrized at some standard $Q_0^2 = 2$ GeV^2 as:

$$D_a^h(z, Q_0^2) = N z^\alpha (1-z)^\beta \,, \tag{1.73}$$

where α, β and N are tabulated and can be evolved to other Q^2. For light quarks and gluons fragmenting into pions we will use the KKP fragmentation functions [132], for heavy quarks fragmenting into D and B mesons one can use Peterson fragmentation functions [133, 134], and for decay of heavy mesons into non-photonic electrons via $c \to D \to e$ and $b \to B \to e$ one can use the fragmentation functions from [128].

From the definition of the fragmentation functions, we can express the number of hadrons as

$$dN^h(p_h) = \sum_a \int_0^1 dz D_a^h(z, Q^2) dN^a(p_a) \,, \tag{1.74}$$

and hence

$$\frac{dN^h}{dp_h} = \sum_a \int_0^1 \frac{dz}{z} D_a^h(z, Q^2) \frac{dN^a}{dp_a}\bigg|_{p_a = p_h/z} \,, \tag{1.75}$$

We can now plug this in the definition of the hadronic R_{AB} (1.25) and use the definition

[10] In a process like $e^+e^- \to h + X$, the scale Q^2 is on the order of s, but in our context one typically takes it to be between p_a and $2p_a$.

of the partonic one (1.63) that yields the final expression:

$$R_{AB}^{h}(p_h) = \frac{\sum\limits_{a}\int\limits_{0}^{1}\frac{dz}{z}D_a^h(z,Q^2)\left(d\sigma_{pp\to a}/dp_a\right)_{p_h/z}R_{AB}^{a}(p_h/z)}{\sum\limits_{a}\int\limits_{0}^{1}\frac{dz}{z}D_a^h(z,Q^2)\left(d\sigma_{pp\to a}/dp_a\right)_{p_h/z}}\,. \tag{1.76}$$

Chapter 2

Jet quenching in QCD

As we saw in the previous chapter, one of the most important signals of the formation of quark-gluon plasma in heavy ion collisions is jet quenching, i.e. attenuation (or disappearance) of hadrons that hadronized from a parton that lost energy while traveling through the hot and dense medium. Before going on to the holographic description of energy loss, in this chapter we will describe how one treats the energy loss in QCD matter using perturbative QCD.

We start with a general discussion of medium-induced energy loss in QCD in Section 2.1, where we briefly mention the collisional energy loss and focus on the more dominant, radiative energy loss, including a discussion of the major radiative energy loss models "on the market". In Section 2.2 we focus on the energy loss model of Djordjevic, Gyulassy, Levai and Vitev (DGLV) and outline its main assumptions and physics behind it. Finally, in Section 2.3, we describe the development of our numerical Monte Carlo model [135] for calculating the DGLV radiative energy loss at arbitrary orders in opacity and discuss some interesting numerical results at intermediate opacity.

2.1 Energy loss mechanisms in QCD

As noted before, we will focus on partons that have high transverse momentum $p_T \gg \Lambda_{\mathrm{QCD}}$, which originate from "hard" scatterings with $Q^2 \gg \Lambda^2_{\mathrm{QCD}}$, and are consequently well described by perturbative QCD. After this hard scattering, the parton travels through the quark-gluon plasma, loses energy through interactions with the medium, and eventually fragments non-perturbatively into a set of final state hadrons. The main underlying assumption in applying the methods of perturbative QCD to study this energy loss is that the parton and the medium interact weakly, i.e. that the typical exchanged momentum is high, $\langle q \rangle^2 \gg \Lambda^2_{\mathrm{QCD}}$. That is, the medium is still considered to be strongly coupled, but the interactions of the partons with it are assumed to be weak. In the next chapter, when we turn to gauge/gravity duality and start studying the energy loss holographically, we will be doing so under the assumption of strong coupling between the medium and the parton.

There are two main mechanisms responsible for energy loss of a parton moving through the quark-gluon plasma: the collisional energy loss, due to elastic processes, and the radiative energy loss, due to inelastic processes. Effects of other energy losses, such as due to synchrotron or Cherenkov radiation, are generally less important.

2.1.1 Collisional energy loss

The collisional energy loss originates from elastic scatterings of the parton with the medium constituents and is generally more important at low momenta. The first work on this topic was by Bjorken [80], and starting from his results, various improvements were implemented since. The Bjorken model starts with the elastic cross section $d\sigma_{ij}/dt$ for a particular qq, qg and gg scattering, where $t = q^2$, the momentum transfer in the given process. In the high energy limit $E \gg k$, where E is the energy of the scattering parton and k the momentum of parton in the medium, this cross section can be approximated by

$$\frac{d\sigma_{ij}}{dt} \approx C_{ij}\frac{4\pi\alpha_s^2}{t^2}\,, \tag{2.1}$$

where $C_{ij} = 9/4, 1$ and $4/9$ is the color factor for a gg, gq and qq scattering, respectively. To get the energy loss per unit length z, one essentially integrates (2.1), times the energy lost in the process, from some $t_{\min}$ to $t_{\max}$ and averages over the momenta k, assuming simple Bose-Einstein and Fermi-Dirac distributions of quarks and gluons in the medium. This yields the Bjorken energy loss formula, which for light quarks and gluons has the following form:

$$\frac{dE_{\rm Bj}}{dz} = -\pi C_R\alpha_s^2 T^2\left(1+\frac{N_f}{6}\right)\log\left(\frac{ET}{\mu^2}\right)\,, \tag{2.2}$$

where C_R is the quadratic color Casimir of the jet (for gluons $C_A = 3$, and for quarks $C_F = 4/3$) and T is the temperature of the medium. In obtaining (2.2) one uses the leading order perturbative value for the Debye screening mass,

$$\mu^2 = g^2T^2\left(1+\frac{N_f}{6}\right)\,, \tag{2.3}$$

as the minimum momentum transfer $t_{\min}$, while for the maximum one simply uses $t_{\max} \sim ET$. Although rough in the way the IR and UV divergences are treated, the result (2.2) tells us that the collisional energy loss is path independent and that it depends on the energy of the jet only logarithmically. This approach has been improved by numerous works, including more careful treatment of the IR divergences [136], UV divergences [137, 138], the inclusion of the running of the coupling [139] and many more.

2.1.2 Radiative energy loss

Radiative energy loss originates from inelastic scatterings of the parton with the medium and generally dominates at high momenta. Interactions of the parton with the medium induce the splitting of the parton into the parton and a gluon; that is, the parton radiates a gluon, a process called the medium-induced gluon bremsstrahlung. Since the parton is losing energy on account of the energy of gluon, one typically expresses the radiative energy loss as the gluon bremsstrahlung spectrum in energy ω and transverse momentum $\vec{k}_\perp$ of the gluon, $\omega d^2 I_{\rm rad}/d\omega dk_\perp^2$. Since the medium-induced multiple gluon emission is considered to be, as we will see, the dominant mechanism[1] of how highly energetic partons lose energy in the quark-gluon plasma, we will focus from now on mainly on that.

We first start with the radiation in the vacuum, which is dictated by the DGLAP splitting functions, $P_{q\to qg}(x)$ and $P_{g\to gg}(x)$, which express the vacuum probability for $q \to qg$ and $g \to gg$ splittings, where $x \equiv \omega/E$. The gluon distribution in $\vec{k}_\perp$ and x, radiated from a massless parton, is given by [141]

$$x\frac{dN^{(0)}}{dxdk_\perp^2} = \frac{\alpha_s}{2\pi}\frac{xP_R(x)}{k_\perp^2}\,, \tag{2.4}$$

where by dN we denote the "number" of radiated gluons (so that $\omega dN = dI_{\rm rad}$) and with the superscript "(0)" we denote the vacuum radiation (i.e. the "zero opacity" limit, a notation that will soon become more clear). In the limit of small $x \ll 1$, which we will often assume (the soft radiation approximation), the splitting functions differ only by the color Casimir factor, $P_R \approx 2C_R/x$. In this limit, formula (2.4) seems $x-$independent, but x appears in the final $dI^{(0)}/dx$ distribution through the limits of k^2-integration. With the special attention to kinematic bounds (see e.g. [142]), we can integrate this and obtain

[1] However, some of the recent developments [140] show that the collisional energy loss plays an important role as well, especially for heavy quarks. We discuss this briefly at the end of Section 2.2.3.

the energy loss outside a cone with $k_\perp > \mu$:

$$\Delta E^{(0)} = \frac{4C_R\alpha_s}{3\pi} E \log\left(\frac{E}{\mu}\right) . \tag{2.5}$$

Radiated gluon spectrum for a heavy quark differs from (2.4): due to kinematic constraints, the radiation is suppressed at angles smaller than $\theta_0 = M/E$ where M is the mass of the quark:

$$x\frac{dN^{(0)}}{dxdk_\perp^2} = \frac{\alpha_s C_F}{\pi} \frac{k_\perp^2}{(k_\perp^2 + x^2M^2)^2} , \tag{2.6}$$

where we again assumed small x. This is the so-called "dead cone" effect [143], and results in the reduction of the total gluon radiation by heavy quarks. As we will see soon, the vacuum gluon radiation will be quantitatively the most dominant component of the full gluon radiation spectrum, with the medium-induced radiation being a small (but important) correction on top of that.

Let us now turn to the medium and how we generally model the parton interactions with it. We imagine the parton traveling in the z direction in the medium, and we generally assume that it has high enough energy E so that it is moving eikonally. The medium is modeled as a collection of scattering centers that the parton encounters along the way at positions z_k, where the parton interacts with the medium according to some potential, leading to induced gluon radiation. An important scale in the problem will therefore naturally be the mean free path $\lambda = 1/(\rho\sigma_{\rm el})$, where ρ is the density of the medium and where $\sigma_{\rm el}$ is the elastic cross section for the particle-medium interaction. For a medium of length L, we define the opacity $\bar{n} \equiv L/\lambda$, the mean number of collisions in the medium.

An important effect that occurs in the medium, due to parton's multiple scatterings, is the (destructive) interference between the radiation amplitudes associated with different collisions. This is the non-Abelian analog of the Landau-Pomeranchuk-Migdal (LPM) effect in QED [144, 145], responsible for the non-trivial reduction of the final spectrum of radiated gluons. In QED, this is a well known effect: consider the amplitude current of a particle that undergoes m collisions at spacetime points x_i^μ at which the particle's momentum changes from p_{i-1}^μ to p_i^μ:

$$J^\mu(k) = \sum_{i=1}^{m} J_i^\mu(k) = ie \sum_{i=1}^{m} e^{ik\cdot x_i} \left(\frac{p_i^\mu}{k\cdot p_i} - \frac{p_{i-1}^\mu}{k\cdot p_{i-1}} \right) . \tag{2.7}$$

The final distribution of radiated photons is obtained by dotting this into the photon's polarization vector ε_μ, squaring and summing over all polarizations, which yields $\omega dN_\gamma/d^3k \propto |J(k)|^2$. The size of the off-diagonal terms in this sum is governed by the phase factors:

$$e^{ik\cdot(x_i - x_j)} \approx \exp\left(i\frac{k_\perp^2}{2\omega}(z_i - z_j) \right) \equiv \exp\left(i\frac{\Delta z_i}{\tau_f} \right) , \tag{2.8}$$

where in the first equality we assumed that the particle travels ultra-relativistically in the z direction and we employed the collinear approximation so that $k_\perp \ll \omega, k_z$. In the second equality we defined the formation time, $\tau_f \equiv 2\omega/k_\perp^2$, which can be understood as the minimal time $\sim \hbar/\Delta E$ needed to resolve a transverse gluon wavepacket of size $\Delta x_\perp \sim \hbar/k_\perp$ from the wave packet of its high energy ($E \gg \omega$) parent. Since, by definition, on the average, $\Delta z_i \sim \lambda$, based on (2.8) we have two extreme limits:

$$\begin{aligned} &\lambda \gg \tau_f, \quad \text{incoherent limit} , \\ &\lambda \ll \tau_f, \quad \text{factorization limit} , \end{aligned} \tag{2.9}$$

which we will talk about more in the next paragraph. In between these two limits, the realistic relationship between λ and τ_f will non-trivially affect the spectrum of the radiated gluons. An intermediate case of this sort is illustrated in Fig. 2.1, where $\tau_f \sim 3\lambda$. In some sense, the formation time is the time it takes for the gluon radiation to come on shell, during which we can have interference (LPM) effects.

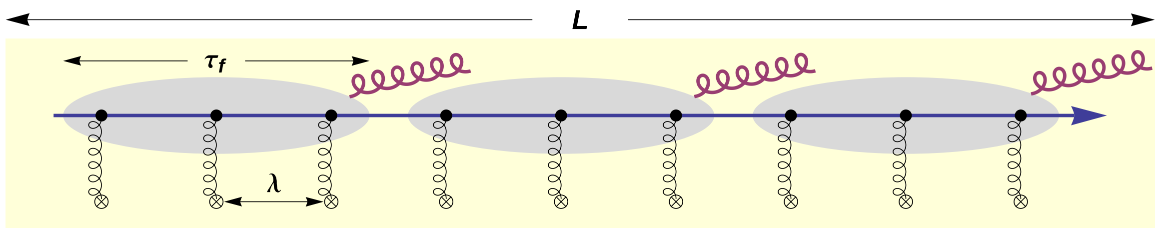

Figure 2.1: *Illustration of the LPM effect in a QCD medium of length L. Formation time τ_f and the mean free path λ are indicated.*

Let us now focus on the two limits in (2.9). In the factorization limit $\lambda \ll \tau_f$, the phase factors are ≈ 1, causing cancellations in the sum in $|J(k)|^2$, leaving only contributions from the radiation from final and initial states. In the incoherent limit $\lambda \gg \tau_f$, the phase factors are large and the off-diagonal elements average to 0, leaving only the diagonal ones. This limit is the QCD analog of the incoherent Bethe-Heitler limit in QED, and the gluon spectrum in this limit was first calculated by Gunion and Bertsch [146]:

$$x\frac{dN_{\rm GB}}{dxd^2k_\perp} = \frac{C_A\alpha_s}{\pi^2}\frac{q_\perp^2}{k_\perp^2(\vec{q}_\perp - \vec{k}_\perp)^2}\,, \tag{2.10}$$

where $\vec{q}_\perp$ is the transverse momentum transfer from the medium. At large $\vec{k}_\perp$, this spectrum has a characteristic power-law tail of $\sim 1/k_\perp^4$. To find the final gluon spectrum from (2.10), one needs to average over $\vec{q}_\perp$, for which we need a distribution of these momenta in the medium, which we will specify in Section 2.2.1.

2.1.3 Major models of radiative energy loss

The theoretical treatment of radiative energy loss in a realistic quark-gluon plasma is notoriously complex: the jet can suffer multiple elastic and inelastic scatterings in the medium, the radiated gluons can rescatter as well (and these amplitudes will interfere with the jet scattering ones), there is a non-trivial interplay between different scales in the problem, and all this needs to be done in a finite-temperature medium which has a complicated spacetime evolution. In an attempt to cope with this set of interesting problems, four major radiative energy loss models have become established "on the market". They mainly differ in their assumptions about the relationships between different scales and in how they model the medium itself. They are, however, all based on the pQCD factorization paradigm (1.24), where the entire effect of the energy loss is in modifying the fragmentation functions from the vacuum ones to the modified ones, as discussed in Section 1.2.3. In this section we will only briefly mention some general features of these models, while more comprehensive reviews of them (and jet quenching in general) can be found in [15–18]. Extensive quantitative comparisons between these models are available in [147, 148].

In the approach of Baier, Dokshitzer, Mueller, Peigne and Schiff (BDMPS) [149–157], one computes the radiated gluon distribution in a plasma modeled by static colored scattering centers, assuming the multiple soft scattering (MSS) approximation in which the parton is essentially performing a Gaussian diffusion in the transverse momentum space. The medium's rescattering properties are fully encoded in the jet transport coefficient,

$$\hat{q} = \rho \int d^2 q_\perp q_\perp^2 \frac{d\sigma}{d^2 q_\perp}\,, \tag{2.11}$$

where ρ is the density of the scattering centers and $d\sigma$ is the parton-medium cross section. Hence, $\hat{q}$ is the average transverse momentum squared transferred from the medium to the parton per unit length and can be expressed as $\hat{q} \sim \mu^2/\lambda$. BDMPS approach is equivalent to Zakharov's light-cone path integral (LCPI) formalism for jet energy loss [158–163] in the dipole approximation (in order to obtain the MSS limit). Armesto, Salgado and

Wiedemann (ASW) [164–170] implemented the (Poissonian) probabilities that the parton loses some fraction of energy due to some number of radiated gluons (quenching weights), which, when convoluted with the vacuum fragmentation functions, yield the medium modified ones.

In the approach of Gyulassy, Levai and Vitev (GLV) [142, 171–176] one computes the opacity expansion of the radiated gluon distribution to an arbitrary order using a recursive diagrammatic procedure called the reaction operator approach. The medium is modeled similarly as in the case of BDMPS (i.e. static scattering centers), only now the properties of the medium depend less trivially on the Debye mass μ^2 and the mean free path λ than through the combination $\mu^2/\lambda = \hat{q}$. The GLV approach does not make the MSS approximation, rather, it starts from a single hard radiation spectrum that is then used to obtain the full multiple scattering spectrum through a recursive procedure. By including the fluctuations through the same Poisson distribution as in BDMPS, one arrives at the medium modified fragmentation functions. Together with Djordjevic, GLV was generalized to include finite masses of quarks and effective gluon masses (DGLV) [177]. The DGLV approach (and its differences with respect to the BDMPS approach) will be the topic of the rest of this chapter.

In the higher twist (HT) approach [178–187], one computes the change in the distribution of hadrons directly from the medium modified fragmentation function, which is calculated from the power corrections to the leading-twist cross section for parton's scattering processes. This medium modified fragmentation function differs from the vacuum one by an additive piece which is calculated from the medium modified splitting functions. The latter depend on the properties of the medium through the jet transport parameter $\hat{q}$, which is in turn directly related to the gluon distribution density of the medium.

In the approach by Arnold, Moore and Yaffe (AMY) [78, 188–192], one computes the change in the distribution of partons starting from a well defined medium which is a thermally equilibrated, hot plasma made of quark and gluon quasiparticles. The properties of the medium, such as the dispersion relations and various interactions, are given by the hard thermal loop (HTL) approximation in the finite temperature field theory. The distribution of the partons is essentially calculated from the transition rates of a hard parton to another parton plus a radiated gluon, through a Fokker-Planck-like equation using the HTL effective theory and assuming high temperature. This distribution is then convoluted with the vacuum fragmentation functions to obtain the medium modified ones.

2.2 DGLV model of energy loss

One of the two most common approximations made in addressing the medium-induced gluon radiation are the "thin" and "thick" plasma approximations; former assuming a single hard scattering of the parton (or several, that can be treated explicitly) and the latter assuming an infinite number of soft scatterings in the medium (as in e.g. the BDMPS approach). However, a simple estimate [142] shows that, for conditions relevant to RHIC and LHC, the mean number of collisions in the medium, the opacity $\bar{n} = L/\lambda$, is in fact moderately small ($\bar{n} < 10$). Therefore, an alternate approach was necessary to handle this realistic "mesoscopic" case, and this has been successfully addressed by GLV with an opacity expansion of radiative energy loss for massless quark and gluon jets propagating through the quark-gluon plasma. This approach was later generalized to DGLV [177] to include finite masses of quarks and effective gluon masses.

2.2.1 Gyulassy-Wang plasma model

The GLV approach is based on the Gyulassy-Wang (GW) plasma model [144, 145], in which one considers multiple scatterings of a high energy parton in the color neutral plasma, composed of m static partons located at $\vec{x}_i = (z_i, \vec{x}_{\perp i})$, where $z_{i+1} > z_i$. The static scatterers are assumed to be well separated, i.e. $(z_{i+1} - z_i) \gg \mu^{-1}$, and each of them has an associated Debye-screened potential,

$$V_i^a(\vec{q}) = g T_i^a \frac{1}{\vec{q}^2 + \mu^2} e^{-i\vec{q}\cdot\vec{x}_i}\,, \tag{2.12}$$

where T_i^a is a d_i-dimensional $SU(N)$ generator associated with the representation of the i-th scatterer. One also assumes that the temperature is high enough, so that the effective coupling g is small (as discussed in Section 1.1.2). In this case, since the typical transverse momentum $\vec{q}_\perp$ in potential (2.12) is on the order of $q_\perp \lesssim \mu \propto gT$ and since the typical thermal energy of the plasma constituents is $E_{\text{th}} \sim T$, the average energy loss per elastic scattering is $-q^0 \approx q_\perp^2/2E_{\text{th}} \sim g^2 T$. This is smaller than the average transverse momentum transfer by a factor of $\sim g$, hence justifying the assumption of static scattering centers. Furthermore, we will assume that the incoming jet has a very large energy $E \gg \mu$, so that the typical momentum transfers are on average very small. Of course, although very small, we still assume that $q_\perp \gg \Lambda_{QCD}$, justifying the perturbative treatment.

We start by studying a single scattering in the potential (2.12). The amplitude for a scattering at $\vec{x}_i$ from an incident jet momentum p_{i-1}^μ to p_i^μ is given by

$$M_i(p_i, p_{i-1}) = 2\pi\delta(p_i^0 - p_{i-1}^0) A_i(\vec{q}_i) e^{-i\vec{q}_i\cdot\vec{x}_i}\,, \tag{2.13}$$

This expression has the same form as the analogous QED amplitude, only now A_i carries non-trivial color information,

$$A_i(\vec{q}_i) = -2igET^a V_i^a(\vec{q}_i)\,. \tag{2.14}$$

From amplitude (2.13), by standard averaging over the initial states and summing over the final states, we can get the elastic cross section between the jet and the target parton in the low momentum transfer limit:

$$\frac{d\sigma_{\mathrm{el},i}}{d^2q_{\perp i}} \approx \frac{C_R C_{2i}(T)}{d_A} \frac{|v(\vec{q}_{\perp i})|^2}{(2\pi)^2}\,, \tag{2.15}$$

where

$$v(\vec{q}_\perp) = \frac{4\pi\alpha_s}{q_\perp^2 + \mu^2}\,, \tag{2.16}$$

and where $d_A = N^2 - 1 = 8$ and C_R and $C_{2i}(T)$ are the second Casimirs of the jet and the target parton (scatterer), respectively.

To study multiple scatterings with target partons between, say, i and j, in which the jet's momentum changes from p^μ_{i-1} to p^μ_j, we would need to include amplitudes such as (2.13) for every site, connected by the propagators $i\Delta(p_i)$:

$$M_{ji}(p_j, p_{i-1}) = \int \frac{d^4p_i}{(2\pi)^4} \cdots \int \frac{d^4p_{j-1}}{(2\pi)^4} M_j(p_j, p_{j-1}) i\Delta(p_{j-1}) \cdots i\Delta(p_i) M_i(p_i, p_{i-1})\,. \tag{2.17}$$

Ultimately, we are interested in the amplitude for radiating a gluon of some polarization ε_μ and color c after the $k-$th elastic scattering, which can be obtained by an insertion of an emission vertex $\propto igp^\mu_k \varepsilon_\mu T^c$ in amplitudes such as (2.17). The final gluon distribution will be given similarly as in the case of QED, eq. (2.7), only this time the effective current J^μ will have additional color factors, due to the non-Abelian nature of the interactions. Nevertheless, one still ends up with phase factors as in (2.8), leading to the QCD version of the LPM effect. However, now one has to take into account that gluons, after being emitted, can interact with the medium and rescatter. This significantly complicates the analysis and this is what the GLV model was designed to address.

2.2.2 GLV formalism

An example of what kind of complications one encounters when considering gluon rescatterings is illustrated in Fig. 2.2. In the notation in the figure, $M_{n_s,m,l}$ denotes the amplitude that includes n_s scattering centers, the emission of the gluon between sites at z_m and z_{m+1} and the combined gluon and jet rescattering pattern encoded by $l \equiv \sum_{i=1}^{n_s} \sigma_i 2^{i-m-1}$ where σ_i is 0 or 1 depending on whether the scattering was with the jet or the gluon. However, as we will soon see, this notation will not be enough to capture all the relevant diagrams.

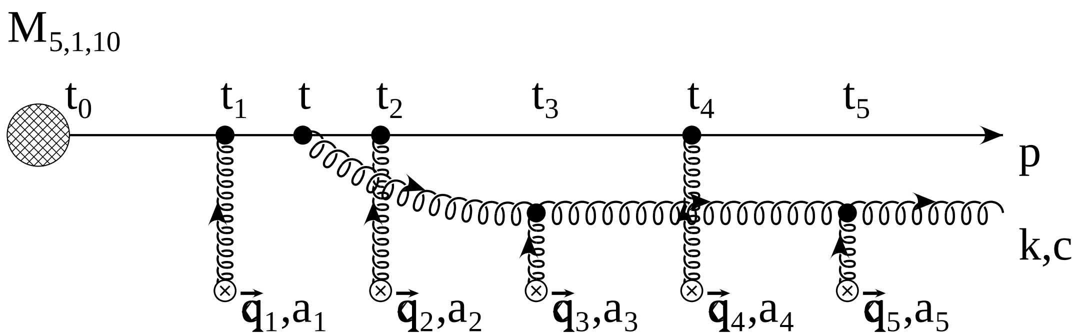

Figure 2.2: *An amplitude contributing to fifth (and higher) orders in opacity in the GLV opacity expansion of radiative energy loss. The crosses denote the Debye-screened Yukawa interactions and the blob at t_0 is the initial hard jet amplitude. (Taken from [172].)*

Before we continue with this, let us clearly state the main assumptions of the GLV approach and set up some notation. Employing the light-cone coordinates, we denote the initial light-cone energy of the jet by E^+, and for the radiated gluon we define x as the its fractional light-cone momentum, i.e. $k^+ = xE^+$, while its transverse momentum is denoted with $k_\perp$ and energy with ω. For the jet in the final state, we have $p^+ = (1-x)E^+$ and, as in the GW plasma model, we assume that there is no energy transfer with the medium. We assume that both the energy of the jet and the energy of the gluon are much larger than the transverse momentum transfers from the medium, i.e. $E \gg q_\perp$ and

$\omega \gg q_\perp$ (eikonal approximation), as well as that the gluons are emitted at small angles from the jet, i.e. $\omega \gg k_\perp$ (collinear radiation). Finally, we assume soft radiation, so that $x \ll 1$.

In the GLV approach one assumes, as is relevant to the heavy ion collisions, that the hard probe is produced inside the plasma, at some finite time at position z_0 (as opposed to the Gunion-Bertsch problem, where the jet is prepared in the remote past). The amplitude for this initial hard production (and its accompanying gluon radiation) is

$$G_0 = -2ig\frac{\vec{\varepsilon} \cdot \vec{k}_\perp}{k_\perp^2} e^{i\omega_0 z_0} c \,, \tag{2.18}$$

where ε^μ and c are the polarization and the color of the radiated gluon, respectively. In the language of the previous notation, $G_0 = M_{0,0,0}$. Because of this, even when there is only one scattering in the medium (i.e. at first order in opacity), one can have the LPM effect, due to the interference with the associated production radiation (2.18).

In order to preserve unitarity, in addition to the single Born scattering ("direct") diagrams as in Fig. 2.2, one also needs to include the so-called double Born ("virtual") diagrams (as discussed in [156]), composed of contact interactions in which $z_{i-1} \to z_i$ (see Fig. 2.3 for an illustration of this).

The idea is to organize diagrams into classes of order n in opacity by defining suitable operators $\hat{D}_m$ and $\hat{V}_m$ which insert a direct or a virtual interaction at a scattering center m and also implicitly sum also over all possible kinds of interactions (i.e. with the jet or the gluon, or both, in case of a virtual interaction). Including also the possibility that there is no interaction at a site, we can define this class as

$$\mathcal{A}_{i_1 \cdots i_n} = \prod_{m=1}^{n} \left(\delta_{0,i_m} + \delta_{1,i_m} \hat{D}_m + \delta_{2,i_m} \hat{V}_m \right) G_0 \,, \tag{2.19}$$

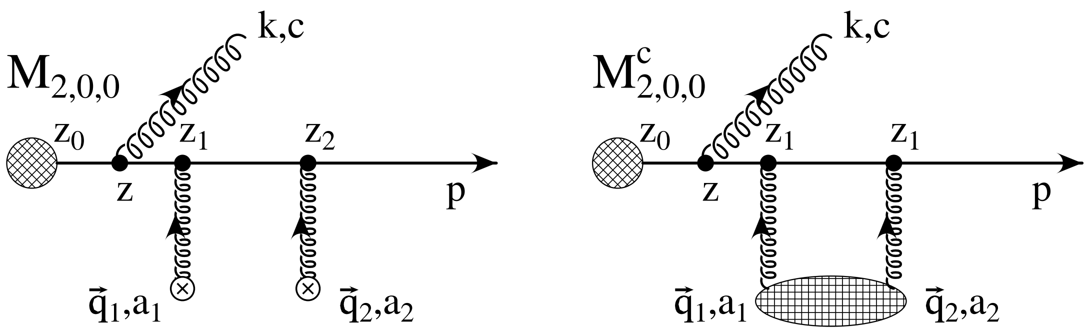

Figure 2.3: *The $M_{2,0,0}$ "direct" diagram that contributes to the second order in opacity, and its contact limit $z_1 = z_2$ ("virtual") diagram, that can contribute to the first order in opacity as well. (Taken from [142].)*

where $i_m = 0, 1, 2$ encodes what happens at which site and where G_0 is defined in (2.18). Obviously, diagrams in a given class n have different powers of the coupling α_s, but if we include an exactly complementary class of diagrams $\bar{\mathcal{A}}$ such that

$$\bar{\mathcal{A}}_{i_1 \cdots i_n} = \prod_{m=1}^{n} \left(\delta_{0,i_m} \hat{V}_m + \delta_{1,i_m} \hat{D}_m + \delta_{2,i_m} \right) G_0 \, , \tag{2.20}$$

then we can define a "probability" distribution at n-th order in opacity,

$$P_n = \bar{\mathcal{A}}^{i_1 \cdots i_n} \mathcal{A}_{i_1 \cdots i_n} \, , \tag{2.21}$$

with an implicit sum over indices. In sum in (2.21) every term contributes with the same power of α_s^{2n+1}, where one power of α_s comes from the gluon radiation vertex and the rest of α_s^2 powers come from n elastic scatterings. As demonstrated in [142], one can construct P_n recursively from classes of diagrams of lower opacity, by defining the "reaction operator" $\hat{R}_m \equiv \hat{D}_m^\dagger \hat{D}_m + \hat{V}_m + \hat{V}_m^\dagger$, so that:

$$P_n = \bar{\mathcal{A}}^{i_1 \cdots i_{n-1}} \hat{R}_n \mathcal{A}_{i_1 \cdots i_{n-1}} \, . \tag{2.22}$$

Finally, thanks to a specific relationship between the operators $\hat{V}_m$ and $\hat{D}_m$, in [142] the authors were able to recursively sum all the probabilities in a closed form, leading to the final formula for the gluon radiation distribution at all orders in opacity.

2.2.3 DGLV formula for radiated gluon distribution

Based on the previous formalism, one can write the opacity expansion of radiative jet energy loss in the GLV approach, expressed as a radiated gluon number distribution in gluon's fractional light-cone momentum x and its transverse momentum $k_\perp$ at an arbitrary order in opacity n. An important extension of this formalism is the inclusion of the effective gluon masses and finite quark masses. The efforts in this direction started in [193], where the authors studied the QCD analog of the Ter-Mikayelian effect: in the plasma, the gluon radiation associated with hard processes is modified by the dielectric properties of the medium, resulting in the gluons acquiring an effective mass which regulates and suppresses the (otherwise divergent) infrared vacuum radiation. By studying the effects of this on the radiative energy loss, it was found that the gluon propagator can be well approximated by using a fixed gluon mass of $m_g = \mu/\sqrt{2}$. This effect, together with the finite quark masses turned out to modify the effective radiation amplitudes and phase factors in the GLV formalism in a very simple way, leading to the DGLV formula for radiated gluon distribution [177]:

$$
\begin{aligned}
x\frac{dN^{(n)}}{dx\,d^2k_\perp} &= \frac{C_R\alpha_s}{\pi^2}\frac{1}{n!}\int\prod_{i=1}^{n}\left(d^2q_{\perp i}\,\frac{L}{\lambda_g(i)}\left[\bar{v}_i^2(\vec{q}_{\perp i})-\delta^2(\vec{q}_{\perp i})\right]\right)\,\times \\
&\quad\times\Bigg(-2\,\vec{C}_{(1,\cdots,n)}\cdot\sum_{m=1}^{n}\vec{B}_{(m+1,\cdots,n)(m,\cdots,n)}\,\times \\
&\quad\times\left[\cos\left(\sum_{k=2}^{m}\Omega_{(k,\cdots,n)}\Delta z_k\right)-\cos\left(\sum_{k=1}^{m}\Omega_{(k,\cdots,n)}\Delta z_k\right)\right]\Bigg)\,. \qquad (2.23)
\end{aligned}
$$

Here the amplitudes are

$$
\begin{aligned}
\vec{H} &= \frac{\vec{k}_\perp}{k_\perp^2+\beta^2}\,, & \vec{C}_{(i_1 i_2\cdots i_m)} &= \frac{(\vec{k}_\perp - \vec{q}_{\perp i_1} - \vec{q}_{\perp i_2} - \cdots - \vec{q}_{\perp i_m})}{(\vec{k}_\perp - \vec{q}_{\perp i_1} - \vec{q}_{\perp i_2} - \cdots - \vec{q}_{\perp i_m})^2 + \beta^2}\,, \\
\vec{B}_i &= \vec{H} - \vec{C}_i\,, & \vec{B}_{(i_1 i_2\cdots i_m)(j_1 j_2\cdots j_n)} &= \vec{C}_{(i_1 i_2\cdots i_m)} - \vec{C}_{(j_1 j_2\cdots j_n)}\,.
\end{aligned}
\tag{2.24}
$$

where the factor $\beta^2 \equiv m_g^2 + M_q^2 x^2$ encodes the effect of the finite quark and gluon masses M_q and m_g, respectively. These amplitudes are sometimes referred to as the "hard" (associated with initial hard amplitude (2.18)), "cascade" (describing the rescatterings of the radiated gluon) and the "Gunion-Bertsch" amplitude (associated with the incoherent gluon radiation), respectively. The $\vec{q}_{\perp i}$ are the transverse momentum transfers from the medium to the parton, over which the ensemble average was taken in (2.23). The physics of the LPM effect is encoded in the last term with the phase factors, where, as before, the distances between two successive scatterings are denoted with $\Delta z_k \equiv z_k - z_{k-1}$, and where $\Omega_{(m,\cdots,n)}$ denote the inverse formation times:

$$
\Omega_{(m,\cdots,n)} \equiv \frac{(\vec{k}_\perp - \vec{q}_{\perp m} - \cdots - \vec{q}_{\perp n})^2 + \beta^2}{2xE}\,,
\tag{2.25}
$$

where E is the energy of the jet.

In (2.23) $\bar{v}(q_\perp)$ is the normalized Yukawa potential (so that $\int d^2 q_\perp |\bar{v}(q_\perp)|^2 = 1$) from the GW model (2.16). Because of this, one gets an overall factor of σ_{el} at each order in opacity, but since one sums over all possible diagrams involving both the jet (which may be a gluon or a quark) and the radiated gluon, one may expect to end up with a complicated sum of gluon and jet elastic cross sections. However, as shown in [142], summing over all possible direct and virtual diagrams and taking into account that $C_R \sigma_g = C_A \sigma_{\mathrm{el}}$ (eq. (2.15), where C_R is the color Casimir of the jet), one ends up with a simple factor of $C_A C_2(T)/d_A$ at each order in opacity, implying that it is the gluon cross section one finally ends up with. After performing an additional impact parameter average (that is also understood in (2.23)) which yields a factor of $1/A_\perp$, and using $\lambda_g = 1/(\rho\sigma_g)$ (where $\rho = N/(A_\perp L)$, N being the total number of scatterers), one ends up with the opacity factor L/λ_g as in (2.23), where with $\lambda_g(i)$ we allow for different elastic cross sections along the jet's path. The $n!$ factor in (2.23) comes from the combinatorial factor of $N!/(n!(N-n)!) \approx N^n/n!$ that counts the number of ways we can select n scatterers out of N.

Assuming a smooth, normalized distribution $\bar{\rho}(z_1, ..., z_n)$ of the scattering centers in (2.23), we can, as in [142], replace:

$$x\frac{dN^{(n)}}{dx\, d^2k_\perp} \to \int dz_1 ... \int dz_n\; \bar{\rho}(z_1, ..., z_n) x \frac{dN^{(n)}}{dx\, d^2k_\perp} \,. \tag{2.26}$$

Assuming an uncorrelated medium, the linear kinetic theory gives [172]:

$$\bar{\rho}(z_1, \cdots, z_n) = \prod_{j=1}^{n} \frac{\theta(\Delta z_j)}{L_e(n)} e^{-\Delta z_j / L_e(n)} \,, \tag{2.27}$$

where $L_e(n)$ is fixed to be $L_e(n) = L/(n+1)$ from the requirement that $\langle z_k - z_0 \rangle = kL/(n+1)$. Numerical results that will be presented in the next section were obtained using this distribution (which also allows for an analytic evaluation of the z_i-integrals), but, as we will explain in more detail in the next section, it is easy to implement any other distribution in our code.

At first order in opacity (which, as we will see, is the dominant contribution), formula (2.23) is rather tractable, and, for the sake of analiticity, ignoring the kinematic bounds, the total energy loss of a massless parton can be expressed as:

$$\Delta E^{(1)} = \frac{C_R \alpha_s}{4} \frac{L^2 \mu^2}{\lambda_g} \log\left(\frac{E}{\mu}\right) . \tag{2.28}$$

As we can see, at high energies, this is a subleading effect compared to the vacuum radiation (2.5). In practice, finite kinematic bounds will affect this result and generally lead to the reduction of the energy loss relative to (2.28). This expression is also directly comparable to the BDMPS result [149]:

$$\Delta E_{\text{BDMPS}} = \frac{C_R \alpha_s}{8} \frac{L^2 \mu^2}{\lambda_g} \log\left(\frac{L}{\lambda_g}\right) . \tag{2.29}$$

The common feature of these two formulas is that the energy loss depends on path length as L^2, a characteristic signature of the LPM effect.

Comparing expressions (2.28) and (2.29) with (2.2), we see that the collisional energy loss is generally suppressed by one power of α_s with respect to the radiative one, and plugging in some typical numbers gives $dE_{\text{col}}/dL \sim \mathcal{O}(2\,\text{GeV/fm})$ while $dE_{\text{rad}}/dL \sim \mathcal{O}(10\,\text{GeV/fm})$. However, because of the dead cone effect for heavy quarks (eq. (2.6)), the collisional energy loss turns out to play an important role there; more careful treatment of this (in the case of light quarks as well) led [140] to go beyond the static approximation in modeling of the radiative energy loss, and consider a dynamical medium, hence allowing for collisional energy loss as well.

Finally, we should mention that, as is obvious from the construction in Section 2.2.2, the DGLV diagrams have only one external gluon line, and multiple gluon emission is generally added a posteriori in an incoherent fashion, according to some distribution. As noted before, thinking of the gluon radiation as a stochastic process with an associated probability distribution $P(\Delta E/E)$ of radiating some energy ΔE, the simplest procedure to implement multiple gluon emissions is through the Poisson ansatz [174]. Computation of the nuclear modification factor, including the multi-gluon fluctuations and the collisional energy loss, and all this embedded in a realistic geometry (similar to the one in Section 1.3), was done in [194].

2.3 DGLV at intermediate opacity

As discussed earlier, one of the main motivations for the (D)GLV approach was to handle the realistic "mesoscopic" case of radiative energy loss, when the mean number of scatterings in the medium is finite ($\bar{n} < 10$). After the dominant first order in opacity is taken into account, the question is how many more orders in opacity we should compute, in order to get a good approximation for the gluon distribution in a particular case at hand. Some guidance can be obtained from assuming that the probability of the jet scattering off a certain number of scattering centers is approximately Poissonian, with the expectation value equal to the opacity $\bar{n} \sim 5$. In that case, since the probability distribution peaks close to $\bar{n}$, we should compute the induced gluon distribution (2.23) up to some order n between $\sim \bar{n}$ and $\sim 2\bar{n}$ (although, in practice, as we will soon see, the LPM interference effects can speed up the convergence in some cases). As we saw in the previous section, it is possible to evaluate the DGLV formula at the first order in opacity explicitly; however, already at second order in opacity, formula (2.23) becomes highly non-trivial. Because of this, the only way to extract any physically interesting information out of it at relevant intermediate opacities is to evaluate it numerically.

2.3.1 Monte Carlo code

We have developed a flexible and efficient Fortran code to do precisely that: numerical evaluation of the induced gluon distribution at an arbitrary order in opacity. This code was one of first steps in the development of the CUJET model [195, 196], a state-of-the-art implementation of DGLV that includes the dynamical medium effects, collisional energy loss, multi-gluon fluctuations and full spacetime evolution of the medium, as well as running of the coupling constant [197] and was recently coupled to the (2+1)D viscous hydro fields [198].

At the heart of our code is the importance sampling Monte Carlo integration algorithm, which is built from the first principles. In general, importance sampling is one of the best variance reduction techniques for estimating an integral using the Monte Carlo integration method. It samples points according to some probability distribution function $p(x)$, so that the points are concentrated in the regions that make the largest contribution to the integral. In general, we are interested in computing:

$$I = \int\limits_D f(x)dx = \int\limits_D \frac{f(x)}{p(x)} p(x)dx\,, \tag{2.30}$$

where the importance function $p(x)$ is a well behaved function on interval D. Then, for a sample of size N, the estimator of the integral is given by [199]:

$$\langle I \rangle = \frac{1}{N} \sum_{i=1}^{N} \frac{f(x_i)}{p(x_i)}\,, \tag{2.31}$$

where $\{x_i\}$ are sampled according to $p(x)$: in practice, this means that one constructs a cumulative distribution function of p, $\mathrm{CDF}[p](x)$, and feeds the inverse of it with a random real number between 0 and 1. Variance of this estimator is given by:

$$V[\langle I \rangle] = \frac{1}{N} V_p \left[\frac{f}{p}\right]\,, \tag{2.32}$$

where the variance on the right hand side is taken with respect to distribution $p(x)$. This means that by a careful choice of the sampling function, we can reduce this variance, which in practice means that we can use a smaller sample size N and ultimately obtain faster and more accurate results. To summarize, we can approximate the integral (2.30) by:

$$\int\limits_D f(x)dx \approx \langle f/p \rangle_p \pm \sqrt{\frac{\langle (f/p)^2 \rangle_p - \langle f/p \rangle_p^2}{N}}\,, \tag{2.33}$$

where the index p reminds us that the average is taken over a set of points distributed according to $p(x)$.

The DGLV integral (2.23) with replacement (2.26) at opacity order n is a $3n$-dimensional integral (or $2n$, if we use the uncorrelated medium (2.27) and evaluate the z-integrals analytically) and as such is well suited for a Monte Carlo evaluation. We will sample the momenta $q_{\perp k}$ from $d^2q_{\perp k} = q_{\perp k}dq_{\perp k}d\phi_k$ in (2.23) according to the (normalized) $\bar{v}^2(q_{\perp k})$. This is a good choice not only because it samples the momenta better than a plain Monte Carlo method (and therefore reduces the variance) and its inverse CDF is a simple analytical function, but also because we actually simplify the integrand by dividing it with this function. Although, at first sight, the appearance of the δ^2 functions additively with v^2 in (2.23) might seem to complicate these divisions at high orders in opacity (where we have 2^n mixed $\delta^{2l}v^{2k}$ terms), it actually proves to be a simplifying circumstance: if, in a generic expression, we choose $v^2(q_{\perp k})$ from the $(v^2(q_{\perp k}) - \delta^2(q_{\perp k}))$ term, then we simply divide the integrand by $v^2(q_{\perp k})$ and sample $q_{\perp k}$ according to it, but if we choose the $\delta^2(q_{\perp k})$, then we simply do not sample $q_{\perp k}$; in any case, the integrand always remains the same (up to a sign). Also, in this way it is easy to change the interaction potential in the computation: we only need to change the sampling function of $q_{\perp k}$ while the integrand remains the same. Out of similar considerations, we choose to sample z_k according to the (normalized) distribution $\bar{\rho}$ from (2.27), as in that way we practically never have to make the replacement (2.26), and it is also easy to implement a different distribution of the scattering centers by simply changing the sampling function. Angles ϕ_k from $d^2q_{\perp k}$ are sampled uniformly.

Input parameters for our code are gluon's light-cone momentum fraction x, energy of the jet E, mass of the quark M_q, mass of the gluon m_g, size of the medium L, gluon mean free path λ, Debye screening mass μ, opacity order n up to which to calculate the radiated gluon distribution, the range of the gluon transverse momenta $k_\perp$ at which to calculate the distribution and the number of sampling points N. The output is the inclusive radiated gluon distribution $x\frac{dN^{(1+\ldots+n)}}{dx\,d^2k_\perp}$ evaluated at every $k_\perp$ in the input, and a statistical error for each of them, calculated according to (2.33).

With the described integration method and by exploiting some of the regularities in the explicit form of the DGLV integral, we were able to construct a relatively fast algorithm: roughly, with 10^6 sampling points, evaluation at each $k_\perp$ at an opacity order n takes about $(2.6)^n$ seconds on an average personal computer, when the $z-$integration is done analytically for an uncorrelated medium (2.27). Our code has been tested up to 9th order in opacity by comparing its results to the results from [200]. With this code one can now efficiently compute and study triple differential (jet shape) effects at an arbitrary order in opacity.

2.3.2 General features of gluon distribution at finite opacity

Throughout this and the next section, we have used fixed $\alpha_s = 0.3$ and $C_R = 4/3$ for quark jets. Also, in plots, when not written explicitly otherwise, all the quantities with dimension of length are expressed in fm and those with the dimension of energy in GeV.

As a first example let us look at a radiated gluon $k_\perp$-distribution from a light quark jet at 100 GeV shown in Fig. 2.4. This plot is very instructive as it shows a number of important features of the opacity series.

In the plot, we have chosen to look at low-x gluons, because the low-x region is especially "hard" for the opacity series, since the formation times become small and the LPM phases (2.25) become large, which consequently slows down the convergence of the series. We see explicitly from Fig. 2.4 that, for $L/\lambda = 6$, it was enough to go to the 9th order in opacity series to achieve a satisfactory convergence. Due to these reasons, the question of how far we have to go in the opacity series really becomes a pragmatic

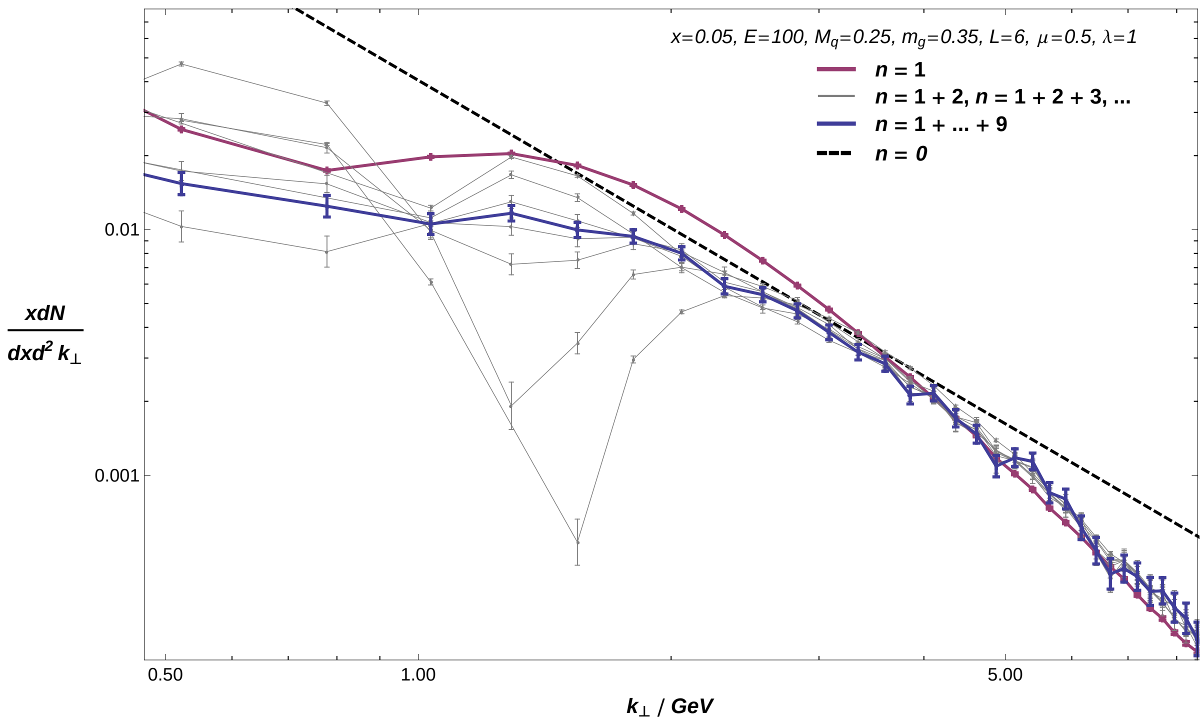

Figure 2.4: *The $k_\perp$-distribution of radiated $x = 0.05$ gluons for a light quark jet of energy 100 GeV. The dashed curve is the vacuum gluon distribution (2.4) ($n = 0$ order in opacity), the red curve is the first order in opacity, the blue one is the (inclusive) ninth order and the gray curves are all the other inclusive orders in between. Error bars indicate statistical errors computed using (2.33).*

matter. For example, for $x = 0.5$ and all the other parameters the same as in Fig. 2.4, a satisfactory convergence can be achieved already at the second order in opacity.

As we can see in Fig. 2.4, there are noticeable oscillations of the gluon distributions at small $k_\perp$: the curves corresponding to the inclusive even orders in opacity remain on one side of the convergent curve and the curves corresponding to the odd orders on the other side, a kind of an "even-odd" effect. This is an expected effect at low x and low $k_\perp$ in the DGLV opacity series, originating from the (partial) cancellations between the $(n + 1)$-th order unitarity correction and the direct n-th order term.

Lastly, we see how all the opacity orders for large enough transverse momenta converge to a characteristic hard power law. However, as we can see from Fig. 2.4, even for $k_\perp$ as large as $\sim xE$, this power-law is $\sim 1/k_\perp^3$, somewhat softer than the expected $1/k_\perp^4$. This also points to the importance of keeping the kinematic bounds on transverse momenta finite when calculating the x-spectrum of radiated gluons, xdN/dx: that is, the contributions to xdN/dx from momenta $k_\perp > xE$ may not be negligible and approximations of extending the upper limit $k_{\perp\max}$ to infinity have questionable validity. For these reasons, it is important to know what exactly these kinematic bounds are, i.e. what is the relevant $k_{\perp\max}$, a non-trivial problem (due to the collinear approximation assumed in the GLV formalism), which was carefully analyzed in [201].

2.3.3 Numerical comparison of DGLV and BDMPS/ASW

As noted in Section 2.1.3, one of the main differences between the GLV and the BDMPS approaches is the assumption of the multiple soft scatterings (MSS) of the latter. In addition to that, in BDMPS the medium's influence on the radiated gluon distribution is completely determined from the jet transport coefficient $\hat{q} \sim \mu^2/\lambda$ (eq. (2.11)). In this section we will use our Monte Carlo code to numerically inspect the differences between these two approaches at intermediate orders in opacity.

Neglecting the finite kinematic bounds on transverse momenta and integrating the x- and $k_\perp$- distribution in the MSS limit over all $k_\perp$, one obtains the analytical formula of BDMPS for dN/dx [149], which predicts a simple scaling of the induced x-spectrum with $\hat{q}$ via the variable z:

$$\omega \frac{d}{d\omega}(I - I_{\rm vac}) = \frac{\alpha_s}{\pi} x P_{\rm s\to g}(x) \ln \left| \cos\left(\sqrt{-iz}\right)\right| , \tag{2.34}$$

where the energy of the gluon is $\omega = xE$ for small x and $P_{\rm s\to g}(x)$ is the splitting function.

Here z is defined as:

$$z \equiv \left|\omega_0^2\right| L^2, \quad \omega_0^2 \equiv -i\frac{\left[(1-x)C_A + x^2 C_s\right]\hat{q}}{2x(1-x)E}\,. \tag{2.35}$$

For small x we have $z \sim (\mu^2 L^2)/(\lambda x E) \sim L/\tau_f$. As pointed out in [202], one can make a Taylor expansion of the BDMPS formula in z, which can be interpreted as an opacity series:

$$\ln\left|\cos\left(\sqrt{-iz}\right)\right| = \frac{1}{12}z^2 - \frac{17}{2520}z^4 + \frac{691}{935550}z^6 - \ldots\,. \tag{2.36}$$

We have shown, by explicit calculations of the DGLV radiated gluon spectrum up to 6th order in opacity, that the z-scaling predicted by (2.34) is broken by up to 100% (Fig. 2.5). Our results not only show how important it is to take into account the finite kinematic bounds (something the discussion in the previous section already hinted at), but also demonstrate that the energy loss spectrum at intermediate opacity (relevant to RHIC and LHC conditions) depends in detail on the screening mass μ and the mean free path λ, and not only through a simple combination in $\hat{q} \sim \mu^2/\lambda$.

Also, as discussed in [202], the BDMPS opacity series (2.36) is predicted to break at roughly $z \sim 1$, indicated by the dashed curves in Fig. 2.5. However, since this series misses the first order in opacity contribution (i.e. there is no linear term in (2.36)), the leading term in the opacity series, and neglects the finite kinematic bounds, it cannot be used for making predictions on convergence of a realistic opacity series, which, as we have explicitly shown, converges for $z > 1$. In addition to this, we should also note that, at least for $L > 1$ fm, the LHC conditions exclude the $z < 1$ domain.

To better understand the scaling breakdown from Fig. 2.5, we should go one step back and inspect the radiated gluon $k_\perp$-distribution in the MSS limit by keeping the transverse momentum kinematics finite, which was studied by ASW [164]. A direct comparison of our

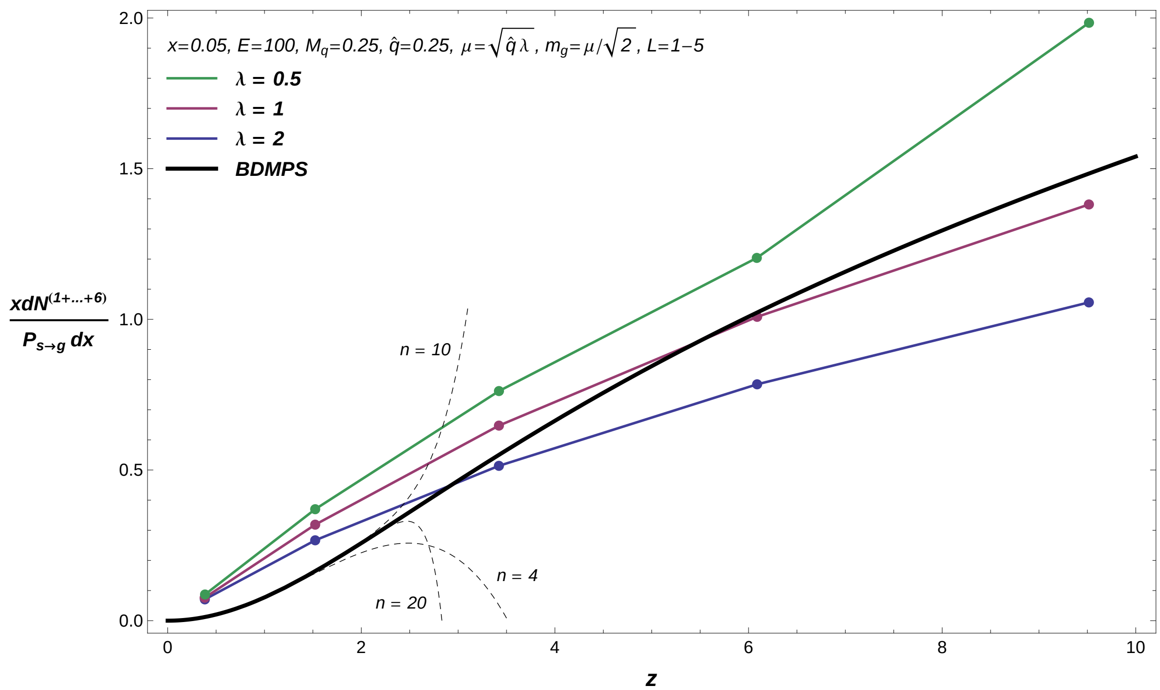

Figure 2.5: *The x-spectrum of radiated gluons (weighted by the splitting function) as a function of the variable z (eq. (2.35)) for a light quark jet of energy 100 GeV, compared to the BDMPS analytic formula (2.34). Black curve is the BDMPS limit, dashed curves represent its opacity series (2.36) truncated at different n, and the colored curves are the inclusive 6th order in opacity DGLV results. Each color represents results for different mean free paths λ, while different points on a particular curve are obtained by varying the medium size L. $\hat{q}$ is kept constant for all points on all curves.*

DGLV results and the ASW distributions in the MSS limit for a heavy quark jet of 20 GeV is shown in Fig. 2.6, where one explicitly sees how the finite opacity DGLV successfully interpolates between the thin ($n = 1$) and thick ($n = \infty$) plasma approximations.

In general, we expect that at low $k_\perp$, where the numerics of the DGLV opacity series are experiencing the "even-odd" oscillations, the gluon distributions should be better approximated by the Gaussian diffusion of the ASW in the MSS limit; of course, the opacity series will eventually converge to it, as we can clearly see in Fig. 2.6 (where, due to relatively high x, it was enough to go the 5th order in opacity to reach a satisfying

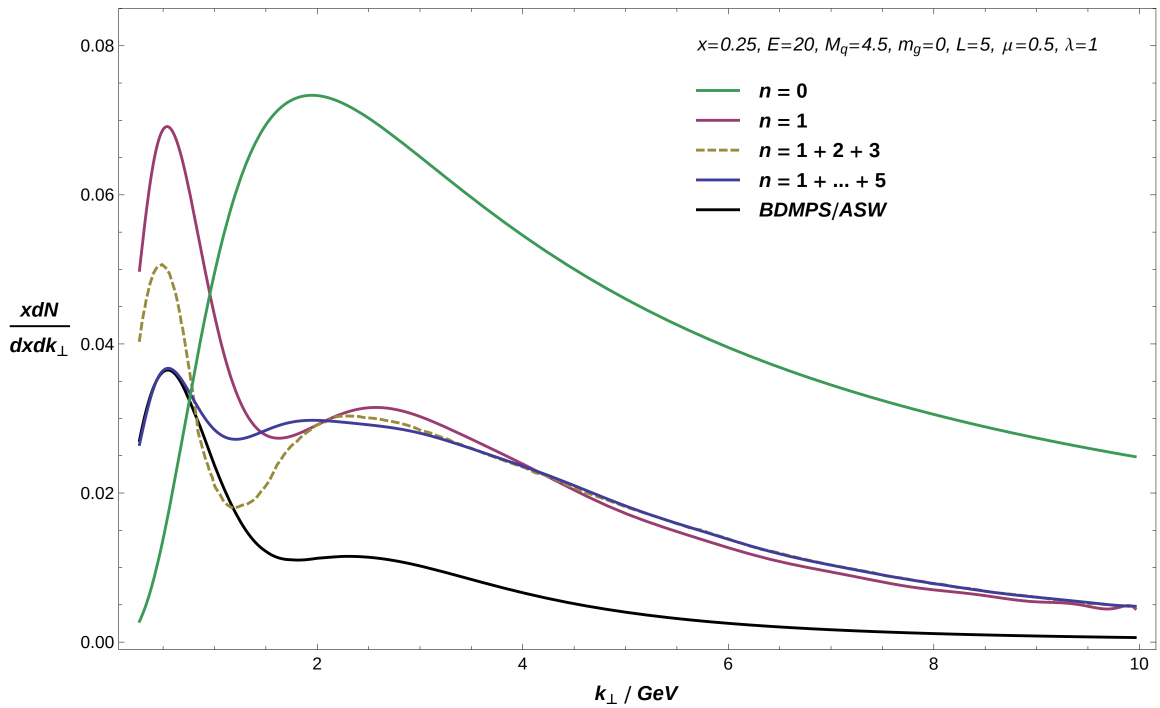

Figure 2.6: *The x- and $k_\perp$- radiated gluon distributions as a function of $k_\perp$ for a heavy quark jet of energy 20 GeV, compared to the BDMPS/ASW limit. Colored curves are the inclusive DGLV distributions at various orders in opacity (in particular, red is the "thin plasma" approximation), and the black curve is the ASW distribution in the MSS limit (the "thick plasma" approximation).*

convergence). However, at high transverse momenta, DGLV should better describe the expected hard power-law tails and in Fig. 2.6 we see how, expectedly, DGLV is harder at high $k_\perp$ than the MSS approximation. In the plot one can also see the kinematical dead cone effect at $n = 0$ (eq. (2.6)), and how this dead cone is already "filled" at first order in opacity by the medium-induced gluon radiation.

Chapter 3

The AdS/CFT correspondence

After studying jet quenching in perturbative QCD, starting from this chapter, we are turning towards the description of energy loss in gauge/gravity duality. In order to do so, we first need to set the stage by introducing the AdS/CFT correspondence and its most important aspects, as well as outlining some general results that will be used in the rest of the thesis.

We start with Section 3.1, where we explain the motivation and some early indications for gauge/gravity duality, as well as introduce some of the concepts in string theory we will need. In Section 3.2 we formulate the AdS/CFT correspondence and outline its most important aspects and implications. Extensions of these constructions and some immediate applications are discussed in Section 3.3, as well as in Section 3.4, where we introduce higher derivative corrections. In Section 3.5 (partly based on our [203]), we consider more general gravity duals to include field theories more similar to QCD. We conclude with Section 3.6, where we, following the logic and presentation from our [33], study the dynamics of classical strings, which will be directly related to the details of (holographic) energy loss.

3.1 Introducing the correspondence

Some of the first indications that string theories and gauge theories may be related have roots in the very beginnings of string theory. In Section 1.1.1 we saw how relativistic strings can serve as a good effective description of the QCD color electric flux tubes between a quark and an antiquark pair, leading to a simple description of confinement and the explanation of the Regge trajectories.

However, the link we will be after is more profound and relates the two theories in a deep and non-trivial way. In fact, the AdS/CFT correspondence [3–5] is the most successful realization of the holographic principle [1, 2], which states that a theory of quantum gravity in a some bounded region of space should be described by a non-gravitational theory living at the boundary of that region.

As we will see, large-N gauge theories really do look like string theories: the AdS/CFT correspondence is a formal duality between the two theories, not based on an assumption that the world is actually built out of small quantum relativistic strings. That is, one still considers the standard Yang-Mills theories to be the best description of the world around us; however, in certain regimes, where the problems in gauge theories are not tractable with usual techniques, the gauge/gravity duality allows us to formally cast them into simpler problems in string theory. This, in some sense, has partly relabeled string theory from being a "theory of everything" to being a "theory for everything".

3.1.1 Large-N gauge theories

One of the most direct indications of a relation between string theories and gauge theories comes from 't Hooft, who realized in the seventies that, perhaps counter-intuitively, $SU(N)$ gauge theories may simplify if we take the number of the colors N to be very large [204]. The idea was to solve the relevant problems in this limit and then do a perturbative expansion in $1/N = 1/3$ that would bring us closer to the real world QCD with three colors. Before taking the $N \to \infty$ limit, let us look at the β function of the $SU(N)$ theory (1.1) (without quarks) more explicitly:

$$\mu \frac{dg_{YM}}{d\mu} = -\frac{11}{3} N \frac{g_{YM}^3}{16\pi^2} + \mathcal{O}\left(g_{YM}^5\right) . \tag{3.1}$$

We see that when we take the $N \to \infty$ limit, we need to keep the combination

$$\lambda \equiv g_{YM}^2 N \tag{3.2}$$

fixed, so that the leading terms in (3.1) are of the same order. Quantity in (3.2) is called the 't Hooft coupling and the $N \to \infty$ limit is called the 't Hooft limit.

When N is large, the propagator for the adjoint fields becomes approximately equal to the product of a fundamental and an antifundamental field propagator, because the (additive) difference between the two goes like $1/N$. This allows for a convenient geometrical view of Feynman diagrams in this limit: each diagram is a simplicial decomposition (or triangulation) of a surface, i.e. each diagram becomes a compact, closed and oriented surface. This in turn allows for a simple analysis of the relative importance of each of the diagrams in an expansion of an amplitude, by counting vertices, edges and faces of the decomposition that represents it. By doing so, one realizes that the leading order diagrams are the ones that are planar (i.e. so that no propagator crosses another one), since they depend on N as $\propto N^2$, while all other classes of diagrams have smaller powers of N, and hence are subleading in the 't Hooft limit.

This geometrical description leads to a surprising connection with string theory: the $1/N$ expansion of the diagrams in terms of their geometrical features is actually the same one finds for closed, oriented strings in a perturbative string theory, provided one identifies $1/N$ as the string coupling constant g_s. This identification will actually end up being correct once we precisely formulate the AdS/CFT correspondence in Section 3.2, but, more importantly, this signifies a much deeper connection that was uncovered by taking the large N limit: in this limit, gauge theories and weakly coupled string theories look the same.

3.1.2 Elements of string theory

We start with a brief overview of some basic concepts in string theory that we will need to in order to formulate the AdS/CFT correspondence. More on this topic can be found in the standard literature, e.g. [205–207].

String theory is a quantum theory of relativistic strings. Classical relativistic strings are one-dimensional objects that sweep a two-dimensional surface M, the worldsheet, in some spacetime with metric[1] $G_{\mu\nu}$. The location of the string in the target spacetime is described by the embedding functions $X^\mu(\sigma,\tau)$, where σ and τ are the coordinates on the worldsheet (see Fig. 3.1 for an illustration). One often thinks of τ as the timelike coordinate, while σ parametrizes the string at some fixed "time" τ.

We can define an induced metric on the string worldsheet as

$$\gamma_{ab} = G_{\mu\nu}\partial_a X^\mu \partial_b X^\nu \,, \tag{3.3}$$

where with roman indices a and b we typically denote the worldsheet coordinates, i.e. $\sigma^a = (\sigma,\tau)$. In the differential geometry language, (3.3) is a pullback of the spacetime metric on a two-dimensional manifold. As the relativistically invariant action for a point particle is just the length of its worldline, a relativistically invariant action for the classical

[1]This is the so-called string frame metric, while the Einstein frame metric (the one in which the effective gravitational action has the Einstein-Hilbert form) may differ from this, if there is a non-trivial running of the dilaton. This is discussed more in Appendix B.1 and Section 3.5.6.

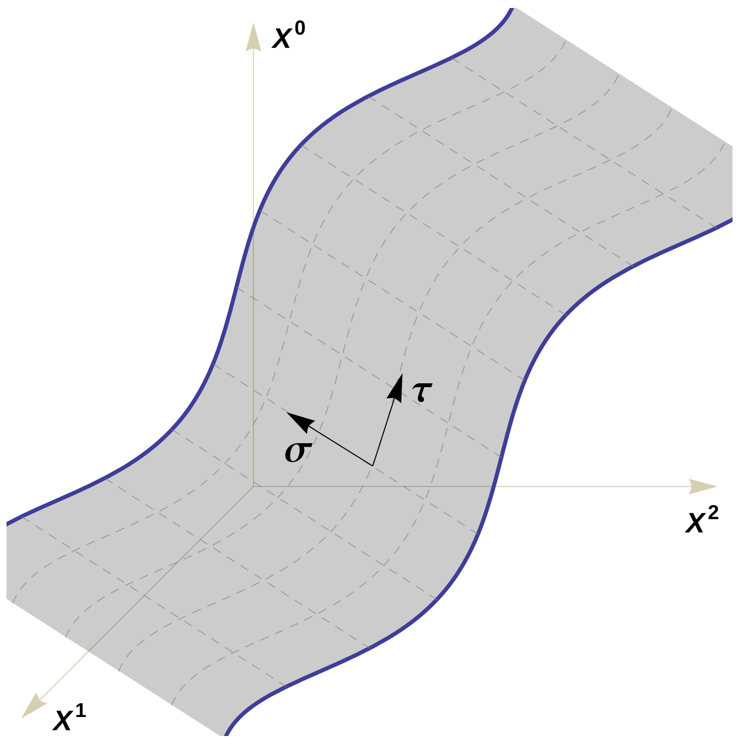

Figure 3.1: *Worldsheet of an open string in a (2+1)-dimensional spacetime. The thick blue lines denote the string endpoints and the dashed gray lines indicate the (σ, τ) coordinate system on the worldsheet.*

(bosonic) string will be the area of its worldsheet:

$$S_{NG} = -\frac{1}{2\pi\alpha'} \int_M d^2\sigma \sqrt{-\gamma}\,, \tag{3.4}$$

where $\gamma \equiv \det(\gamma_{ab})$ and $\alpha' = l_s^2$ is the squared fundamental string length. The constant in front of the action is called the string tension, which we will often denote with $\tau_f \equiv 1/(2\pi\alpha')$. Action (3.4) is called the Nambu-Goto action. We defer a more detailed discussion of the dynamics of classical strings to Section 3.6.

Varying the action (3.4), we can get the equations of motion of the string, plus a set of boundary terms. The boundary conditions force the string to be either open ($\partial_\sigma X^\mu(0,\tau) = \partial_\sigma X^\mu(\pi,\tau) = 0$), or closed ($\partial_\sigma X^\mu(0,\tau) = \partial_\sigma X^\mu(\pi,\tau),\ X^\mu(0,\tau) = X^\mu(\pi,\tau)$), where with

$\sigma = 0$ and π we denote the string endpoints. Utilizing the freedom to choose a particular gauge (i.e. a system of coordinates) on the worldsheet, one can drastically simplify the equations of motion. Focusing on flat space and choosing the light-cone gauge, by setting $X^+(\sigma,\tau) = x^+ + p^+\tau$, where x^+ and p^+ are constants and $X^\pm \equiv X^0 \pm X^1$, one sees that all the string dynamics is given by the transverse coordinates $X^i(\sigma,\tau)$, since X^- can be determined from the constraint equations that impose this gauge. Furthermore, the equations of motion in this gauge become a simple set of two-dimensional wave equations, whose general solution, for the case of open string boundary conditions, is

$$X^i(\sigma,\tau) = x_0^i + \sqrt{2\alpha'}\alpha_0^i\tau + i\sqrt{2\alpha'}\sum_{n\neq 0}\frac{1}{n}\alpha_n^i e^{-in\tau}\cos(n\sigma)\,, \tag{3.5}$$

where α_n^i are constants. This is a standing wave in the σ coordinate, while in the case of closed strings we get a superposition of two oppositely (left- and right-) moving traveling waves.

Let us now quantize these strings. One of the simplest ways to do it (which will be sufficient for our discussion) is the canonical quantization: one promotes the oscillators α_n^i to creation and annihilation operators that satisfy the appropriate equal-τ commutation relations. The states are then built in the standard way, by acting with $\hat{\alpha}_n^{i\dagger}$ on some suitably defined ground state $|0;p^\mu\rangle$. This ground state turns out to be a tachyonic state, i.e. $-\hat{p}^2 = M^2 < 0$, a known problem in the bosonic string theory; this issue is resolved in the full, superstring theory, once the fermions are added. The first excited states turn out to be massless: in the case of open strings they will be of form $\hat{\alpha}_1^{i\dagger}\,|0;p^\mu\rangle$ (and will naturally contain vector fields, as we will see in the next section), while in the case of closed strings they will be $\hat{\alpha}_1^{i\dagger}\hat{\tilde{\alpha}}_1^{j\dagger}\,|0;p^\mu\rangle$ (one oscillator from the left-moving wave and one from the right-moving one). The massless spectrum of the closed string contains the graviton (the symmetric part of $\hat{\alpha}_1^{i\dagger}\hat{\tilde{\alpha}}_1^{j\dagger}\,|0;p^\mu\rangle$), the Kalb-Ramond field (the antisymmetric part), and the dilaton (the trace).

The next step is to add fermions, by adding worldsheet spinors to the classical bosonic string action. In order to achieve spacetime supersymmetry, the spectrum of the quantized superstring needs to be truncated via the GSO projection [208, 209], which also removes the problematic tachyon state, inherited from the bosonic sector. Furthermore, the requirement of absence of negative norm states constrains the spacetime dimension of the superstring theories to be $D = 10$. It turns out that, from the spacetime perspective, one cannot have more than $N = 2$ supersymmetries. String theory that, in addition to closed strings, contains open strings can have only $N = 1$ supersymmetry (due to the open string boundary conditions): this is called the type I string theory. Theories with only closed strings can have $N = 2$ and, for that reason, are called type II theories; these are further divided into two classes, depending whether the two spinors have the opposite (type IIA) or same (type IIB) handedness.

We will be particularly interested in type IIB superstring theory [210, 211], as it will be the theory we will formulate the AdS/CFT correspondence in. Being a theory of closed strings, its massless spectrum includes the graviton $G_{\mu\nu}$ and the dilaton Φ, and being a supersymmetric theory, it also contains their supersymmetric partners. The end result is that the low energy (two-derivative) effective action of type IIB theory is the type IIB supergravity [212, 213],

$$S_D^{\text{tree}} = \frac{1}{2\kappa_D^2} \int d^D x \sqrt{-G^{(s)}} e^{-2\Phi} \left[R + 4 \left(\nabla \Phi \right)^2 + ... \right] , \tag{3.6}$$

where R is the Ricci scalar and where with superscript "(s)" we emphasized that this is the string frame metric. By considering amplitudes of processes involving joining and splitting of strings, one finds that e^{Φ} plays the role of an effective coupling. For this reason $g_s = e^{\Phi}$ is called the string coupling, which, as we see, is not a free parameter, and is instead determined by the dilaton.

3.1.3 D-branes and gauge theories

One of the crucial ingredients in formulating the AdS/CFT correspondence are the D-branes, as the gauge theory from one side of the duality will live on the worldvolume of the branes. In this section we present a somewhat informal discussion meant to illustrate the mechanism of how D-branes naturally host gauge theories on their worldvolumes, while a more comprehensive treatment of the subject can be found in [214, 215].

Dp-branes are solitonic, extended objects in p spatial dimensions on which open strings can end [216]. The letter "D" stands for Dirichlet, since the endpoints of open strings must satisfy Dirichlet boundary conditions in the directions transverse to the brane. Let us denote by $X^0, ..., X^p$ the directions in which the brane extends and with $X^{p+1}, ..., X^d$ the directions transverse to it. For simplicity, we focus on simple Dp-branes that are hyperplanes in flat d-dimensional space. This means that the endpoints of open strings can move freely in the $X^0, ..., X^p$ directions (i.e. the string embedding functions will satisfy Neumann boundary conditions), while in the $X^{p+1}, ..., X^d$ directions they are constrained to be on the brane (Dirichlet boundary conditions).

The ground states of the quantized string will be labeled only by the momenta in the $X^2, ..., X^p$ directions, since there are no momenta in the transverse directions: $|p^+, p^2, ..., p^p\rangle$. The first thing to notice is that these fields seem to "live" on the D-brane itself: a Fourier transformation of the states reveals that that their wavefunctions depend on the $X^0, ..., X^p$ coordinates. The general state is then obtained by acting on these ground states with oscillator operators $\hat{\alpha}^i_n$ (eq. (3.5)). The ground state $|p^+, p^2, ..., p^p\rangle$ is obviously a scalar field from the perspective of the brane, and as noted before, is tachyonic, with $M^2 < 0$. The next states will have one oscillator acting on them, $\hat{\alpha}^{i\dagger}_n |p^+, p^2, ..., p^p\rangle$, and are massless. For $2 \leq i \leq p$ (i.e. for the directions along the brane), these states will transform as a (massless) vector field on the brane with $(p+1)-2$ components: i.e. this is a Maxwell gauge field. But, for $p+1 \leq i \leq d$, this index is not a Lorentz index from the perspective of the brane and simply enumerates different states: these states are hence massless scalars. Note that we have as many scalars as there are normal directions to the brane, leading to a pleasing physical interpretation that these scalars describe the transverse excitations of the D-brane.

Therefore, at low energies, the effective action of a D-brane is one of free Maxwell fields A^i and scalars ϕ^i. It is possible to go beyond the low energy limit and resum all the higher derivative α'-corrections exactly, yielding the full Dirac-Born-Infeld (DBI) action [217, 218] of a Dp-brane:

$$S_{\text{DBI}} = -\frac{1}{(2\pi)^p g_s l_s^{p+1}} \int d^{p+1}\xi e^{-\Phi} \sqrt{-\det\left(P\left[G_{\mu\nu} + 2\pi\alpha' F_{\mu\nu}\right]_{ab}\right)}\,, \tag{3.7}$$

where the factor in front is the tension of the D-brane (inversely proportional to g_s, reflecting its solitonic nature), ξ^a are the coordinates on its worldvolume, and with P we denote the pullback of the combination of the background metric $G_{\mu\nu}$ and the field strength $F_{\mu\nu}$ on the worldvolume of the brane. For a vanishing $F_{\mu\nu}$, (3.7) is proportional to the volume of the Dp-worldvolume, i.e. it becomes a higher dimensional generalization of the Nambu-Goto action (3.4).

Let us now consider two parallel D-branes (call them 1 and 2), separated by some distance L, and the possible string excitations of this system. In this case we have four possible classes, or four sectors, of open strings (see Fig. 3.2 for illustration): in addition to the open strings that start and end on the same brane (which we just discussed), we now also have open strings that stretch between the two branes, and since the open strings are oriented (the direction of increasing σ), we have two possible sectors of those. These four different sectors are usually denoted by $[i, j]$ symbols, indicating that the strings are stretching from brane i to brane j (also historically called the Chan-Paton indices).

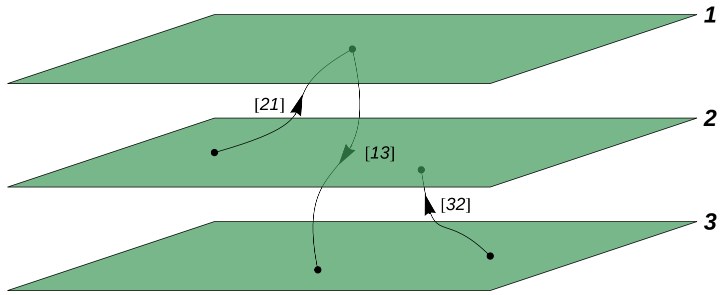

Figure 3.2: *Illustration of the open string excitations between parallel D-branes.*

Analysis of open strings from sectors $[1, 1]$ and $[2, 2]$ is the same as before, but the $[1, 2]$ and $[2, 1]$ strings have slightly different boundary conditions than before, and their quantization will yield an additional constant term in the expression for the mass M^2 of the form $L^2/(2\pi\alpha')^2$. This is to be expected, since $\tau_f = 1/(2\pi\alpha')$ is the tension of the string and L is its minimal length, so $L/(2\pi\alpha')$ is the energy of a classical stretched string. The intuitive interpretation that the quantized states of the $[1, 1]$ and $[2, 2]$ strings live on the worldvolumes of their respective branes cannot be simply extended to the case of $[1, 2]$ and $[2, 1]$ strings, i.e. they certainly live on some $(p + 1)$-dimensional volume, but not necessarily the worldvolume of any particular brane. Also, because of the constant mass term, the scalars and the Maxwell fields will now be massive, but if we let $L \to 0$, i.e. consider coincident (but still distinguishable) branes, then the lowest lying fields again become massless. Since now we have 4 massless vector fields that can interact, we naturally get a $U(2)$ Yang-Mills gauge theory on the worldvolume of (now coincident) branes [219]. These interactions consist in e.g. endpoints of two different strings joining and forming a single open string (see Fig. 3.2) and so on. Analogously, if we have N coincident Dp-branes, we get N^2 interacting gauge fields, naturally generating a $U(N)$ Yang-Mills theory.

Let us now consider a particular case of N coincident D3-branes, as the AdS/CFT correspondence will be based on them. We consider these branes in the full IIB superstring theory, so that the string spectrum is supersymmetric and the embedding space is 10-dimensional. As before, we will have N^2 interacting gauge fields generating a (3+1)-dimensional $U(N)$ Yang-Mills theory with 6 massless scalars, but in addition to that we will also have 4 fermions, due to the underlying supersymmetry. Because of this, the gauge theory on the branes will have $\mathcal{N} = 4$ supersymmetries. For these reasons, this theory is called $\mathcal{N} = 4$ super Yang Mills (SYM) [208, 219, 220].

$\mathcal{N} = 4$ SYM is a remarkable theory, which is, although at a first glance quite complicated, in fact rather simple, which is why it is sometimes referred to as the "harmonic oscillator of the 21st century". The main reason for this is the large amount of supersymmetries, which not only completely determines the Lagrangian of the theory, but also ensures that the theory is exactly conformal, that is, the β function is zero at all loop orders and the coupling never runs [221–223]. Also, since the field content of $\mathcal{N} = 4$ SYM comes from the open string excitations of the D3-branes, all of the fields are in the adjoint representation of the gauge group.

3.2 Overview of the correspondence

Now that we have reviewed some basic motivation and early indications for the gauge/gravity duality and covered some basic terminology in string theory that we will need, in this section we will formulate the correspondence precisely and discuss its most important implications. A classic review of AdS/CFT is [224], while another great one, with special emphasis on applications to heavy ion physics, is available in [225].

3.2.1 Formulating the correspondence

The AdS/CFT correspondence, as presented in the original paper by Maldacena [3], is based on looking at the system of N coincident D3-branes in type IIB string theory from two different points of view.

The first perspective is based on inspecting the low energy limit of the effective action of the system. Type IIB string theory contains only closed strings, and with the addition of D3-branes, we now also have open strings, as excitations of the D-branes (see Fig. 3.3 for illustration). The low energy limit consists of taking the energy to be lower than the only dimensionful scale in the string theory, $E \ll 1/\sqrt{\alpha'}$, or, equivalently, by taking $\alpha' \to 0$, while keeping the energy E and other parameters, such as N, fixed. In this limit, only the massless string states are excited. The massless states of open strings on coincident D-branes, as we have seen in Section 3.1.3, generate $\mathcal{N} = 4$ vector supermultiplet on the (3+1)-dimensional worldvolume of the branes, and hence their effective Lagrangian is the one of $\mathcal{N} = 4$ $U(N)$ SYM gauge theory. Massless states of closed strings generate the gravity supermultiplet in the 10-dimensional background and their effective Lagrangian is the one of type IIB supergravity, as we saw in Section 3.1.2. Of course, these massless modes of open and closed strings also interact, so we can write the full effective action of the system as

$$S = S_{\text{bulk}} + S_{\text{brane}} + S_{\text{int}} \,, \tag{3.8}$$

where S_{bulk} is the supergravity action, S_{brane} is the $\mathcal{N} = 4$ SYM action, and S_{int} captures the interactions between these two sectors. The action (3.8) is effective, in the sense that it involves only massless fields, while the massive ones are, due to the low energy limit, integrated out and appear as higher derivative α'-corrections in S_{bulk} and S_{brane}: these corrections however come with positive powers of α', and therefore vanish in the low energy $\alpha' \to 0$ limit.

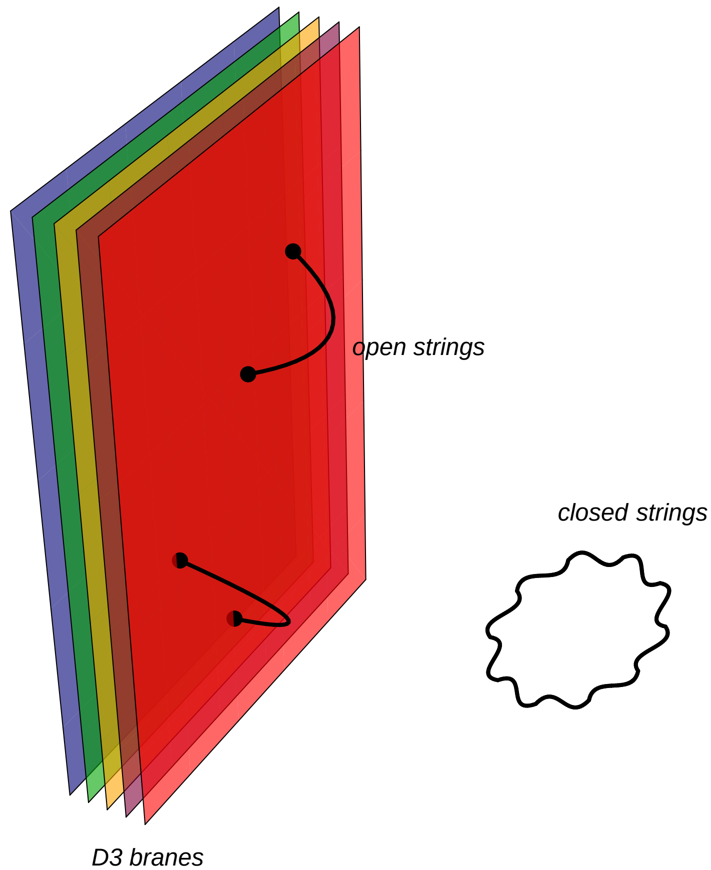

Figure 3.3: *Illustration of the degrees of freedom of the system: the closed strings of type IIB theory and open strings as perturbative excitations of a stack of coincident D3-branes.*

As is well known, in the low energy (long distance) limit, gravity becomes a theory of free spin-2 fields, and, similarly, the supergravity in the bulk also becomes free, and S_{bulk} will describe the propagation of free, massless modes. Similarly, all the interactions with the brane fields come at positive powers of α' and also vanish in the low energy limit, so $S_{\text{int}} \to 0$ as $\alpha' \to 0$. Therefore, in the low energy limit we have two decoupled systems: free (super)gravity in the bulk and a (3+1)-dimensional Yang-Mills gauge theory on the branes.

The second perspective on the system of D3-branes is based on the fact that they are massive charged objects and therefore curve the spacetime. In fact, Dp-branes represent a full string theory description of p-brane solutions in supergravity [216], higher dimensional analogs of charged black holes, which we discuss in details in Appendix B.1. This means that in the low energy limit, we can replace the stack of D3-branes by the geometry they source, the (extremal) 3-brane solution in (B.9) with $p = 3$:

$$ds^2 = \frac{1}{\sqrt{H(r)}}\left(-dt^2 + d\vec{x}^2\right) + \sqrt{H(r)}\left(dr^2 + r^2 d\Omega_5^2\right) , \tag{3.9}$$

where r is the radial coordinate, $d\vec{x}^2 \equiv dx_1^2 + dx_2^2 + dx_3^2$ and we relabeled $L \equiv r_+$ from (B.10), so

$$H(r) = 1 + \frac{L^4}{r^4}, \qquad L^4 = 4\pi g_s N \alpha'^2 . \tag{3.10}$$

To take the low energy limit in this context, we need to look at how one measures energies in geometry (3.9). Since the tt-component of the metric is not constant, the energies measured at different r will differ by a redshift factor: if an observer at r measures the energy of an object to be E_r, then the energy E of the same object measured by an observer at $r \to \infty$ will be given by

$$E = H(r)^{-1/4} E_r . \tag{3.11}$$

That means that no matter how energetic the object might be at some r, as long as that r is sufficiently small (i.e. close to the horizon $r = 0$), this object will appear to have small energy for an observer at infinity. Hence, the low energy limit in this context is the near-horizon ($r \to 0$) limit. In this limit we have two kinds of low energy excitations: the low energy modes in the bulk and excitations of any energy that are close to the horizon $r = 0$. These two sectors decouple in the low energy limit: first, the low energy cross section for the absorption of massless modes in the bulk of energy ω by the horizon goes like $\sigma \sim \omega^3 L^8$ [226], where L is given by (3.10) (essentially, the cross section vanishes because the particles have wavelengths much larger than the typical size of the brane L), and second, the particles close to the horizon find it harder and harder to climb the gravitational potential and escape to the bulk (see Fig. 3.4 for illustration).

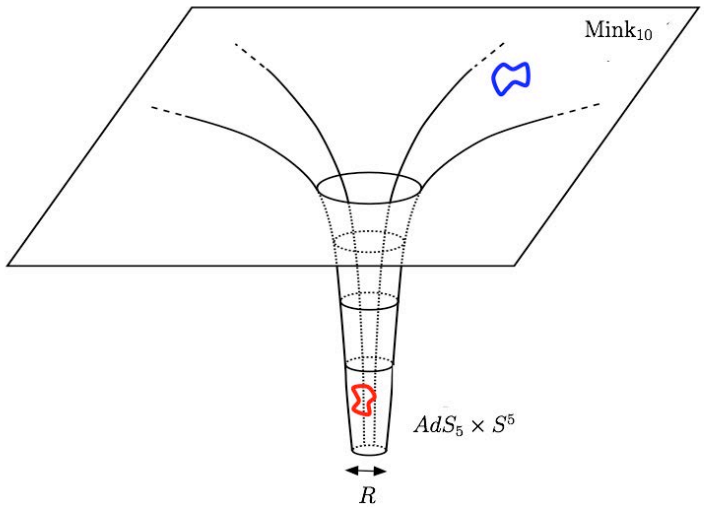

Figure 3.4: *Closed strings of type IIB theory in the 3-brane metric (3.9) sourced by D3-branes. (Taken from [225].)*

We therefore again have two decoupled systems: free (super)gravity in the bulk and full IIB string theory in the near-horizon ($r \to 0$) region of the 3-brane metric (3.9):

$$ds^2 = \frac{r^2}{L^2}\left(-dt^2 + d\vec{x}^2\right) + \frac{L^2}{r^2}dr^2 + L^2 d\Omega_5^2\,, \tag{3.12}$$

Geometry (3.12) is the geometry of a five-dimensional Anti-de Sitter space of radius L, times a five-dimensional sphere of the same radius, $AdS_5 \times S^5$. In both descriptions of the system of D3-branes, we have that one of the decoupled systems is free supergravity in flat space, so it is natural to identify the other two systems in the two perspectives. This leads us to identify the $\mathcal{N} = 4$ $U(N)$ super-Yang Mills gauge theory in (3+1)-dimensional flat spacetime with type IIB superstring theory on $AdS_5 \times S^5$. This is the AdS/CFT correspondence [3].

3.2.2 Aspects of the correspondence

Before discussing some interesting implications and consequences of the just stated correspondence, let us first mention a subtlety. In the string theory in the bulk of AdS, all of the field content interacts with the gravity (i.e. there are no decoupled modes), while its dual field theory is a $U(N)$ gauge theory, in which the $U(1)$ part is free and decoupled from the rest of the $SU(N)$ gauge theory (and it can be understood as describing the motion of the whole system of D-branes). This means that the bulk AdS theory is in fact describing the $SU(N)$ part of the gauge theory.

In the previous section we have stated the AdS/CFT correspondence as an equivalence between two seemingly very different physical theories: a string theory on a very specific curved spacetime and a conformal field theory with a large amount of supersymmetries. The first check of this equivalence is to inspect whether the symmetries of the two theories match. The isometry groups of AdS_5 and S^5 are $SO(4,2)$ and $SO(6)$, respectively; how are these realized in the dual field theory? $\mathcal{N}=4$ SYM is a (3+1)-dimensional conformal theory and the conformal group in (3+1)D is precisely $SO(4,2)$. The fact that the conformal invariance of the theory is reflected in the AdS geometry of the near-horizon region will be important later on when we try to extend this construction and consider more general dualities. Finally, $SO(6)$ isometry is dual to the global $SU(4)$ (which is locally isomorphic to $SO(6)$) R-symmetry of $\mathcal{N}=4$ that rotates the six scalars[2].

Since the two theories are conjectured to be equivalent, we can relate their respective parameters. An interesting thing to notice is that the number of "colors" N is actually the (RR) charge of the 3-brane solution (B.5) (i.e. each of the D3-branes carries one unit of that charge). But one of the most important relationships is the one between the couplings of the two theories. The dynamics of the D3-branes is described by the

[2] R-symmetry is a symmetry that transforms different supercharges, and in this case it is $SU(4)$ because in the dual field theory we have $\mathcal{N}=4$ supercharges.

DBI Lagrangian (3.7) in which the string coupling enters as $1/g_s$; in the low energy limit, this Lagrangian becomes the Lagrangian of $\mathcal{N}=4$ SYM, which contains the Yang-Mills coupling as $1/g_{YM}^2$, so we can relate the two:

$$g_{YM}^2 = 4\pi g_s \,. \tag{3.13}$$

We should note that α' alone is not related to any of the quantities in the field theory, because it is dimensionful and is hence used as a scale to measure other dimensionful quantities; this means that it will appear only in dimensionless combinations such as L^2/α', as we will soon see.

Let us now inspect how big or small should these parameters be in order for the limits we assumed earlier remain valid. In an $SU(N)$ gauge theory where the number of colors N is kept general, as we saw in (3.1), we need the 't Hooft coupling $\lambda = g_{YM}^2 N$ (eq. (3.2)) to be small, in order to be in the perturbative regime. The Yang-Mills coupling is related to the string coupling via (3.13), which is, in turn, related to the AdS radius L via (3.10). Let us, for clarity, summarize these relations in one line:

$$\lambda = g_{YM}^2 N = 4\pi g_s N = \frac{L^4}{\alpha'^2} \,. \tag{3.14}$$

From here we see that a small λ implies

$$\text{want } \lambda \ll 1 \quad \Rightarrow \quad \frac{L^4}{\alpha'^2} \ll 1 \,. \tag{3.15}$$

On the string theory side, however, we want to perform classical gravity calculations (i.e. neglect stringy corrections), so the typical size of the space L needs to be much bigger than the string scale l_s, which then, following (3.14), implies

$$\text{want } \frac{L^4}{\alpha'^2} \gg 1 \quad \Rightarrow \quad \lambda \gg 1\,. \tag{3.16}$$

We see that the two regimes (3.15) and (3.16) are completely incompatible, that is, when one theory is strongly coupled, the other one is weakly coupled, and vice versa. This is the reason why the statement of equivalence of the two theories is called duality, and the reason why it is so useful, but also hard to prove. The limit that is going to be useful to us is when the field theory is strongly coupled, $\lambda \gg 1$. From (3.16) we see that this means that the stringy corrections are negligible, but, in addition to this, we also need to require that $g_s \ll 1$ so that the loop corrections are negligible as well and the string theory is classical. From (3.14) we see that this means we need to take the following limit:

$$N \gg \lambda \gg 1\,, \tag{3.17}$$

which is sometimes also referred to as the 't Hooft limit. In this limit, the strongly coupled gauge theory is dual to a classical, two-derivative supergravity, in which the calculations are tractable.

One should also note that the AdS/CFT correspondence is only a conjecture, since we have treated the string theory perturbatively (closed and open strings are perturbative excitations of vacuum and D-branes, respectively). For this reason, there are several different forms of the conjecture, depending on the size of g_s and N; for us the most useful one will be the weak form, in which one postulates that the gravity description of the gauge theory is valid only for large g_sN, while the full string theory on AdS might not agree with the field theory (the strongest form of the conjecture states that the two theories are exactly equivalent at all values of g_s and N).

Finally, let us briefly comment on the $AdS_5 \times S^5$ geometry[3] (3.12). An extensive discussion of the structure of Anti-de Sitter space is available in Appendix B.2, where we show how the geometry (3.12), also called the Poincaré patch, covers only one half of the entire AdS space. We also show how the AdS space is bounded, with a boundary located at $r \to \infty$. Another useful set of coordinates is achieved by defining

$$z \equiv \frac{L^2}{r}\,, \tag{3.18}$$

in which case the AdS part of the metric (3.12) becomes a (4+1)-dimensional Minkowski space with a simple "warp" factor:

$$ds^2 = \frac{L^2}{z^2}\left(-dt^2 + d\vec{x}^2 + dz^2\right)\,. \tag{3.19}$$

That is, every "z-slice" of the AdS space in these coordinates is conformally symmetric (up to a warp factor) to the $\mathbb{R}^{3+1}$, which is also the geometry of the boundary (which is now at $z = 0$).

3.2.3 The field/operator correspondence

In this section we will present a more concrete, operational statement of the correspondence, by relating fields and operators in the two theories.

$\mathcal{N} = 4$ SYM is a conformal field theory, and as such, it does not have asymptotic states (nor, consequently, an S-matrix), essentially because the theory has no scale, so there is no notion of what "asymptotically far away" is. This means that we should consider

[3]We will often be interested in the dynamics of fields only in the AdS_5 part of the metric, assuming that we are at a fixed point in S^5, or, since S^5 is compact, that we can expand the full 10-dimensional fields in terms of spherical harmonics. This is because the dynamics in AdS_5 is directly mappable to the dynamics in the boundary field theory directions, while the motion in S^5 is related to the motion in the internal space of the scalar fields of $\mathcal{N} = 4$.

operators and try to relate them to the quantities in the dual string theory. Now, the field theory coupling constant g_{YM} is related to the string theory coupling constant g_s through (3.13), which is, as noted in Section 3.1.2, related to the expectation value of the dilaton field, $\langle \Phi \rangle$, which, in turn, is determined by the boundary conditions at the infinity (i.e. the boundary of AdS). Hence, changing the coupling constant in the field theory amounts to changing the boundary value of the dilaton.

With this specific example in mind, let us consider a more general case of a source $\phi_0(x)$ (where by x we abbreviate the field theory directions $(t, \vec{x})$) that couples to some local, gauge-invariant operator $\mathcal{O}(x)$ in a standard way. That is, we consider adding a term of the form $\int d^4x \phi_0(x)\mathcal{O}(x)$ to the field theory Lagrangian (if the operator $\mathcal{O}$ is already present in the theory, then ϕ_0 is its total coefficient). Following the example of the dilaton, it is natural to assume that this addition will change the boundary condition for the dilaton (or some other general field ϕ) at the boundary of AdS to $\phi_0(x)$, i.e. $\phi(x, z \to 0) = \phi_0(x)$. This leads to the following general statement of the equality of the partition functions of the two theories [4, 5]:

$$\left\langle \exp\left[\int d^4x \phi_0(x)\mathcal{O}(x)\right]\right\rangle_{\mathrm{CFT}} = \mathcal{Z}_{\mathrm{string}}\left[\phi(x,z)|_{z\to 0} = \phi_0(x)\right] , \tag{3.20}$$

where the quantity of the left hand side is the generating function of correlation functions of $\mathcal{O}$ in the field theory (which are generated by taking functional derivatives $\delta/\delta\phi_0$ and setting $\phi_0 = 0$ afterwards), and the right hand side is the full partition function of the string theory with the boundary condition of $\phi = \phi_0$ at the boundary of AdS. This relation is called the field/operator correspondence, valid for any ϕ, i.e. for any field ϕ in the bulk of AdS, there is a 1-to-1 correspondence with an operator in the field theory.

In general, there is no precise way to determine these field/operator duals, apart from various symmetry considerations, such as in the case of conserved currents J_μ (associated with some global symmetries), that couple to the external sources A_μ in the standard way, $\delta S = \int d^4x A_\mu J^\mu$. An important example of this is the energy momentum tensor $T^{\mu\nu}$, which is conserved as long as the theory is translationally invariant, and which is sourced by the metric:

$$\delta S = \int d^4x g_{\mu\nu}(x) T^{\mu\nu}(x) \tag{3.21}$$

where $g_{\mu\nu}(x)$ is the background metric of the field theory and is hence the limit of the bulk AdS metric as we approach the boundary, $g_{\mu\nu}(x) = \lim_{z\to 0} G_{\mu\nu}(x,z)$. Comparing this with (3.20) we say that the field theory energy momentum operator $T^{\mu\nu}$ is dual to the bulk metric $G_{\mu\nu}$.

Therefore, we can calculate $n-$point functions of various operators in a strongly coupled gauge theory by taking derivatives of the right hand side of (3.20). In the 't Hooft limit (3.17), the string partition function is dominated by the classical solution and (3.20) becomes

$$\mathcal{Z}_{\text{CFT}} = \mathcal{Z}_{\text{string}} \approx \exp\left(-S_{\text{clas.}}\left[\phi(x,z)|_{z\to 0} = \phi_0(x)\right]\right) , \tag{3.22}$$

where $S_{\text{clas.}}$ is the (renormalized) on-shell action of a classical supergravity, expressed as a functional of the boundary values $\phi_0(x)$. This means that we first need to solve the relevant classical supergravity equations of motion in AdS_5, and the simplest case is the one of massive scalar (which will also be the case of particular interest later on).

The action of a massive scalar field in AdS_5 is

$$S = \frac{1}{2\kappa_5^2}\int d^5x\sqrt{-G}\left[\frac{1}{2}G^{\mu\nu}\partial_\mu\phi\partial_\nu\phi + \frac{1}{2}m^2\phi^2\right] , \tag{3.23}$$

where $G_{\mu\nu}$ is the metric of AdS_5, which we take in coordinates (3.19). The equation of motion is just the usual Klein-Gordon equation (in curved space),

$$\left(\Box - m^2\right)\phi = 0\,, \tag{3.24}$$

where $\Box \equiv \nabla_\mu \partial^\mu$. Because the metric in the Poincaré patch is conformally equivalent to the Minkowski metric, with an $\vec{x}$-independent warp factor, the solution in those directions is just a plane wave,

$$\phi(\vec{x}, z) = e^{i\vec{p}\cdot\vec{x}} Z(z)\,, \tag{3.25}$$

while for the radial direction we first define $u \equiv pz$, with $p \equiv |\vec{p}|$, and $Z(u) \equiv y(u)u^2$, yielding

$$u^2 y''(u) + u y'(u) - \left(u^2 + 4 + m^2 L^2\right) y(u) = 0\,. \tag{3.26}$$

This is just the modified Bessel equation, whose solutions are the standard modified Bessel functions, I and K:

$$Z(u) = \alpha u^2 I_{\Delta-2}(u) + \beta u^2 K_{\Delta-2}(u)\,, \tag{3.27}$$

where

$$\Delta \equiv 2 + \sqrt{4 + m^2 L^2}\,. \tag{3.28}$$

In order for the solution (3.27) to be real, we need to have

$$m^2 \geq -4/L^2\,. \tag{3.29}$$

Negative mass is allowed in AdS, in the sense that it will not lead to instabilities, as long as it satisfies (3.29): this is called the Breitenlohner-Freedman bound [227, 228].

Close to the boundary $z \to 0$, the full solution (3.25) will have the following form:

$$\phi(\vec{x}, z) \xrightarrow{z\to 0} A(\vec{x}) z^{4-\Delta} + B(\vec{x}) z^{\Delta}\,. \tag{3.30}$$

As we approach the boundary, the second term in (3.30) vanishes, while the first, non-normalizable term (with respect to some suitably defined inner product), according to (3.20), corresponds to the deformation of the field theory Lagrangian,

$$S \to S + \int d^4x A(x)\mathcal{O}(x)\,. \tag{3.31}$$

Also note that in this general, massive case, when $\Delta \neq 4$, (3.20) should be generalized so that the sources are given by $(z^{\Delta-4}\phi(x,z))|_{z\to 0} = \phi_0(x)$. The second term in (3.30) is normalizable, and those modes are elements of the Hilbert space in the bulk; in the view of the AdS/CFT correspondence, these modes are naturally identified with the gauge theory states [229, 230]. We should also note that Δ in (3.28) is in fact the conformal dimension of the operator $\mathcal{O}$, for the following reason. An isometry in the bulk of the form $x^\mu \to \lambda x^\mu$, $z \to \lambda z$ is a scale transformation in the field theory. Since ϕ is a scalar in the bulk, (3.30) implies that $A(x)$ should transform as $A \to \lambda^{\Delta-4}A$, and then (3.31) implies that the operator $\mathcal{O}$ must have a (mass) scaling dimension of Δ.

Finally, let us emphasize an important physical point. In the view of the field/operator correspondence (3.20) (and the holographic principle), where the connection of the field theory quantities to the bulk physics happens at the boundary of AdS, one can perhaps imagine the field theory as "living on the boundary". Furthermore, if we consider an object of size d (in $\vec{x}$ directions) in the bulk at some radial position z away from the boundary (in coordinates (3.19)), then, because of the AdS warp factor, at the boundary the size of the object will be $d_{\text{bnd}} \propto zd$. That is, the further the object is from the boundary, the more "smeared" it appears there. If the (proper) energy of this object is E, then its energy measured at the boundary will be $E_{\text{bnd}} \propto E/z$, since energy is conjugate to time. In other words, some field theory process of energy E_{bnd} is associated with a bulk process localized at $z \propto 1/E_{\text{bnd}}$. Therefore, high energy processes in the field theory (UV) correspond to the bulk physics near the boundary, while the low energy processes (IR) correspond to the bulk physics far away from it. This is called the UV/IR relation [231, 232] and it leads to a correspondence between the radial direction in AdS and the renormalization group flow of the gauge theory. Therefore, in the 't Hooft limit (3.17), the classical physics in the bulk at different "z-slices" corresponds to processes in its dual quantum field theory at different energy scales.

3.3 Further constructions and applications

The topic of the previous section was the standard formulation of the AdS/CFT correspondence, while in this section we will present some extensions to that construction by introducing finite temperatures and fundamental matter, as well as look at some immediate applications that are of interest in the context of QCD and heavy ion physics.

3.3.1 Finite temperatures

A simple, but for us very important extension of the story from the previous sections is the duality with the field theory at finite temperatures. The way we have arrived to the result that it is the AdS metric that is dual to $\mathcal{N} = 4$ SYM was by taking the extremal limit in the general solution for the black 3-brane metric (B.3), which consisted of setting $r_+ = r_-$. The Hawking temperature of extremal black holes vanishes (i.e they emit no Hawking radiation) and hence they are naturally dual to zero-temperature field theories, as we saw earlier. Therefore, we might expect that having the D3-brane degrees of freedom at a finite temperature will correspond to a non-extremal black 3-brane metric in which we allow $r_+ > r_-$ [20, 21]. Absorbing r_- in the definition of the radial coordinate as in

(B.8), we are left with a horizon at r_+, so the metric in the near horizon limit looks like:

$$ds^2 = \frac{r^2}{L^2}\left(-f(r)dt^2 + d\vec{x}^2\right) + \frac{L^2}{r^2}\frac{dr^2}{f(r)} + L^2 d\Omega_5^2\,, \tag{3.32}$$

where

$$f(r) = 1 - \frac{r_H^4}{r^4}\,, \quad r_H = \pi T L^2\,, \tag{3.33}$$

is the blackening function with T being the Hawking temperature. Note that as we approach the boundary, $r \to \infty$, the metric (3.32) asymptotes to pure $AdS_5 \times S^5$, eq. (3.12). The "AdS part" of the solution (3.32) is also called AdS_5-Schwarzschild, as it is the black hole solution of the five-dimensional Einstein-Hilbert action with a negative cosmological constant,

$$S_{\mathrm{AdS}_5} = \frac{1}{2\kappa_5^2}\int d^5x\sqrt{-G}\left[R + \frac{12}{L^2}\right]\,. \tag{3.34}$$

Of course, pure AdS_5 is another classical solution of the same action.

In the dual description, one identifies the field theory temperature T with the black hole Hawking temperature in (3.33), as can be seen from Euclideanizing the time $t \to -i\tau$: on the gravity side, as is well known, one arrives at a conical singularity close to the horizon which can be removed by making the Euclidean time coordinate periodic [233]. On the field theory side this corresponds to considering the theory at non-zero temperature, since, in the Poincaré patch, the time coordinate of AdS is the same as the time coordinate on the boundary.

One of the first computations based on these analyses was the computation of the free energy of $\mathcal{N} = 4$ SYM plasma at a finite temperature. On the gravity side, the entropy is just the usual Bekenstein-Hawking entropy of the black hole solution, $S = A/(4G_N)$, where A is the area (really a volume) of the black hole (3.32), from where we can get the free energy

$$F_{\mathrm{SUGRA}} = -\frac{\pi^2}{8} N^2 V T^4 \,, \tag{3.35}$$

where the V is the 3-dimensional volume of the D3-branes. This expression makes sense, since the powers of V and T are dictated by the scale invariance, and N^2 is the number of degrees of freedom in the plasma at large N. Expression (3.35) is believed to be a good guide for the free energy of $\mathcal{N} = 4$ SYM at large λ [20], but it is very hard to independently verify this result with standard field theory calculational techniques. The computation of the free energy at zero coupling in the field theory yields a result surprisingly similar to the strong coupling one, up to a "mysterious factor" of 4/3 [20]:

$$F_{\mathrm{SYM}} = \frac{4}{3} F_{\mathrm{SUGRA}} \,. \tag{3.36}$$

This remarkable result that, in $\mathcal{N} = 4$, the free energy (as well as the pressure and entropy density) at infinite coupling is only 3/4 of its value at zero coupling has been approximately observed in lattice simulations of deconfined non-supersymmetric theories [59, 234] (see Fig. 1.1), all the way to about $T \sim 3T_c$.

3.3.2 Introducing quarks

In $\mathcal{N} = 4$ SYM, as mentioned before in Section 3.1.3, all of the field content is in the adjoint representation of the gauge group, so if we want to have fields that look like quarks, we need to add some extra content to the constructions we described. In this section we will describe the model of [19] for adding fundamental matter to AdS/CFT; a great review of that model, as well as mesons in holography, is available in [235].

Quarks are fermions in the fundamental representation of the gauge group, but at large N, their spin is irrelevant and their defining feature becomes the fact that they are fundamental matter. This is because, for example, the free energy of the fields in the adjoint representation scales like $\sim N^2$, while for the fundamental matter it scales like $\sim N_f N$, where N_f is the number of "flavors". So, we obviously need some additional content, and from the string theory point of view, this means some new brane content, in addition to D3-branes that generate $\mathcal{N} = 4$ SYM. This is because open strings that have both of their endpoints on D3-branes naturally generate adjoint fields, while those that have only one endpoint on them will generate fields in the fundamental representation. This means that we need to put the other end of those strings on some extra, "flavor" brane.

If this new flavor brane is separated from the D3-branes in the direction that is perpendicular to them, then the string of minimum length has a non-zero energy and the corresponding quark will be massive, with its mass given simply by the product of the string's tension and its length, $M = l/(2\pi\alpha')$ (as we saw in Section 3.1.3). Strings with both ends on the flavor brane will be in the adjoint of $U(N_f)$ and will naturally describe mesonic degrees of freedom. Since these strings describe the fluctuations of the flavor branes in the background geometry, this offers a nice example of many geometrical interpretations of field theory concepts that the gauge/gravity duality offers: small oscillations of D-branes are dual to gauge theory mesons.

What kind of brane should this flavor brane be? Since we are working in type IIB theory, only Dp-branes with p odd are allowed[4] and hence we have D3, D5, D7, and D9 at our disposal. It is not possible to use a D9-brane, since it is a space filling brane and we cannot separate it from the stack of D3-branes. And since D3- and D5-branes lead to theories with defects, the only one left is the D7-brane [19]. Assuming that the D3-branes span the $(0, 1, 2, 3)$ directions in the flat 10-dimensional background, then the D7-brane

[4] In type IIA string theory, Dp-branes with p even are stable, while in type IIB theory, p must be odd [216]. The reason for this is essentially because these branes are the lightest states that carry RR charges, so the conservation of charge prevents them from decaying.

will span $(0, 1, ..., 7)$ directions, so that they are separated in the directions $(8, 9)$ (see Fig. 3.5 for an illustration).

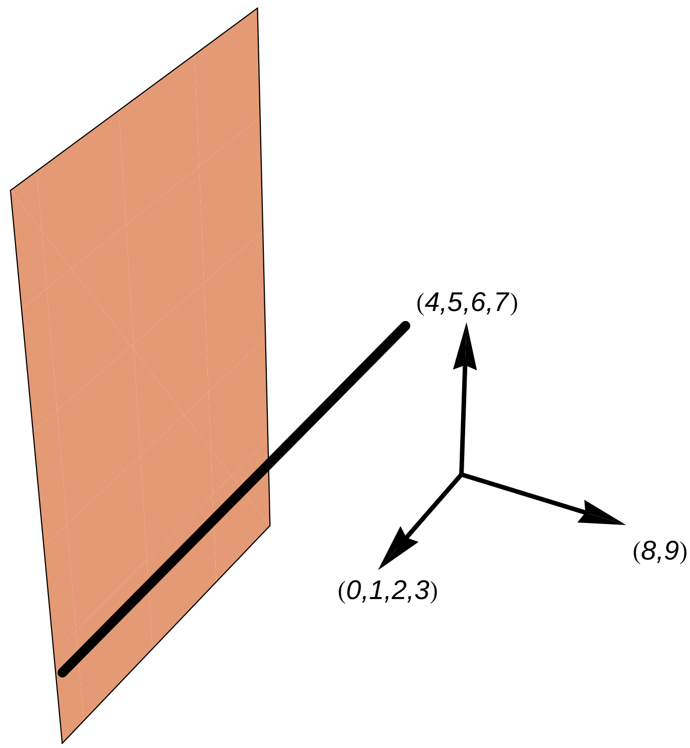

Figure 3.5: *Illustration of the relation between the brane content in the Karch-Katz model of introducing fundamental matter. The thick black line represents the stack of D3-branes, while the amber plane represents the D7 flavor brane.*

With this additional brane content, the full brane configuration (N_f D7-branes plus N coincident D3-branes) will be dual to $\mathcal{N} = 2$ $U(N)$ SYM, which, in addition to all the field content of $\mathcal{N} = 4$, also contains N_f massive $\mathcal{N} = 2$ hypermultiplets[5] that are in the fundamental representation of the gauge group. Therefore, the field content now consists of an $\mathcal{N} = 4$ SYM multiplet, which is generated by the massless open string modes on D3-branes, and the $\mathcal{N} = 2$ hypermultiplet generated by the modes of the strings stretching

[5]The extra matter naturally comes in supermultiplets, because of the underlying supersymmetry of the string theory. $\mathcal{N} = 2$ hypermultiplets are supersymmetry multiplets made of two $\mathcal{N} = 1$ chiral multiplets, which are pairs of a scalar and a fermion field, (ϕ, ψ).

between the D3- and D7-branes, with $U(N_f)$ as the global flavor group. There are also modes on the D7-D7 strings, but those decouple from the rest of the theory in the low energy ($\alpha' \to 0$) limit.

To simplify the calculations, we take the probe limit $N_f \ll N$, so that the background geometry is still $AdS_5 \times S^5$, and the backreaction from the D7-branes on it is suppressed by powers of N_f/N. On the field theory side, this is dual to neglecting the quark loops and hence quenching the gauge theory. Therefore, we need to embed the D7-branes in the classical background described by the metric $G_{\mu\nu}$. Let us write the $AdS_5 \times S^5$ metric (3.12) in the following way:

$$ds^2 = \frac{r^2}{L^2}\eta_{ij}dx^i dx^j + \frac{L^2}{r^2}\left(d\rho^2 + \rho^2 d\Omega_3^2 + dw_5^2 + dw_6^2\right) , \tag{3.37}$$

where $\rho^2 = w_1^2 + ... + w_4^2$ is the radial coordinate of the S^3 of S^5, so the radial coordinate of AdS_5 is given by $r^2 = \rho^2 + w_5^2 + w_6^2$, where w_5 and w_6 denote the directions in which the D7-branes will be separated from the D3-branes. That is, we simply foliate the flat six-dimensional subspace in the brackets in (3.37) not with 5-spheres as in (3.12), but "cylinders". The low energy degrees of freedom (open string fluctuations) of a D-brane are described by the DBI action (3.7). Plugging the ansatz (3.37) in (3.7) (with $F_{\mu\nu} = 0$) we get explicitly

$$S_{D7} = -\mu_7 \int d^8\xi \rho^3 \sqrt{1 + \dot{w}_5^2 + \dot{w}_6^2}\,, \tag{3.38}$$

where μ_7 denotes the tension of the D7-brane and $\dot{w}_i \equiv dw_i/d\rho$. The equations of motion are:

$$\frac{d}{d\rho}\left[\frac{\rho^3}{\sqrt{1 + \dot{w}_5^2 + \dot{w}_6^2}}\frac{dw_i}{d\rho}\right] = 0\,, \tag{3.39}$$

and these have a particularly simple solution:

$$w_5, w_6 = \text{const.}\,, \tag{3.40}$$

i.e. the D7-brane simply lies stationary in space. The choice of w_5 and w_6 corresponds to choosing the quark mass and the fact that they are constant is a statement of non-renormalization of mass (a typical characteristic of the supersymmetric gauge theories), since ρ is a holographic radial coordinate and hence, as we saw in Section 3.2.3, corresponds to an RG scale. We can therefore choose, say, $w_5 = 0$ and $w_6 = l$ and separate the D7-branes from the stack of D3-branes. In that case ρ^2, the radius of the S^3 that the D7-brane wraps, is given by $\rho^2 = r^2 - l^2$ and hence at $r = l$, it vanishes, i.e. the S^3 shrinks to zero. From the perspective of r^2, the radial coordinate of AdS_5, the D7-brane simply "vanishes in thin air" at $r = l$, since its tension is proportional to the radius of S^3 (see Fig. 3.6).

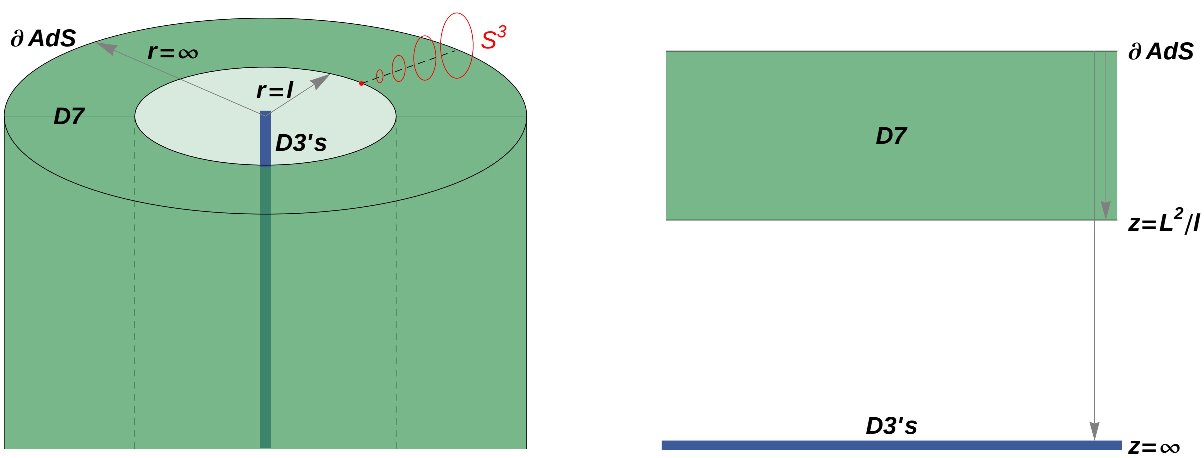

Figure 3.6: *Introduction of the fundamental matter to AdS/CFT in the probe limit. In the left illustration we see the setup in global AdS, where we imagine the D3-branes sitting at the center of AdS, while in the right one we see the perspective from the Poincaré patch.*

As we said, the (Lagrangian) mass of the quark M will be equal to the product of distance between the D3- and D7-branes l and the string tension τ_f, or, in the Poincaré coordinates where the boundary is at $z = 0$ (eq. (3.19)):

$$M = \frac{\sqrt{\lambda}}{2\pi} \frac{1}{z_M}\,, \tag{3.41}$$

where $z_M \equiv L^2/l$. At finite temperatures, part of the AdS geometry gets "cut off" by the horizon (eq. (3.32)), yielding the following result for the rest mass of a quark in a thermal medium:

$$M_{\text{th}}(T) = M \left[1 - \frac{\Delta M(T)}{M} + \mathcal{O}\left(\left(\frac{\Delta M(T)}{M} \right)^4 \right) \right], \qquad \Delta M(T) \equiv \frac{\sqrt{\lambda}}{2} T\,. \tag{3.42}$$

Here the first two terms are simply the energy of a straight string in geometry (3.32), while the higher order terms arise due to the change of the embedding of the D7-brane as a response to the introduction of the horizon, and these can be determined numerically [236, 237]. At $M \approx 0.92 \Delta M(T)$, the bottom of the D7-brane jumps discontinuously to the horizon; that is, the minimal value of M_{th} is $\approx 0.02 \Delta M(T)$.

3.3.3 Transport coefficients

As one of the first immediate results of special importance for applications of holography to quark-gluon plasma, let us briefly summarize the derivation of the expression for the ratio of shear viscosity to entropy density, η/s, in AdS/CFT.

Shear viscosity is an example of a transport coefficient, which are defined in general for any conserved current, and which describe how small deviations away from the equilibrium relax back towards it. Other examples of transport coefficients include the bulk viscosity ζ and conductivity σ. Using the linear response theory and the fluctuation-dissipation theorem it is possible to derive the general Kubo-Green formula for a transport coefficient

χ (see e.g. [238]),

$$\chi = -\lim_{\omega\to 0}\lim_{\vec{k}\to 0}\left[\frac{1}{\omega}\mathrm{Im}G_R(\omega,\vec{k})\right], \tag{3.43}$$

where $G_R(\omega,\vec{k})$ is the retarded Green's function of some operator $\mathcal{O}$ that describes the change of the ensemble average of $\mathcal{O}$ when one introduces a current J that couples to $\mathcal{O}$ in a standard way (i.e. $\int d^4x\mathcal{O}J$): $\delta\langle\mathcal{O}\rangle = JG_R$.

As we saw in Section 3.2.3, the AdS/CFT correspondence is particularly well suited for calculation of the correlation functions in strongly coupled field theories. However, the field/operator correspondence (3.20) is formulated in the Euclidean signature, while the transport coefficients need to be calculated in the Lorentzian signature, because the response of the thermal ensemble to small perturbations that drive it out of equilibrium can only be learned from real-time retarded Green's functions G_R. Of course, we can, in principle, obtain them by analytic continuation from the Euclidean ones,

$$G_R(\omega,\vec{k}) = G_E(-i(\omega+i\varepsilon),\vec{k}), \tag{3.44}$$

but a common problem is that, for general ω and $\vec{k}$, we can often calculate the Euclidean correlators only numerically, so a procedure such as (3.44) may not be applicable in a general case. Son and Starinets have devised a general prescription to calculate the correlation functions in real time [239], where one starts from the very basics and calculates the correlators in the Lorentzian AdS/CFT[6].

The shear viscosity η is a transport coefficient for the off-diagonal component of the energy-momentum tensor T^{xy}, as it describes the response of the system when one changes the metric by some off-diagonal h_{xy}. For Einstein (i.e. two-derivative) gravity in a geom-

[6]There are several complications that arise in the Lorentzian version of AdS/CFT, that are absent in the Euclidean case. An immediate complication is that the correlation functions have to be time ordered. Another one is that the requirement of regularity of the solution and fixing of the boundary conditions is not enough to specify a solution, and one must also impose the so-called in-falling boundary conditions at the horizon (since we are considering the theory at finite temperature).

etry with no off-diagonal components in the background metric, one can show that the Einstein equations to linear order in perturbations $h_{\mu\nu}$ become a simple massless Klein-Gordon equation for $\phi \equiv h_x{}^y$. This means that the effective action for ϕ is precisely the action of a massless scalar, (3.23) with $m^2 = 0$. Starting from here, Policastro, Son and Starinets first computed the shear viscosity in the strongly coupled $\mathcal{N} = 4$ plasma using the AdS/CFT correspondence in [240], which was published before the general method in [239], but because the transport coefficients are calculated in the limit of small ω and $\vec{k}$, it is possible to carry out the computation without the need for any particular general method.

In [241] the shear viscosity was calculated using the so-called membrane paradigm, a rather concise and a very illustrative method that is equivalent to the general method of [239], but also emphasizes the importance of the role the classical equations of motion for the off-diagonal graviton play in the final result. In short, using this method, one can express the retarded correlator that enters (3.43) via the canonical momentum Π_z conjugated to ϕ with respect to the radial z direction,

$$G_R(k_\mu) = -\lim_{z\to 0} \frac{\Pi_z(z, k_\mu)}{\phi(z, k_\mu)}\,, \tag{3.45}$$

where $k^\mu \equiv (\omega, \vec{k})$ and where now, since we are in the Lorentzian signature, one must also impose the in-falling boundary conditions on ϕ at the horizon. Eq. (3.45) is true for any k_μ, but in order to calculate the transport coefficients, we only need the low frequency limit, which, as one can see by inspecting the equations of motion, are quite simple and in the end yield

$$\frac{\eta}{s} = \frac{1}{4\pi}\,, \tag{3.46}$$

where s denotes the entropy density, expressed as the Bekenstein-Hawking formula for the entropy, divided by the worldvolume of D3-branes.

Equation (3.46) is an important result, because although it was derived for $\mathcal{N} = 4$ SYM at infinitely strong coupling, it actually applies to a wide variety of strongly coupled gauge theory whose gravity dual is given by Einstein gravity coupled to matter fields, i.e. the theory may or may not be conformal, confining, or supersymmetric. The important thing is, as illustrated in the previous discussion, that the effective action for the off-diagonal graviton is that of a massless scalar. The result (3.46) becomes even more important when we consider the heavy ion program at RHIC (and LHC): there, the values of η/s needed for the hydrodynamic models to match the elliptic flow data were precisely on the order of $1/4\pi$ (see Fig. 1.7).

As we will see in Section 3.4.2, at finite coupling, the result (3.46) will be modified, so that, in $\mathcal{N} = 4$ SYM, for $\lambda \approx 7$ we have $\eta/s \approx 2/(4\pi)$, even closer to the values at RHIC and LHC. As discussed in Section 1.2.2, at weak coupling (very low and very high temperature regimes in QCD), the mean free path diverges and, consequently, the shear viscosity, diverges as well. Based on these considerations, it was conjectured [242] that the result (3.46) may in fact be a universal lower bound (the so-called KSS limit) in the sense that it is a generic property of strongly coupled theories. However, as we will see in Section 3.4.3, introducing certain higher derivative corrections to the Einstein-Hilbert action will change the equations of motion for $h_x{}^y$ and, starting from (3.45), one gets η/s that can be in some cases smaller than $1/(4\pi)$.

3.3.4 Wilson loops

Wilson loops were discussed in Section 1.1.1, where we pointed out that their expectation values can give us the effective potential between a quark and an anti-quark. We saw in Section 3.3.2 that quarks can be introduced to AdS/CFT by adding D7-branes to the stack of D3-branes, in such a way that the separation between the two is proportional to the quark mass. Quarks are then dual to the endpoints of strings that stretch between the D7- and the D3-branes (Fig. 3.6), with the bulk of the string (in the finite temperature case) encoding the medium disturbance due to the introduction of the quark (i.e. its "gluon cloud").

In Section 3.1.3 we saw how D-branes support gauge fields on their worldvolume, under which the string endpoints are charged. However, strings also "pull" on the brane, deforming its shape: these deformations, as noted before, are described by the scalars living on the worldvolume of D-branes. This leads to a generalization of the Wilson loop (1.7) in $\mathcal{N} = 4$ which now, in addition to gauge fields A_μ, must also include the adjoint scalars ϕ_i [243, 244]. Since Wilson loop is a functional of some closed path $\mathcal{C}$ in spacetime (giving the partition function of the quark traversing that path) and since quarks are identified with the string endpoints on the D7-brane, the boundary of the string worldsheet $\partial\Sigma$ should be precisely the quark's path $\mathcal{C}$. Therefore, it makes sense that the expectation value of the Wilson loop is given by its dual string partition function [243, 244],

$$\langle W(\mathcal{C})\rangle = \mathcal{Z}_{\text{string}}[\partial\Sigma = \mathcal{C}] \to e^{-S_{\text{clas.}}[\mathcal{C}]}\,, \tag{3.47}$$

where in the last step we assumed the 't Hooft limit, in which the string's partition function is dominated by the classical string solution. This means that by extremization of the simple, classical Nambu-Goto action, we can find expectation values of Wilson loops in the dual gauge theory at strong coupling.

The first obvious application of this is to find the $\bar{q}q$ potential in $\mathcal{N} = 4$ SYM, starting with the zero temperature case. We can do so by simply fixing the endpoints of the string at some distance R in the field theory direction $\vec{x}$ and solve the classical equations of motion, which yields a characteristic U-shaped string profile (approximately the colored strings in Fig. 3.7). Computing the on-shell action yields the total energy of the system, so subtracting the masses of the heavy quarks finally gives the effective potential [243, 244]:

$$V_{\rm SYM}(R) = -\frac{4\pi^2}{\Gamma^4(1/4)}\frac{\sqrt{\lambda}}{R}\,, \tag{3.48}$$

where $\sqrt{\lambda} = L^2/\alpha'$ is the 't Hooft coupling (eq. (3.14)), which will often emerge in calculations involving strings. The length dependence of $V(R) \propto 1/R$ could have also been predicted simply from the conformal invariance of $\mathcal{N} = 4$.

At finite temperature, the situation is similar and one gets again the U-shaped string configurations, but at some separation R_c, due to the presence of the horizon, it becomes more favorable for the system to effectively "split" into two disjointed strings (see Fig. 3.7) [245, 246]. More precisely, the configuration of two disjointed strings has a lower energy past R_c and the path integral in (3.47) is dominated by that solution. Once $R > R_c$, the $\bar{q}q$ pair has "melted", the potential becomes constant and the two quarks are perfectly screened by the plasma between them. In QCD, due to confinement, the potential becomes linear at large distances; however, $\mathcal{N} = 4$ is not a confining theory. In a simple confining theory, as in e.g. [21], one effectively has a "soft wall" at some constant z_0, so once the bottom of the string reaches it, more and more of the string lays down on it as the quarks separate, and the energy of the system increases linearly with the distance.

We conclude this section with mentioning the holographic calculation of the jet quenching parameter $\hat{q}$, defined in (2.11), which tells us the average transverse momentum squared transferred from the medium to the jet per unit length, and which, in some models of energy loss in QCD (as discussed in Section 2.1.3), completely determines the details of the radiated gluon spectrum. It has been shown [247] that this parameter can be calculated from a light-like Wilson loop, composed of two x^3- directed light-like Wilson

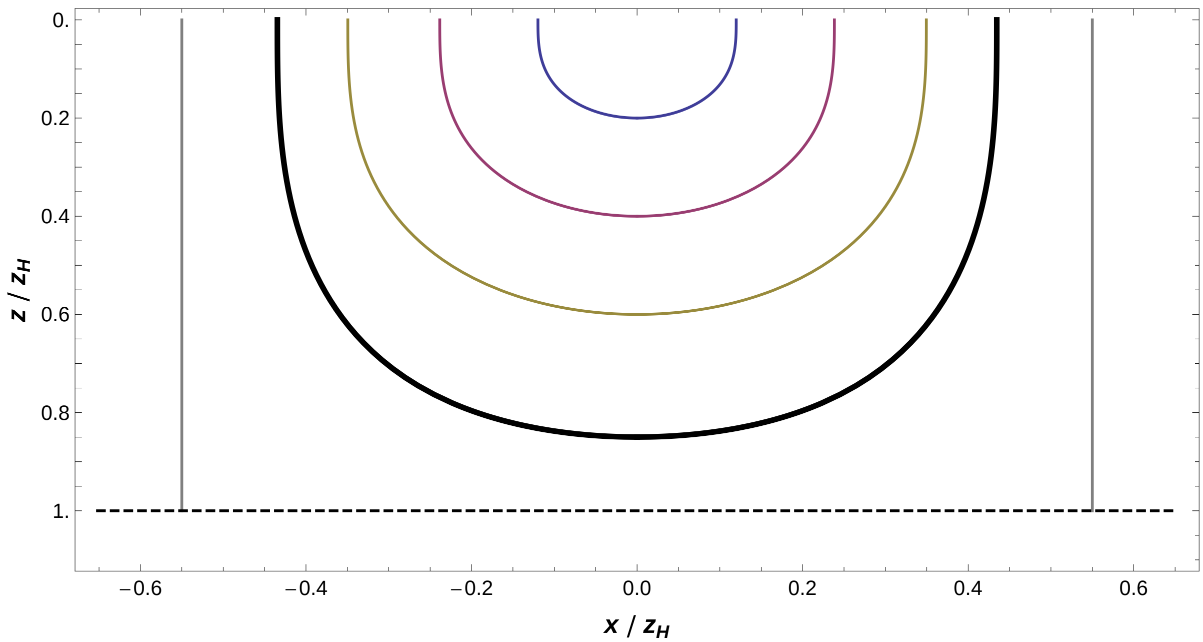

Figure 3.7: *String configurations (in Poincaré patch), associated with a heavy $\bar{q}q$ pair in a finite-temperature $\mathcal{N}=4$ plasma. The three colored, U-shaped strings describe the $\bar{q}q$ at separations where the connected configurations are favored, the black string is the critical case where the free energy of the connected configuration is equal to the free energy of the separated strings, after which the disconnected configuration, consisting of two straight strings (gray) is preferred.*

lines, separated in the $x_\perp$ direction:

$$\hat{q}_{\rm SYM} = \frac{\pi^{3/2}\Gamma(3/4)}{\Gamma(5/4)}\sqrt{\lambda}T^3\,. \tag{3.49}$$

Plugging in some typical values of $T \sim 300MeV$ and $\alpha_s \sim 1/3$, we get $\hat{q} \sim 5$ GeV^2/fm, a rather reasonable value as indicated by various jet quenching models.

3.4 Higher derivative corrections

All of the calculations presented so far are valid in the 't Hooft limit, when λ and N are large. However, in the real world QCD, $N = 3$ and λ is on the order of a few, and because of this, it is important to consider finite-λ and finite-N corrections. On the string theory side, these are encoded in the α'-corrections to the two-derivative bulk action and the quantum corrections to the classical string worldsheet.

3.4.1 Quantum corrections to string worldsheet

The quantum corrections to the classical string worldsheet are in general notoriously complex and are known only in very special cases, most notably when one is interested in the expectation values of various Wilson loops, as the corrections can be computed by considering worldsheet fluctuations around the classical solution that dominates the expectation value of the loop. Examples include the corrections to the $q\bar{q}$ potential in $\mathcal{N}=4$,

$$V_{\mathrm{SYM}}(R) = -\frac{4\pi^2}{\Gamma^4(1/4)}\frac{\sqrt{\lambda}}{R}\left(1+\frac{\kappa_V}{\sqrt{\lambda}}+\mathcal{O}\left(\lambda^{-1}\right)\right), \tag{3.50}$$

where $\kappa_V \approx -1.34$ [248, 249], and the jet quenching parameter $\hat{q}$,

$$\hat{q}_{\mathrm{SYM}} = \frac{\pi^{3/2}\Gamma(3/4)}{\Gamma(5/4)}\sqrt{\lambda}T^3\left(1+\frac{\kappa_q}{\sqrt{\lambda}}+\mathcal{O}\left(\lambda^{-1}\right)\right), \tag{3.51}$$

where $\kappa_q \approx -1.97$ [250].

3.4.2 R^4 corrections to type IIB action

The higher derivative corrections to the type IIB supergravity action (3.6) are accompanied by powers of α', and are hence also called α'-corrections. These α'-corrections to the bulk are much more tractable and can be easily used in various calculations of interest, as one only needs to change the spacetime metric. A rather special property of type IIB theory is that the first possible set of higher derivative corrections, R^2, identically vanish and hence the first non-vanishing ones are R^4, which have been computed in [251]. In the Poincaré coordinates (3.32), the α'-corrected near-horizon metric of a non-extremal[7] stack of D3-branes is given by:

$$\begin{aligned} G_{tt} &= -\frac{L^2}{z^2} f(z) \left(1 + \gamma \mathcal{T}(z) + \mathcal{O}\left(\gamma^2\right)\right) , \\ G_{zz} &= \frac{L^2}{z^2} \frac{1}{f(z)} \left(1 + \gamma \mathcal{Z}(z) + \mathcal{O}\left(\gamma^2\right)\right) , \\ G_{xx} &= \frac{L^2}{z^2} , \end{aligned} \tag{3.52}$$

where

$$\begin{aligned} \mathcal{T}(z) &= -15(5\tilde{z}^4 + 5\tilde{z}^8 - 3\tilde{z}^{12}) , \\ \mathcal{Z}(z) &= 15(5\tilde{z}^4 + 5\tilde{z}^8 - 19\tilde{z}^{12}) , \end{aligned} \tag{3.53}$$

with $\tilde{z} \equiv \pi T z$ and $f(z) = 1 - \tilde{z}^4$. The expansion is made in γ defined as

$$\gamma \equiv \frac{\zeta(3)}{8} \left(\frac{\alpha'}{L^2}\right)^3 = \frac{\zeta(3)}{8} \lambda^{-3/2} . \tag{3.54}$$

These corrections will be therefore dual to the finite-λ corrections on the gauge theory side. For the case of shear viscosity, we have [253, 254]

$$\frac{\eta}{s} = \frac{1}{4\pi} \left[1 + \frac{15\zeta(3)}{\lambda^{3/2}} + \mathcal{O}\left(\lambda^{-5/2}\right)\right] , \tag{3.55}$$

for the case of the jet quenching parameter,

$$\hat{q}_{\mathrm{SYM}} = \frac{\pi^{3/2}\Gamma(3/4)}{\Gamma(5/4)} \sqrt{\lambda} T^3 \left(1 + \frac{\tilde{\kappa}_q}{\lambda^{3/2}} + \mathcal{O}\left(\lambda^{-5/2}\right)\right) , \tag{3.56}$$

where $\tilde{\kappa}_q \approx -1.765$ [255], and the related work on the $\bar{q}q$ potential is available in [256]. It is interesting to note that the finite coupling corrections (3.51) and (3.56) consistently

[7] It was shown in [252] that the $AdS_5 \times S^5$ solution of type IIB supergravity is in fact not modified by the R^4 corrections (for further discussion on this, see also [251]). However, the non-extremal, i.e. AdS_5-Schwarzschild case, dual to finite temperature $\mathcal{N} = 4$ SYM, is affected by those corrections.

reduce the jet quenching parameter, and increase η/s (eq. (3.55)), suggestive of a smooth interpolation between the strong coupling regime and the perturbative results.

3.4.3 Model R^2 corrections

As mentioned in the previous section, it is a very special property of type II string theory that the first curvature correction comes in at this high order. We do not particularly expect that the true dual of QCD (assuming there is such a thing) shares this special property. So it is perhaps more representative to look at the generic R^2 corrections to the gravity sector of AdS_5.

We will model the R^2 corrections by a Gauss-Bonnet term, which is a particular linear combination of the three possible higher derivative R^2 terms. We will do so because in that case we know the black hole solution exactly. Therefore, we will consider the R^2 corrections to the AdS action (3.34) of the following form [257]:

$$S = \frac{1}{2\kappa_5^2}\int d^5x\sqrt{-G}\left[R + \frac{12}{L^2} + L^2\frac{\lambda_{GB}}{2}\left(R^2 - 4R_{\mu\nu}^2 + R_{\mu\nu\rho\sigma}^2\right)\right], \tag{3.57}$$

where λ_{GB} is a dimensionless parameter, constrained by causality [258] and positive-definiteness of the boundary energy density [259] to be:

$$-\frac{7}{36} < \lambda_{GB} \leq \frac{9}{100}\,. \tag{3.58}$$

The black hole solution in this case is known analytically [260]:

$$ds^2 = \frac{L^2}{z^2}\left(-a^2 f_{GB}(z)dt^2 + dx^2 + \frac{dz^2}{f_{GB}(z)}\right), \tag{3.59}$$

where

$$
\begin{aligned}
f_{GB}(z) &= \frac{1}{2\lambda_{GB}}\left(1-\sqrt{1-4\lambda_{GB}(1-z^4/z_H^4)}\right)\,,\\
a^2 &= \frac{1}{2}\left(1+\sqrt{1-4\lambda_{GB}}\right)\,.
\end{aligned}
\tag{3.60}
$$

In solution (3.59) any value of a is allowed, but this particular one has been chosen so that the boundary speed of light can be unity, i.e.

$$
a^2 f_{GB}(z) \xrightarrow{z\to 0} 1\,. \tag{3.61}
$$

This also means that, as we approach the boundary, $1/f_{GB}$ in front of dz^2 in (3.59) becomes a^2. Because of this, from the perspective of relating the 't Hooft coupling to L, the effective curvature is hence aL, and we have

$$
\sqrt{\lambda} = a^2 \frac{L^2}{\alpha'}. \tag{3.62}
$$

Also, because of a^2 in front of dt^2, it is iat that needs to be periodic in order to avoid the conical singularity at the horizon, which means that the temperature is given by

$$
T = \frac{a}{\pi z_H}\,. \tag{3.63}
$$

Because of the smallness of λ_{GB} (eq. (3.58)), all the calculations in AdS-GB background (3.59) will be amenable to a perturbative expansion in that parameter.

Let us also note another interesting result in the presence of the Gauss-Bonnet term, that will be useful for us later. Since Gauss-Bonnet term is a higher derivative correction, the equations of motion for the off-diagonal gravitons are not as simple as in the two-derivative case (see discussion in Section 3.3.3). This means that the shear viscosity will be different from the $\mathcal{N} = 4$ result [258]:

$$\frac{\eta}{s} = \frac{1 - 4\lambda_{GB}}{4\pi}\,, \tag{3.64}$$

which is an exact result, up to all orders in λ_{GB}. Hence, positive values of λ_{GB} clearly violate the KSS bound [242], while the negative values of λ_{GB} increase the viscosity. In other words, the Gauss-Bonnet term allows us to simply parametrize (and change) the shear viscosity of the (still conformal) theory. A higher viscosity typically indicates a less strongly coupled medium, possibly leading to energy loss that is smaller than its two-derivative limit, which is something we will explore in the coming chapters.

3.5 Bottom-up modeling of QCD

We would like to eventually use the gauge/gravity duality to study QCD at strong coupling. However, in the best studied example of the duality, the AdS/CFT correspondence, the gauge theory we know the gravity dual to is $\mathcal{N} = 4$ SYM. Although there are some similarities between these two theories at strong coupling (and high enough temperatures), there are many important differences.

One of the main sources of differences between $\mathcal{N} = 4$ and QCD is the fact that $\mathcal{N} = 4$ is an exactly conformal theory: this leads to the lack of important features of QCD, such as the confinement, asymptotic freedom, chiral condensate, running of the coupling constant and phase transitions in thermodynamics. In addition to this, $\mathcal{N} = 4$ is supersymmetric and has a different number of degrees of freedom from QCD (at the same number of colors). Finally, the AdS/CFT correspondence is useful only in the 't Hooft limit, where both the coupling λ and the number of colors N are very large.

However, these differences are not irreconcilable. There are several ways one can try to account for a different number of degrees of freedom in the two theories (one of which we will use later [261]), and in Section 3.4 we saw how one can compute finite-λ and finite-N corrections. But, most importantly, at high enough temperatures (above several T_c), QCD becomes conformal (and the supersymmetry is broken in $\mathcal{N} = 4$), so in some sense, the two theories become more similar. However, since the quark-gluon plasma produced in heavy ion collisions lives in the proximity of T_c, the non-conformal details of the real world QCD will be important. This is precisely the motivation behind considering more general applications of holography to more realistic, and in particular, non-conformal field theories.

3.5.1 Top-down and bottom-up models

One possible approach to constructing duals of non-conformal field theories is the so-called "top-down" approach; some of the most well-known and successful models include the Sakai-Sugimoto model [21, 28, 262] and the Klebanov-Strassler model [27, 263–265]. The idea here is that, instead of considering only a stack of coincident D3-branes, one considers more general D-brane configurations and applies similar reasoning as in the original AdS/CFT approach of Section 3.2.1. Namely, one looks at this system from two different points of views: one is to consider the low energy effective action of the system to find out the gauge theory in question, and the other is to look at the supergravity solution sourced by this system to find out to what gravity background this gauge theory will be dual to. Because of this, the holographic dictionary is well known and there is a high level of theoretical control, which makes this approach very reliable. However, a practical difficulty is that the relevant theoretical constraints are ofter very strong and it is generally hard to obtain a theory which resembles QCD more quantitatively.

The other approach is the "bottom-up" approach; here some of the most successful and most studied models include Kiritsis' Improved Holographic QCD (IHQCD) [29, 30, 266–271], as well as Gubser's relevant deformation model [31, 32, 272]. Here the idea is to use some general string theory reasoning as a motivation to construct *ad-hoc* potentials for the low energy fields of type IIB theory (usually the dilaton) and in such a way explicitly break the conformal invariance. The parameters of these potentials can then be constrained by demanding that the dual gauge theory (by using an extended version of the usual holographic dictionary) has certain properties of QCD (for example, confinement, meson spectra, thermodynamics, etc.). The advantage here is that these models have a great potential for phenomenological use, as one can, by fine-tuning the parameters of the potential, come arbitrarily close to some of the properties of the real world QCD. However, there is an obvious lack of theoretical consistency, as one implicitly assumes (but does not prove) that there exists some sort of D-brane configuration that would be responsible for these potentials, which also leads to the lack of a precise holographic dictionary.

3.5.2 Gubser's relevant deformation model

In this section we will describe the bottom-up model developed by Gubser and collaborators [31, 32], and use it in the coming chapters to inspect the generic effects of the breaking of conformal invariance on the energy loss of light and heavy quarks. The main idea in this approach is to postulate a potential for the dilaton field ϕ on the gravity side, which will be dual to a relevant deformation of the $\mathcal{N} = 4$ theory.

In the case of AdS_5 solution, the dilaton is a constant (see (B.6), for $p = 3$). Some of the motivation behind considering potentials that would result in a non-trivial dilaton profile (apart from being the simplest modification of the standard construction) comes from our aim to reproduce the non-trivial QCD thermodynamics: the thermodynamics of large-N QCD is dominated by the adjoint degrees of freedom and the dilaton ϕ is dual to the TrF^2 operator in the gauge theory (in the sense of the field/operator correspondence, Section 3.2.3). Therefore, the simplest bottom-up effective realization of a gravity theory dual to a non-conformal gauge theory is a five-dimensional gravity theory coupled to a scalar field (dilaton):

$$S = \frac{1}{2\kappa_5^2} \int d^5x \sqrt{-G} \left(R - \frac{1}{2}(\partial\phi)^2 - V(\phi) \right) , \tag{3.65}$$

where $V(\phi)$ is the dilaton potential, κ_5 is the five-dimensional gravitational constant and $G_{\mu\nu}$ is the five-dimensional metric in the Einstein frame.

The first constraint on the model will come from the requirement that the potential should give asymptotically ($\phi \to 0$) AdS_5 spacetime, which, as discussed in Section 3.2.2, translates into conformal invariance of the dual field theory in the UV, and hence corresponds to a relevant deformation. In order to obtain the AdS_5 spacetime with radius L as $\phi \to 0$, the potential must asymptote to a negative (cosmological) constant, so in general it needs to have the following form:

$$V(\phi) = -\frac{12}{L^2} + \frac{1}{2} m^2 \phi^2 + \mathcal{O}(\phi^4) \,. \tag{3.66}$$

Such a potential translates into a deformation of the conformal field theory:

$$\mathcal{L}_{\rm CFT} \to \mathcal{L}_{\rm CFT} + \Lambda_\phi^{4-\Delta} \mathcal{O}_\phi \,. \tag{3.67}$$

Here Λ_ϕ is the scale of the deformation and Δ is the dimension of the field theory operator $\mathcal{O}_\phi$ dual to ϕ, which we know from the analysis of the massive scalar in Section 3.2.3 to be given by (3.28).

The requirement of an asymptotically conformal theory originates from the idea of making the connection with QCD by matching the dimension Δ of $\mathcal{O}_\phi$ to the dimension of TrF^2 operator in QCD at some UV scale Q; this UV matching to QCD essentially means that the asymptotic freedom of QCD gets replaced (or approximated) by conformal invariance. Therefore, our dual theory will not be asymptotically free, which is also already visible from the fact that η/s is $1/(4\pi)$ at all temperatures, since the action (3.65) does not contain any higher derivative terms (as discussed in Section 3.3.3). This in turn means that the validity of this model should not be extended to temperatures too far above or too far below the crossover temperature T_c.

We will be interested in $\Delta < 4$, because in QCD, the dimension of Tr$F^2 < 4$. From (3.28) we see that in order to have $\Delta < 4$, we need to have $m^2 < 0$, which is allowed in AdS, as long as it obeys the Breitenlohner-Freedman bound (3.29).

3.5.3 Solving equations of motion

We will use the following ansatz for the metric in the Einstein frame:

$$ds^2 = G_{\mu\nu}dx^\mu dx^\nu = e^{2A(r)}\left(-h(r)dt^2 + d\vec{x}^2\right) + e^{2B(r)}\frac{dr^2}{h(r)}, \quad \phi = \phi(r)\,, \tag{3.68}$$

which is dictated by the requirements of translational invariance in the $(t, \vec{x})$ directions, the rotational invariance in the $\vec{x}$ directions, and where the $SO(3,1)$ boost invariance in the $(t, \vec{x})$ directions is broken by the finite temperature, i.e. presence of a regular horizon at some finite $r = r_H$ defined by $h(r_H) = 0$. In ansatz (3.68) we still have some gauge freedom left to reparametrize the radial direction r, so we will follow [31] and use the gauge choice $\phi(r) \equiv r$, which means that the boundary is at $r = 0$. Note also that, with this choice of gauge, r is dimensionless (since ϕ is) and hence e^{2B} must have units of length squared.

With this choice of ansatz, the equations of motion are:

$$
\begin{aligned}
A'' - A'B' + \frac{1}{6} &= 0\,, && (3.69)\\
h'' + (4A' - B')h' &= 0\,, && (3.70)\\
6A'h' + h(24A'^2 - 1) + 2e^{2B}V &= 0\,, && (3.71)\\
4A' - B' + \frac{h'}{h} - \frac{e^{2B}}{h}V' &= 0\,, && (3.72)
\end{aligned}
$$

where by primes we denote the derivatives with respect to ϕ. Following [31], we can solve these equations of motion by defining a generating function $G(\phi)$, such that

$$
A'(\phi) = G(\phi)\,. \tag{3.73}
$$

This means that, if we can find G, then from (3.69)-(3.72) we can easily get the metric:

$$
\begin{aligned}
A(\phi) &= A_0 + \int_{\phi_0}^{\phi} d\tilde{\phi}\, G(\tilde{\phi})\,, && (3.74)\\
B(\phi) &= B_0 + \int_{\phi_0}^{\phi} d\tilde{\phi}\, \frac{G'(\tilde{\phi}) + 1/6}{G(\tilde{\phi})}\,, && (3.75)\\
h(\phi) &= h_0 + h_1 \int_{\phi_0}^{\phi} d\tilde{\phi}\, e^{-4A(\tilde{\phi}) + B(\tilde{\phi})}\,, && (3.76)\\
V(\phi) &= \frac{1}{2} h(\phi) e^{-2B(\phi)} \left[1 - 24G(\phi)^2 - 6G(\phi)\frac{h'(\phi)}{h(\phi)}\right]\,, && (3.77)
\end{aligned}
$$

where A_0, etc. are all constants of motion. We can manipulate equations (3.69)-(3.72) to derive a "master equation" for G. For example, dividing (3.71) by (3.72) and using (3.74) and (3.75) we get:

$$
\frac{G'}{G + \frac{V}{3V'}} = -\tilde{h} - 4G + \frac{G'}{G} + \frac{1}{6G}\,, \tag{3.78}
$$

where $\tilde{h} \equiv h'/h$. On the other hand, using (3.70) we see that the right hand side of (3.78) is equal to $d(\log \tilde{h})/d\phi$ and expressing $\tilde{h}$ in terms of G from (3.78), we arrive at the master equation

$$\frac{G'}{G + \frac{V}{3V'}} = \frac{d}{d\phi} \log \left[\frac{G'}{G} + \frac{1}{6G} - 4G - \frac{G'}{G + \frac{V}{3V'}} \right] . \tag{3.79}$$

Before we go on to solving this equation, let us look at a special case, when G is a constant. Then, from (3.79) we have

$$\left(\frac{1}{6G} - 4G \right) \left(G + \frac{V}{3V'} \right) = 0 . \tag{3.80}$$

Discarding the solution $G = \pm 1/\sqrt{24}$, we have a solution for which $V/V' = \text{const.} \equiv 1/\gamma$:

$$V = V_0 e^{\gamma\phi}, \qquad G_{\text{CR}} = -\frac{1}{3\gamma} . \tag{3.81}$$

This is the Chamblin-Reall solution [273], which will be useful when we start constructing the potential $V(\phi)$ that will fit the thermodynamics data from lattice QCD.

Let us now proceed to solving the master equation (3.79). This is a second order, non-linear differential equation, for which we need to specify two boundary conditions, $G(\phi_0)$ and $G'(\phi_0)$ at some ϕ_0. Since at the horizon, $\phi = \phi_H$, the blackening function h vanishes, we get from (3.71) and (3.72) that

$$G(\phi_H) = -\frac{V(\phi_H)}{3V'(\phi_H)} . \tag{3.82}$$

Taking the derivative of (3.72) and simplifying it using (3.69) and (3.70), we get:

$$G'(\phi_H) = \frac{1}{6} \left[\frac{V''(\phi_H)V(\phi_H)}{V'(\phi_H)^2} - 1 \right] . \tag{3.83}$$

We can of course continue this procedure and obtain any derivative of G at the horizon, but equations (3.82) and (3.83) will be enough, as we can use them as the boundary conditions to numerically solve the master equation (3.79).

Once we solve the master equation and obtain the generating function G, we can use (3.74)-(3.77) to obtain the metric components, but we need to know something about their values at some point ϕ_0, i.e. A_0 and B_0. If we choose ϕ_0 to be close to the boundary, we can use the fact that our setup is asymptotically AdS_5 and that, because of (3.66), we simply have a massive scalar in AdS_5, whose solution is well known (Section 3.2.3). The first step is to pass to a more standard gauge, rather than $\phi = r$. To do that, consider for a moment AdS_5 in the Poincaré patch (3.19) with boundary at $z = 0$. Then defining $\tilde{z}$ as

$$-\frac{L}{z}dz = d\tilde{z}\,, \tag{3.84}$$

the metric becomes

$$ds^2 = e^{2\tilde{z}/L}\left[-dt^2 + d\vec{x}^2\right] + d\tilde{z}^2\,, \tag{3.85}$$

with the boundary at $\tilde{z} \to \infty$. Our metric (3.68) will asymptote to this if choose the gauge $B = 0$, and then close to the boundary we have, according to (3.85), the following asymptotics:

$$A \xrightarrow{\text{bnd}} \frac{\tilde{z}}{L}, \qquad h \xrightarrow{\text{bnd}} 1\,. \tag{3.86}$$

We found the solution for the massive scalar in AdS_5 in z coordinates in eq. (3.27) in terms of modified Bessel functions. From the asymptotic behavior of these functions (eq. (3.30)), we have

$$\phi(z) \xrightarrow{\text{bnd}} (\Lambda L)^{4-\Delta} e^{(\Delta-4)A}\,, \tag{3.87}$$

where we relabeled β from (3.27) as $\beta \equiv \Lambda^{4-\Delta}$ and used (3.86). Now, noting that this gauge is just another parametrization of the radial r direction (as is the $\phi = r$ gauge), this means that A and ϕ are the same in this gauge as they are in the $\phi = r$ gauge, only expressed as functions of $\tilde{z}$ and z, rather than ϕ. Therefore, from (3.87), we have

$$A \xrightarrow{\phi\to 0} \frac{\log\phi}{\Delta-4}\,. \tag{3.88}$$

Knowing this, we can use (3.74) with $\phi_0 = \phi_H$ and compare that expression at some small ϕ with (3.88) written as a simple integral over ϕ, from where we can finally extract $A_H \equiv A(\phi_H)$:

$$A_H = \frac{\log\phi_H}{\Delta-4} + \int_0^{\phi_H} d\phi \left[G(\phi) - \frac{1}{(\Delta-4)\phi}\right]\,. \tag{3.89}$$

This expression is also particularly convenient for numerical integration, as the extra term in the integral makes the overall integrand finite as one approaches the boundary (i.e. serves as a UV regulator).

We can use a similar method to find B_H. From the defining equation of the $B=0$ gauge (analogous to (3.84)), we have

$$e^{2B(\phi)}d\phi^2 = d\tilde{z}^2\,. \tag{3.90}$$

At small ϕ (or large $\tilde{z}$), we know how ϕ depends on $\tilde{z}$ from (3.87), and we can obtain:

$$B \xrightarrow{\phi\to 0} \log\left(-LG(\phi)\right)\,. \tag{3.91}$$

As before, we can use (3.75) with $\phi_0 = \phi_H$ and compare that expression at some small ϕ with (3.91) and extract B_H:

$$B_H = \log\left[\frac{LV(\phi_H)}{3V'(\phi_H)}\right] + \int_0^{\phi_H} d\phi \frac{1}{6G(\phi)}\,. \tag{3.92}$$

Values of A and B at the horizon will be important in obtaining the temperature and entropy of the solution in the next section, but they can also serve as the constants of motion in obtaining the full solution for the metric, by using $\phi_0 = \phi_H$ in (3.74) and (3.75). Alternatively, we could use a ϕ_0 that is close to the boundary, in which case we would use (3.88) and (3.91) for A_0 and B_0 and manipulate (3.74) and (3.75) to obtain numerically well behaved integrals as in (3.89) and (3.92):

$$A(\phi) = \frac{\log \phi}{\Delta - 4} + \int_0^{\phi} d\tilde{\phi} \left[G(\tilde{\phi}) - \frac{1}{(\Delta - 4)\tilde{\phi}} \right], \tag{3.93}$$

$$B(\phi) = \log\left(-LG(\phi)\right) + \int_0^{\phi} d\tilde{\phi} \frac{1}{6G(\tilde{\phi})}. \tag{3.94}$$

We can also derive a more convenient expression for the blackening function h that does not involve the additional integrals as in (3.76). Eliminating $h'(\phi)$ in (3.71) by using (3.72) we get:

$$h(\phi) = -\frac{e^{2B(\phi)}}{3G'(\phi)} \left(V(\phi) + 3G(\phi)V'(\phi) \right). \tag{3.95}$$

3.5.4 Thermodynamics

In this section, we will find the expressions for the entropy density and the temperature of the solution (3.68), so that we can compare them to the lattice QCD results and find the potential $V(\phi)$ that best matches them.

The first step is to find the area of the black hole in (3.68):

$$A = \int d^3x \sqrt{g|_{\mathrm{hor.}}} = e^{3A(r_H)} \int d^3x \,, \tag{3.96}$$

where $\int d^3x \equiv V$ is the volume of the gauge theory. Hawking's formula for entropy then simply gives:

$$s = \frac{1}{V}\frac{A}{4G_N} = \frac{2\pi}{\kappa_5^2} e^{3A_H} \,. \tag{3.97}$$

To find the temperature, we could use Wald's formula for surface gravity [274],

$$\kappa^2 = -\frac{1}{2}(\nabla^\mu \chi^\nu)(\nabla_\mu \chi_\nu) \,, \tag{3.98}$$

where $\chi^\mu = \delta^\mu_t$ is the timelike Killing vector[8] which defines the Killing horizon of the black hole solution (3.68). Noting that the only non-vanishing Christoffel symbols in metric (3.68) with at least one t index are

$$\Gamma^t_{tr} = A' + \frac{h'}{2h} \,, \quad \Gamma^r_{tt} = \frac{1}{2} e^{2A-2B} h(2hA' + h') \,, \tag{3.99}$$

from (3.98) we explicitly have the temperature:

$$T = \frac{\kappa}{2\pi} = \frac{1}{4\pi} e^{A_H - B_H} \left| h'(r_H) \right| \,. \tag{3.100}$$

It is possible to derive a more convenient formula for T that does not involve finding h, which can be done by expressing $h'(r_H)$ in terms of $V'(r_H)$ from (3.72), which yields:

$$T = \frac{1}{4\pi} e^{A_H + B_H} \left| V'(r_H) \right| \,. \tag{3.101}$$

Once we find the temperature and entropy for different r_H using (3.97) and (3.101), we can easily find the speed of sound as a function of temperature using formula (1.45):

$$c_s^2(r_H(T)) = \frac{T'(r_H) s(r_H)}{T(r_H) s'(r_H)} \,, \tag{3.102}$$

[8]Killing vector field χ^μ is essentially a vector field that preserves the metric. More precisely, Killing vector fields generate isometries $x^\mu \to x^\mu + \varepsilon \chi^\mu$ under which the metric is form-invariant, $g_{\mu\nu}(x) = g'_{\mu\nu}(x)$.

where we assumed that we have numerically inverted $T(r_H)$ to get $r_H(T)$. We will use this for comparison to the lattice QCD results in the next section. A good guiding case in fitting our results to the lattice ones is the Chamblin-Reall solution (3.81). Since in that case G is a constant, A and B are linear functions of ϕ and using (3.97) and (3.101) we immediately get:

$$c_{s,\mathrm{CR}}^2 = \frac{1}{3} - \frac{\gamma^2}{2}\,. \tag{3.103}$$

This simple formula clearly shows how non-zero (non-conformal) values of γ drive the theory away from the conformal limit of 1/3.

3.5.5 Fitting the lattice

First, in order to compare the results from the bottom-up model to the lattice QCD data (and other observables) we need a way to translate the dimensionless numbers we get from the numerical code into dimensionful quantities in units of GeV and fm.

All the quantities in the bottom-up model scale with L: for example, from the expression for the temperature, (3.101), we see that, since e^B is proportional to L and V' to $1/L^2$, the temperature is $T = \#_T/L$, where $\#_T$ is some dimensionless number we can get from the numerical code by setting $L = 1$. Now, plotting the holographic speed of sound (3.102) as a function of this T, we will (as we will soon see) obtain a minimum at some $T_{\min}$ (i.e. we will work with potentials that will have this feature). From lattice QCD, we obtain the speed of sound as a function of T in GeV, with a minimum at some T_c[9]. It is natural to then translate between the two with

$$\frac{T[\mathrm{GeV}]}{T_c} = \frac{T[1/L]}{T_{\min}}\,. \tag{3.104}$$

[9]This is not the critical temperature for the phase transition, as usually reported in the lattice calculations (although it will be close to it); here, we simply define T_c as the minimum of the speed of sound, that we will use for unit conversion.

For any other quantity Q that scales with L, we will extend the usual prescription from the conformal case, where one equates products such as QT on the gravity and the gauge theory side. Using (3.104), we get

$$Q_{\text{GeV}} = Q\frac{T_{\min}}{T_c}\,. \tag{3.105}$$

Of course, to get Q in fm, we would need to multiply this by $\hbar c$. Hence, the pocket formula for translating from units of L to GeV is to simply replace

$$L \to \frac{T_{\min}}{T_c}\,. \tag{3.106}$$

Let us now try to construct the potential $V(\phi)$ that could fit the speed of sound from lattice QCD (dashed curves in Fig. 3.8). As mentioned earlier, the Chamblin-Reall type of potential, $V \propto e^{\gamma\phi}$, gives a constant, γ-dependent speed of sound (eq. (3.103)), that is different from the conformal limit of 1/3. As we can see from Fig. 3.8, this is precisely what we would like to have in the IR, or for large ϕ. On the other hand, in the UV, QCD becomes conformal and the speed of sound approaches 1/3, which means that we would need to have a constant, γ-independent potential at small ϕ. Therefore, a natural choice for one of the terms in the potential is $\cosh(\gamma\phi)$ [31], as it interpolates between those two limits, and should give a non-trivial, temperature-dependent speed of sound. However, γ then defines the effective mass m^2 in the potential (eq. (3.66)) and therefore, through (3.28), fixes the dual operator dimension Δ. In order to have more freedom in choosing this dimension, we can introduce an additional ϕ^2 term in the potential. We will also introduce additional ϕ^4 and ϕ^6 terms to fine-tune the fit of the cross-over behavior of the lattice results. Finally, the potential we will be working with has the following form:

$$V(\phi) = \frac{1}{L^2}\left(-12\cosh(\gamma\phi) + b_2\phi^2 + b_4\phi^4 + b_6\phi^6\right) . \tag{3.107}$$

A somewhat different kind of dilaton potential has been studied in the bottom-up approach of IHQCD [29, 30, 275], where the potential was constructed in such a way so that the desired β function is obtained in the UV and confinement in the IR. We do not attempt to provide a string theory derivation[10] of a potential of form (3.107), but rather, in the context of our effective approach, simply aim to construct a potential that will reproduce the QCD thermodynamics.

Using the procedure described in the previous sections, we can numerically determine the parameters in (3.107) by fitting our speed of sound (3.102) to the lattice QCD data of [62]. Satisfactory fits were obtained using the following values [203]:

$$\gamma = 0.606, \quad b_2 = 0.703, \quad b_4 = -0.12, \quad b_6 = 0.00325\,, \tag{3.108}$$

which corresponds to dimension $\Delta \approx 3$. Our fit together with the lattice results is shown in Fig. 3.8. Of course, after fitting the speed of sound, all other thermodynamic quantities, such as the trace anomaly, entropy, etc. are automatically fitted as well.

3.5.6 Polyakov loops

After fitting the lattice QCD thermodynamics data with the bottom-up model, we will want to eventually introduce strings to that geometry and inspect their dynamics, as that will be directly related to the energy loss of quarks they are dual to. However, strings

[10] From the perspective of a five-dimensional, non-critical string theory, as argued in [29, 268], one can expect these kinds of effective dilaton potentials arising from integrating out higher α'-corrections of the RR 4-form (sourced by the D3-branes that generate the $U(N)$ gauge group), which, in five dimensions, is non-dynamical.

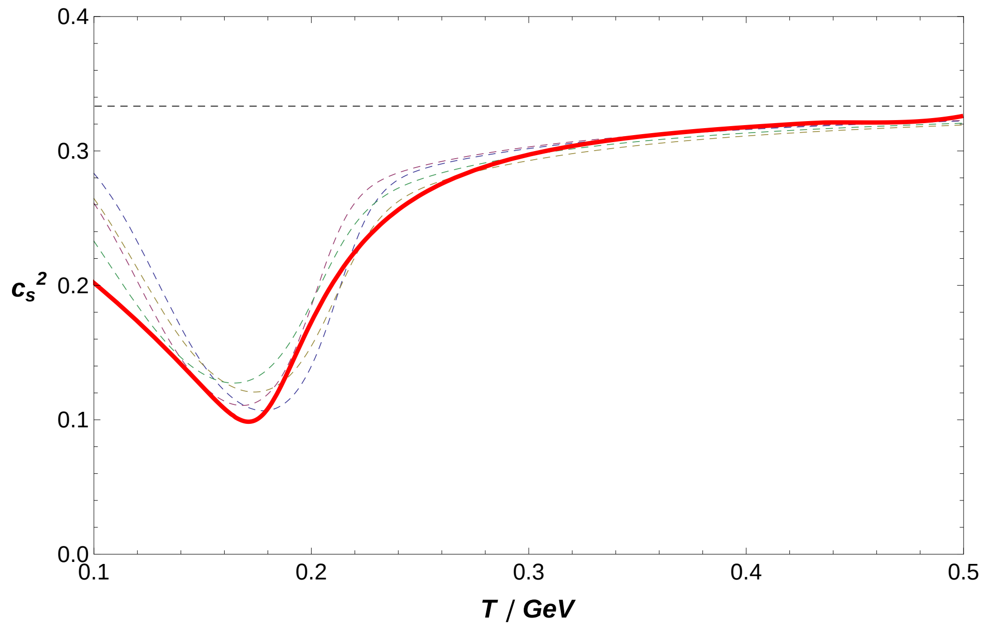

Figure 3.8: *Comparison of the speed of sound as a function of temperature from the non-conformal holographic model (red curve) and the lattice results from the HotQCD collaboration [62] for various actions (dashed curves). The straight dashed line indicates the conformal limit of 1/3.*

propagate in the string-frame metric, while our ansatz (3.68) is in the Einstein frame. In the AdS_5 space the dilaton is non-dynamical, and hence the string-frame and the Einstein-frame metrics are identical, but due to the introduction of the potential (3.107), the dilaton is now dynamical and there is a non-trivial relationship between the metrics in the two frames.

A physically reasonable link between the two frames was first proposed in [29], where the authors considered a non-critical (i.e. $D \neq 10$) string theory in D dimensions. Starting from the two-derivative type IIB action in D dimensions (3.6), where Φ is the type IIB dilaton, and superscript (s) stands for the metric in the string frame, one defines the metric in the Einstein frame as

$$G_{\mu\nu} \equiv \exp\left[-\frac{4}{D-2}\Phi\right] G^{(s)}_{\mu\nu}\,, \tag{3.109}$$

as then the action (3.6) will have the standard Einstein-Hilbert form,

$$S_{D,E}^{\text{tree}} = \frac{1}{2\kappa_D^2}\int d^D x\sqrt{-G}\left[R - \frac{4}{D-2}\left(\nabla\Phi\right)^2 + ...\right] . \tag{3.110}$$

For us, by setting $D = 5$ and performing a simple field redefinition,

$$\sqrt{\frac{4}{3}}\Phi = \sqrt{\frac{1}{2}}\phi\,, \tag{3.111}$$

we end up with the same prefactor of the kinetic term as in (3.65). Denoting in general the function relating the Einstein and string frame metrics in (3.109) as $e^{q(\phi)}$, we see that in our case,

$$q(\phi) = \sqrt{\frac{2}{3}}\phi\,, \tag{3.112}$$

although, in principle, different choices of $q(\phi)$ may be applicable as well.

The only unknown parameter left in the model is the effective $\alpha' = l_s^2$ in the string action. We will find this by computing the expectation value of the Polyakov loop and compare it to the lattice data[11], as first proposed in [276]. As discussed in Section 1.1.2, the expectation value of the (regularized) Polyakov loop is related to the (regularized) free energy of a single quark $F_{Q,R}$ as

$$\langle L_R\rangle = e^{-F_{Q,R}/T}\,. \tag{3.113}$$

Following a similar reasoning as in Section 3.3.4, the idea here is that the disconnected contribution to the Polyakov loop at large N may be computed by considering straight probe strings that stretch from the boundary to the horizon. Energy of such a string may

[11] Alternatively, in a confining bottom-up model, such as IHQCD [269], one can find l_s^2 by computing the string tension σ from the area law.

be computed in the $\sigma = r$ and $\tau = t$ gauge as

$$\begin{aligned} E &= -\int d\sigma \sqrt{-h}\, \Pi_0^\tau(\sigma, t) \\ &= \frac{1}{2\pi\alpha'} \int d\sigma \sqrt{-h} h^{0b} (\partial_b t) G_{tt} e^{q(\phi)} \,, \end{aligned} \tag{3.114}$$

where Π_0^τ is a component of the spacetime momentum worldsheet current and $h_{ab} = \gamma_{ab}$ is the worldsheet metric (this will be derived in detail in Section 3.6). The embedding function of a straight string is simply $X^\mu = (t, \vec{0}, r)$, and we have

$$h_{ab} = \partial_a X^\mu \partial_b X^\nu G_{\mu\nu} = \mathrm{diag}(G_{tt}, G_{rr})\,. \tag{3.115}$$

Plugging this is in (3.114), we get

$$F_Q(T) = \frac{1}{2\pi\alpha'} \int\limits_0^{r_H(T)} dr \exp\left[q(\phi(r)) + A(r) + B(r)\right] . \tag{3.116}$$

This expression suffers from standard UV divergences near the boundary and needs to be regulated. Since these are UV divergences, they are temperature-independent, and hence in a given regularization scheme i, we have

$$F_Q(T) = F_{Q,R}^{(i)}(T) + C_R^{(i)}\,, \tag{3.117}$$

where $F_{Q,R}^{(i)}(T)$ is the regularized free energy and $C_R^{(i)}$ denotes the temperature-independent regularizing constant. The lattice data for Polyakov loops have their own regularization scheme, and they differ from whichever scheme we choose by some constant. This means that we can write:

$$L_R(T) = \exp\left[-\frac{F_{Q,R}(T)|_{\alpha'=1} + C_R}{\alpha' T}\right] . \tag{3.118}$$

Once we calculate $F_{Q,R}(T)$ for several different temperatures, we can use (3.118) to fit this to the lattice data, with α' and C_R as the fitting parameters. Choosing a different regularization scheme will change the value of C_R, but not α'. The scheme we will choose is rather standard: we will subtract the UV limit of the integrand in (3.116):

$$\varepsilon_{\mathrm{UV}} \equiv \lim_{r\to 0} \exp\left[q(\phi(r)) + A(r) + B(r)\right] = \frac{L}{4-\Delta} r^{\frac{5-\Delta}{\Delta-4}}\,, \tag{3.119}$$

where we used the UV asymptotics (3.88) and (3.91). Therefore, we will calculate the free energy as follows[12]:

$$F_{Q,R}(T) = \frac{1}{2\pi\alpha'} \int\limits_0^{r_H(T)} dr \left[e^{q(\phi(r))+A(r)+B(r)} - \frac{L}{4-\Delta} r^{\frac{5-\Delta}{\Delta-4}}\right] - \frac{L}{2\pi\alpha'} r_H^{\frac{1}{\Delta-4}}\,, \tag{3.120}$$

and, in practice, we will also terminate the numerical integration at some small r, i.e. a simple UV cutoff is also implied.

Computing the regularized free energy (3.120) at different temperatures, we see from Fig. 3.9 that the Polyakov loop has the right qualitative behavior, and a satisfactory fit to the lattice data was achieved for $\alpha'/L^2 \approx 1.1$ [203]. With this somewhat large value of α', it would be interesting to inspect the effects of higher α'-corrections[13], but in the context of our effective bottom-up model, we, for now, contend ourselves with simply

[12] One might be tempted to take derivatives of formula (3.120) with respect to r_H, to avoid the need for numerical integration. However, this produces an unwanted term:

$$\frac{dF_{Q,R}}{dr_H} = \frac{1}{2\pi\alpha'} e^{q(r_H)+A_H+B_H} + \frac{1}{2\pi\alpha'} \int_0^{r_H} dr \frac{\partial}{\partial r_H} \left[e^{q(\phi(4))+A(r)+B(r)}\right]\,,$$

where the second term comes from the fact that all the metric elements are implicitly dependent on the value of r_H, i.e. their functional form in principle changes as we change r_H, which is not something that occurs in the highly special case of AdS_5.

[13] As discussed in [29, 268], in non-critical string theory duals of large-N_c gauge theories, one may indeed expect to have curvatures on the order of $\sqrt{\alpha'}$. Also, as discussed there, at least part of these α'-corrections (those coming from the RR 4-form) is thought to be captured by the various terms in the effective potential.

matching the real world QCD data. Also, as discussed in [269], the gauge theory coupling $\sqrt{\lambda}$ in these models is (at least in the UV) related to L^2/α' up to an, *a priori*, unknown coefficient.

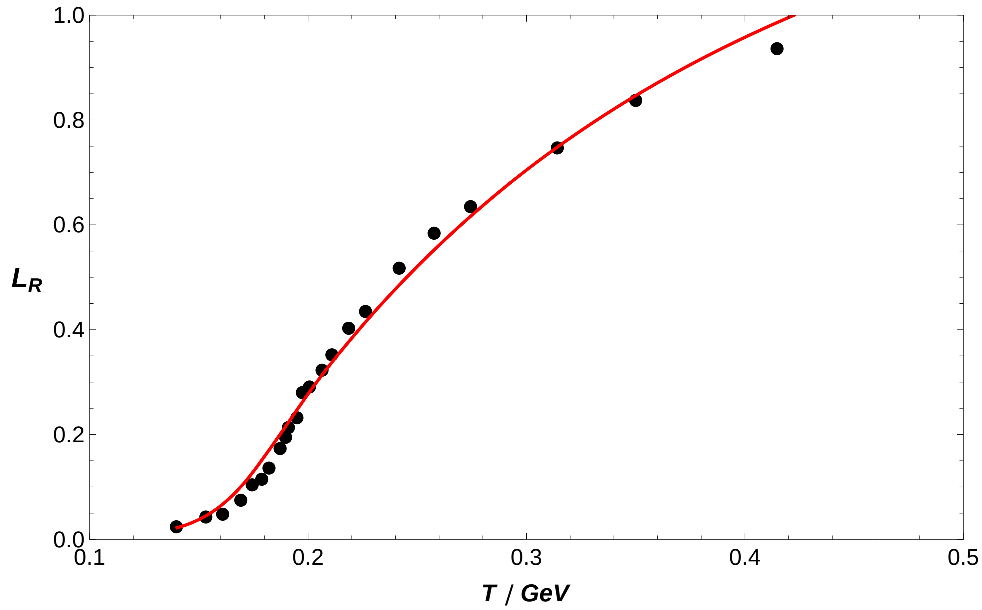

Figure 3.9: *Comparison of the expectation value of the Polyakov loop as a function of temperature from our non-conformal holographic model (red curve) to the lattice results from the HotQCD collaboration [62] (black dots).*

3.5.7 Solution at zero temperature

So far, we have assumed that there is a horizon in the metric (3.68), which translates into having the dual gauge theory at a finite temperature. However, we will also need the zero-temperature solution later on.

At zero temperature, we have:

$$h = 1, \qquad h' = 0\,, \tag{3.121}$$

and we can follow the derivation of the master equation up until (3.78), in which we simply set $\tilde{h} = 0$ and obtain right away

$$\frac{G_0'}{G_0 + \frac{V}{3V'}} = -4G_0 + \frac{G_0'}{G_0} + \frac{1}{6G_0}\,, \tag{3.122}$$

where by subscript "0" we denote the zero-temperature solution. Unlike the $T \neq 0$ master equation, (3.122) is a first order differential equation and hence we need only one boundary condition. Since we don't have a horizon, we could for example choose some small ϕ_0 close to the boundary, where the generating function has the same from as the $T \neq 0$ one (eq. (3.88)), i.e.

$$G_0(\phi) \xrightarrow{\phi\to 0} \frac{1}{(\Delta - 4)\phi}\,. \tag{3.123}$$

However, since now arbitrarily large values of ϕ are available, there is a numerically more stable option of choosing a boundary condition in that region because, as we can see from (3.107), the potentials we will be interested in will have Chamblin-Reall large-ϕ asymptotics, i.e.

$$V(\phi) \xrightarrow{\phi\to\infty} V_0 e^{\gamma\phi}\,, \tag{3.124}$$

and in this limit we know the solution to be (3.81), which can be also checked explicitly from (3.122). Hence, choosing some numerically large ϕ_{max}, we can solve (3.122) by imposing

$$G_0(\phi_{\mathrm{max}}) = -\frac{1}{3\gamma}\,. \tag{3.125}$$

The rest of the metric components will then be given by (3.93)-(3.95).

3.6 Dynamics of classical strings

In the context of AdS/CFT, we will be generally working in the 't Hooft limit, $N \gg \lambda \gg 1$, where, on the string theory side, one can neglect the stringy α'-corrections and the loop quantum g_s-corrections, leaving us with classical supergravity. We ultimately want to use the gauge/gravity duality to study the dynamics of energetic partons plowing through a strongly coupled thermal medium and, in particular, how they lose energy. We will see in the following chapters that these partons are naturally represented as highly-excited, string-like excitations of the brane content at our disposal. Because of the 't Hooft limit, one can neglect the backreaction of the metric due to the introduction of strings (the probe approximation) and neglect the quantum corrections to the motion of the strings. This means that we will be studying the dynamics of classical strings in the background given by some spacetime metric $G_{\mu\nu}$, which is the topic of this section.

3.6.1 The Polyakov action

In Section 3.1.2 we introduced the Nambu-Goto action (3.4) for classical strings, but, from a perspective of differential geometry, however, (3.4) is not a particularly pleasant action, as, apart from having a potentially troublesome square root, it does not allow one to choose the metric on the worldsheet. For this reason, we consider the Polyakov action,

$$S_P = -\frac{1}{4\pi\alpha'}\int\limits_M d^2\sigma\sqrt{-h}h^{ab}(\partial_a X^\mu)(\partial_b X^\nu)G_{\mu\nu}\,, \tag{3.126}$$

where h_{ab} is the worldsheet metric, which is considered as a dynamical variable in this action. For the rest of this chapter, we assume that $G_{\mu\nu}$ is the metric in the string frame, which, in general, can be related to the metric in the Einstein frame, through a string-dilaton coupling $e^{q(\phi)}$, as explained in Section 3.5.6. Let us now vary this action with respect to h_{ab}, for which we will need to know how to vary determinants:

$$\delta\left(\sqrt{-h}\right) = -\frac{1}{2}\sqrt{-h}h_{ab}\delta h^{ab}\,, \tag{3.127}$$

where we used the identity $\log\det M = \mathrm{Tr}\log M$, valid for a general matrix M, and that $\delta h_{ab}h^{ab} = -\delta h^{ab}h_{ab}$, since $h_{ab}h^{ab} = 2$. Using (3.127), the equations of motion for h_{ab} are

$$\gamma_{ab} = \left(\frac{1}{2}h^{cd}\gamma_{cd}\right) h_{ab}\,, \tag{3.128}$$

that is to say, the worldsheet metric is conformally equivalent to the induced one. The scalar function in the brackets can be also cast in a different form by taking the determinant of both sides of (3.128), yielding

$$\frac{\gamma_{ab}}{\sqrt{-\gamma}} = \frac{h_{ab}}{\sqrt{-h}}\,. \tag{3.129}$$

Notice also that, because the worldsheet metric enters the Polyakov action in a combination $\sqrt{-h}h^{ab}$, any conformally rescaled worldsheet metric $\tilde{h}^{ab} = \Omega^2 h^{ab}$ is also a solution: this is called the Weyl invariance. Equations (3.129) are constraint equations, as they contain only first derivatives in X^μ. It is easy to see that plugging the h_{ab} equations of motion (3.129) into the Polyakov action (3.126), we obtain back the Nambu-Goto action (3.4), which means that these two actions are classically equivalent.

The Polyakov action (3.126) can be viewed as a classical field theory action of a collection of free scalar fields X^μ on a curved two-dimensional manifold described by the metric h_{ab}. As mentioned earlier, this feature of the Polyakov action makes it much more pleasing to use than the Nambu-Goto action: it allows us to perform coordinate transformations on the worldsheet and see how the worldsheet vectors and tensors change under them (which will be important in the study of the instantaneous energy loss), it admits a consistent modification of the boundary terms (which will be important later on when we add the finite momentum to the string endpoints), and, from a practical standpoint, it will also be useful for numerical evaluations, since a clever choice of the worldsheet metric will greatly improve the stability of the numerics, as we will see later.

3.6.2 Analyzing the action

Let us now define the canonical momentum densities:

$$\Pi^a_\mu \equiv \frac{1}{\sqrt{-h}} \frac{\delta S_P}{\delta(\partial_a X^\mu)} = -\frac{1}{2\pi\alpha'} h^{ab} (\partial_b X^\nu) G_{\mu\nu} \,, \tag{3.130}$$

where $\sqrt{-h}$ is here to ensure that the quantity in Π^a_μ is a proper worldsheet vector. To simplify notation, we also introduce

$$P^a_\mu \equiv \sqrt{-h} \Pi^a_\mu \,. \tag{3.131}$$

If the Polyakov action (3.126) is invariant with respect to constant spacetime translations in the μ direction, $X^\mu \to X^\mu + \epsilon^\mu$, the momentum densities (3.130) are just the associated conserved Noether currents on the worldsheet, with μ being just a label for different currents. Because of this, these worldsheet currents describe the flow of the μ component of the spacetime momentum of the string along the a direction on the worldsheet (see e.g. [205]) and that is the reason why they are important in the study of energy loss. We will discuss them and their transformations more in the next section.

Let us now look at the equations of motion for the embedding functions X^μ from the Polyakov action:

$$\partial_a P^a_\mu - \Gamma^\kappa_{\mu\lambda} \partial_a X^\lambda P^a_\kappa = 0 \,, \tag{3.132}$$

where we used the definition (3.131) and the metric compatibility,

$$\nabla_\mu G_{\rho\sigma} = \partial_\mu G_{\rho\sigma} - G_{\lambda\sigma} \Gamma^\lambda_{\rho\mu} - G_{\rho\lambda} \Gamma^\lambda_{\sigma\mu} = 0 \,. \tag{3.133}$$

Note that if the metric does not depend on some X^μ, the second term in (3.132) vanishes and we have a covariant conservation law for the momentum densities:

$$\partial_a P^a_\mu = \sqrt{-h}\nabla_a \Pi^a_\mu = 0\,. \tag{3.134}$$

Along with the bulk equations of motion (3.132), we are also left with a total derivative (assuming we are considering open strings), which we will express in a bit more general way[14] than found in the usual literature, as this will be useful later when we introduce finite momentum at the endpoints. The first thing to note is that the total derivative term can be written as:

$$\int\limits_M d^2\sigma \partial_a \left[\delta X^\mu P^a_\mu\right] = \int\limits_M d\left(\star V\right)\,, \tag{3.135}$$

where we defined a worldsheet one-form $\star V$, with $V^a = \Pi^a_\mu \delta X^\mu$ a proper worldsheet vector. Now we can use Stokes' theorem to write this as a boundary term:

$$\int\limits_M d\left(\star V\right) = \int\limits_{\partial M} \star V = \int\limits_{\partial M} d\sigma^a \tilde{\varepsilon}_{ab} V^b\,, \tag{3.136}$$

where $\tilde{\varepsilon}_{ab} = \sqrt{-h}\varepsilon_{ab}$ is the Levi-Civita two-form and $\varepsilon_{\tau\sigma} = +1$ for a boundary that is traversed counter-clockwise. In order to set this boundary term to zero, we have two options for a given μ. One possibility is to choose $\delta X^\mu = 0$, which are called the Dirichlet boundary conditions: this means that in this μ direction the string endpoint must be attached to some plane, i.e. the D-brane. The other option is to allow the endpoints to be free, i.e. $\delta X^\mu \neq 0$, in which case we have the following boundary condition from (3.136):

$$\dot{\sigma}^a \varepsilon_{ab} P^b_\mu = 0\,, \tag{3.137}$$

[14] Some basic concepts and useful identities in the differential geometry of curved manifolds can be found in e.g. [277], whose conventions we will use here.

where we introduced ξ as the parametrization of the boundary so $\dot{\sigma}^a = d\sigma^a/d\xi$.

The boundary of the worldsheet is defined by the endpoints, which we usually take to be at some fixed σ, e.g. $\sigma = 0, \pi$ (later, when we introduce the endpoint momentum, this will not be possible anymore). In this case, $\dot{\sigma} = 0$ and $\dot{\tau} = 1$ (choosing $\xi = \tau$), and (3.137) simplifies to the standard boundary condition:

$$P^\sigma_\mu|_{\sigma=0,\pi} = 0\,. \tag{3.138}$$

It is easiest to analyze this condition and the effects it has on the endpoint motion in the conformal gauge, $h_{ab} = \mathrm{diag}(-1, 1)$. In that case, (3.138) gives

$$G_{\mu\nu}(X^\nu)' = 0\,, \tag{3.139}$$

where we use the notation $A' \equiv \partial_\sigma A$ and $\dot{A} \equiv \partial_\tau A$ for any quantity A. Once we impose a certain gauge, we also have to obey the constraint equations (3.128) which in this case give:

$$G_{\mu\nu}(X^\mu)'\dot{X}^\nu = 0\,, \tag{3.140}$$

$$G_{\mu\nu}\dot{X}^\mu\dot{X}^\nu + G_{\mu\nu}(X^\mu)'(X^\nu)' = 0\,, \tag{3.141}$$

which are of course valid at the boundary as well. Because of (3.139), the second term in (3.141) is identically zero at the boundary, and since the endpoints are at fixed σ, the first term in (3.141) tells us that the endpoints are lightlike, i.e. that they are moving at the local speed of light. On the other hand, since $\dot{X}^\mu$ is a vector in the direction of the motion of the endpoints and $(X^\mu)'$ is tangent to the string at its endpoints, (3.140) tells us that the endpoints always move locally perpendicular to the string. These are the standard results for the motion of free endpoints of open strings.

3.6.3 Worldsheet currents

In this section, following the logic and notation of our [33], we will carefully study the worldsheet currents (3.130), as they determine the energy of the string, as well as the flow of energy along it.

In general, whenever we have a covariant conservation law on a differentiable manifold, such as (3.134), one defines the charge (whose flow is described by Π^a_μ) that passes through some hypersurface γ as

$$p^\gamma_\mu = -\int_\gamma \star\Pi_\mu = -\int_\gamma d\epsilon\, n_a \Pi^a_\mu\,, \tag{3.142}$$

where in the second equation $d\epsilon$ is the induced volume element on the hypersurface γ and n_a is the unit vector field normal to the hypersurface. In our case, we have a two-dimensional manifold, so γ represents an (open) curve on the worldsheet and p^γ_μ is the μ component of the spacetime momentum that flows through this curve. Therefore, in our case, we can simply write

$$p^\gamma_\mu = -\int_\gamma ds\, h_{ab} n^a \Pi^b_\mu\,, \tag{3.143}$$

where ds is the line element of the curve γ. It is important to note that, in the context of the AdS/CFT correspondence, these momenta p_μ can be identified with the momenta of the boundary gauge theory for $\mu = 0, 1, 2, 3$, essentially because they are momenta defined with respect to the same Killing vectors $\partial/\partial x^\mu$ as on the boundary (for more details on this, see [278]).

We now choose to work in the static gauge where $\tau = t$, so σ parametrizes the string at some physical time t. We can now ask what is the total μ component of the momentum of the string at some fixed time t. This means that we need to take the curve γ to be the curve of constant t, which means that its tangent vector t^a is in the σ-direction, i.e. $t^a = (1, 0)$, where the first entry is the σ coordinate and the second the t coordinate.

The normal vector $n^a = (n^\sigma, n^\tau)$ can then be found by requiring its orthogonality to the tangent vector and the usual normalization condition:

$$t \cdot n = 0, \;\; n \cdot n = -1 \,, \tag{3.144}$$

where the dot products are taken with the worldsheet metric h_{ab}. Using these two equations, we can solve for the components of the normal vector:

$$n^a = \left(-\frac{1}{\sqrt{-h}} \frac{h_{\sigma\tau}}{\sqrt{h_{\sigma\sigma}}}, \frac{\sqrt{h_{\sigma\sigma}}}{\sqrt{-h}} \right) . \tag{3.145}$$

Finally, since for this particular curve we have $d\tau = 0$, we can express the worldsheet line element ds^2 as

$$ds_\gamma^2 = h_{ab} d\sigma^a d\sigma^b = h_{\sigma\sigma} d\sigma^2 \,. \tag{3.146}$$

Using (3.145) and (3.146) in (3.143), we have

$$p_\mu(t) = \int d\sigma \, P_\mu^\tau(\sigma, t) \,. \tag{3.147}$$

This is of course true no matter what the parametrization σ of the string is, the only requirement here is that we are dealing with a constant-t curve. Similarly, we can repeat the same procedure for a constant-σ curve, integrating over some period of time:

$$p_\mu(\sigma, \Delta t) = \int\limits_{\Delta t} dt \, P_\mu^\sigma(\sigma, t) \,, \tag{3.148}$$

which then gives the momentum that has flown down the string (i.e. in the direction of increasing σ) at position σ during the time Δt.

Now consider an open string with free endpoint boundary conditions (3.138) and take a closed loop γ on the string worldsheet, composed of two constant-t curves at times t_1 and t_2, going from $\sigma = 0$ to some chosen $\sigma = \sigma_\kappa$, connected by the two corresponding constant-σ curves. If the worldsheet currents in the X^μ direction are conserved, we have:

$$\begin{aligned}&\oint\limits_\gamma \star\Pi_\mu = 0\\ &\quad = -\int\limits_{t_1}^{t_2} dt P_\mu^\sigma(\sigma_\kappa, t) + \int\limits_{\sigma_\kappa}^{0} d\sigma P_\mu^\tau(\sigma, t_2) - \int\limits_{t_2}^{t_1} dt P_\mu^\sigma(0, t) + \int\limits_{0}^{\sigma_\kappa} d\sigma P_\mu^\tau(\sigma, t_1)\,.\end{aligned} \tag{3.149}$$

Due to the free endpoint boundary condition (3.138) (which can now be interpreted as the condition that there is no momentum flow in or out of the endpoint), the third term on the right hand side is zero, while the integrals over time, according to (3.147), represent the spacetime momentum of the part of the string between $\sigma = 0$ and $\sigma = \sigma_\kappa$ at times t_1 and t_2:

$$p_\mu^{\sigma_\kappa}(t_2) - p_\mu^{\sigma_\kappa}(t_1) = -\int\limits_{t_1}^{t_2} dt P_\mu^\sigma(\sigma_\kappa, t)\,. \tag{3.150}$$

This equation clearly shows how the momentum of some part of the string can change only if the Π_μ^σ component of the worldsheet current carries it away. The negative sign on the right hand side indicates that, for a positive Π_μ^σ, the momentum of that part of the string will decrease, consistent with the fact that this current component describes the flow of the momentum in the direction of increasing σ, i.e. away from the part of the string under consideration. Incidentally, if we take a string configuration which is symmetric around $\sigma_\kappa = \pi/2$, then, due to this symmetry, $\Pi_\mu^\sigma(\pi/2, t)$ must vanish. In that case $p_\mu^{\sigma_\kappa}(t)$ represents the momentum of one half of the string and, from (3.150), we see that this momentum for such a symmetric string configuration does not change with time.

We will eventually be interested in making a general coordinate transformation on the worldsheet $(\sigma, \tau) \to (\tilde{\sigma}, \tilde{\tau})$, which can be defined by the following matrix:

$$\tilde{M}^a{}_b \equiv \frac{\partial \tilde{\sigma}^a}{\partial \sigma^b}, \quad M^a{}_b \equiv \frac{\partial \sigma^a}{\partial \tilde{\sigma}^b} = (\tilde{M}^{-1})^a{}_b\,. \tag{3.151}$$

One of the most obvious reasons for this will be when we solve the equations of motion in some convenient coordinate system (where e.g. numerics are well behaved) and then transform to a more physical gauge, e.g. the static gauge. The worldsheet currents (3.130) and the worldsheet metric of course transform as proper worldsheet tensors under (3.151):

$$\tilde{h}_{ab} = M^c{}_a M^d{}_b h_{cd}\,, \tag{3.152}$$

$$\tilde{\Pi}^a_\mu = \tilde{M}^a{}_b \Pi^b_\mu\,. \tag{3.153}$$

Chapter 4

Heavy quarks in AdS/CFT

In the last chapter we covered the basics of the AdS/CFT correspondence, and saw how to introduce massive quarks, as well as how to study the dynamics of classical strings they will be dual to. Starting from this chapter, we will use those tools and study holographic quark energy loss, starting with heavy quarks.

We begin by modeling the heavy quark with a simple trailing string in Section 4.1, and use it to calculate the drag force the quark feels in a strongly coupled plasma. We expand on this in Section 4.2, where we discuss the limits of validity of the trailing string model, consider more general dispersion relations and briefly outline other important applications of the trailing strings. Finally, in Section 4.3, we use the trailing string model to calculate the energy loss and the nuclear modification factor R_{AA} of charm and bottom quarks in non-conformal holography, as in our [203] and [279].

4.1 Heavy quarks as trailing strings

In Section 3.3.2 we showed that it is possible to introduce fundamental degrees of freedom of mass M to $\mathcal{N} = 4$ SYM by introducing a D7-brane in the bulk of AdS_5 [19]. This D7-brane, as viewed from the Poincaré patch, fills the geometry between the boundary $z = 0$ and $z = z_M \propto 1/M$[1] (see Fig. 3.6). Assuming that the quark is sufficiently heavy (so that its mass is much larger than the temperature) and that we are interested in its motion at large time scales (much larger than the relaxation scale of the plasma), we can describe the quark with a Wilson line along its worldline. As we saw in Section 3.3.4, Wilson lines in AdS/CFT (in the 't Hooft limit (3.17)) are given by classical open strings with one endpoint attached to the D7-brane. And since the quarks are assumed to be heavy, the "bottom" of this brane will be close to the boundary (i.e. $z_M \ll z_H$).

4.1.1 The trailing string ansatz

One of the simplest configurations one can study in this context is a heavy quark moving at a constant velocity. From the AdS perspective one can consider an infinitely heavy probe quark, so that the endpoint of the string is attached to the boundary, where we simply prescribe that the endpoint is moving with some constant velocity v. For quarks of finite mass, we can imagine turning on a $U(1)$ field A_μ on the D7-brane under which the string endpoints are charged, which will then drag the endpoint along the bottom of the brane with a constant velocity. This can be implemented by adding an extra boundary term to the string action:

$$S = S_P + \int_{\partial M} d\xi A_\mu(X)\dot{X}^\mu \,, \tag{4.1}$$

[1] At finite temperatures, this relation between the quark mass M and the bottom of the D7-brane z_M changes, as discussed in Section 3.3.2.

where S_P is the Polyakov action (3.126), ∂M is the boundary of the worldsheet and ξ is its parametrization. This will change the standard open string boundary condition (3.138) to:

$$P^r_\mu = F_{\mu\nu}\dot{X}^\nu \,, \tag{4.2}$$

where we assumed the radial $\sigma = r$ parametrization. As discussed in Section 3.6.3, P^r_μ gives the momentum flux into the endpoint, which is now non-zero, due to presence of the electric field. After enough time has passed, any details of the string initial conditions will be washed out and the string will attain a universal, steady-state trailing string profile [22, 23]. See Fig. 4.1 for an illustration of this.

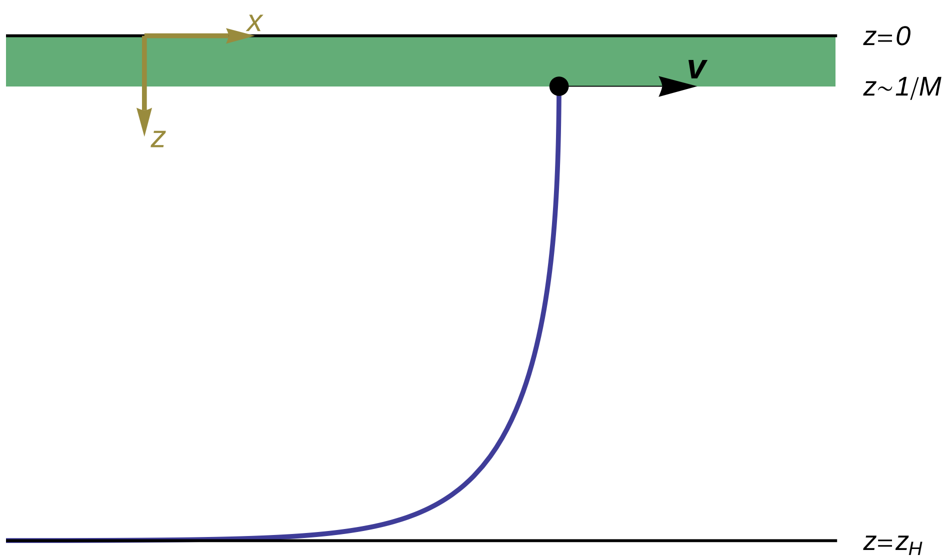

Figure 4.1: *Illustration of the trailing string model in AdS_5-Schwarzschild in Poincaré coordinates (3.32) with boundary at $z = 0$. The endpoint is forced to move with a constant velocity along the bottom of the D7 flavor brane (green), while the rest of the string trails behind it. The horizon is located at $z = z_H$.*

Anticipating applications to more general (non-conformal) theories, we will work in the general metric setup (3.68) of Section 3.5.3, which we copy here for convenience:

$$ds^2 = G_{\mu\nu}dx^\mu dx^\nu = e^{2A(r)}\left(-h(r)dt^2 + d\vec{x}^2\right) + e^{2B(r)}\frac{dr^2}{h(r)}\,, \tag{4.3}$$

where the boundary is at $r = 0$. The trailing string ansatz consists in simply requiring that the endpoint is moving in the $X^1 \equiv x$ direction at a constant velocity v and that the rest of the string trails behind it:

$$X^1(t,r) = vt + \xi(r), \quad X^2 = X^3 = 0\,, \tag{4.4}$$

where $\xi(r)$ is the string profile function which will be determined from the equations of motion, and where we have also chosen to work in the static gauge ($\tau = t$) with a radial string parametrization ($\sigma = r$). We will set the worldsheet metric h_{ab} to be the induced one, γ_{ab}, and using the ansatz (4.4) and the definition of γ_{ab} (eq. (3.3)) we have explicitly:

$$\begin{aligned}
\gamma_{rr} &= e^{2A_s}(\xi')^2 + \frac{e^{2B_s}}{h}\,,\\
\gamma_{tt} &= e^{2A_s}(v^2 - h)\,,\\
\gamma_{tr} &= e^{2A_s}v\xi'\,,
\end{aligned} \tag{4.5}$$

where with subscript "s" we denote the string frame metric, which is related to the Einstein frame metric via $G^{(s)}_{\mu\nu} = e^{q(\phi)}G_{\mu\nu}$ (as discussed in Section 3.5.6), since now the dilaton, in general, has a non-trivial profile.

Since we chose the induced metric for the worldsheet metric, we can work with the Nambu-Goto action, where the Lagrangian is

$$\mathcal{L}_{NG} = -\tau_f\sqrt{e^{4A_s}h(\xi')^2 - e^{2A_s+2B_s}\left(\frac{v^2}{h} - 1\right)}\,, \tag{4.6}$$

where $\tau_f = 1/(2\pi\alpha')$. Following [22], we can obtain the equations of motion from here by defining Π_ξ, the momentum conjugate to ξ, and realizing that, since (4.6) does not contain ξ, this momentum is conserved:

$$\Pi_\xi \equiv \frac{\partial \mathcal{L}_{NG}}{\partial \xi'} = \text{const.} \tag{4.7}$$

Now we can simply solve (4.7) for the profile function ξ':

$$\xi'(r) = -\Pi_\xi \frac{e^{B_s - A_s}}{h} \sqrt{\frac{v^2 - h}{\Pi_\xi^2 - \tau_f^2 h e^{4A_s}}}\,, \tag{4.8}$$

where we, assuming that $\Pi_\xi > 0$, chose the negative solution, as it corresponds to the string trailing behind the endpoint, rather than in front of it. Now, in order for ξ' to be real, the expression under the square root in (4.8) must remain non-negative for all r. However, since $v \leq 1$ and the blackening function $h(r)$ is bounded between 0 and 1, at some point, call it r_*, the numerator under the square root in (4.8) will change its sign:

$$h(r_*) = v^2\,. \tag{4.9}$$

The only way to retain the positive sign of the fraction under the square root in (4.8) is that the denominator changes sign at the same point as well. This fixes the value of the ξ-conjugated momentum to be:

$$\Pi_\xi = \tau_f v e^{2A_s(r_*)}\,. \tag{4.10}$$

This condition is equivalent to preserving the negative sign of the determinant of the worldsheet metric (4.5). We will discuss some interesting physical implications of r_* in Section 4.2.1.

The method described in the previous paragraph was employed to solve the trailing string in [22, 23] in the case of AdS_5. However, in the general case, where the dilaton is allowed to run, we need to make sure that the function in the denominator of (4.8) changes sign only once (at $r = r_*$), as does the numerator. That translates into a requirement that he^{4A_s} is a monotonic function of r, which will be the case for the particular bottom-up non-conformal model we considered in Section 3.5.2, but may not be true in more general cases[2]. From now on we assume that this condition is met and that he^{4A_s} is a monotonically decreasing function, and, therefore, that the choice (4.10) makes ξ' real everywhere.

With Π_ξ defined as in (4.10), we can integrate (4.8) and hence solve for the trailing string profile. Let us look at this in the case of AdS_5 in Poincaré coordinates (3.32) with the boundary at $z = 0$, where

$$e^A = e^B = \frac{L}{z}, \quad h(r) = f(z) = 1 - \frac{z^4}{z_H^4}, \quad \phi = 0\,. \tag{4.11}$$

Plugging this in (4.8) we get

$$\xi'_{\rm AdS}(z) = -v\frac{\sqrt{1-f(z)}}{f(z)}\,. \tag{4.12}$$

In this special case, this can be analytically integrated, yielding

$$\xi_{\rm AdS}(z) = \frac{1}{4}z_H v\left[2{\rm Tan}^{-1}\left(\frac{z}{z_H}\right) + \log\left(\frac{z_H - z}{z_H + z}\right)\right]\,, \tag{4.13}$$

precisely the profile plotted in Fig. 4.1. We should note that, as $z \to z_H$, this expression diverges to $x \to -\infty$, so we can imagine the other endpoint of the string lying down on the horizon, infinitely far away.

[2]For example, in bottom-up models that incorporate confinement (such as the IHQCD [270]), a necessary condition is that A_s has a minimum at some r.

4.1.2 Drag force

Let us now look at the rate at which the trailing string is losing momentum, or, equivalently, the rate at which the momentum needs to be supplied to the string by the external electric field (4.2). According to the analysis of worldsheet currents that govern the transport of the spacetime momentum on the string worldsheet (Section 3.6.3), this rate is given by (3.148):

$$\frac{dp}{dt} = -P_1^r = \tau_f \sqrt{-\gamma}\gamma^{rb}(\partial_b X^1) G_{xx}^{(s)}\,, \tag{4.14}$$

where we introduced a conventional minus sign and where we used the definition of the worldsheet currents (3.131). Plugging in the trailing string ansatz (4.4) and (4.5), and its solution (4.8), we get

$$\frac{dp}{dt} = -\Pi_\xi = -\tau_f v e^{2A_s(r_*)}\,, \tag{4.15}$$

where r_* is defined by (4.9). This means that the flux of the momentum down the string is equal everywhere on the string and that the electric field (4.2), necessary to counteract the drag force (4.15), is constant. In a similar way one can get the energy flux down the string:

$$\frac{dE}{dx} = \frac{1}{v} P_0^r = -\Pi_\xi\,, \tag{4.16}$$

which implies that a simple relativistic dispersion relation $dE = vdp$ is obeyed.

In the case of AdS_5, eq. (4.11), we get the drag force of [22, 23]:

$$\frac{dp}{dt} = -\frac{\pi}{2}\sqrt{\lambda} T^2 \frac{v}{\sqrt{1-v^2}}\,. \tag{4.17}$$

Assuming that the standard relativistic dispersion relation $p = \gamma M v$ is valid, (4.17) can be cast in a suggestive form,

$$\frac{dp}{dt} = -\eta_D p\,, \qquad \eta_D = \frac{\pi\sqrt{\lambda}T^2}{2M}\,, \tag{4.18}$$

i.e. a simple Langevin equation with η_D as the drag coefficient. This is parametrically quite different from the standard pQCD result: there (in the LPM regime), one gets a formula similar to (2.28) (see e.g. [177]):

$$\frac{dp_{\rm pQCD}}{dt} \sim -\frac{LT^2}{\lambda_g}\log\left(\frac{p}{M}\right)\,, \tag{4.19}$$

where L is the length of the plasma with a constant temperature T, and λ_g is the radiated gluon's mean free path. We will comment more on the phenomenological consequences of this difference in Section 4.3.1.

4.2 More on trailing strings

One of the simplest results immediately available in the trailing string model is the drag force (4.15). In this section we will analyze this model in more details, including the range of its validity and some interesting physics encoded in r_* (4.9), calculate the energy of the trailing string, and finally comment on other interesting theoretical developments.

4.2.1 Physical significance of r_*

We introduced r_* in (4.9) as the radial position at which the value of the of blackening function $h(r)$ equals the value of the velocity of the string endpoint squared, v^2. Assuming that $r_* > r_M$ and that the function he^{4A_s} is monotonically decreasing, we obtained the energy loss as a constant (4.15) determined by the value of the string frame metric at

$r = r_*$.

The assumption of $r_* > r_M$ is important, otherwise, for high enough velocities, the condition (4.9) will never be met, and hence we will not get (4.10) which fixes the value of the (constant) energy loss. At a first glance, naively, one might say that this means that the energy loss will not be constrained to have a fixed value. However, $\sqrt{h(r_M)}$ is the local speed of light in the x-direction in metric (4.3) at $r = r_M$ where the string endpoint is attached to the D7-brane. The velocity v can never be greater than this, which yields a simple "speed limit" for the applicability of the trailing string model:

$$v < \sqrt{h(r_M)}\,. \tag{4.20}$$

In the case of AdS_5, (4.20) can be written explicitly as

$$\gamma < \frac{4M^2}{\lambda T^2}\,, \tag{4.21}$$

where we used the zero-temperature relation between r_M and the mass M, $M = \sqrt{\lambda}/(2\pi r_M)$ (eq. (3.41)).

We can gain a different perspective on the speed limit (4.20) by inspecting the Born-Infeld action (3.7) of the flavor D7-brane with a constant electric field of (4.1), necessary to drag the string endpoint. For the trivial (static) embedding of the D7-flavor brane (discussed in Section 3.3.2) and a constant electric field in the x-direction we get

$$\mathcal{L}_{\text{D7}} \propto \sqrt{e^{4A_s}h - (2\pi\alpha' F_{01})^2}\,. \tag{4.22}$$

From here we see that as we increase the drag force F_{01}, at some point we will reach the critical value of

$$F_{\text{crit.}} = \tau_f e^{2A_s(r_M)}\sqrt{h(r_M)}\,, \tag{4.23}$$

when the sign of the expression under the square root in the D-brane Lagrangian (4.22) becomes negative, indicating an instability. This can be also viewed as the sign that we have not accounted for all the degrees of freedom properly. More precisely, the electric field becomes so great that the D7-brane responds by creating D7-D7 stringlets, dual to pairs of quarks and anti-quarks[3] [281]. Note that (4.23) is precisely the expression for the drag force when $r_* = r_M$, which then leads to the speed limit (4.20).

At r_*, the local speed of light in the x-direction is equal to v and, at $r > r_*$, it is smaller than v[4]. Hence, this is a rather special position, since parts of the string at r_* cannot do anything else but move forward in the x-direction. This means that if we send a signal (a perturbation) along the string from some $r > r_*$ or $r < r_*$, then this signal cannot get past r_*, making parts of the string below it and above it causally disconnected. This is an intuitive way to see that $r = r_*$ behaves as a worldsheet horizon [282], perhaps already visible from the fact that $\gamma_{tt}(r_*) = 0$ (eq. (4.5)), making the worldsheet at $r > r_*$ spacelike. This effective "black hole on the worldsheet" has also an associated temperature, which can be shown to be equal to $T_* = T/\sqrt{\gamma}$ in the case of AdS_5-Schwarzschild. This will be a part of a very interesting physical picture when we discuss the momentum fluctuations of the trailing string in Section 4.2.3.

4.2.2 Energy and momentum of the trailing string

The drag force (4.15), i.e. the energy loss in the trailing string model, is given as a function of the velocity v of the string endpoint, while, for phenomenological applications, we need to have it expressed in terms of the momentum and energy of the quark. Some of the

[3] This is essentially a holographic dual of the Schwinger effect [280].

[4] Naively, thinking of the trailing string as a boosted object being translated in the x-direction, one might (incorrectly) reach a conclusion that the parts of the string at $r > r_*$ are superluminal. Of course, that is not the case as the determinant of the worldsheet metric (4.5) is negative everywhere, and the trailing string "stretches", i.e. the motion of different string "bits" (those with fixed σ) is always locally perpendicular to the string profile and hence, depending on the local profile curvature, these bits move in the radial direction as well.

first works on comparing the trailing string energy loss to the heavy ion suppression data [283, 284] used the standard relativistic dispersion relation, $p = \gamma M v$, where M is the bare quark mass, which will be our starting point in Section 4.3 as well. However, in a strongly coupled thermal medium and at intermediate energies, this simple dispersion relation may be modified, and the search for a more realistic dispersion relation starts with a calculation of the energy and the momentum of the trailing string.

The energy of the trailing string can be calculated by simply plugging the expression for the string profile (4.8) in the energy density P_0^t (eq. (3.147)). A direct calculation, after some rearrangement of the terms, leads to an interesting expression:

$$E = -\int_{r_M}^{r_H} dr\, P_0^t = \int_{r_M}^{r_H} dr\, e^{B_s - A_s} \sqrt{\frac{\Pi_\xi^2 - \tau_f^2 h e^{4A_s}}{v^2 - h}} + \left|\frac{dE}{dx}\right| \Delta x\,, \tag{4.24}$$

where dE/dx is given by (4.16) and where we defined $\Delta x \equiv X^1(t, r_M) - X^1(t, r_H)$, which may be identified with the (infinite) distance the endpoint of the string has traveled (imagining the string as initially upright). Before drawing any conclusions from the form of this equation, let us do the same with the momentum in the x-direction:

$$p = \int_{r_M}^{r_H} dr\, P_1^t = \int_{r_M}^{r_H} dr\, \frac{e^{B_s - A_s}}{v} \frac{\left|\Pi_\xi^2 - \tau_f^2 v^2 e^{4A_s}\right|}{\sqrt{(v^2 - h)(\Pi_\xi^2 - \tau_f^2 h e^{4A_s})}} + \left|\frac{dp}{dt}\right| \Delta t\,, \tag{4.25}$$

where in the last line we defined $\Delta t \equiv \Delta x / v$ and where dp/dt is given by (4.15). We see that in both (4.24) and (4.25) energy and momentum decompose into a finite part plus the net input of energy (momentum) required to move the endpoint a distance Δx (time Δt) at a velocity v. The latter is formally divergent, reflecting the unbounded energy input into the trailing string via the electric field that has been applied for an infinite amount of time, necessary to maintain the steady-state motion. This interesting decomposition was first noticed in [23], where these relations have been derived in the case of AdS_5.

Having in mind this interpretation, it perhaps makes sense to define the "renormalized" energy and momentum associated with the heavy quark as the finite parts in equations (4.24) and (4.25):

$$E_R \equiv \int_{r_M}^{r_H} dr\, e^{B_s - A_s} \sqrt{\frac{\Pi_\xi^2 - \tau_f^2 h e^{4A_s}}{v^2 - h}}\,, \tag{4.26}$$

$$p_R \equiv \int_{r_M}^{r_H} dr\, \frac{e^{B_s - A_s}}{v} \frac{\left|\Pi_\xi^2 - \tau_f^2 v^2 e^{4A_s}\right|}{\sqrt{(v^2 - h)(\Pi_\xi^2 - \tau_f^2 h e^{4A_s})}}\,. \tag{4.27}$$

However, this interpretation is not without caveats, as noted in [23], as it neglects the initial period of acceleration. This was treated more carefully in [285], where it was shown that, when this period is taken into account, the finite parts in (4.26) and (4.27) can get extra additive pieces. However, as we will see in the next chapter, in the high energy limit, expressions (4.26) and (4.27) will be crucial for developing analytical expressions for stopping distance of light quarks.

We conclude with the "renormalized" energy and momentum in the case of a trailing string propagating in AdS_5:

$$E_{R,\mathrm{AdS}} = \frac{\sqrt{\lambda}}{2\pi} \frac{1}{\sqrt{1 - v^2}} \left(\frac{1}{r_M} - \frac{1}{r_H}\right)\,, \tag{4.28}$$

$$p_{R,\mathrm{AdS}} = \frac{\sqrt{\lambda}}{2\pi} \frac{v}{\sqrt{1 - v^2}} \left(\frac{1}{r_M} - \frac{1}{r_H}\right)\,. \tag{4.29}$$

These expressions nicely show how the energy of a heavy quark is just its thermal mass (eq. (3.42)), boosted to velocity v, and how in this case, a simple dispersion relation $p_R = vE_R$ is obeyed, but as we can see from (4.26) and (4.27) this may not be the case in general.

4.2.3 Other developments

Since the trailing string model is rather simple and analytical, it allowed for applications to many other interesting phenomena involving heavy quarks, besides the energy loss.

An interesting next step is to include a noise term $\vec{\xi}(t)$ to the right hand side of the simple Langevin equation (4.18). This noise term encodes the random momentum "kicks" the heavy quark receives from the medium. For random forces transverse to the direction of the motion of the quark, their two-point function has the form of

$$\langle \xi_T(t)\xi_T(t')\rangle = \kappa_T \delta(t-t')\,, \tag{4.30}$$

and similar for the longitudinal forces. Here κ_T is a constant that determines the average transverse momentum acquired by the heavy quark after some time t, $\langle p_T^2(t)\rangle \approx 2\kappa_T t$. This leads to transverse momentum "broadening", an effect visible in the structure of jets in heavy ion collisions. These momentum fluctuations are computable in terms of linearized transverse fluctuations around the steady state trailing string solution (4.13) in AdS_5, yielding [286, 287]:

$$\kappa_T = \sqrt{\lambda\gamma}\pi T^3\,. \tag{4.31}$$

In fact, this was computed using a Kubo formula (3.43), where κ_T was expressed as a transport coefficent for operator $\mathcal{O}(t) = -dp_\perp/dt$, dual to the transverse fluctuation $\delta x_\perp$. In deriving this relation, the temperature one uses is precisely the effective worldsheet horizon temperature $T_* = T/\sqrt{\gamma}$ we mentioned in Section 4.2.1. This leads to an interesting physical picture, where the worldsheet fluctuations of a classical string arise due to the Hawking radiation originating from the worldsheet horizon.

Now that we have seen how the medium affects the heavy quark, a natural next question is how does the quark affect the medium. This can be answered by solving the so-called bulk-to-boundary problem. The underlying idea is the following. The classical string in AdS has an associated energy-momentum tensor $t_{\mu\nu}$, which will act as a source and back-react, i.e. change the geometry of the space: $G^{\text{AdS}}_{\mu\nu} \to G^{\text{AdS}}_{\mu\nu} + h_{\mu\nu}$. The hard problem is to now solve the five-dimensional Einstein equations, linearized in $h_{\mu\nu}$. Once that is done, the behavior of $h_{\mu\nu}$ near the boundary will determine the expectation value of the energy momentum operator $\langle T_{\mu\nu} \rangle$ in the field theory, according to the field/operator correspondence (Section 3.2.3). Since the trailing string solution is known analytically, the bulk-to-boundary problem in this case is tractable [288] and one can compute the change in the energy density of the strongly coupled boundary theory due to the presence of a heavy quark moving at a constant velocity. This analysis has demonstrated how supersonic quarks create Mach cones in energy density and diffusion wakes in momentum density [289, 290].

Finally, we should briefly mention some of the many works on the heavy quark energy loss in conditions that are somewhat more realistic than a motion at a constant velocity in a uniform $\mathcal{N} = 4$ plasma that we presented in Section 4.1.1. This includes a more careful inspection of the initial period of acceleration and the energy loss during it [285, 291, 292], and studies of trailing strings in more general, asymptotically AdS geometries [293], as well as expanding [294, 295], charged [296] and non-conformal plasmas [203, 270, 271, 279].

4.3 Energy loss of heavy quarks in non-conformal holography

In this section we will apply the trailing string framework of Section 4.1 to calculate the heavy quark energy loss in the non-conformal model of Section 3.5.2 and use it to compute the (partonic) nuclear modification factor R_{AA} of charm and bottom quarks at RHIC and

LHC, as in our [203] and [279].

4.3.1 Heavy quark puzzle

The motivation for this work comes from the "heavy quark puzzle", an apparent inconsistency of the pQCD models of heavy quark energy loss and the experimental results for the suppression of the non-photonic electrons at RHIC [297, 298]. As noted before, the non-photonic electrons come from the semileptonic decays of heavy quarks via $c \to D \to e$ and $b \to B \to e$, and their R_{AA} was measured to be rather small (Fig. 4.2), quite similar to the R_{AA} of pions. This indicated that, surprisingly, the heavy quarks may be as much quenched as the light quarks, something that was inconsistent with any pQCD-based energy loss model. This, in turn, signaled that there may be some non-trivial strong coupling effects at play, which motivated some of the first attempts at confronting the trailing string model of energy loss with the heavy ion data [283, 284].

As noted earlier, there is an important parametric difference between the heavy quark energy loss in a strongly (eq. (4.18)) and a weakly (eq. (4.19)) coupled plasma. Most notably, the momentum and mass dependence of energy loss in pQCD goes like $\sim \log(p_T/M)$, while in AdS/CFT it is $\sim p_T/M$. This means that the ratio of the energy losses of two heavy quarks at the same p_T in AdS/CFT will depend on the inverse of their mass ratios, a much stronger mass dependence than in pQCD. More importantly, the relative energy loss (for a given heavy quark), $\epsilon = \Delta E/E$, in pQCD asymptotes to 0 at high energies, while in AdS/CFT it asymptotes to a constant determined by the mass of the quark. This is important because the nuclear modification factor is sensitive to ϵ, especially at high p_T. In Section 1.4.1 we developed a simple pocket formula, eq. (1.72): $R_{AA} \sim (1-\epsilon)^{n_Q-1}$, where n_Q is the power-law index of the pp production spectrum for quark Q, which, at high p_T, becomes approximately independent of p_T.

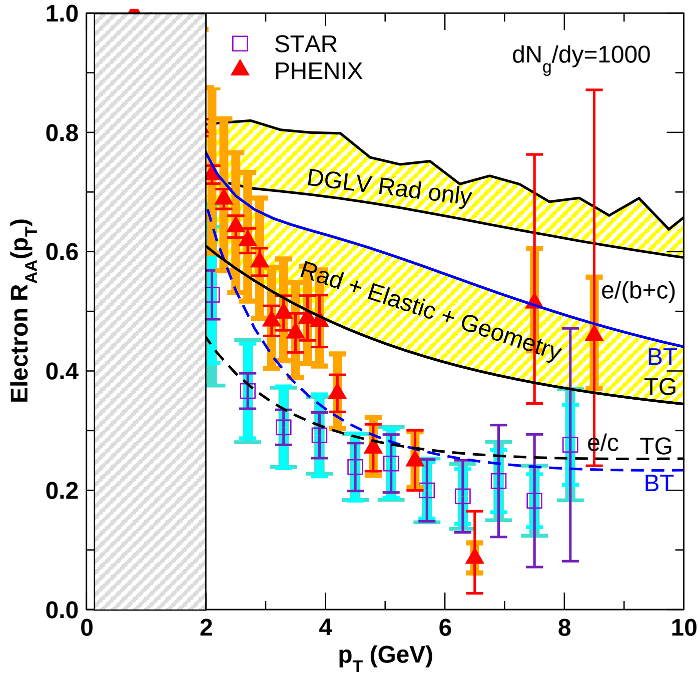

Figure 4.2: *Comparison of the non-photonic electron R_{AA} from the WHDG model [194] to the PHENIX [297] and STAR [298] data. The upper yellow band represents a calculation involving only radiative pQCD energy loss (DGLV), while the bottom band is the WHDG calculation that also includes the elastic energy loss, as well as the jet path length fluctuations. (Taken from [194].)*

Therefore, at high p_T, we expect to see the pQCD heavy quark R_{AA} to asymptote to unity, while in AdS/CFT, we expect to see it asymptoting to a constant smaller than 1, something perhaps suggested by the electron suppression data in Fig. 4.2. This was studied in detail in [283], where it was suggested that the ratio of charm to bottom R_{AA}'s should be a robust observable that can be used to search for these strong coupling deviations from pQCD predictions: in pQCD this ratio asymptotes to unity, while in AdS/CFT we have $R^c_{AA}/R^b_{AA} \approx M_c/M_b \approx 0.26$. Our goal in this section is to extend this work and inspect whether this simple mass dependence of the ratio of energy losses in a conformal theory still holds in non-conformal holography, where the QCD trace anomaly is explicitly taken into account.

We should also note that the heavy quark puzzle has been recently solved by the CUJET [195] (discussed in Section 2.3.1), showing that one of the keys in solving it was the inclusion of the dynamical effects in the medium (i.e. going beyond the approximation of static scattering centers, see Section 2.2.3), which were especially important for heavy quarks. Also, it will soon become possible to disentangle the contributions of the bottom and charm quark energy losses to the experimental observables through the measurements of the suppression of D mesons [299] and the upcoming measurements of the B mesons at the LHC.

4.3.2 Energy loss and R_{AA}

In this section we will compute the energy loss of heavy quarks [203] in the non-conformal model of Section 3.5, where the conformality was explicitly broken by the introduction of a potential for the dilaton, which was tuned in such a way so that the thermodynamics of the dual theory would match the lattice QCD data. In addition to that, by matching the lattice data for the Polyakov loops, the effective L^2/α' was also determined, so the model is completely constrained and the energy loss becomes a prediction.

In this section we will simply assume that the trailing string model is applicable to both charm and bottom quarks, i.e. that they are heavy enough, with respect to the relevant range of temperatures (so that $r_M \ll r_H$) and momenta (so that $r_M < r_*$). We will discuss the validity of these assumptions in the next two sections. In the generalized drag force formula (4.15), we will use the simple dispersion relation $p = \gamma M v$.

Fig. 4.3 shows the energy loss in our non-conformal model as a function of temperature for a fixed transverse momentum, compared to the conformal limit, i.e. (4.18) where the same L^2/α' was used.

The first thing to notice is that the typical values of energy loss are rather reasonable,

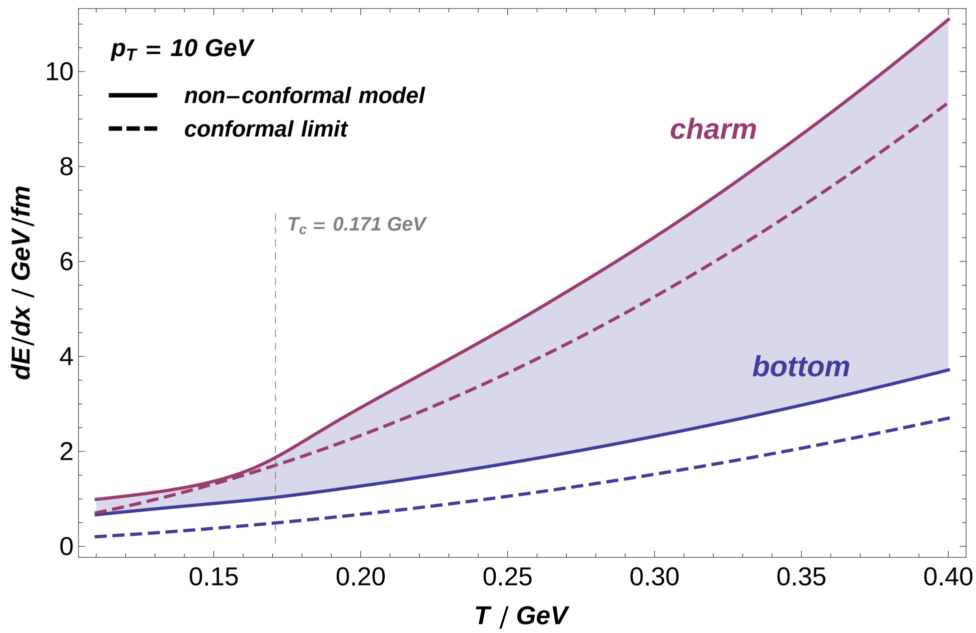

Figure 4.3: *Energy loss of charm and bottom quarks as a function of temperature T for a fixed transverse momentum of p_T =10 GeV, predicted in our non-conformal holographic model, compared to the conformal limit of the model.*

on the order of several GeV/fm. We also see that the energy loss increases monotonically with temperature, which can be expected for any holographic model in which the trailing string is well defined, for the following reasons. As we increase the temperature, the horizon approaches the boundary (in AdS_5, $r_H \propto 1/T$), and for a fixed momentum, the value of r_* decreases. Energy loss (4.15) is determined by the value of $\sqrt{h(r)}e^{2A_s(r)}$ at $r = r_*$ and, as noted in Section 4.1.1, this function needs to be monotonic, in order for the trailing string model to be well defined.

Close to T_c, there are some noticeable effects of the non-trivial QCD trace anomaly on the energy loss, which should become more apparent in the relative ratio of energy losses in Fig. 4.4. There we see that a significant deviation from the conformal result (which is just given by the inverse ratio of masses) is found for temperatures around T_c, where the trace anomaly is maximal. As we increase the temperature and the momentum, the results start to approach the conformal limit, which is to be expected as our model is asymptotically conformal.

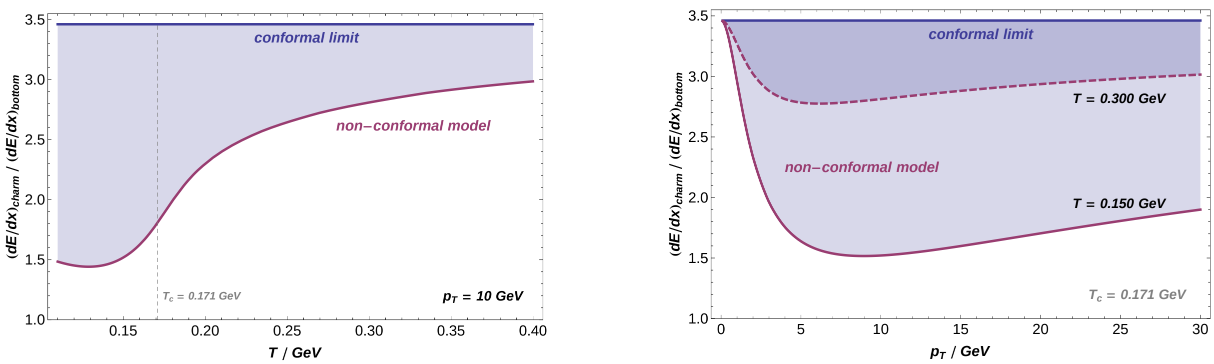

Figure 4.4: *Ratio of energy losses of charm and bottom quarks as a function of temperature T (for a fixed transverse momentum of p_T =10 GeV) and transverse momentum p_T (for fixed temperatures of 150 and 300 MeV) predicted in our non-conformal holographic model, compared to the conformal limit.*

Since a heavy quark traveling through a realistic quark-gluon plasma probably spends a significant amount of time in the temperature region close to T_c, we may expect that the results shown in Fig. 4.4 affect the relative relationship of charm and bottom R_{AA}'s. We will follow the procedure from Sections 1.3 and 1.4 to compute the partonic R_{AA} of charm and bottom quarks in an expanding plasma with Glauber initial conditions [279]. The results are shown in Fig. 4.5.

For bottom quarks, R_{AA} flattens out already at $p_T \sim 10$ GeV, which is a consequence of the asymptotic conformal invariance of our model and, as discussed in the previous section, the conformal R_{AA} is expected to be flat at high p_T. Another thing to note is that the values of R_{AA} at RHIC and LHC are quite similar, even though the production spectra (see Fig. 1.13) are quite different. At the LHC, the maximum temperature is higher than at RHIC, an effect which competes with the increased steepness of the spectral indices at RHIC with respect to LHC, ultimately leading to the heavy quark R_{AA} not changing by much when one increases $\sqrt{s}$ by one order of magnitude.

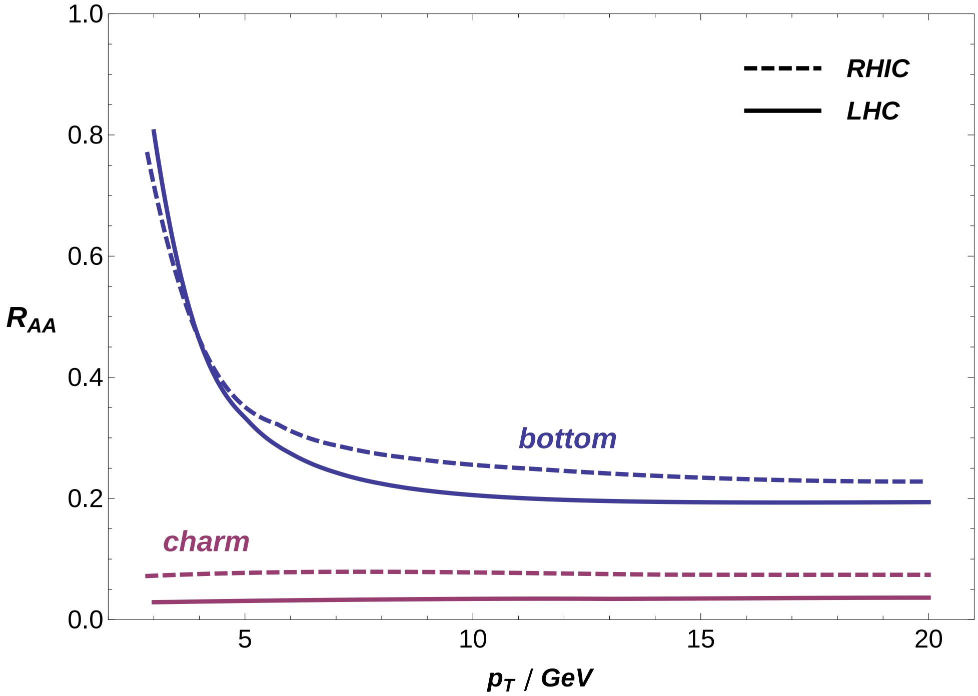

Figure 4.5: *Nuclear modification factor R_{AA} at impact parameter $b = 3$ fm for charm and bottom quarks in an expanding plasma as a function of the transverse momentum p_T for RHIC (dashed curve) and LHC (solid curve). We used the initial time of $\tau_0 =1$ fm/c and the freeze-out temperature of $T_{\rm fo} =150$ MeV (eq. (1.65)).*

For charm quarks, R_{AA} is relatively small, which is due to the fact that the trailing string energy loss in any holographic model decreases monotonically with mass. Even though the ratio of charm and bottom energy losses came close to 1 around T_c, this was not enough to bring their respective R_{AA}'s much closer. However, as we will see in the next two sections, the applicability of the trailing string ansatz in the case of charm quark may be questionable.

4.3.3 Finite quark masses

As noted in the previous section, we need $r_M < r_*$ and, of course, $r_M < r_H$, in order for the trailing string model to be applicable. Since the drag force formula (4.15) does not depend on r_M explicitly, we could take a somewhat less rigorous approach and simply assume that we are dealing with a test quark attached to the boundary of the geometry, and take the results of the previous section as a good guidance (at least when it comes to relative ratios) of what the energy loss of charm and bottom quarks should be in a non-conformal plasma.

Or, we could try and repeat the analogous procedure from the AdS case: assuming that there is a flavor D-brane that extends from the boundary to some r_M, we can relate the bare masses of the charm and bottom quarks to it by computing the energy of a static, straight string stretching from r_M to infinity in the zero-temperature case:

$$M \equiv E(v=0, T=0) = \frac{1}{2\pi\alpha'} \int_{r_M}^{\infty} dr\, e^{A_{s,0}+B_{s,0}} \,. \tag{4.32}$$

To solve this equation for r_M, one first needs to obtain $A_0(\phi)$ and $B_0(\phi)$ at zero temperature, which can be done using the procedure described in Section 3.5.7. We get the following values for charm and bottom D-branes:

$$r_{M,c} = 0.931\, L\,, \qquad r_{M,b} = 0.045\, L\,. \tag{4.33}$$

Now we need to pass to the finite temperature case, and the idea is to use (4.33) as a guide to where the endpoints of the trailing strings dual to charm and bottom quarks should be placed. As discussed in Section 3.3.2, in the metric with a horizon, the relation between r_M and the bare mass changes, due to the change in the embedding of the flavor D-brane. Since it is quite non-trivial to calculate these effects in our case, we could make an uncontrolled first approximation and take (4.33) at face value. In that case, from Fig. 4.6 we see that, already at modestly high temperatures, the horizon r_H reaches the bottom of the charm D-brane, violating the assumptions of $r_M < r_H$ and $r_M < r_*$.

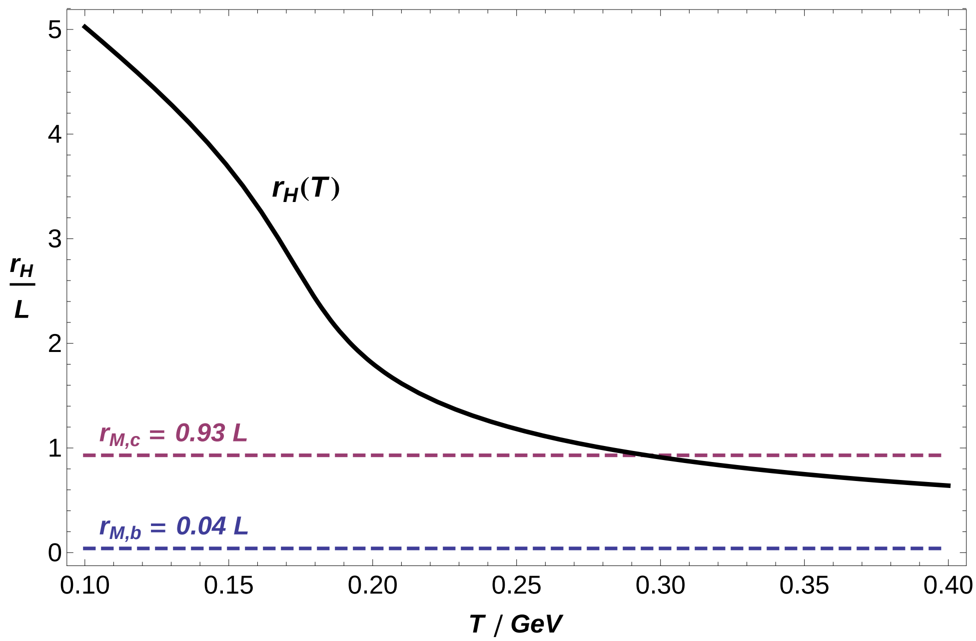

Figure 4.6: *Radial location of the horizon r_H as a function of temperature T in our non-conformal holographic model. Dashed lines indicate the zero-temperature locations (4.33) of the bottom of the flavor D-branes for charm and bottom quarks.*

Although extrapolating the values in (4.33) to the finite temperature case should be taken with a grain of salt, it nevertheless points to an interesting possibility that the charm quark might effectively become a light quark at modestly high temperatures, and different methods may be needed to treat this "hybrid" case. This effect may even be the key in reducing the gap between the charm and bottom R_{AA}'s from Fig. 4.5.

4.3.4 Dispersion relation

We discussed earlier how the simple dispersion relation $p = \gamma M v$ may not be applicable for heavy quarks at modest temperatures and momenta, and how the "renormalized" expression (4.27) may provide a more realistic expression for the momentum of a heavy quark. Computing the renormalized momentum at different velocities and temperatures, one notices that, at a fixed temperature, it is very similar to the usual relativistic dispersion relation, only with a different effective mass, i.e. $p_R = M_{\text{eff}}\gamma v$. These effective kinetic masses for charm and bottom as a function of temperature are shown in Fig. 4.7.

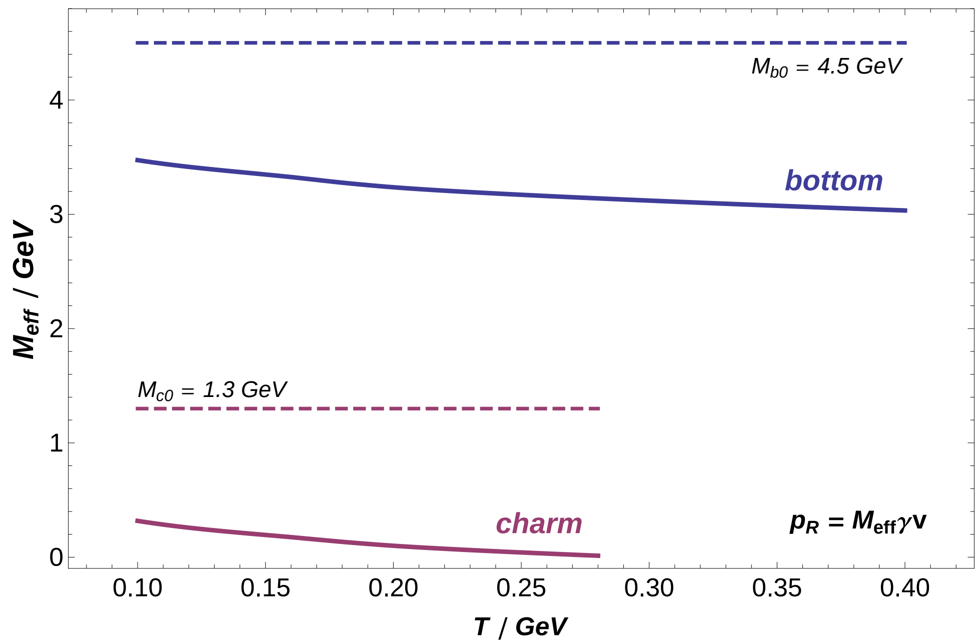

Figure 4.7: *Effective kinetic masses for charm and bottom quarks as a function of temperature.*

In Fig. 4.7 we see that, since the integrand in (4.27) is positive-definite, increasing the temperature will generally decrease the effective mass, as was the case in AdS_5 (eq. (4.29)). Also, for both charm and bottom, the effective masses get shifted by roughly the same amount, which is to be expected, since the integrand in (4.27) is the same for both charm and bottom and the effect of the finite temperature is that the part of this integral from $r = r_H$ to $r = \infty$ gets cut off. For charm, as announced in the previous section, this effect is drastic: already at about 280 MeV, its effective mass becomes virtually zero, as the horizon approaches the bottom of its flavor D-brane.

Because the effective mass shifts for charm and bottom are approximately the same, using the dispersion relation (4.27) will not result in a significant change of the relative gap between the charm and bottom R_{AA}'s, although, as noted before, other dispersion relations that take into account the initial period of acceleration may be more relevant [285].

Chapter 5

Light quarks in AdS/CFT

Now that we have studied the energy loss of heavy quarks in gauge/gravity duality in the last chapter, the next natural step is to turn to light quarks. A somewhat more complex problem of holographic energy loss of light quarks constitutes the central part of this thesis, and is the subject of this and the next chapter.

We start with Section 5.1, where we describe how light quarks can be modeled in AdS/CFT with falling strings, and use this model to find their stopping distance. We also present a fully analytical method from our [35] to calculate this distance, and apply it to compute the stopping distance in the Gauss-Bonnet gravity, as in our [36]. We then outline a general method in Section 5.2 to solve the falling strings numerically, and compare the solutions in a conformal and a non-conformal plasma. Section 5.3 is based on [33], where we derive a general formula for the instantaneous energy loss in non-stationary string configurations, an application of which to the case of falling strings reveals a seemingly linear path dependence, which we also confirm analytically [36]. Finally, in Section 5.4, we develop a phenomenological model of light quark energy loss, as in our [34], and use it to compute the nuclear modification factor R_{AA}.

5.1 Stopping distance of light quarks

From Section 3.3.2 we know that the introduction of the fundamental degrees of freedom ("quarks") of mass M to a strongly coupled $\mathcal{N} = 4$ SYM is dual to the introduction of a D7-brane in the bulk of AdS_5 [19], which fills the geometry between the boundary $z = 0$ and $z = z_M \propto 1/M$. In the case of heavy quarks, the bottom of the D7-brane was close to the boundary, but in order to introduce light quarks to a finite temperature plasma, the D7-brane needs to fill the entire AdS_5-Schwarzschild geometry. In the classical gravity limit, the dressed light $q\bar{q}$ pairs are represented by classical, open strings with both endpoints on the D7-brane, which can now fall towards the horizon [24, 300]. The main idea is that by studying the free motion of these falling strings we can study the energy loss of light quarks.

5.1.1 Light quarks as falling strings

The endpoint of the string attached to the D7-brane is charged under a $U(1)$ gauge field living on the brane (as explained in Section 3.1.3). This gauge field will be naturally dual to a baryon density current on the boundary[1], in the sense of the field/operator correspondence (Section 3.2.3), representing the entire dressed excitation; see Fig. 5.1 for illustration. One naturally identifies the quark itself is with the endpoint of the string, while the details of its "gluonic cloud" are encoded in the bulk of the string.

We hence imagine the endpoint moving in the x-direction and at the same time slowly falling towards the horizon. The baryon current density is localized (in the x-direction) close to the x-position of the endpoint (modulo retardation effects), and the degree of localization depends on how close the endpoint is to the boundary. As the endpoint starts to fall towards the horizon, the baryon density starts to diffuse, until the endpoint

[1] In fact, the boundary of AdS act as a perfect conductor [301], so the string endpoint which sources the gauge field on the D7-brane will induce an image current density on the boundary, as in Fig. 5.1.

finally reaches the horizon[2]. At that point, the endpoint cannot continue moving in the x-direction (as the local speed of light at the horizon vanishes), and hence the same is true for its boundary baryon density: this is identified as the stopping distance of a light quark [300]. This is yet another example of an appealing geometrical interpretation of a field theory phenomenon: thermalization in a finite temperature plasma is dual to classical string endpoints falling into the black hole.

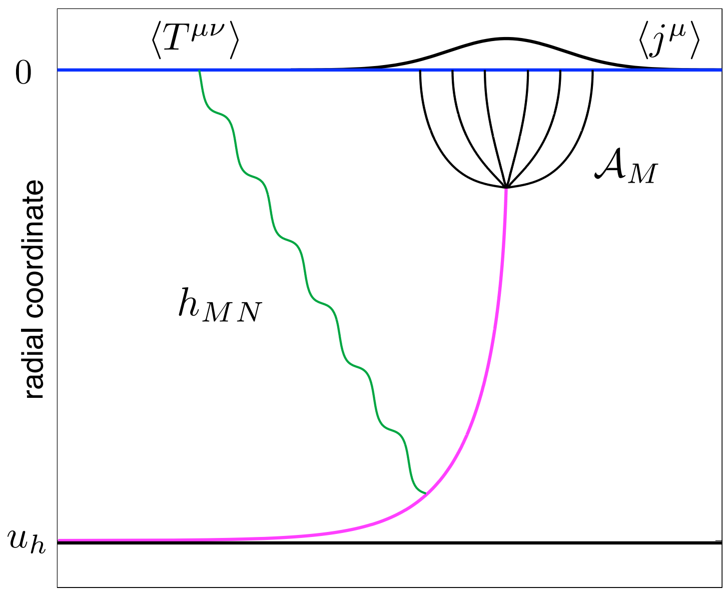

Figure 5.1: *Illustration of the falling string model in AdS_5-Schwarzschild. The $U(1)$ gauge field sourced by the endpoint induces an image baryon current density on the boundary at $u = z = 0$. As the endpoint is falling towards the horizon, the baryon density becomes more delocalized. (Taken from [24].)*

Since the energy of the classical string is conserved, it is generally hard to disentangle which parts of the string contribute to the thermalized energy deposited in the plasma and which parts contribute to the energy of the quark itself; this will be discussed more in Section 5.3. Now, the presence of the string also induces metric perturbations on top of the background AdS_5 geometry and the behavior of these perturbations close to the

[2] Of course, from the bulk perspective, the endpoint will never exactly reach the horizon, as the local speed of light there reaches zero, and the endpoint's rate of approach decreases indefinitely.

horizon determines the change in the energy momentum tensor of the boundary theory (see Sections 3.2.3 and 4.2.3): the closer some part of the string is to the boundary, the more localized its dual energy density is. Therefore, we generally think of the parts of the string that are "lying" on the horizon as being thermalized and the parts of the string that are more "upright" as being associated with the jet itself.

In the quark-gluon plasma, an initial hard scattering event creates a pair of back-to-back jets. In the dual description, this will be represented by the production of a classical string where the endpoints have some initial velocity in the opposite directions along the x-axis. We generally consider this "pointlike" string created close to the boundary so that we initially have a well collimated excitation in the dual theory. As the endpoints move away from each other, the bulk of the string is falling towards the horizon and the string attains a typical U-shaped profile (see e.g. Fig. 5.4); at the boundary, this corresponds to two peaks of energy density moving away from each other and slowly spreading as the endpoints are approaching the horizon.

We should however point out that there are no jets in a strongly coupled $\mathcal{N} = 4$ SYM [259, 302]: the final state produced in a high-energy scattering would, instead of displaying jet-like features such as the angular collimation, result in a spherically symmetric outflow of energy, as perhaps expected in a conformal theory[3]. Our aim here is to simply prepare a string configuration that is dual to some energetic excitation which resembles a collimated quark jet.

One of the first results for light quark energy loss in gauge/gravity duality was obtained in [300]. There it was shown, by analyzing null geodesics in AdS_5-Schwarzschild and relating them to the energy of a falling string, that the maximum stopping distance in a

[3]However, by considering a test quark moving in a circle in a zero-temperature $\mathcal{N} = 4$ SYM, it was found [303, 304] that the beam of radiated gluons is very similar to the synchrotron radiation, exhibiting tight angular collimation and propagating forever without spreading in angle.

strongly coupled $\mathcal{N} = 4$ SYM plasma is given by

$$\Delta x_{\max} = \frac{\mathcal{C}}{T}\left(\frac{E}{\sqrt{\lambda}T}\right)^{1/3}, \tag{5.1}$$

where T is the temperature, E is the energy of the light quark and $\mathcal{C} \approx 0.526$. The form of this result is essentially dictated by the scale invariance, the only unknowns were the power of $1/3$ and the numerical factor $\mathcal{C}$. The result (5.1) is parametrically different from the typical pQCD result: there (in the LPM regime), one gets $\Delta x_{\rm pQCD} \sim E^{1/2}$ (see (2.28) and (2.29)).

Let us emphasize the meaning of the maximum stopping distance: the result (5.1) is the maximum distance a light quark of a fixed energy E can traverse. For a given energy, the distance the quark will travel may be smaller than (5.1) as it is dependent on how we prepare the initial wavepacket: on the gravity side these internal degrees of freedom are encoded in the initial conditions for the classical string (i.e. the initial string profile and its corresponding velocity profile, constrained to give the same energy).

A similar approach to [24, 300] has been undertaken in [25] to study the energy loss of gluons in $\mathcal{N} = 4$ SYM plasma. Gluons, since they are adjoint degrees of freedom, are naturally modeled as folded (doubled) strings with both endpoints on the D3-branes (which can be imagined to be “behind the horizon”). By realizing that the tip of the folded string is following a null geodesic (as the whole string is falling towards the horizon), and by relating the parameters of that geodesic to the energy of the string, the authors of [25] have arrived at the parametrically same result as in (5.1), only with a slightly different value of $\mathcal{C}$ than [300] (due to a somewhat different estimate of the energy of the string). In this context, the only difference between quarks and gluons would be to replace $E \to 2E$ in (5.1), since the energy of a folded string is approximately twice the energy of a falling string, and they have similar dynamics. Interestingly, this is approximately what we would expect in a generic pQCD model of energy loss (see e.g. (2.28) and (2.29)), where dE/dx scales linearly with the quadratic Casimir of the jet C_R, and $C_A/C_F = 9/4 \approx 2$ for $N = 3$.

A parallel line of development started in [302], where the authors studied the dynamics of a wavepacket falling towards the horizon, dual to the evolution of an R-charge jet in $\mathcal{N} = 4$ SYM. Their approach has also yielded the same energy scaling of the maximum stopping distance as in (5.1). A complementary approach to all these was developed in [305, 306], where the authors specified the initial high-energy excitation on the field theory side and solved for its evolution by computing real-time 3-point correlators using the AdS/CFT correspondence. Their studies have confirmed the $E^{1/3}$ scaling of the maximum stopping distance as well, but they have also found that the typical (rather than the maximal) stopping distance scales as $(EL)^{1/4}$, where L is the initial size of the excitation.

5.1.2 Stopping distance (numerically)

In this section we will briefly present the approach of [300] for calculating the stopping distance (5.1) of light quarks in a strongly coupled $\mathcal{N} = 4$ plasma, in order to set the stage for an analytical derivation of these results in the next section.

As discussed in the previous section, one starts with a string which is initially pointlike at some radial height z_c and gives it some velocity profile with which the string then evolves in the radial and x-directions according to the classical equations of motion. We will work in the Poincaré coordinates of AdS_5-Schwarzschild (3.32), which we copy here for convenience:

$$ds^2 = \frac{L^2}{z^2}\left(-f(z)dt^2 + d\vec{x}^2 + \frac{dz^2}{f(z)}\right) , \tag{5.2}$$

where $f(z) = 1 - z^4/z_H^4$ with $z_H = 1/(\pi T)$ and the boundary of the space is at $z = 0$.

We assume that the string is moving in the x-z plane and choose the static gauge ($\tau = t$ and $\sigma = z$), so that the only string embedding function we need to know is $x(z,t)$. This can be written, quite generally, as the stationary solution plus a perturbation:

$$x(z,t) = \xi t + x_0(z) + \delta x(z,t)\,, \tag{5.3}$$

where ξ is a constant. Although the stationary solution looks like the trailing string ansatz (4.4), the boundary conditions are different, as the endpoint is now free. We can write the motion of the endpoint as:

$$\mathcal{Z}(t) = \mathcal{Z}_0(t) + \delta\mathcal{Z}(t)\,, \tag{5.4}$$

where $\mathcal{Z}_0(t)$ corresponds to the motion when $\delta x(z,t) = 0$. Plugging (5.3) with $\delta x = 0$ in the classical equations of motion (3.132), one gets a non-linear differential equation for the profile function $x_0(z)$, whose general solution is given by

$$\left(\frac{\partial x_0}{\partial z}\right)^2 = \frac{z^4(\xi^2 - f)}{z_H^4 f^2 (1 - Cf)}\,, \tag{5.5}$$

where C is an integration constant. We still have to include the free string endpoint boundary conditions (3.138), which yield:

$$\left(\frac{\partial x_0}{\partial z}\right)^2_{\text{endpoint}} = \frac{\xi^2 - f}{f^2}\,, \tag{5.6}$$

$$\left(\frac{d\mathcal{Z}_0}{dt}\right)^2 = \frac{f^2(\xi^2 - f)}{\xi^2}\,. \tag{5.7}$$

The first thing to notice is that (5.7) is the equation for null geodesics (we will discuss these more in the next section). In addition to that, by comparing (5.6) to (5.5), we see that the boundary conditions force C to be 1. Plugging (5.5) with $C = 1$ in the expression for the determinant of the worldsheet metric γ quickly reveals that it is degenerate, i.e. $\gamma = 0$ everywhere. That is, in the steady state solution, the string is null (i.e. every part of it is moving at the local speed of light) and the endpoints are following null geodesics.

For a null string, every canonical momentum density P^a_μ diverges, as they are given by $\delta S_{NG}/\delta(\partial_a X^\mu) \propto (-\gamma)^{-1/2}$ (eq. (3.131)). This means that the energy of the null string is infinite, and, in order to get a finite energy string configuration, one needs to look for the perturbations $\delta x(z,t)$ to the null string solutions in (5.3). In [300], the authors have found the general solutions to the equations of motion linearized in δx and expressed the energy of the string E_* (whose endpoint is at a radial location z_*) in terms of these perturbations.

The key point was to realize how these perturbations scale with z_* in the high-energy limit $z_* \ll z_H$, because then we know how the UV part of the energy of a falling string scales with z_*. Once that is done, it is easy to relate the total spatial distance Δx the endpoint travels (and hence the stopping distance of its dual light quark) to z_*, since the string endpoints approximately follow null geodesics. Relating Δx and E_* through z_*, one finally obtains that the maximum distance a light quark of energy E travels in a strongly-coupled $\mathcal{N} = 4$ SYM is given by (5.1), where the value of $\mathcal{C}$ was obtained by inspecting the limit of stopping distances of many numerically generated string solutions.

5.1.3 Analytical derivation of the stopping distance

In this section we will demonstrate how one can obtain the result (5.1) for the stopping distance of endpoints of highly energetic falling strings using relatively simple analytical arguments of our [35]. The main idea in our argument is to recognize that the energy of a falling string with the initial conditions considered in [300] can be well approximated by the UV part of the energy of a trailing string whose endpoint is moving at the same radial height at the local speed of light.

To see why this is so, we first start by considering the approximate motion of the endpoints in more details. In the previous section, we showed that the endpoints of highly energetic falling strings move close to the boundary ($z \ll z_H$) and approximately follow null geodesics (as the whole string is close to being null). To find the null geodesics in background (5.2), first note that the vector fields $\xi^\mu = \delta^\mu_t$ and $\xi^\mu = \delta^\mu_x$ are Killing vector fields, since the metric does not explicitly depend on t or x. For any Killing vector field, quantity $u_\mu \xi^\mu$, where u_μ is the four-velocity, is constant along any geodesic. More physically, the non-zero components of these Killing vectors are just the conserved momenta of a particle following a geodesic:

$$p_\mu = \frac{1}{\eta} G_{\mu\nu} \dot{X}^\nu \,, \tag{5.8}$$

where η is the worldline metric and the dot denotes the derivative with respect to some parameter ξ that parametrizes the worldline. Hence, p_t and p_x are conserved on a geodesic and we can use them to label the geodesics with

$$R \equiv \frac{p_t}{p_x} = -f \frac{\dot{t}}{\dot{x}} \,. \tag{5.9}$$

For null geodesics, we need to use the null condition $ds^2 = 0$, which, together with (5.9), yields the null geodesic equation:

$$\frac{dx_{\text{geo}}}{dz} = \frac{1}{\sqrt{R^2 - f(z)}} = \frac{1}{\sqrt{f(z_*) - f(z)}} \,, \tag{5.10}$$

where z_* is the minimal radial distance the geodesic reaches, which we related to the parameter $R = -\sqrt{f(z_*)}$ (assuming a sub-critical geodesic, i.e. a geodesic that never reaches the boundary). See Fig. 5.2 for an illustration of this. We are interested in the high-energy regime in which string endpoints start (with no initial radial velocity) at $z = z_* \ll z_H$. As we can see from (5.10) (and Fig. 5.2), the endpoints stay approximately at constant $z = z_*$ for a long time compared to z_*, and since they are null, they must be approximately moving at the local speed of light in the x-direction, $v = \sqrt{f(z_*)}$. Because of this, a sensible expectation is that, near the endpoints, the string assumes the shape of the trailing string moving at this velocity v before the endpoint falls to appreciably larger values of z.

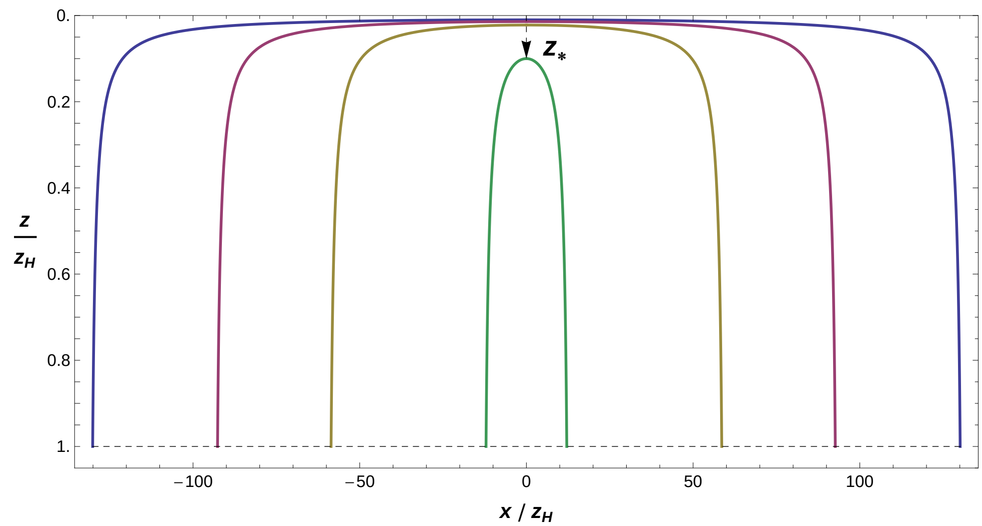

Figure 5.2: *Null geodesics in AdS$_5$-Schwarzschild (5.2), for several different minimal distances from the boundary z_*.*

Consider then the energy of a trailing string whose endpoint is held at $z = z_*$ and forced to move in the x direction at velocity v:

$$E_{\text{trailing}} = \frac{L^2}{2\pi\alpha'}\frac{1}{\sqrt{1-v^2}}\left[\frac{1}{z_*} - \frac{1}{z_H}\right] + \frac{1}{v}\frac{dE}{dt}\Delta x(z_*, z_H)\,. \tag{5.11}$$

which is the form we already found in (4.24), first recognized in [23]. Here dE/dt is the drag force (4.15) and $\Delta x(z_*, z_H) = x(t, z_*) - x(t, z_H)$ can be identified with the distance the endpoint of the string has traveled while being dragged. As noted in Section 4.2.2, this expression shows that the energy of the trailing string is just the boosted static energy plus the net input of energy required to move the endpoint a distance Δx at a velocity v, the latter being divergent. For the falling string we do not have the last term in (5.11), as there is no external force applied. Hence we see that the UV part of the energy of the falling string for $z_* \ll z_H$ can be associated with

$$E_* = \frac{\sqrt{\lambda}}{2\pi}\frac{1}{z_*}\frac{1}{\sqrt{1-v^2}} = \frac{\sqrt{\lambda}}{2\pi}\frac{z_H^2}{z_*^3}\,, \tag{5.12}$$

where in the second equality we used that the local speed of light in the x-direction is $v = \sqrt{f(z_*)}$. This is just the "renormalized" energy (4.26) of Section 4.2.2.

The distance in the x-direction this endpoint travels (the stopping distance) can be obtained simply by integrating (5.10):

$$\Delta x_{\text{stop}} = \frac{z_H^2}{z_*}\frac{\sqrt{\pi}\,\Gamma(\frac{5}{4})}{\Gamma(\frac{3}{4})} - {}_2F_1\left(\frac{1}{4},\frac{1}{2},\frac{5}{4},\frac{z_*^4}{z_H^4}\right) z_H\,, \tag{5.13}$$

where ${}_2F_1$ is the ordinary hypergeometric function. In the limit $z_* \ll z_H$, the last term can be neglected, and we can easily relate Δx_{stop} to E_* through the common UV scale z_*:

$$\Delta x_{\text{stop}} = \left[\frac{2^{1/3}}{\sqrt{\pi}}\frac{\Gamma\left(\frac{5}{4}\right)}{\Gamma\left(\frac{3}{4}\right)}\right]\frac{1}{T}\left(\frac{E_*}{\sqrt{\lambda}T}\right)^{1/3}\,, \tag{5.14}$$

where we used $z_H = 1/(\pi T)$. The numerical factor in the brackets is ≈ 0.526, precisely the value of $\mathcal{C}$ in (5.1), obtained numerically in [300].

5.1.4 Stopping distance in Gauss-Bonnet gravity

The success of this simple analytical procedure of [35] immediately prompts for applications of these ideas in calculating the stopping distance in more general geometries. An interesting and analytically tractable case is the case of AdS_5 with higher derivative R^2 corrections, described in Section 3.4.3, which we model with the Gauss-Bonnet term (3.57). This results in an analytical black hole solution (3.59), parametrized by a small dimensionless λ_{GB}, eq. (3.58).

As before, the idea is to compute the energy of a trailing string hanging from a small z_*, discard the IR-divergent drag force term and take the UV limit $z_* \ll z_H$. Then we need to compute the range of the null geodesic that starts at that z_* parallel to the boundary and again take the $z_* \ll z_H$ limit. All this is done perturbatively in λ_{GB}, keeping only the linear terms (although it is straightforward to go to higher orders). Finally, this range and the "renormalized" energy are related via z_* that folds into the final answer (5.20).

If we define $\tau \equiv at$ (where a is defined in (3.60)), the AdS_5-GB geometry (3.59) has the same form as AdS_5-Schwarzschild (5.2) with $f(z)$ replaced by $f_{GB}(z)$ and we can directly apply the formula (4.26) for the regularized energy of a trailing string. After multiplying this by a to get the energy conjugated to Killing time t, we arrive at:

$$E_* = \frac{L^2}{2\pi\alpha'}\frac{a}{z_*^2}\int\limits_{z_*}^{z_H} dz \frac{1}{z^2}\left[\frac{z^4 f_{GB}(z_*) - z_*^4 f_{GB}(z)}{f_{GB}(z_*) - f_{GB}(z)}\right]^{1/2} . \tag{5.15}$$

Note that in the case of AdS_5-Schwarzschild, the term in the brackets is equal to z_H^4, yielding a simple $\propto 1/z^2$ integrand.

Defining $E_* = \int \varepsilon dz$, we can plug in the expressions for a and f_{GB} (3.60), express L^2/α' and z_H via the coupling λ and the temperature T using (3.62) and (3.63), respectively, and finally expand in λ_{GB}:

$$\varepsilon = \frac{\sqrt{\lambda}}{2\pi^3 T^2 z^2 z_*^2}\left[1-\left(1+\frac{1}{2}\pi^8 T^8 z^4 z_*^4 - \frac{1}{2}\pi^4 T^4\left(z^4+z_*^4\right)\right)\lambda_{GB} + \mathcal{O}\left(\lambda_{GB}^2\right)\right]. \quad (5.16)$$

Since we are interested in the $z_* \ll z_H$ limit, only the first term in the $\mathcal{O}(\lambda_{GB})$ order matters and we easily get:

$$E_* = \frac{\sqrt{\lambda}}{2\pi^3 T^2}\frac{1}{z_*^3}(1-\lambda_{GB})\,. \quad (5.17)$$

Now we do the same with the null geodesic, which has the same form as (5.10):

$$\begin{aligned}\frac{dx_{\text{geo}}}{dz} &= \frac{1}{\sqrt{f_{GB}(z_*)-f_{GB}(z)}}\\ &= \frac{1}{\pi^2 T^2\sqrt{z^4-z_*^4}}\left[1-\left(2-\frac{1}{2}\pi^4 T^4\left(z^4+z_*^4\right)\right)\lambda_{GB}+\mathcal{O}\left(\lambda_{GB}^2\right)\right]. \quad (5.18)\end{aligned}$$

Again, we integrate, take the $z_* \ll z_H$ limit, and end up with

$$\Delta x = \frac{\Gamma\left(\frac{5}{4}\right)}{\pi^{3/2}T^2\Gamma\left(\frac{3}{4}\right)}\frac{1}{z_*}\left(1-2\lambda_{GB}\right)\,. \quad (5.19)$$

We can now express z_* in terms of E_* from (5.17), plug it in (5.19) and expand in λ_{GB} yielding finally:

$$\Delta x = \left[\frac{2^{1/3}}{\sqrt{\pi}}\frac{\Gamma\left(\frac{5}{4}\right)}{\Gamma\left(\frac{3}{4}\right)}\right]\frac{1}{T}\left(\frac{E_*}{\sqrt{\lambda}T}\right)^{1/3}\left(1-\frac{5}{3}\lambda_{GB}\right)\,. \quad (5.20)$$

This formula can be confirmed numerically, by generating string solutions for a variety of initial conditions and observing how they asymptote to the limit in (5.20), see Fig. 5.3.

For a maximally negative $\lambda_{GB} = -7/36$, formula (5.20) gives about a 30% higher stopping distance than in the case with no higher derivative Gauss-Bonnet corrections. Although this may not seem like a lot, because of the $E^{1/3}$ scaling, this means that now jets that have about 2.5 times smaller energy stop at the same distance. As discussed in

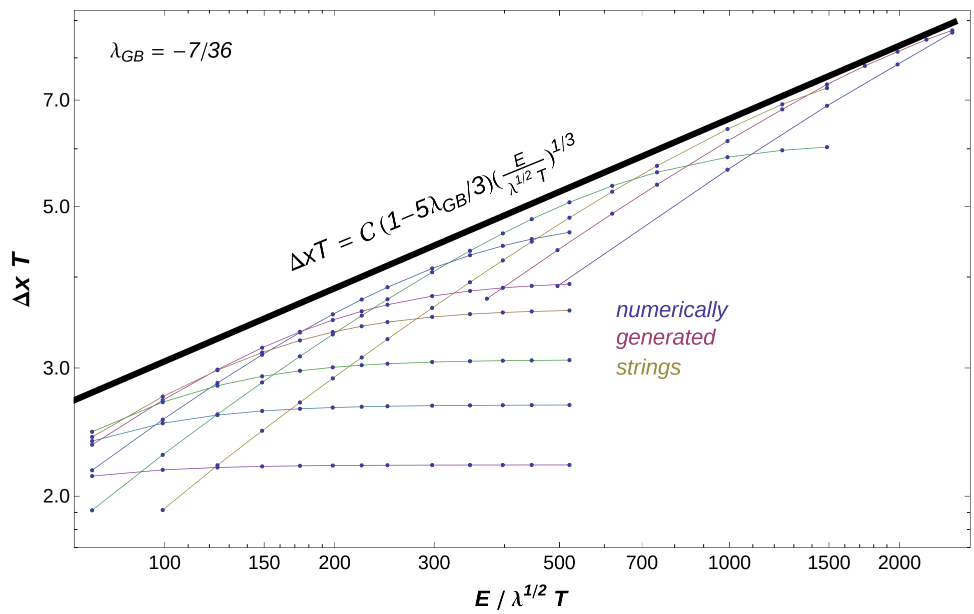

Figure 5.3: *Stopping distance Δx of numerically generated falling strings (using the procedure from Section 5.2) as a function of the string energy E for a variety of initial conditions (dots connected by lines are in the same family of initial conditions) in the AdS_5-GB geometry (3.59) with $\lambda_{GB} = -7/36$. The black line indicates the maximum stopping distance (5.20).*

Section 3.4.3, negative values of λ_{GB} increase η/s, in some sense indicating a less strongly coupled system, which nicely resonates with the result (5.20) which indicates reduced jet quenching.

Another straightforward application of the ideas from Section 5.1.3 is to the non-conformal holographic model of Section 3.5.2: it would be interesting to inspect how the overall coefficient of the stopping distance, and perhaps even the scaling power, gets modified by the trace anomaly.

5.2 Numerical string solutions

In this section we will describe a tractable numerical procedure for solving the classical string equations of motion, that was originally suggested in [23] and later on used in [300] to calculate stopping distances for a variety of falling string solutions and obtain the numerical factor $\mathcal{C}$ in (5.1).

We will work in the AdS_5-Schwarzschild geometry (5.2), but this method can be easily extended to more general geometries, such as (3.68). The main problem in solving the falling string equations of motion is that, as the time evolves, parts of the string approach the horizon, which in the coordinate system of (5.2) will naturally cause numerical instabilities. The alternative is of course to work in a coordinate system where the metric is regular at the horizon, such as the Eddington-Finkelstein coordinates, but this has its own downsides and will be addressed in the next chapter. The idea of [23] was to choose the worldsheet metric h_{ab} to have the following form:

$$h_{ab} = \text{diag}(-s(\sigma,\tau), 1/s(\sigma,\tau))\,, \tag{5.21}$$

where the first entry is the $\tau\tau$ component and the second is the $\sigma\sigma$ component. This is a simple generalization of the usual conformal gauge, where the "stretching function" $s(\sigma,\tau)$ is chosen in such a way that the numerical computation is well behaved, as we will see soon. Choosing the worldsheet metric in this way represents merely a choice of parametrization on the worldsheet (i.e. a choice of gauge) and the constraint equations (3.129) are there to ensure that the embedding functions change accordingly. Explicitly, the constraint equations are

$$G_{\mu\nu}(X^\mu)'\dot{X}^\nu \;=\; 0\,, \tag{5.22}$$

$$G_{\mu\nu}\left(\dot{X}^\mu\dot{X}^\nu + s^2(X^\mu)'(X^\nu)'\right) \;=\; 0\,, \tag{5.23}$$

where we use the notation of Section 3.6, where dots denote differentiation with respect to the τ coordinate and primes the differentiation with respect to the σ coordinate.

As usual, we assume that the string is moving in the $x-z$ plane and, following [300], choose the "pointlike" initial conditions, where the string is initially a point at some radial coordinate z_c:

$$t(\sigma,0)=0, \quad x(\sigma,0)=0, \quad z(\sigma,0)=z_c\,. \tag{5.24}$$

Then $(X^\mu)'(\sigma,0)=0$, which automatically satisfies the first constraint equation (5.22), and now we have to choose an initial velocity profile (i.e. functions $\dot{X}^\mu(\sigma,0)$) such that the second constraint equation $G_{\mu\nu}\dot{X}^\mu\dot{X}^\nu=0$ is satisfied, as well as the free string endpoint boundary conditions (3.138), which in this case are just $(X^\mu)'=0$ at $\sigma=0,\pi$. Following [300], we choose

$$\dot{x}(\sigma,0) \;=\; Az_c\cos(\sigma)\,, \tag{5.25}$$

$$\dot{z}(\sigma,0) \;=\; z_c\sqrt{f(z_c)}(1-\cos(2\sigma))\,, \tag{5.26}$$

where A is a constant determining the amplitude of the velocity profile. Then $\dot{t}(\sigma,0)$ is determined by the constraint equation (5.23):

$$\dot{t}(\sigma,0)=\frac{z_c}{\sqrt{f(z_c)}}\sqrt{A^2\cos^2(\sigma)+(1-\cos(2\sigma))^2}\,. \tag{5.27}$$

For this set of initial conditions we choose the following stretching function:

$$s(\sigma,\tau) = s(z) = \frac{1 - z/z_H}{1 - z_c/z_H}\left(\frac{z_c}{z}\right)^2 . \tag{5.28}$$

In particular, its most important feature, as announced earlier, is that it matches the singularity of the G_{tt} metric component near the horizon, so that the embedding functions can remain well behaved as parts of the string approach the horizon.

As discussed in Section 5.1.1, the physical motivation behind the choice of initial conditions (5.24) is that they should resemble a quark-antiquark pair produced by some local current, with the quarks having enough energy to move away in the opposite directions. The velocity profiles (5.25) and (5.26) are one of the simplest profiles that satisfy the open string endpoint boundary conditions and uniformly evolve the string towards the black hole (which should resemble the process of thermalization of the interaction energy described by the body of the string) with the endpoints moving away in the opposite directions. The energy density profile in the boundary theory dual to such a string evolution will have two peaks concentrated around the endpoints, and a smooth, U-shaped profile between the peaks that will slowly decrease in magnitude.

With this procedure, we can now solve the string equations of motion (3.132) numerically, obtain the embedding functions $X^\mu(\sigma,\tau)$ and then plot them in the $x-z$ plane at fixed times t. An example of such a numerically generated string solution is shown in Fig. 5.4, where we compare the string shapes at several fixed times t in the AdS_5-Schwarzschild background (5.2) and in the non-conformal model of Section 3.5.2, with the analogous initial conditions.

Although it may seem that the endpoints of the string propagating in the non-conformal background travel somewhat further than the endpoints of the string in the conformal background, a direct comparison between the string profiles in the two back-

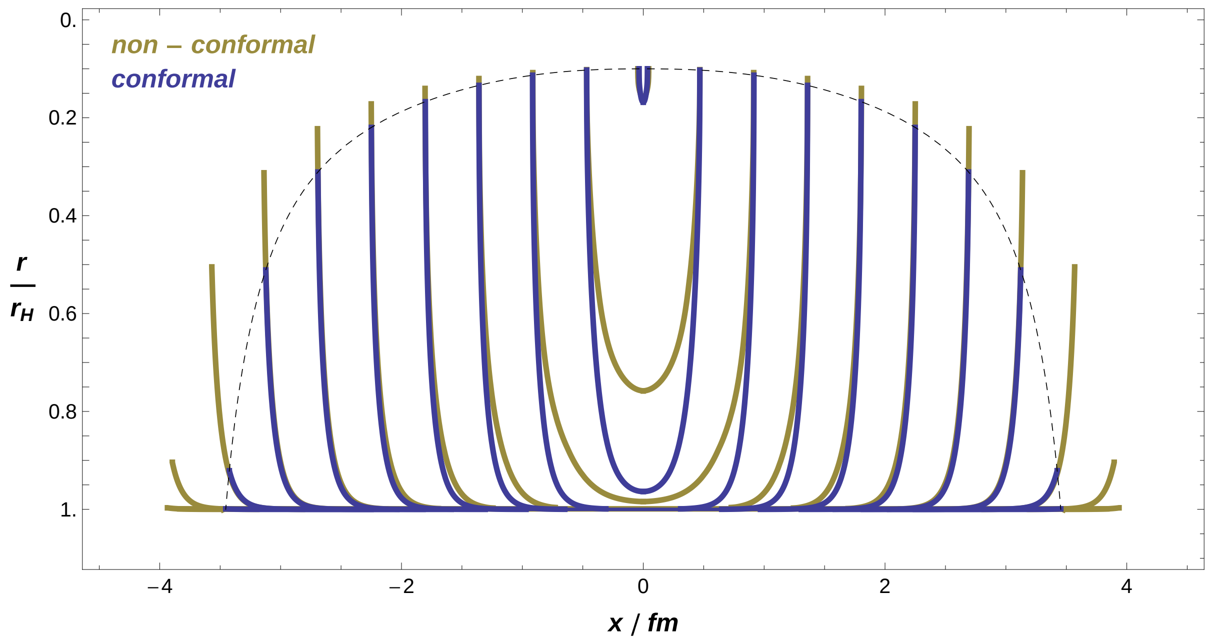

Figure 5.4: *Comparison of the falling string shapes in the $x-r$ plane at different fixed times in the non-conformal model of Section 3.5.2 and the conformal AdS_5-Schwarzschild background (5.2) (here $r \equiv z$). The initial conditions were chosen so that in both cases the string was created at the same relative radial coordinate r_c/r_H =0.1, and the constants A in the velocity profiles (5.25) of the two strings were tuned so that in both cases the initial energy of the string was $E/\sqrt{\lambda}$ =50 GeV. The temperature was T =180 MeV (T_c is at 171 MeV), and in the non-conformal model the quantities were translated to units of GeV and fm using the procedure described in Section 3.5.5. Dashed line indicates, for clarity, the motion of the endpoints of the conformal string.*

grounds is not without caveats, due to differences in “translating” the quantities to units of GeV and fm (see Section 3.5.5) in the two cases. A more direct answer to this should be provided once the method of Section 5.1.3 is applied to find the maximum stopping distance in the non-conformal background.

5.3 Instantaneous energy loss

From a phenomenological perspective, the maximum stopping distance (5.1) is an interesting quantity which can be used as a guideline on how strong the light quark jet quenching is. However, in order to calculate observables such as the nuclear modification factor R_{AA}, we need to know the instantaneous energy loss dE/dx as a function of temperature, energy and distance. Details of the instantaneous energy loss in non-stationary string configurations such as the falling strings cannot be extracted from the *maximum* stopping distance (5.1), and we need to analyze the worldsheet currents that govern the spacetime momentum transport on the string, which is the topic of this section.

In addition to this obvious incentive to calculate the holographic R_{AA}, the additional motivation is provided by the so-called "high-p_T v_2 problem", an apparent inability of the various pQCD models to simultaneously match the light hadron central R_{AA} data and the elliptic flow v_2 at high transverse momenta (see e.g. [122, 307]). A standard pQCD result for radiative energy loss of light quarks (eqns. (2.28) and (2.29)) has a linear path length dependence, i.e. $dE/dx \propto x$. The general tendency of the pQCD models is to underpredict the v_2 data at high p_T (once the model is constrained by fitting the central R_{AA} data), signaling that one may need a stronger path length dependence than the linear one, and therefore perhaps hinting that there may be some strong coupling effects at play. In fact, an extensive analysis [308, 309] shows that the data seems to favor a $dE/dx \propto x^2$ path length dependence. The "*AdS*-inspired" x^2 model of [308] was based on results of [310, 311], where it was found that the path length dependence of energetic heavy quarks should have this form. In addition to this, some of the early numerical work on energy loss in falling strings [300] seemed to suggest a similar length dependence for light quarks.

5.3.1 Defining the instantaneous energy loss

The heavy quark energy loss from Section 4.1.2 was particularly simple to calculate: it was obtained for stationary trailing strings, and the simplicity of that ansatz resulted in a constant energy flow down the string, given by a concise analytical formula (4.15). In the case of light quarks we don't have this luxury: falling strings are explicitly time-dependent, non-stationary string configurations, and in order to understand the details of energy loss in such environments, one needs to carefully analyze the worldsheet currents.

In this section we will follow [33], in which, based on the analysis of the worldsheet currents from Section 3.6.3, we suggest a definition of the instantaneous energy loss, in which the details of the geometry on the worldsheet become important. This definition originates from [300], but a more careful analysis of the worldsheet currents will identify an additional term that was originally omitted. This will lead to potentially important phenomenological consequences for light quark energy loss: as we will see, the instantaneous energy loss will not exhibit a well pronounced Bragg-like peak at late times, as previously believed.

The instantaneous (differential) energy loss, can be obtained, as before, by letting $t_1 \to t_2$ in (3.150):

$$\frac{dp_\mu}{dt}(\sigma, t) = -\sqrt{-h}\, \Pi^\sigma_\mu(\sigma, t)\,. \tag{5.29}$$

This quantity gives the flow of the μ component of the spacetime momentum along the string at position σ at time t. Of course, this is the well known expression for energy flow used in the case of trailing strings, but the analysis of Section 3.6.3 gave us more insight into its validity; namely, it pointed out that (5.29) is valid only for constant-σ curves.

Consider the following coordinate transformation on the worldsheet:

$$(\sigma, t) \to (\tilde{\sigma}(\sigma, t), t)\,, \tag{5.30}$$

i.e. we stay in the static gauge and only change the string parametrization using some well defined function $\tilde{\sigma}(\sigma, t)$. We can then again apply (3.150) and see that, in this coordinate system, for a constant-$\tilde{\sigma}$ curve, we also have

$$\frac{d\tilde{p}_\mu}{dt}(\tilde{\sigma}, t) = -\sqrt{-\tilde{h}}\tilde{\Pi}^\sigma_\mu(\tilde{\sigma}, t)\,. \tag{5.31}$$

We can relate these to the corresponding quantities in the (σ, t) coordinate system by using standard coordinate transformations (3.152) and (3.153), which for this particular transformation are given by

$$\begin{aligned} \sqrt{-\tilde{h}} &= \frac{\sqrt{-h}}{|\tilde{\sigma}'|}\,, & (5.32) \\ \tilde{\Pi}^\sigma_\mu &= \tilde{\sigma}'\Pi^\sigma_\mu + \dot{\tilde{\sigma}}\Pi^t_\mu\,, & (5.33) \end{aligned}$$

Plugging this in (5.31) we have

$$\frac{d\tilde{p}_\mu}{dt}(\tilde{\sigma}, t) = \mathrm{sgn}(\tilde{\sigma}')\left[\frac{dp_\mu}{dt} - \sqrt{-h}\frac{\dot{\tilde{\sigma}}}{\tilde{\sigma}'}\Pi^t_\mu\right]_{(\sigma(\tilde{\sigma},t),t)}\,. \tag{5.34}$$

If we want to evaluate the energy loss at different times, we have to make a choice of what points on the string (at different times) we are going to evaluate the currents in (5.34) on. We choose that these points on the string have a constant $\tilde{\sigma}$ coordinate at all times (i.e. this is how we define the, so far, arbitrary $\tilde{\sigma}$-parametrization), while in the σ-parametrization, these points are defined by a function $\sigma_\kappa(t)$. The physical motivation behind such a choice is to say that, at some time t, the jet is defined as the part of the string between the endpoint $\sigma = 0$ and some $\sigma = \sigma_\kappa(t)$. In [300], this choice was such that the spatial distance (i.e. in the x-direction) between the string endpoint and those points was of the order $\sim 1/(\pi T)$. This will be discussed more in Section 5.3.2.

Now, since $\tilde{\sigma}(\sigma_\kappa(t), t)$ is constant at all times, we have

$$\frac{d\tilde{\sigma}}{dt} = 0 = \left[\tilde{\sigma}' \frac{d\sigma_\kappa(t)}{dt} + \dot{\tilde{\sigma}}\right]_{\sigma=\sigma_\kappa(t)} . \tag{5.35}$$

Plugging this in (5.34) we arrive at

$$\frac{d\tilde{p}_\mu}{dt}(\tilde{\sigma}, t) = \mathrm{sgn}(\tilde{\sigma}') \left[\frac{dp_\mu}{dt} + \sqrt{-h}\,\Pi^t_\mu \frac{d\sigma_\kappa}{dt}\right]_{(\sigma_\kappa(t),t)} . \tag{5.36}$$

This is the central result of this section. This formula gives the appropriate expression for energy loss in terms of quantities expressed in any parametrization (σ, t) in which the function $\sigma_\kappa(t)$ is known. Here we were making use of the simple expression for the energy loss in the special $\tilde{\sigma}$-parametrization (in which the coordinate of the points on which we evaluate the currents is constant), but in using this formula one does not need to know what that parametrization really is, since the right hand side of (5.36) is given only in terms of quantities in the (σ, t) parametrization.

Now, the argument for calling some quantity dE/dt the energy loss comes from the idea that, when integrated over some period of time Δt, this integral should give the amount of energy that the jet (that is, some predefined part of the string) has lost over some period of time Δt:

$$\Delta E(\Delta t) = \int_{\Delta t} dt \frac{dE}{dt} . \tag{5.37}$$

Identifying dE/dt with $-dp_0/dt$ in the $(\sigma = z, t)$ parametrization (essentially just the Π^z_t component of the worldsheet current), as implied in [300], means that this amount of energy lost should be given by

$$\Delta E_{\mathrm{app}}(\Delta t) = -\int_{\Delta t} dt \frac{dp_0}{dt}(z_\kappa(t), t) , \tag{5.38}$$

where the subscript *app* stands for "apparent" and where $z_\kappa(t)$ corresponds to the points at some fixed spatial distance $\sim 1/(\pi T)$ from the string endpoint at all times. However, this formula (i.e. that the energy loss is given only by the σ component of the worldsheet current), as we showed before, is valid only if one uses a constant-σ curve, which is not the case in this parametrization. Then, in order to be able to use that simple expression, we need to find a parametrization $\tilde{\sigma}$ in which the coordinates of the points given by $z_\kappa(t)$ are constant. In this case, the energy lost would indeed be

$$\Delta E(\Delta t) = -\int\limits_{\Delta t} dt \frac{d\tilde{p}_0}{dt}(\tilde{\sigma}, t)\,. \tag{5.39}$$

The difference between this and the apparent energy loss is then explicitly given by (5.36):

$$\Delta E(\Delta t) = \Delta E_{\text{app}}(\Delta t) - \int\limits_{\Delta t} dt \left[\sqrt{-h}\,\Pi^t_0 \frac{dz_\kappa}{dt}\right]_{(z_\kappa(t),t)}\,. \tag{5.40}$$

In the following section we will numerically examine the effect of this correction in the case of falling strings in AdS_5-Schwarzschild.

One should point out that this correction does not affect the result for the maximum stopping distance (5.1), since that expression was derived from purely kinematical considerations, by analyzing the equations of motion and relating the total energy of the string to the approximate endpoint motion described by the null geodesics. In other words, the worldsheet currents (actually, their identification with the energy loss) were not used in that derivation.

We should also point out that this correction does not affect the well established drag force results of [22] and [23], since the trailing string is a stationary string configuration where $d\sigma_\kappa/dt = 0$.

5.3.2 Numerical evaluation

We will use the numerical method from Section 5.2 in order to solve the string equations of motion numerically and obtain the embedding functions $X^\mu(\sigma,\tau)$. Then, to compute the actual energy loss, we simply use the formula (5.36) with the worldsheet fluxes expressed in the static gauge (σ, t) using (3.152) and (3.153):

$$\frac{dE}{dt} = \frac{L^2}{2\pi\alpha'}\left[\frac{f}{z^2}\frac{1}{|\dot{t}|}\left(st' - \frac{d\sigma_\kappa}{dt}\left(s\,(t')^2 - \frac{\dot{t}^2}{s}\right)\right)\right]_{(\sigma_\kappa(t),t)} . \tag{5.41}$$

The apparent energy loss is given by (5.29) in the (z,t) parametrization, so we need to use formulas (3.152) and (3.153) again, giving

$$\left(\frac{dE}{dt}\right)_{\text{app}} = \frac{L^2}{2\pi\alpha'}\left[\frac{f}{z^2}\frac{sz't' - \frac{1}{s}\dot{z}\dot{t}}{\left|z'\dot{t} - \dot{z}t'\right|}\right]_{(\sigma_\kappa(t),t)} . \tag{5.42}$$

The results are shown in Fig. 5.5. One can clearly see that the correction, derived in (5.36), becomes especially important at late times, when dz_κ/dt grows, as the relevant parts of the string start falling towards the horizon faster and faster. More generally, the importance of the correction in (5.36) depends on how fast the coordinates of these points change in time in that parametrization, i.e. on the magnitude of the $d\sigma_\kappa(t)/dt$ function. In the example of falling strings, we have seen that this correction becomes especially important at late times and substantially decreases the magnitude of the apparent Bragg-like peak at late times.

We should note that the energy of the part of the string between $\sigma = 0$ and $\sigma = \sigma_\kappa(t_{\text{th}})$ at the thermalization time t_{th} (when the string endpoint stops moving in the x-direction), is generally nonzero. This means that the area under the solid blue curve in Fig. 5.5 is always less than 1, and represents the relative amount of energy lost from the part of the string defined by $\sigma_\kappa(t)$, as evident from (3.150). On the other hand, the area under

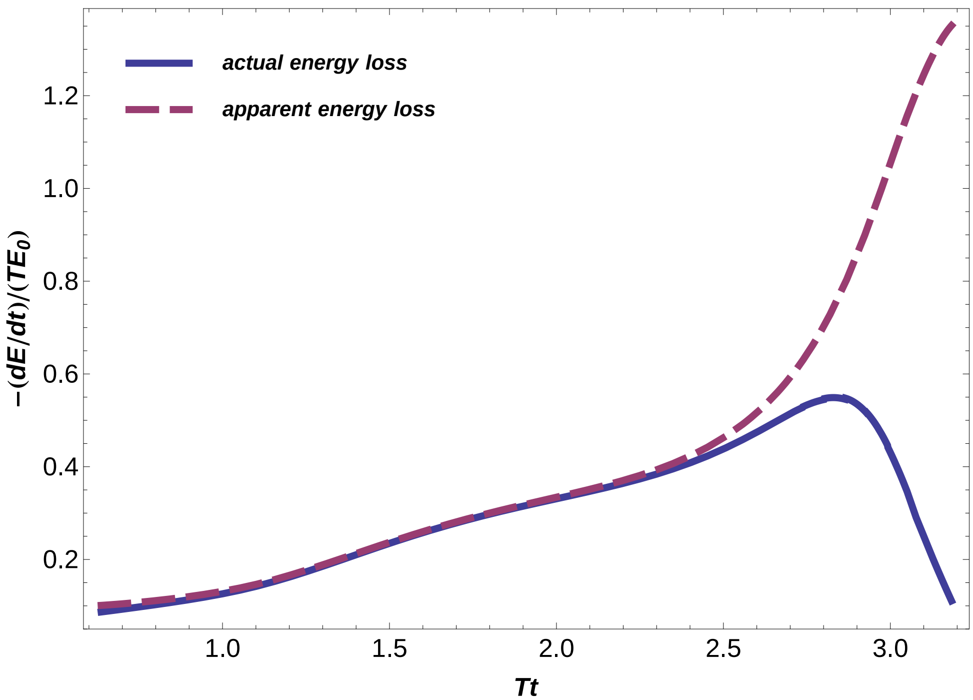

Figure 5.5: *Comparison of the (normalized) instantaneous energy loss as a function of time with and without the correction in (5.36). The dashed red curve shows the apparent energy loss $(dE/dt)_{app}$ in the radial $\sigma = z$ parametrization (Eq. (5.42)), while the solid blue curve is the actual energy loss dE/dt, as given by (5.41). The energy loss was evaluated at points at a fixed spatial distance from the string endpoint, chosen in such a way that the correction in (5.36) appears clearly. The normalization constant E_0 is the energy of half of the string and $T = 1/(\pi z_H)$ is the temperature. The numerical parameters used are A =50 and $z_c = z_H/10$.*

the dashed red curve is not known *a priori*, and could be < 1 or > 1, depending on the magnitude of the correction in (5.36). Specifically, if we decrease the spatial distance from the endpoint at which we evaluate the energy loss (keeping the same initial conditions), the area under the red curve increases and eventually becomes > 1 (in the figure it is already slightly higher than 1).

We should also note that the “jet definition” used here was first considered in [300], where the jet was defined as the part of the string within a certain Δx distance from the endpoint. As discussed in [300], the physical motivation behind this choice is that the baryon density in the boundary theory should be well localized on scales of order $\Delta x \sim 1/\pi T$. On the gravity side, this spatial distance corresponds to the "upright" part of the string (see e.g. Fig. 5.4), and, as discussed in Section 5.1.1, it makes sense to identify this part of the string as describing the energetic jet, while the part of the string that is lying flat on the horizon represents the energy deposited to the medium. Of course, there is no clear distinction between the two contributions and other jet definitions may be more appropriate. Finally, we should also note that, since parts of the string we evaluate the worldsheet fluxes on can be far away from the boundary, the retardation effects may be important and a full bulk-to-boundary problem needs to be solved to see precisely how the field theory excitation is losing energy.

5.3.3 Linear path dependence

An immediate observation in Fig. 5.5 is that the energy loss seems to be approximately linear in time, $dE/dt \sim t$, until very late times when the endpoint falls into the horizon. In fact, numerical studies suggest that, although the early time behavior of the energy loss is susceptible to the initial conditions and "jet definitions", the linearity of it seems to be a remarkably robust feature, as illustrated in Fig. 5.6, where these two parameters have been varied around the solution from Fig. 5.5. In this section, using the analytical methods of [35], reviewed in Section 5.1.3, we will provide additional analytical support to this numerical observation [36].

As noted before, our main point in [35] was to recognize that the energy of an energetic falling string can be well approximated by the UV part of the energy of a trailing string without the drag force term, whose endpoint is moving at the same radial height at the

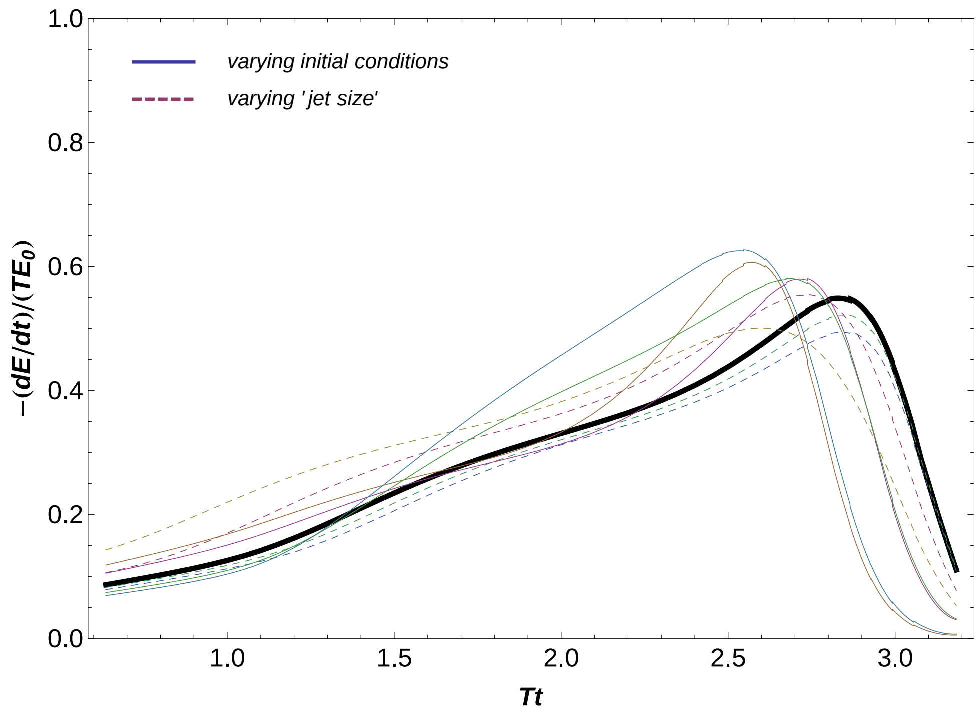

Figure 5.6: *Instantaneous energy loss in the falling string model as a function of time, for several initial conditions and "jet sizes". The black curve is the solution from Fig. 5.5, the solid curves represent solutions where the jet definition was kept the same, but the initial conditions were varied (constrained to give the same energy), and the dashed curves represent solutions where the initial conditions were kept the same, but the distance from the endpoint at which the energy loss is evaluated ("jet size") was varied.*

local speed of light, eq. (5.12):

$$E_* = \frac{\sqrt{\lambda}}{2\pi}\frac{1}{z_*}\frac{1}{\sqrt{1-v^2}}\,, \tag{5.43}$$

for a falling string in AdS_5-Schwarzschild whose endpoint is at $z = z_*$ and is moving at the local speed of light v in the $x-$direction. Using this result, together with the fact that the endpoints approximately follow null geodesics whose minimum radial distance to the boundary is z_*, resulted in an analytical expression (5.14) for the stopping distance of light quarks. As noted earlier, the endpoints stay close to $z_* \ll z_H$ for a long time compared to z_* and from the null geodesic equation (5.10) we can easily get that in this regime

$$\frac{dz_{\text{geo}}}{dx} = \frac{2z_*^3}{z_H^4}x\left[1 + \mathcal{O}\left(\frac{x^2 z_*^2}{z_H^4}\right)\right], \tag{5.44}$$

where, for simplicity, we assumed that at $x = 0$ the endpoint was at $z = z_*$. To get the energy loss, we can simply take the derivative of (5.43) where now z and v are slowly changing as the endpoint is falling down:

$$\frac{dE}{dx} = \frac{\sqrt{\lambda}}{2\pi}\frac{d}{dz}\left(\frac{1}{z}\frac{1}{\sqrt{1-v(z)^2}}\right)\frac{dz_{\text{geo}}}{dx}. \tag{5.45}$$

Again, we are interested in the regime where the endpoints stay close to z_*, which lasts arbitrarily long in the small z_* (high energy) limit. In this case, the leading, $z-$independent term in the expansion in $(z - z_*)$ of the term in front of dz_{geo}/dx is finite and non-zero, which means that the only $x-$dependence in (5.45) comes from (5.44), hence showing that the energy loss is linear[4] in x to the leading order in small z_*, and thus reaffirming the numerical indications from Fig. 5.6.

We should note that, although one could argue that the linearity observed in the numerical simulations depended on the way we defined the "jet" (i.e. as a part of the string within some distance $\Delta x \sim 1/(\pi T)$ from the endpoint), the analysis in this section did not depend on this definition, and hence suggests that this linearity should indeed be a more universal feature.

[4]In a recent work [312], a different path length dependence of the instantaneous energy loss of light quarks was obtained by studying a holographic version of the "brick problem". The finite brick of $\mathcal{N} = 4$ SYM plasma was modeled by a blackening function $f(z)$ with a theta function: inside the brick, it was given by its usual expression in AdS_5-Schwarzschild, while outside (in the vacuum) it was equal to unity.

5.4 Phenomenological model of light quark energy loss

Now that we have a more clear understanding of the instantaneous energy loss of light quarks in AdS/CFT, the next natural step is to try to compute the nuclear modification factor R_{AA}. However, in order to do this, one needs to have a definite temperature T, initial energy E_0 and path length x dependence of the energy loss, which at this point we do not have. Motivated by [313], we will present a first attempt [34] at a simple phenomenological modeling of the energy loss of light quarks, based on what we have learned so far.

As we have shown in Sections 5.3.2 and 5.3.3, the energy loss has an approximately linear path dependence in the phenomenologically relevant range and hence we can write:

$$\frac{dE}{dx}(E_0, T, x) = -c(E_0, T)x\Theta\left[\Delta x_{\text{stop}}(E_0, T) - x\right] , \tag{5.46}$$

where Δx_{stop} is the stopping distance and Θ is the step function. The initial energy and the additional temperature dependence have been packed into an unknown function $c(E_0, T)$ which can be determined by assuming that the stopping distance Δx_{stop} can be estimated by the maximum stopping distance (5.1). Therefore, from the requirement that

$$\int_0^{\Delta x_{\text{max}}} dx \frac{dE}{dx}(E_0, T, x) = -E_0 \, , \tag{5.47}$$

we can determine the unknown function $c(E_0, T)$ and obtain:

$$\frac{dE}{dx} = -\chi E_0^{1/3} x T^{8/3} \, , \tag{5.48}$$

where we have defined an effective coupling

$$\chi \equiv 2\lambda^{1/3}/\mathcal{C}^2\,, \tag{5.49}$$

which determines the overall magnitude of the energy loss and is the only free parameter in this formula. For $\mathcal{C} \approx 0.526$ and a critically small $\lambda = 1$, we have $\chi \approx 8$.

An interesting thing to note is that formula (5.48) bears a surprising similarity to the standard pQCD result for radiative energy loss of light quarks (eqns. (2.28) and (2.29)), in terms of the path length dependence and even the energy dependence ($\log E$ and $E^{1/3}$ differ numerically by only a few percent up to $\sim$ 200 GeV). One may even entertain a tempting idea that the phenomenon of light quark jet quenching may have a roughly universal qualitative character, regardless of whether one deals with a strongly or a weakly coupled medium.

With formula (5.48), we can now compute the nuclear modification factor R_{AA} of light quarks at the LHC following the procedure described in Sections 1.3 and 1.4. The results are compared to the LHC light hadron[5] suppression data from CMS [84] in Fig. 5.7, where we see that the value of $\chi = 8$ (dashed green) gives an R_{AA} of a very low magnitude, indicating strong quenching.

This strong quenching may be partially resolved by including the higher derivative Gauss-Bonnet corrections, as we saw in Section 5.1.4: there we showed that including these corrections increases the stopping distance for $\lambda_{GB} < 0$, i.e. one has effectively $\mathcal{C} \to \mathcal{C}(1 - 5\lambda_{GB}/3)$, which, for a maximally negative λ_{GB} of $-7/36$, gives about a 30% increase. And as we can see from (5.49), this effect will significantly reduce the overall

[5] At this point it is perhaps premature to compare our results to the suppression data for pions, as we need to take into account the gluons, and then together with quarks, fragment them into pions. This will be discussed in the next chapter in more detail, but we should note that, having in mind that these two effects have opposite tendencies (i.e. including gluons brings the R_{AA} down and including fragmentation effects brings it up) and that we are, for now, interested in the ballpark comparisons, the light hadron suppression data serve as a good reference point.

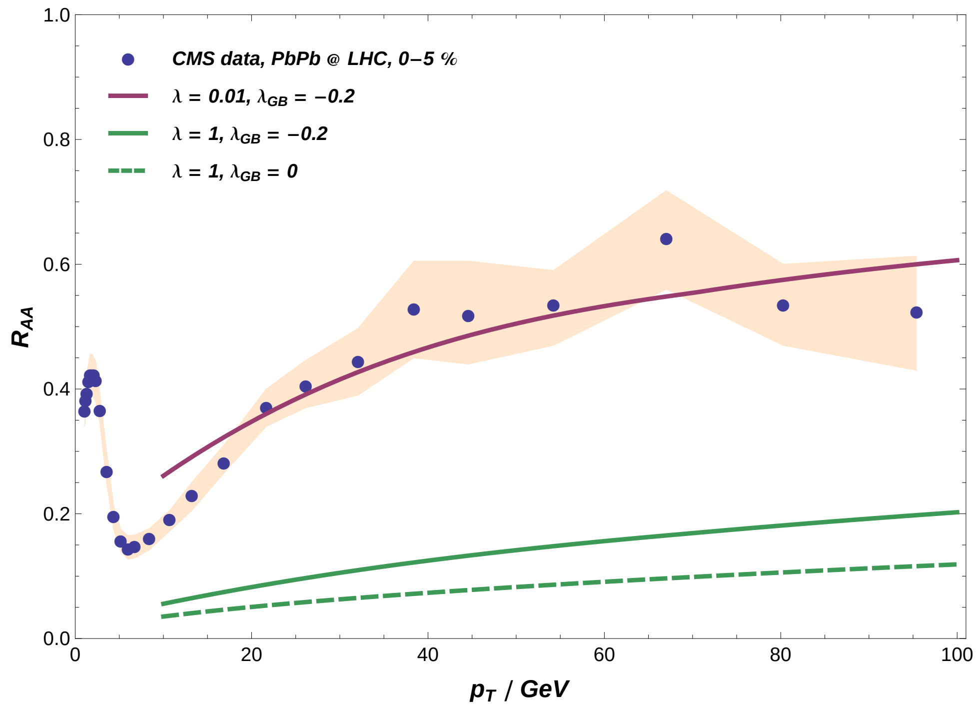

Figure 5.7: *Nuclear modification factor R_{AA} for light quarks as a function of the final parton energy E for several different values of the effective coupling χ, compared to the LHC light hadron suppression data from CMS [84]. The dashed curve is the calculation without the Gauss-Bonnet corrections, while the solid curves include them. The plasma formation time was τ_0 =1 fm/c, the impact parameter was b =3 fm, and the freeze-out temperature was T_{fo} =150 MeV.*

magnitude of the energy loss[6]. As we can see from Fig. 5.7, this has an effect of increasing the magnitude of R_{AA} by almost 100% (solid green) but we are still far from the data.

We could now take an even more phenomenological approach and consider χ as a free fitting parameter, and simply ask what value is necessary to bring our calculations close to the data. As we can see from Fig. 5.7, one needs $\chi \approx 1$ (solid red curve), which, according to (5.49) (with the Gauss-Bonnet corrections included), translates into a very low $\lambda \approx 0.01$, that takes us far away from the supergravity limit of $\lambda \gg 1$, in which these

[6]Note that the path length dependence of the energy loss is still linear in the presence of the Gauss-Bonnet term, since, in the high energy limit, the endpoints are close to the boundary and the black hole solution in the presence of the Gauss-Bonnet term is asymptotically AdS.

calculations are valid. Similar values of λ were reached in a recent work [314], based on the light quark energy loss derived from studying the holographic "brick problem" [312].

This problem may have already been anticipated just by evaluating the stopping distance (5.1) for some typical values: for example, for a light quark of an initial energy of 100 GeV moving through a plasma at a temperature of 300 MeV, we get that this quark stops after only 2.4 fm for $\lambda = 1$, which is a very strong energy loss. Therefore, no matter how we model the energy loss, we are still bounded from above by the maximum stopping distance (5.1).

However, as we can see from Fig. 5.7, R_{AA} has the correct qualitative behavior as displayed by the CMS data, which suggests that the main problem could be simply in the low magnitude of R_{AA}, or, equivalently, too strong quenching, and we may need more radical ideas to bring the holographic calculations of light quark energy loss close to the data without leaving the regime of validity of the supergravity approximation. We propose such an approach in the next chapter.

Chapter 6

Finite endpoint momentum strings

In the previous chapter we saw how difficult it is to reconcile the model of light quark energy loss based on falling strings with the pion suppression data at the LHC. Motivated by this problem, in this chapter we present our perhaps most original contribution, and consider adding finite momentum to string endpoints [35] and inspect the phenomenological relevance of this idea via the "shooting strings" [36].

We start with Section 6.1, where we show how classical strings, both bosonic and supersymmetric, can have finite energy and momentum at their endpoints, and how that leads to simple motion of the endpoints, which now, in a general curved background, must exactly follow null geodesics. In Section 6.2 we consider motions of finite endpoint momentum strings in AdS_5-Schwarzschild, show how the endpoints can now travel a greater distance than has been possible for falling strings, and construct some explicit numerical solutions. Finally, in Section 6.3 we propose a natural scheme for determining the energy loss in this context, and show how an application of this formula in the "shooting string" limit to compute the nuclear modification factor of pions at RHIC and LHC reveals a rather good match with the data for reasonable choice of parameters.

6.1 Introducing finite momentum at string endpoints

As we saw in Section 3.6.2, the standard boundary conditions for open strings are that the endpoints move along lightlike trajectories which are always locally transverse to the string. However, one of the most obvious and well studied classical solutions of the open string explicitly violates these boundary conditions: namely the so-called "yo-yo" solution, where a string extended a length $2L$ along the x axis is released from rest at time 0 and shrinks to a point at time $t = L$, then re-expands to its original length and repeats.

The yo-yo solutions and generalizations of them were studied quite early [315] and play a prominent role in the Lund model [316], a successful phenomenological account of fragmentation. The Lund model is based on the notion of energetic quarks moving apart while linked by a (yo-yo) string; when the string coupling constant g_{str} vanishes, all that can happen is that the massless quark and anti-quark oscillate in a linear potential, while $g_{\text{str}} \neq 0$ allows for fragmentation events.

6.1.1 The yo-yo string

In order to see why we need the finite endpoint momentum in classical strings, in this section we analyze the well known classical yo-yo solution in details.

We will work in (2+1)-dimensional flat space $\mathbb{R}^{2,1}$, and choose the conformal gauge, $h_{ab} = \text{diag}\{-1, 1\}$. Let us consider strings centered at the origin and symmetrical with respect to reflections through the spatial origin. The standard way to see the yo-yo solution emerge is to start with an interpolation between the Regge (rigidly rotating string) and the yo-yo strings, which can be constructed through the following vectorvalued function $Y^\mu(\xi)$:

$$\frac{dY^\mu}{d\xi} = \begin{pmatrix} \sqrt{\ell_1^2 \sin^2 \xi + \ell_2^2 \cos^2 \xi} \\ \ell_1 \sin \xi \\ \ell_2 \cos \xi \end{pmatrix}, \quad Y^\mu(0) = \begin{pmatrix} 0 \\ -\ell_1 \\ 0 \end{pmatrix}. \tag{6.1}$$

One can easily check that Y^μ is a lightlike trajectory, but not a piecewise geodesic unless $\ell_1 = 0$ or $\ell_2 = 0$. In the conformal gauge in flat space the string (bulk) equations of motion (3.132) are simply $\partial_+ \partial_- X^\mu = 0$, where $\partial_\pm = \frac{1}{2}(\partial_\tau \pm \partial_\sigma)$. That means that the solution can be easily constructed from (6.1) as

$$X^\mu(\sigma, \tau) = \frac{1}{2} Y^\mu(\tau - \sigma) + \frac{1}{2} Y^\mu(\tau + \sigma). \tag{6.2}$$

See Fig. 6.1 for an illustration of this solution. It is also easy to see that X^μ satisfies the constraint equations (3.129), since in this gauge they are simply $\partial_+ X^\mu \partial_+ X_\mu = \partial_- X^\mu \partial_- X_\mu = 0$, and these are automatically satisfied because Y^μ is a lightlike trajectory. The lightlike character of Y^μ, together with the fact that $X^\mu(\tau, 0) = Y^\mu(\tau)$, allows us to prescribe that one of the endpoints is at $\sigma = 0$, while the other, for the same reasons, can be at $\sigma = \pi$. It can be explicitly checked that, with this choice of endpoint locations, the solution (6.2) obeys the standard open string boundary conditions (3.138), which in this case are simply $\partial_\sigma X^\mu = 0$. As discussed in Section 3.6.2, these boundary conditions imply that there is no endpoint momentum.

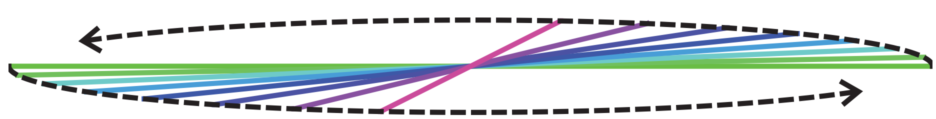

Figure 6.1: *Several snaphsots of the rotating string solution (6.2) at fixed τ, for $\ell_2 = \ell_1/10$.*

The case of $\ell_1 = \ell_2$ is the rigid rotating rod (i.e. the Regge string), while we will be interested in the yo-yo limit, where $\ell_2 \to 0$. The solution (6.2) then explicitly becomes

$$X^\mu = \begin{pmatrix} X^0(\sigma,\tau) \\ -\ell_1 \cos\tau\cos\sigma \\ 0 \end{pmatrix}, \tag{6.3}$$

where, for $\tau \in (0, \pi/2)$,

$$X^0 = \begin{cases} \ell_1(1-\cos\tau\cos\sigma) & \text{for } \sigma \in (0,\tau) \\ \ell_1 \sin\tau\sin\sigma & \text{for } \sigma \in (\tau, \pi-\tau) \\ \ell_1(1+\cos\tau\cos\sigma) & \text{for } \sigma \in (\pi-\tau, \pi)\,. \end{cases} \tag{6.4}$$

The central triangular region, $\sigma \in (\tau, \pi-\tau)$, maps to the bulk of the string, in a mapping which is conformal: that is, the metric in the space of worldsheet coordinates induced from the flat metric on spacetime takes the form

$$ds^2 = \Omega(\sigma,\tau)^2(-d\tau^2 + d\sigma^2)\,. \tag{6.5}$$

Outside the central triangular region, the mapping of worldsheet coordinates to spacetime is not one-to-one; instead, it collapses a whole region in the (σ,τ) plane into a lightlike interval in spacetime; see Fig. 6.2 for an illustration of this. The induced metric in the space of worldsheet coordinates vanishes identically, so the form (6.5) still holds, in a degenerate sense: Ω vanishes. Standard boundary conditions $\partial_\sigma X^\mu = 0$ still hold at the endpoints, except when $\tau = 0$. Physically, one can imagine part of the string as being "rolled up" at the endpoints, except at discrete instants of time, such as $\tau = 0$, when snap-back occurs.

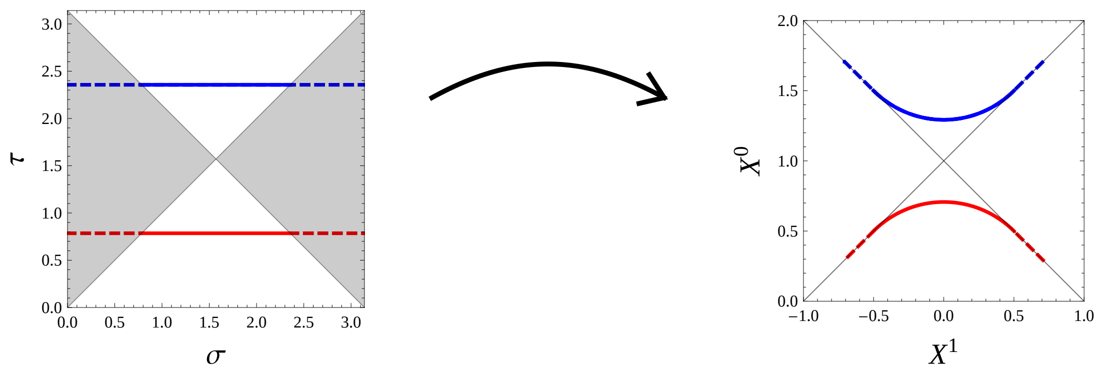

Figure 6.2: *The worldsheet mapping for the yo-yo solution in the form* (6.3)*. The gray area of the worldsheet maps to the edge of the string.*

This "rolling up" of the string is, in some sense, really a sign of "bunching" of a finite amount of momentum on the endpoints: a finite region of the worldsheet (with finite momentum) maps onto the lightlike spacetime trajectories of the endpoints. More formally, this is also a sign that the conformal gauge we have chosen breaks down in this limit. Let us analyze this problem then in a simpler, static gauge, where (t, x) are worldsheet coordinates. In this case, however, it is not possible to impose the standard boundary conditions, since they imply endpoint motion that is transverse to the string, while in the yo-yo limit, the endpoint is moving longitudinally to the string. Let us nevertheless try this and see what we need to change in order to get an energy conserving description of the yo-yo string.

For brevity, we omit the second spatial direction and write ℓ in place of ℓ_1. The string embedding is trivial: $X^0 = t$ and $X^1 = x$, with $t \in (0, \ell)$ and $x \in (-\ell + t, \ell - t)$ corresponding to the patch of the worldsheet described in (6.3). The total string energy, expressed as an integral over the bulk energy density P^t_0 (eq. (3.147)) is however not conserved now, so let's add finite energy to the endpoints to correct for that:

$$E = -\int_{-\ell+t}^{\ell-t} dx\, P^t_0 - 2p_0 = \frac{\ell - t}{\pi\alpha'} - 2p_0\,, \tag{6.6}$$

where $-p_0$ is the so far unknown energy at one endpoint. From the requirement that the total energy of the string (6.6) must be conserved, we can determine what the endpoint energy should be:

$$E_{\text{endpoint}} = -p_0 = \frac{E}{2} - \frac{L-t}{2\pi\alpha'} = \frac{t}{2\pi\alpha'}\,, \tag{6.7}$$

where in the last equation we used that the endpoint momentum vanishes (by assumption) at $t = 0$. This equation offers a nice picture of how, as the string is contracting, the energy from the bulk is being fed to the endpoints. We will see in the next section that (6.7) is in fact a solution of the general endpoint equation of motion (6.18), and that the yo-yo string in the static gauge will be the solution to the full string action that includes the finite endpoint momentum.

The yo-yo type trajectories can be obtained as limits of string configurations obeying the usual boundary conditions (i.e. with zero endpoint momentum), so they are definitely part of the classical theory. As we saw, the finite endpoint momentum allows us to give an energy conserving description of the yo-yo in gauges where the worldsheet mapping is non-degenerate and one-to-one. And it is important to work in such gauges if we want to study the worldsheet currents, which determine the dual energy loss.

6.1.2 Augmenting the bosonic string action

In the last section we saw how finite endpoint momentum is a part of the classical string theory. In flat space, the solutions of the bosonic string equations of motion with finite endpoint momentum are well known [316], and one of their notable features is that the endpoint trajectories are piecewise null line segments along which the endpoint momentum is a linear function of coordinates, which we also saw in the previous section. In this section we will follow our [35] and show that one obtains an analogous situation in a general, curved spacetime: namely, in the presence of finite endpoint momentum, the endpoint trajectories are piecewise null geodesics along which the endpoint momentum evolves according to equations that do not refer to the bulk shape of the string.

For the classical bosonic string, the simplest action that includes momentum at the endpoints can be obtained by augmenting the classical action (3.126) by an explicit boundary term whose form is the classical massless particle [35]:

$$S = -\frac{1}{4\pi\alpha'}\int_M d\tau d\sigma\,\sqrt{-h}h^{ab}\partial_a X^\mu \partial_b X^\nu G_{\mu\nu} + \int_{\partial M} d\xi\,\frac{1}{2\eta}\dot{X}^\mu \dot{X}^\nu G_{\mu\nu}\,, \tag{6.8}$$

where, as in Section 3.6.1, M denotes the worldsheet and ∂M is its boundary, which is traversed counter-clockwise in a picture where $\tau = \sigma^0$ points upward and $\sigma = \sigma^1$ points to the right. Dots denote differentiation by ξ, which (thus far) is an arbitrary way of parametrizing the boundary. As usual, h_{ab} is an auxiliary worldsheet metric whose equation of motion give the constraint equations (3.129), which essentially say that the worldsheet metric h_{ab} is conformally equivalent to the induced metric γ_{ab}. The field η is also an auxiliary field (essentially, the metric on the worldline of the particle), and its equation of motion is simply

$$\dot{X}^\mu \dot{X}^\nu G_{\mu\nu} = 0\,, \tag{6.9}$$

which tells us that the endpoints of the string do move at the speed of light in spacetime.

Eq. (6.9) gives rise to the first major difference from the usual, zero endpoint momentum case. Since, at the boundary, the parametrization of the worldsheet (σ,τ) must agree with the boundary parametrization ξ, we have:

$$\dot{X}^\mu = \dot{\sigma}^a(\xi)\partial_a X^\mu\,, \tag{6.10}$$

where $\sigma^a(\xi)$ denotes the location of the boundary (i.e. the endpoints) in the worldsheet coordinates, and $\dot{\sigma}^a \equiv d\sigma^a(\xi)/d\xi$. Plugging this in (6.9), we immediately get that the endpoints must be lightlike on the worldsheet as well, i.e.

$$h_{ab}\dot{\sigma}^a\dot{\sigma}^b = 0\,. \tag{6.11}$$

This means that we cannot assign the endpoints fixed σ coordinates, as before (e.g. $\sigma = 0, \pi$).

Let us now analyze the equations of motion for the string and the endpoint. We define the canonical momentum densities as in (3.131) and the endpoint momentum in the usual way, which we here, for convenience, copy:

$$\begin{aligned} P^a_\mu &= -\frac{1}{2\pi\alpha'}\sqrt{-h}h^{ab}G_{\mu\nu}\partial_b X^\nu\,, \\ p_\mu &= \frac{1}{\eta}G_{\mu\nu}\dot{X}^\nu\,. \end{aligned} \tag{6.12}$$

With these definitions, the equations of motion following from (6.8) can be concisely expressed as

$$\begin{aligned} \partial_a P^a_\mu - \Gamma^\kappa_{\mu\lambda}\partial_a X^\lambda P^a_\kappa &= 0\,, \\ \dot{p}_\mu - \Gamma^\kappa_{\mu\lambda}\dot{X}^\lambda p_\kappa &= \dot{\sigma}^a\epsilon_{ab}P^b_\mu\,, \end{aligned} \tag{6.13}$$

where ϵ_{ab} is antisymmetric with $\epsilon_{\tau\sigma} = 1$. The bulk equations of motion have been derived before in (3.132), as has been the righthand side of the endpoint equation of motion (eq. (3.137)) which, when there is no endpoint momentum, must vanish, yielding the standard open string boundary conditions. The lefthand side of the endpoint equation of motion is just the usual geodesic equation for a particle in a curved spacetime. If there was no string, the endpoint equation of motion in (6.13) would just be the one of a free particle, while now we have a "force term" due to the presence of the string, i.e., in an abuse of language, a curved space version of "$F = ma$".

Before we added the finite momentum, the endpoint equation of motion was just a constraint equation (i.e. it involved only first derivatives of the embedding functions), while now we have a true, second order equation of motion. At a first glance, it may seem that this could horribly complicate the already complex classical string dynamics, but as we will now see, it in fact simplifies it. The crucial part is to realize that the righthand side of the endpoint equation of motion in (6.13) (the "force term") can be written in terms of the endpoint quantities, by using (6.10).

We start by plugging the definition of P^a_μ from (6.12) in the force term in (6.13):

$$\dot{\sigma}^a \varepsilon_{ab} P^b_\mu = -\tau_f M^c_a \dot{\sigma}^a G_{\mu\nu} \partial_c X^\nu \,, \tag{6.14}$$

where $\tau_f = 1/(2\pi\alpha')$ and where we defined $M^c_a \equiv \epsilon_{ab}\sqrt{-h}h^{bc}$. Noting that this matrix squares to unity, let's look for its eigenvectors with eigenvalues ± 1. This is easiest to do in the conformal gauge $h_{ab} = \mathrm{diag}\{-1, 1\}$, where M^c_a has a simple form:

$$M^c_a = \begin{pmatrix} 0 & 1 \\ 1 & 0 \end{pmatrix} . \tag{6.15}$$

Its eigenvectors are obviously $(1, \pm 1)$ with eigenvalues ± 1. In the conformal gauge, these are precisely the null worldsheet trajectories that the endpoints are following. This means that $\dot{\sigma}^a$ are eigenvectors of M^c_a with eigenvalues ± 1, where the eigenvalue $+1$ corresponds to the endpoint moving longitudinally outward on a null trajectory. Hence, we can write (6.14) as:

$$\dot{\sigma}^a \varepsilon_{ab} P^b_\mu = \mp \tau_f \dot{\sigma}^c G_{\mu\nu} \partial_c X^\nu \,. \tag{6.16}$$

But, according to (6.10), $\dot{\sigma}^c \partial_c X^\nu = \dot{X}^\nu$, which together with the definition of the endpoint momentum (6.12) allows us to write (6.16) as:

$$\dot{\sigma}^a \varepsilon_{ab} P^b_\mu = \mp \tau_f \eta p_\mu \,. \tag{6.17}$$

This identity is important because we can now simplify the equation for the endpoint momentum (6.13):

$$\dot{p}_\mu - \Gamma^\kappa_{\mu\lambda} \dot{X}^\lambda p_\kappa = \mp \frac{\eta}{2\pi\alpha'} p_\mu = \mp \frac{1}{2\pi\alpha'} G_{\mu\nu} \dot{X}^\nu \,, \tag{6.18}$$

where in the last step we have used the definition (6.12) of p_μ to eliminate η. Note that this equation, apart from the presence of α', is completely independent of the bulk string quantities and suggests that the endpoint motion may be independent of the string. In fact, note that (6.18) can be rewritten in the form

$$\dot{\tilde{p}}_\mu - \Gamma^\kappa_{\mu\lambda} \dot{X}^\lambda \tilde{p}_\kappa = 0 \,, \tag{6.19}$$

where

$$\tilde{p}_\mu = \frac{1}{\tilde{\eta}} G_{\mu\nu} \dot{X}^\nu \tag{6.20}$$

and

$$\tilde{\eta}(\xi) = \eta(\xi) \exp\left(\mp \int^\xi d\tilde{\xi}\, \frac{\eta(\tilde{\xi})}{2\pi\alpha'} \right) \,. \tag{6.21}$$

The equations (6.19) and (6.20) are the standard equations for determining the spacetime geodesics. The key conclusion here is that the string endpoints with finite momentum simply follow null geodesics in the spacetime, independent of what the rest of the string does.

So, kinematically, the endpoints are following null geodesics, but dynamically, their momenta are decreasing or increasing (depending on the sign in (6.18)), because η changes according to (6.21). What happens then when the energy $E = -p_0$ (where 0 is the timelike direction and we are working in the mostly plus signature), reaches zero? In order to demand that the energy always stays non-negative, we utilize the freedom to choose the sign in (6.18) and prescribe that at instants when p_0 vanishes (which are also the instants when all the other components of p_μ will vanish as well, because p_μ is lightlike), the sign in (6.18) switches. We refer to this as the "snap-back". If, before the snap-back, the energy was flowing out of the endpoint (and hence caused it to reach $p_0 = 0$), after the snap-back, the energy will flow in the endpoint, and vice versa. On the worldsheet, the endpoints simply change directions from one null trajectory to the other one, while in the spacetime, we can determine the change in their trajectory by computing the limit of $\partial_a X^\mu$ at the endpoint from the pre-collision side and then demanding that it is continuous during the change of direction. This is the only time when the string influences the motion of the endpoint: the local curvature of the string profile close to the endpoint determines to which spacetime null geodesic the endpoint will switch to.

As previously advertised, the endpoint trajectories are determined by an equation (6.18) that does not refer to the shape of the bulk of the string; only when the endpoint changes direction does the rest of the string enter into the equations. This is perhaps counter-intuitive, because one would naturally suppose that by "shaking" the bulk one could eventually influence the motion of the endpoint. The resolution is that string trajectories with finite endpoint momentum are rather special: general motions of the bulk of the string are not compatible with finite endpoint momentum. That is, by introducing the explicit boundary term in (6.8), we selected of a special class of possible solutions to the bulk equations of motion.

We can now revisit the example of the yo-yo string from the previous section. In the static gauge in flat space, the endpoint equation of motion (6.18) is:

$$\dot{p}_\mu = \mp \frac{1}{2\pi\alpha'} \dot{X}_\mu \,, \tag{6.22}$$

which has a simple solution,

$$p_\mu = p_\mu^{(0)} \mp \frac{1}{2\pi\alpha'} X_\mu \,, \tag{6.23}$$

where $p_\mu^{(0)}$ is some constant vector. The endpoint momentum evolves linearly with the coordinates and when it reaches zero, the sign in (6.23) switches and the string performs a snap-back (see Fig. 6.3 for an illustration).

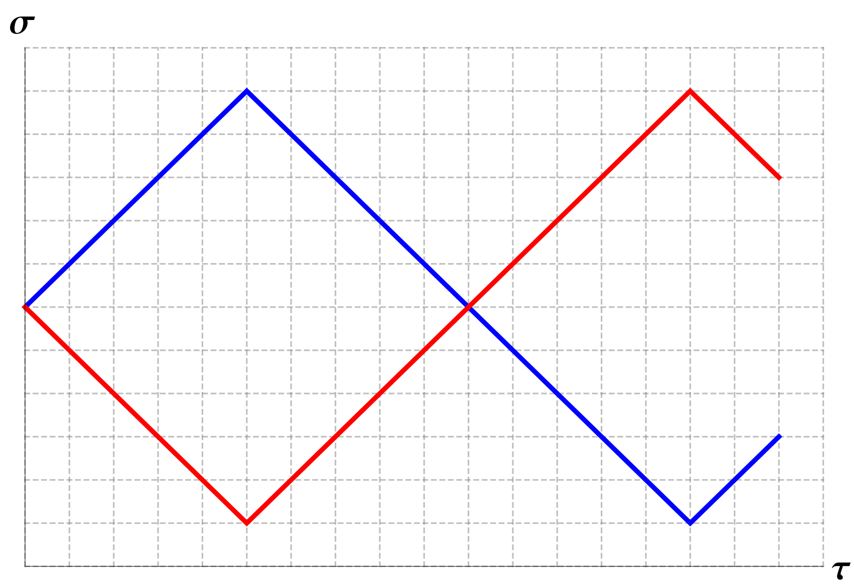

Figure 6.3: *Yo-yo string (in static gauge) performing snap-backs in (1+1)-dimensional flat space. The colored lines indicate the boundary of the string worldsheet, with red and blue colors indicating a particular endpoint. The string starts as a point with all the energy in the endpoints, which are moving apart and bleeding energy into the bulk of the string. When the energy in the endpoints reaches zero, the string snaps back, the sign in (6.18) changes and the energy is now being fed into the endpoints. When the endpoints meet again, the worldsheet "twists" and effectively changes orientation, so the endpoints start losing energy again and the whole process repeats.*

6.1.3 Light-cone Green-Schwarz action

Before we go on and explore the classical open string solutions with finite endpoint momentum in AdS_5-Schwarzschild, and their interesting implications for energy loss via the AdS/CFT correspondence, we should inspect whether the endpoint momentum constructions can be extended to the fermionic sector of the classical string. The reason for this is that in AdS/CFT, even in the classical gravity limit, we are still working in a superstring theory and so we need to inspect whether the bosonic string action, with endpoint momentum included (eq. (6.8)) can be embedded into the action of open superstrings propagating in an $AdS_5 \times S^5$ background. Such actions are quite complicated (see e.g. [317]), but we will take a first step in the desired direction by showing that the Green-Schwarz superstring action in the light-cone gauge [211, 318, 319] admits a generalization to finite endpoint momentum in a manner that preserves sixteen real supercharges in ten dimensions [35].

A standard way to achieve spacetime supersymmetry is to extend the Minkowski space to a superspace, which, in addition to the bosonic coordinates $X^\mu(\sigma,\tau)$, now also contains fermionic anticommuting coordinates $\theta^{Aa}(\sigma,\tau)$ (see e.g. [207]). Index a denotes different spinor coordinates (so that for N supersymmetries, we have $a = 1, ..., N$), while A is the index of the spacetime spinor in D dimensions, so in general $A = 1, ..., 2^{D/2}$. In order to achieve supersymmetry, it turns out that these spinors need to be of Majorana-Weyl type, i.e. real and of definite chirality[1]. Each of this conditions cuts the number of components by a half, so from 32 complex components for a general spinor in 10 dimensions, we get to 16 real components (off-shell).

[1]Majorana condition is simply a reality condition on the fermion fields, while Weyl condition selects spinors of definite chirality, which is defined by a D-dimensional analog of the γ_5 matrix. It can be shown that in $D = 10$ these two conditions are compatible. The 16 real components of a Majorana-Weyl spinor can be related through the Dirac equation, leaving 8 independent propagating degrees of freedom. This is the right number of degrees of freedom to form a supermultiplet with the massless vector field A_μ, which, in 10 dimensions, also has 8 propagating modes.

In this section, we employ the conventions of [207] (for example, $\alpha' = 1/2$), except that instead of using their p^+ we will use $q^+ = p^+/\pi$ and reserve p^+ for the X^+ component of the momentum on the boundary. The light-cone gauge in the bulk of the string consists of setting

$$X^+ = \pi q^+ \tau \,, \qquad \Gamma^+ \theta^a = 0 \,. \tag{6.24}$$

The first equation is just the usual light-cone gauge in the bosonic sector, which results in all the dynamics being in the transverse coordinates, because X^- can be determined from the constraint equations. The second gauge condition in (6.24) is allowed by κ-symmetry, a local fermionic symmetry on the worldsheet, and translates into setting half of the components of θ equal to zero[2]. The Green-Schwarz superstring action in the light-cone gauge is given by:

$$S_{\text{bulk}} = \int_M d^2\sigma \left[-\frac{1}{2\pi} \eta^{ab} \partial_a X^i \partial_b X^i + i q^+ \bar{\theta} \Gamma^- \rho^a \partial_a \theta \right] , \tag{6.25}$$

where $\bar{\theta}^{Aa} \equiv \theta^{Bb} \Gamma^0_{AB} \rho^0_{ab}$, and where Γ^μ are the ten-dimensional spacetime gamma matrices, while ρ^a are the two-dimensional worldsheet gamma matrices. In the light-cone gauge, the $N = 2$ spinor coordinates (from the spacetime perspective) can be packaged into a worldsheet spinor, so θ is a Majorana-Weyl spinor in both the ten-dimensional and two-dimensional senses. The first part in (6.25) is just the usual Polyakov action, while the other term is its fermionic counterpart constructed in [211] so that the whole action can be invariant under supersymmetry transformations (with the usual boundary conditions).

[2] An immediate consequence of this non-trivial local symmetry is that half of the components of θ are always decoupled from the theory. Hence gauge choice (6.24) simply selects which half of them should be set to zero. Also, it can be shown that κ-symmetry cannot be realized for any value of N; in fact, it forces $N \leq 2$, leading to division into type I and type II string theories.

These supersymmetry variations are

$$\delta X^i = 2\bar{\theta}\Gamma^i\epsilon\,, \qquad \delta\theta = \frac{1}{2\pi i q^+}\Gamma^+\Gamma^i\rho^a\partial_a X^i\epsilon\,, \tag{6.26}$$

where ϵ is a (constant) infinitesimal spinor of the same type as θ. A straightforward calculation leads to

$$\delta S_{\text{bulk}} = \int_M d^2\sigma\,\partial_a\left[\frac{1}{\pi}\bar{\theta}\rho^b\rho^a\Gamma^i\partial_b X^i\epsilon\right]\,. \tag{6.27}$$

As a warm-up, let us first see how the variation (6.27) vanishes for the usual set of boundary conditions, when there is no endpoint momentum. We consider a worldsheet boundary at $\sigma = 0$, with the string continuing to negative σ. For simplicity we will ignore any other boundary. Then an application of Stokes' theorem to (6.27) gives

$$\delta S_{\text{bulk}} = \int_{\partial M} d\tau\,\frac{1}{\pi}\bar{\theta}\rho^b\rho^\sigma\Gamma^i\partial_b X^i\epsilon\,. \tag{6.28}$$

The standard open string boundary conditions are:

$$\partial_\sigma X^i = 0\,, \qquad \theta = -i\rho^\sigma\theta\,. \tag{6.29}$$

The first one is just the usual bosonic boundary condition (3.138), while the other one is its fermionic analog, which, in the usual basis, where

$$\rho^\sigma = \begin{pmatrix} 0 & i \\ i & 0 \end{pmatrix}\,, \tag{6.30}$$

becomes simply $\theta^1 = \theta^2$. Because of this, there is an obvious additional (consistency) requirement on ϵ:

$$\epsilon = i\rho^\sigma\epsilon\,, \tag{6.31}$$

which implies that 16 real supercharges are symmetries of the action. Plugging $\partial_\sigma X^i = 0$ into (6.28), one obtains

$$\delta S_{\text{bulk}} = \int_{\partial M} d\xi \, \frac{1}{\pi} \bar{\theta} \rho_3 \Gamma^i \dot{X}^i \epsilon \,, \tag{6.32}$$

where $\rho_3 \equiv \rho^\tau \rho^\sigma$, and where we have used $\xi = \tau$ to parametrize the boundary, with dots denoting $d/d\xi$ as usual. It is easy to see that the boundary conditions (6.29) on θ together with the requirement (6.31) force the integrand in (6.32) to vanish.

In the case of endpoints with finite momentum, the worldsheet boundaries are now along null trajectories on the worldsheet, $\sigma^\pm = 0$. We must impose the same condition (6.31) on the supersymmetries preserved by the action, because an open string might have, for example, one endpoint with finite momentum and one without, and ϵ is a constant both on the worldsheet and in spacetime. To begin with, let's focus on a boundary at $\sigma^- = 0$, meaning $\sigma = \tau$, where as before the string stretches out toward more negative σ. It is convenient to parametrize this boundary using $\xi = \sigma^+$. Our normalization conventions are

$$\sigma^\pm = \frac{\tau \pm \sigma}{\sqrt{2}} \,. \tag{6.33}$$

Using Stokes' theorem, and ignoring any boundary other than the one at $\sigma^- = 0$, variation of the bulk action (6.27) is:

$$\begin{aligned} \delta S_{\text{bulk}} &= -\int_{\partial M} d\xi \, \frac{1}{\pi} \bar{\theta} \rho^+ \rho^- \dot{X}^i \Gamma^i \epsilon \\ &= -\int_{\partial M} d\xi \, \frac{1}{\pi} \bar{\theta} (1 - \rho_3) \dot{X}^i \Gamma^i \epsilon \,. \end{aligned} \tag{6.34}$$

The question now is how to improve the bosonic endpoint action, $\int_{\partial M} d\xi \, \frac{1}{2\eta} \dot{X}_i^2$, in such a way that its variation under the transformations (6.26) cancels against (6.34). The claim is that the requisite boundary action is

$$S_{\text{bdy}} = \frac{1}{2}\int_{\partial M} d\xi\, \frac{1}{\eta}\left[\dot{X}_i^2 + 2\pi i q^+ \bar{\theta}\rho^- \Gamma^- \dot{\theta}\right] , \tag{6.35}$$

where as usual dots represent derivatives with respect to $\xi = \sigma^+$.

In order to demonstrate that the variation δS_{bdy} cancels against (6.28), we will need some partial integrations along the boundary, and so we must know the ξ derivative of $1/\eta$. To obtain this we must consider what light-cone gauge means on the boundary. As a direct consequence of (6.24) together with our choice of $\xi = \sigma^+$, we see that

$$X^+ = \frac{\pi q^+}{\sqrt{2}}\xi\,, \qquad \Gamma^+\theta = 0 \tag{6.36}$$

on the boundary. Using the definition (6.12) of p_μ, we find

$$p^+ = \frac{1}{\eta}\dot{X}^+ = \frac{\pi q^+}{\sqrt{2}\eta}\,. \tag{6.37}$$

On the other hand, we know from the equation of motion (6.18) for p^+ that

$$\dot{p}^+ = -\frac{1}{\pi}\dot{X}^+ = -\frac{q^+}{\sqrt{2}}\,. \tag{6.38}$$

Comparing (6.37) and (6.38), we conclude

$$\frac{d}{d\xi}\left(\frac{1}{\eta}\right) = -\frac{1}{\pi}\,. \tag{6.39}$$

Note that although we have used the equation of motion for p^+, we will not use any additional equations of motion: the supersymmetry holds off-shell with respect to the transverse dynamics.

A straightforward calculation yields the supersymmetry variation of the boundary action to be

$$\delta S_{\mathrm{bdy}} = \int_{\partial M} d\xi \left[\frac{2}{\eta}\dot{\bar{\theta}}\dot{X}^i\Gamma^i\epsilon - \frac{1}{\eta}\dot{\bar{\theta}}\rho^-\rho^+\dot{X}^i\Gamma^i\epsilon + \frac{1}{\eta}\bar{\theta}\rho^-\rho^+\ddot{X}^i\Gamma^i\epsilon\right] . \tag{6.40}$$

To get to the form (6.40), we have already used the identity $\bar{\theta}\Gamma^-\Gamma^+ = 2\bar{\theta}$, which follows from the gauge condition $\Gamma^+\theta = 0$. Terms proportional to $\partial_- X^i$ occur in the variation $\delta\theta$, but they can be dropped because they come with a factor of ρ^-, and $\delta\theta$ is always multiplied on the left by an additional factor of ρ^-, which squares to 0. If we now use the relation $\rho^-\rho^+ = 1 + \rho_3$ and perform partial integrations with respect to ξ in order to eliminate expressions involving $\dot{\theta}$ (dropping all terms which are total ξ derivatives) we obtain

$$\delta S_{\mathrm{bdy}} = \int_{\partial M} d\xi \, \left[\frac{2}{\eta}\bar{\theta}\rho_3\ddot{X}^i\Gamma^i\epsilon + \frac{1}{\pi}\bar{\theta}(1-\rho_3)\dot{X}^i\Gamma^i\epsilon\right] . \tag{6.41}$$

The second term, which cancels against the bulk variation δS_{bulk} from (6.34), arises from terms proportional to $\frac{d}{d\xi}\left(\frac{1}{\eta}\right)$. The first term vanishes under precisely the same boundary conditions, $\theta = -i\rho^\sigma\theta$, that were used in (6.29) for ordinary boundaries of the worldsheet where there is no momentum. Note that we did not need to use any information about boundary conditions on X^i.

So far we treated only the situation where the endpoint is at $\sigma^- = 0$ with the string stretching out to negative σ (meaning positive σ^-). The generalization to arbitrary boundaries is

$$\begin{aligned} S = &\int_M d^2\sigma \left[-\frac{1}{2\pi}\eta^{ab}\partial_a X^i\partial_b X^i + iq^+\bar{\theta}\Gamma^-\rho^a\partial_a\theta\right] \\ &+ \int_{\partial M} d\xi \, \frac{1}{2\eta}\left[\dot{X}_i^2 - 2\pi i q^+\bar{\theta}\Gamma^-\eta_{ab}\rho^a\dot{\sigma}^b\dot{\theta}\right] . \end{aligned} \tag{6.42}$$

We should note that the extra piece in the boundary action is not the superparticle action (although it is quite similar to it), as that action is invariant under supersymmetry variations on its own and wouldn't be able to cancel the extra term coming from the bulk variations. The equations of motion resulting from (6.42) are

$$\partial_a \partial^a X^i = 0\,, \qquad \Gamma^- \rho^a \partial_a \theta = 0 \tag{6.43}$$

in the bulk, and

$$\frac{1}{\eta}\dot{p}^i = \mp\frac{1}{\pi}p^i\,, \qquad \frac{1}{\eta}\Gamma^- \eta_{ab}\rho^a \dot{\sigma}^b \dot{\theta} = 0 \tag{6.44}$$

on the boundary. With the factors of η arranged as in (6.44), one can smoothly take the limit $\eta \to \infty$ and still have correct equations.

We should note that although these were the encouraging first steps in the direction of showing that it is possible to include the finite endpoint momentum in the full supersymmetric action, they only strictly hold in the flat space and the light-cone gauge. It would be therefore interesting to check whether this construction holds in a general gauge and more general spacetime backgrounds. Furthermore, it would be also interesting to check whether the local κ-symmetry can still be realized with this extra boundary term.

6.2 String motions in AdS_5-Schwarzschild

As we saw in Chapter 5, the dynamics of free classical strings in AdS_5-Schwarzschild, whose endpoints are allowed to reach the horizon, is important as it should be dual to processes involving energy loss of light quarks in a strongly coupled plasma. In this section, based on our [35], we will calculate the stopping distance of strings with finite endpoint momentum, and present some explicit numerical solutions. The phenomenological motivation behind something like this is that the endpoint momentum might provide a more realistic dual of energetic quark jets: the initial conditions which assign most of the energy to the endpoints seem quite sensible if one thinks of the endpoints as representing massless quarks, while the string between them represents the color field that they generate.

6.2.1 Falling strings with finite endpoint momentum

In Section 5.1.3, we re-analyzed the problem of finding the maximum stopping distance Δx of light quarks in $\mathcal{N} = 4$ plasma, studied numerically in [300]. The spirit of that problem is to determine the maximum distance traveled by a string in AdS_5-Schwarzschild with a pointlike initial condition in which no part of the string has momentum upward toward the boundary. Intuitively, such an initial condition with fixed energy is supposed to represent the state of a light quark-anti-quark pair just after it is created through a hard scattering event. In this section, we want to revisit the same problem, but with initial conditions that include finite endpoint momentum.

We will work in the Poincaré coordinates of AdS_5-Schwarzschild (3.32), which we copy here for convenience:

$$ds^2 = \frac{L^2}{z^2}\left(-f(z)dt^2 + d\vec{x}^2 + \frac{dz^2}{f(z)}\right) , \tag{6.45}$$

where $f(z) = 1 - z^4/z_H^4$ with $z_H = 1/(\pi T)$, the boundary of the space is at $z = 0$ and, as usual, we assume that the string is moving in the $x - z$ plane. Now let us consider a falling string with a finite endpoint momentum. From the definition of endpoint momenta (6.12), we have in the $\xi = z$ parametrization:

$$p_t = -\frac{1}{\eta}\frac{L^2}{z^2} f\dot{t} \, , \qquad p_x = \frac{1}{\eta}\frac{L^2}{z^2}\dot{x} \, , \qquad p_z = \frac{1}{\eta}\frac{L^2}{z^2}\frac{1}{f} \, , \tag{6.46}$$

where, as usual, by a dot we denote differentiation with respect to $\xi = z$. From the equation of motion for the endpoint momenta (6.18), we have:

$$\dot{p}_t = \mp \frac{\eta}{2\pi\alpha'} p_t = \pm \frac{\sqrt{\lambda}}{2\pi} \frac{f}{z^2} \dot{t} \,. \tag{6.47}$$

As we showed in Section 6.1.2, the right hand side of this equation is completely determined by null geodesics and one does not need to solve the bulk equations of motion. As discussed in Section 5.1.3, the null geodesics in AdS_5-Schwarzschild are given by (5.10) and can be parametrized by $R = -\sqrt{f(z_*)}$, where z_* is the minimal distance from the boundary for this geodesic:

$$\frac{dx_{\text{geo}}}{dz} = \pm \frac{1}{\sqrt{R^2 - f(z)}} = \pm \frac{1}{\sqrt{f(z_*) - f(z)}} \,, \tag{6.48}$$

where the sign of this expression depends on whether we are on a "rising" or a "falling" trajectory. Expressing $\dot{t}$ in (6.47) via the definition of $R \equiv -f\dot{t}/\dot{x}$ (eq. (5.9)) and then expressing $\dot{x}$ via the null geodesic equation (6.48) we have:

$$\frac{dE}{dz} = -\frac{\sqrt{\lambda}}{2\pi} \frac{1}{z^2\sqrt{1 - f/R^2}} \,, \tag{6.49}$$

where we identified p_t with $-E$ at the boundary and we chose the "$-$" sign for the case when the endpoint energy is decreasing with time.

The optimum string configuration is obviously the one which has almost all of its initial energy packed in its endpoint, E_*. As the endpoint falls, its energy evolves according to (6.49); if the energy reaches zero before the endpoints falls in the horizon, the string will perform a snap-back, and we will restrict our attention on string motions without them[3];

[3] In general, performing a snap-back would probably decrease the stopping distance, but one may come up with some cleverly designed trajectory that results in a larger stopping distance for a given initial energy. Therefore, for simplicity, we will not consider snap-backs. On the other hand, intuitively, snap-backs are naturally associated with bound states, and may not be phenomenologically relevant when considering energetic quarks plowing through the quark-gluon plasma.

on the other hand, if the endpoint lands on the horizon with some left-over energy, then we are not being maximally efficient, as we could have reduced the initial energy and still obtained the same stopping distance. Hence, the optimum case will be when the initial energy E_* (for an endpoint starting at z_* on a geodesic with $R^2 = f(z_*)$) is such so that the endpoint energy vanishes just as it reaches the horizon:

$$E_* = \frac{\sqrt{\lambda}}{2\pi} \left[\frac{\sqrt{\pi}\Gamma\left(\frac{3}{4}\right)}{\Gamma\left(\frac{1}{4}\right)} \frac{z_H^2}{z_*^3} - \frac{{}_2F_1\left(\frac{1}{2}, \frac{3}{4}, \frac{7}{4}, \frac{z_*^4}{z_H^4}\right)}{3 z_H} \right] \sqrt{f(z_*)} \,. \tag{6.50}$$

In the high energy limit of $z_* \ll z_H$, we can neglect the last term and $f(z_*) \to 1$. The stopping distance itself is the same as before, i.e. it is given by the range of the associated null geodesic (5.13), only now the endpoints are following null geodesics exactly. Combining (6.50) with (5.13) in the $z_* \ll z_H$ limit, we get for the stopping distance the following expression:

$$\Delta x_{\text{stop}} = \left[\frac{2^{1/3}}{\pi^{2/3}} \frac{\Gamma\left(\frac{5}{4}\right) \Gamma\left(\frac{1}{4}\right)^{1/3}}{\Gamma\left(\frac{3}{4}\right)^{4/3}} \right] \frac{1}{T} \left(\frac{E_*}{\sqrt{\lambda} T} \right)^{1/3} . \tag{6.51}$$

The numerical factor in the brackets is approximately 0.624. Note that this is greater by a factor of $\left(\frac{\Gamma(1/4)}{\sqrt{\pi}\Gamma(3/4)}\right)^{1/3} \approx 1.19$ than the numerical factor in (5.14), obtained for falling strings without endpoint momentum.

As discussed in Section 5.4, the numerical factor in (6.51) is important for phenomenological reasons, as it determines the overall magnitude of jet quenching. And as we saw there, we need this factor to be greater than before in order to come closer to the data, and the 20% increase in (6.51) is a good sign. Intuitively, this relative increase arises because some of the energy in the initial state of a (zero endpoint momentum) falling string is devoted to downward velocity of the bulk of the worldsheet, while now, by packing all of its energy in the endpoint, we are being maximally efficient.

6.2.2 Explicit solutions for falling strings

In this section we will provide an explicit numerical solution of bulk equations of motion (6.13) for the case of falling strings with finite endpoint momentum. Because of finite momentum, the endpoints now follow null geodesics exactly, and their motion is known analytically. Therefore, we can simply use the numerical procedure of [300] (reviewed in Section 5.2) to determine the motion of the bulk of the string, subject to the explicit null geodesic boundary conditions for the endpoints.

As before, we choose the worldsheet metric to have the following form:

$$h_{ab} = \operatorname{diag}\left\{-s(\sigma,\tau), 1/s(\sigma,\tau)\right\} , \tag{6.52}$$

hence modifying the conformal gauge with the "stretching function" $s(\sigma,\tau)$, which is chosen in such a way so that the numerical computation is well behaved. We choose the "pointlike" initial conditions, where the string is initially a point at some radial coordinate z_0:

$$t(\sigma,0) = 0\,, \qquad x(\sigma,0) = 0\,, \qquad z(\sigma,0) = z_0\,. \tag{6.53}$$

Choosing these immediately satisfies the first constraint equation in (5.22). For this set of initial conditions we choose the same stretching function as before, eq. (5.28).

The simplest way to introduce the null geodesic as a boundary condition is to numerically solve the equations of motion for null geodesic in the $\xi = t$ gauge with (6.53) as initial conditions and obtain $x_{\text{geo}}(t)$ and $z_{\text{geo}}(t)$. For endpoints located at $\sigma = 0$ and

$\sigma = \pi$, the null geodesic boundary conditions can then be simply introduced as:

$$\begin{aligned} &\partial_\tau t(\tau,0) = \partial_\tau t(\tau,\pi) = 1, \\ &\partial_\tau x(\tau,0) = -\partial_\tau x(\tau,\pi) = \dot{x}_{\rm geo}(t=\tau), \\ &\partial_\tau z(\tau,0) = \partial_\tau z(\tau,\pi) = \dot{z}_{\rm geo}(t=\tau)\,. \end{aligned} \tag{6.54}$$

The initial velocity profiles are chosen similarly as in Section 5.2, but consistent with the new boundary conditions (6.54):

$$\partial_\tau x(\sigma,0) = \sqrt{f(z_0)}\cos(\sigma)\,, \qquad \partial_\tau z(\sigma,0) = 0\,. \tag{6.55}$$

The initial t-velocity profile is then determined by the second constraint equation in (5.22)

$$\partial_\tau t(\sigma,0) = \left|\cos(\sigma)\right|\,. \tag{6.56}$$

The bulk equations of motion do not have a particularly illuminating explicit form, but can be straightforwardly solved with Mathematica's NDSolve. After obtaining $X^\mu(\sigma,\tau)$, we can transform to the static gauge $X^i(\sigma,t)$ and plot the string shapes at different (fixed) times. A sample numerical solution is presented in Fig. 6.4, for a string initially at $z_0 = 0.2/(\pi T)$.

6.2.3 Strings with one endpoint behind the horizon

So far, in asking how far a string can travel in AdS_5-Schwarzschild, we have restricted our attention to initial conditions in which the initial state has $x \to -x$ symmetry and no upward momentum in the radial direction. Let us now relax both requirements and ask: if we start with an arbitrary state with all parts of the string at $x \leq 0$, with some part of the string behind the horizon, and with a total energy E outside the horizon, what is

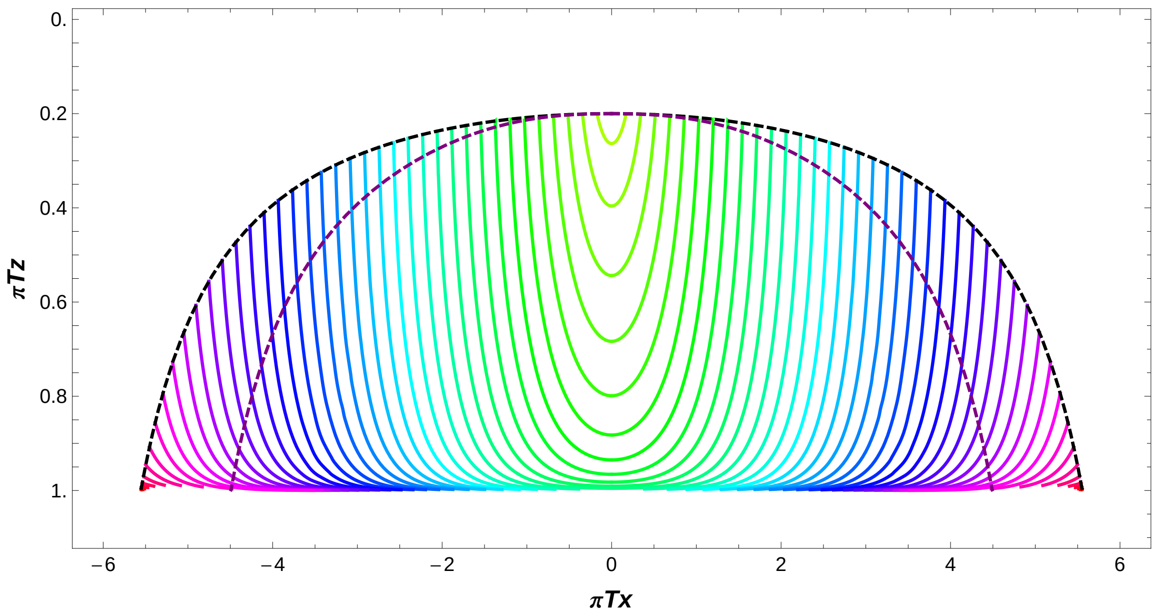

Figure 6.4: *A numerically determined string trajectory with finite momentum at the endpoints for initial $z_0 = 0.2/(\pi T)$. Each string shape is plotted at a fixed time t. The black dashed line indicates the relevant null geodesic trajectory that the endpoints follow. For the purpose of comparison, the purple dashed line indicates the trajectory of endpoints of an analogous falling string with vanishing momentum at its endpoints, whose energy is equal to $2E_*$ from (6.50) and whose initial conditions were taken from [33].*

the maximum positive x that the string can attain without experiencing a snap-back and before falling completely into the horizon?

As before, the optimal string configuration to start with is the one which packs essentially all of its energy into one endpoint, which is located very close to the horizon. The rest of the string is allowed to dangle down into the horizon. The motion of the energetic endpoint is a spacetime geodesic which first rises to a minimum value z_* of the radial coordinate, and then falls back into the horizon. We require, as before, that the endpoint momentum should vanish just as the endpoint finally falls behind the horizon. The energy of the endpoint when it reaches the apex z_* of its trajectory is precisely the value E_* found in (6.50). The initial endpoint energy is $E = 2E_*$. Because the rising and falling parts of the trajectory are symmetrical, Δx_{stop} also doubles relative to the value found in (6.51). Therefore, in the limit of $E \gg T$, the result is simply:

$$\Delta x_{\text{stop}} = \left[\frac{2}{\pi^{2/3}} \frac{\Gamma\left(\frac{5}{4}\right)\Gamma\left(\frac{1}{4}\right)^{1/3}}{\Gamma\left(\frac{3}{4}\right)^{4/3}} \right] \frac{1}{T} \left(\frac{E}{\sqrt{\lambda} T} \right)^{1/3} . \tag{6.57}$$

The numerical factor in brackets is approximately 0.990.

As with falling strings with finite endpoint momentum, it is interesting to construct numerical solutions which implement the sort of trajectory envisioned in the previous paragraph. Finding such a numerical solution is the main aim of this section. Because we consider strings which pass through the horizon, it is important to employ a coordinate system which is regular at the horizon. We will therefore solve the string equations of motion using static gauge in infalling Eddington-Finkelstein coordinates. The first step is to write the AdS_5-Schwarzschild metric (6.45) in the radial coordinate $r = L^2/z$:

$$ds^2 = -g(r)dt^2 + y(r)d\vec{x}^2 + \frac{dr^2}{g(r)} , \tag{6.58}$$

where

$$g(r) = \frac{r^2}{L^2} \left(1 - \frac{r_H^4}{r^4} \right) \qquad \text{and} \qquad y(r) = \frac{r^2}{L^2} . \tag{6.59}$$

The defining equation for Eddington-Finkelstein time, usually denoted v, is

$$dv = dt + \frac{dr}{g(r)} . \tag{6.60}$$

When integrating (6.60), one can insist that v coincides with the Killing time t at the boundary, $r = \infty$. One can straightforwardly show that the metric takes the form

$$ds^2 = -g(r)dv^2 + 2dvdr + y(r)d\vec{x}^2 . \tag{6.61}$$

Trajectories with constant $\vec{x}$ and constant v describe light-rays going directly down into the black hole: thus v is a null coordinate in the bulk, even though it is timelike on the boundary.

As can be shown from (6.61), it takes an infinite amount of Eddington-Finkelstein time to get started going upward from the horizon along a null geodesic, but only a finite time to reach the horizon going down along a null geodesic. Because of this we do not have the slow-down problem near the horizon, which was present in the Killing time coordinates, and because of which we needed to choose a particular modification of the conformal gauge (6.52) in the previous section to be able to solve the equations of motion numerically. This constitutes the main advantage of this coordinate system, as now we can choose to work in the static gauge, which will simplify the equations of motion significantly and allow us to develop a practical numerical scheme in which time-slices of the string are at constant v.

We will work in the static gauge where $\sigma = r$ and $\tau = v$, so that we only need to solve for $x(v, r)$. Note again that the motion of the endpoints is completely determined by null geodesics, which, similarly as before, can be obtained numerically in the $\xi = v$ parametrization, $x_{\rm geo}(v)$ and $r_{\rm geo}(v)$. The equations in (6.13) for the bulk of the string, together with some useful definitions, can be assembled into the following list of equations that can be solved in order to track the classical motion of the string:

$$h \equiv -\det h_{ab} = 1 + gy(\partial_r x)^2 + 2y(\partial_v x)(\partial_r x)\,, \tag{6.62}$$

$$P_x^v = -\frac{\sqrt{\lambda}}{2\pi}\frac{y}{\sqrt{h}}\partial_r x\,, \tag{6.63}$$

$$P_x^r = -\frac{\sqrt{\lambda}}{2\pi}\frac{y}{\sqrt{h}}\left(\partial_v x + g\partial_r x\right)\,, \tag{6.64}$$

$$\partial_v P_x^v + \partial_r P_x^r = 0\,. \tag{6.65}$$

Suppose x and P_x^v are known on a time-slice of constant v. Then we may use (6.63) to obtain h and then solve (6.62) for $\partial_v x$. Next we can obtain P_x^r from (6.64) and then $\partial_v P_x^v$ from (6.65). All these manipulations involve only r-derivatives and algebraic manipulations, so we see that we can design a numerical scheme which advances x and P_x^v from one time-step to the next. The main potential issue with this scheme is that the expressions needed involve $\partial_r x$ and P_x^v as denominators, so if either of them vanishes, there is a problem with the numerical method.

Because of their high level of accuracy and stability, we have decided to use pseudospectral methods for evaluating the r-derivatives (see for example [320]). Pseudospectral methods are useful for casting a system of linear partial differential equations, such as (6.62)-(6.65), into a set of coupled, ordinary differential equations. The way to do this is to discretize one of the coordinates (call it spatial) on some predefined grid; these points are called the collocation points, and are generally chosen specifically for a particular problem at hand. Then each of the functions in the system of PDE's gets a spatial index (i.e. becomes a separate function), denoting to what collocation point it belongs. The spatial derivatives are calculated according to the special pseudospectral expressions, dictated by the choice of the collocation points.

In our case, the idea is to choose the collocation points on a so-called scaled Gauss-Lobatto grid:

$$r_j(v) = r_H + \frac{r_{\text{geo}}(v) - r_H}{2}\left(1 + \cos\frac{\pi j}{N}\right) , \tag{6.66}$$

where j runs from 0 to N. We have chosen this particular grid because most of the collocation points will be grouped close to the endpoint and the horizon, where we need the most accuracy. The r-derivatives on any given time slice can then be taken using standard pseudospectral expressions involving the appropriate cardinal functions. Therefore, the data on a given time slice v is composed of $2N$ numbers x_j and $(P_x^v)_j$ for $0 \leq j < N$, indicating where the string is and what value of P^v_x it has at each of the collocation points r_j. We insist that $x_N = x_{\text{geo}}$ and that $(P^v_x)_N$ satisfies a matching condition:

$$(P^v_x)_N = -\frac{\sqrt{\lambda}}{2\pi}\frac{y\partial_r x}{1 + y\dot{x}_{\text{geo}}\partial_r x}\,, \tag{6.67}$$

found by demanding that the endpoint limit of the quantity $\partial_v x + \dot{r}_{\text{geo}}\partial_r x$ should equal $\dot{x}_{\text{geo}}$. The minus sign here corresponds to the minus sign in (6.18). We therefore have a system of $2N$ coupled first-order ordinary differential equations in v, at solving of which Mathematica's NDSolve is particularly effective.

For studying strings with one of the endpoints behind the horizon, we can use the trailing string profile for the initial ($v = 0$) values of $x(r)$ and $P^v_x(r)$. Its form in the Eddington-Finkelstein coordinates is:

$$x_{\text{trailing}} = \beta\left(v - \frac{L^2}{r_H}\tan^{-1}\frac{r}{r_H}\right)\,, \tag{6.68}$$

where β is the velocity. Essentially this form was found in [281] (though the focus there was on Kruskal coordinates), however now we also have to require that the endpoint moves at the local speed of light, $\beta = \sqrt{g(r_0)/y(r_0)}$, since the endpoints are free. An odd feature is that in this coordinate system, at a fixed "time slice" (meaning fixed v), the string worldsheet is further forward near the horizon than it is near the boundary.

In our sample numerical solution in Fig. 6.5, we chose the initial trailing string profile cut off at $r_0 = 2\pi TL^2$. The endpoints are moving on a null geodesic whose maximum radial height is $r_{\max} = 3.46\,\pi TL^2$. Note that we do not need to specify the value of λ, as it drops out of equations of motions for the bulk of the string and only governs the rate at which the endpoint momentum is being drained.

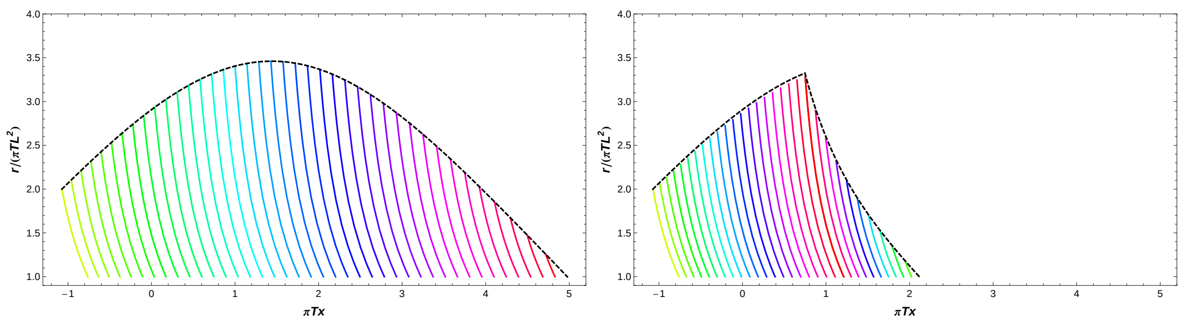

Figure 6.5: *A numerically determined string trajectory with finite momentum at the endpoint in the Eddington-Finkelstein coordinates, with and without the snap-back. Each string shape is plotted at a fixed Eddington-Finkelstein time v. The black dashed line indicates the relevant null geodesic trajectory that endpoints follow. In the left plot, the initial endpoint energy was high enough so that the endpoint falls in the horizon without performing a snap-back, while in the right plot, all the kinematical initial conditions were kept the same, only the initial endpoint energy was reduced, so that it performs a snap-back and switches to a spacetime geodesic determined by the curvature of the string profile close to the endpoint.*

6.3 Energy loss and the shooting string R_{AA}

A challenging question, reviewed in Chapter 5, is how to read off the instantaneous rate of energy loss of an energetic light quark from the falling string description. We discussed how, apart from the inherent dependence on the initial conditions, it is hard to unambiguously define the energy loss, as it is not clear which part of the classical string should be associated with the "jet" and which part with the energy deposited to the plasma. As we will see in this section, the finite endpoint momentum gives a precise and natural way to define energy loss [35], leading to a successful phenomenological implementation via the shooting strings [36].

6.3.1 Energy loss as momentum flow from the endpoint

As noted earlier in Section 6.2, in the finite endpoint momentum framework, it is sensible to think of the endpoints as representing massless quarks with finite momentum, and the string between as representing the color field that the quarks generate. This naturally leads us to identify the energy of the energetic quark with precisely the energy of the string endpoint. Perhaps surprisingly, this is a gauge-invariant way of distinguishing between energy in the hard probe and energy in the color fields surrounding it. This hence provides a natural and unambiguous definition of the energy loss: it is simply the rate at which the energy from the finite momentum endpoint flows into the string.

With this definition, the energy loss is governed by simple equations of motion for the endpoint (6.18), which are independent of the bulk shape of the string, as well as the string initial conditions: rather, they only depend on the null geodesic that the finite momentum endpoint is following. We have actually already obtained the expression for the instantaneous energy loss in (6.49), we just need to use the null geodesic equation (6.48) to express it as dE/dx:

$$\frac{dE}{dx} = -\frac{\sqrt{\lambda}}{2\pi}\frac{\sqrt{f(z_*)}}{z^2}\,, \tag{6.69}$$

where we used $R^2 = f(z_*)$[4]. We see how the energy loss depends essentially only on the radial location of the endpoint, and only weakly on what geodesic (which z_*) the endpoint is following. Also note that (6.69) is valid for both the falling and the rising part of the trajectory, as in the latter case we need to flip the signs in both (6.48) and (6.49). Because of this, the energy loss will be symmetric around $x = \Delta x_{\text{stop}}/2$ from (6.57).

To express dE/dx as a function of x, we need to solve the null geodesic equation (6.48).

[4]It should be noted that this expression, when applied to a trailing string with a finite endpoint momentum, gives precisely the drag force of [22] and [23]. Of course, the finite momentum endpoint, being at some constant elevation z, must move at the local speed of light, $v^2 = f(z)$.

Assuming that initially, at $x = 0$, the endpoint is at $z = z_0$ going towards the boundary, we have:

$$x_{\rm geo}(z) = \frac{z_H^2}{z}\,{}_2F_1\left(\frac{1}{4},\frac{1}{2},\frac{5}{4},\frac{z_*^4}{z^4}\right) - \frac{z_H^2}{z_0}\,{}_2F_1\left(\frac{1}{4},\frac{1}{2},\frac{5}{4},\frac{z_*^4}{z_0^4}\right), \tag{6.70}$$

where ${}_2F_1$ is the ordinary hypergeometric function. Now, for a given z_* and z_0, we can invert (6.70) to obtain $z(x)$ and then plug it in (6.69) to obtain dE/dx as a function of x, an example of which is plotted in Fig. 6.6 for the simple case of $z_0 = z_H$.

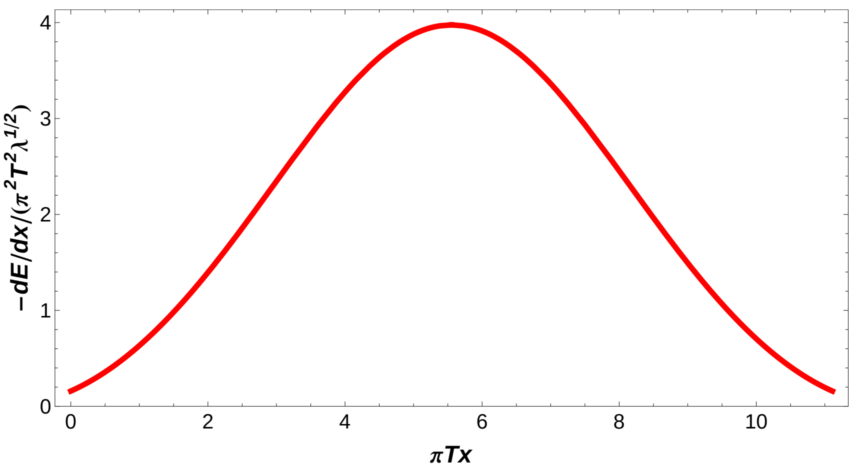

Figure 6.6: *Energy loss (6.69) from a finite momentum endpoint as a function of x for $z_* = 0.2/(\pi T)$ and an endpoint starting close to the horizon ($z_0 = z_H$).*

It is obvious that the previous construction is easily extendable to more general geometries. To explicitly demonstrate this, let us assume that the spacetime metric has the following form:

$$ds^2 = G_{tt}(z)dt^2 + G_{xx}(z)dx^2 + G_{zz}(z)dz^2\,. \tag{6.71}$$

The following simple derivation is easily applicable to metrics more general than this, but many cases of interest are captured by form (6.71). As before, because the metric does not depend explicitly on t nor x, the following is a constant of motion along a geodesic:

$$R = \frac{G_{tt}\dot{t}}{G_{xx}\dot{x}}\,, \tag{6.72}$$

where the dot again denotes differentiation with respect to ξ that parametrizes the geodesic. The finite momentum endpoints will move along null geodesics $ds^2 = 0$ parametrized by R:

$$\left(\frac{dx_{\text{geo}}}{dz}\right)^2 = -\frac{G_{tt}G_{zz}}{G_{xx}(G_{tt} + G_{xx}R^2)}\,. \tag{6.73}$$

If the geometry (6.71) allows for null geodesics such that the denominator of (6.73) vanishes at some $z = z_*$, then the geodesic cannot go past that (minimal) z_* and we can relate it to R:

$$R = -\sqrt{\frac{-G_{tt}(z_*)}{G_{xx}(z_*)}}\,. \tag{6.74}$$

Because the metric (6.71) is not explicitly dependent on t, the flux of energy (6.18) from the endpoint to the bulk of the string is given by a simple formula:

$$\dot{p}_t = -\frac{1}{2\pi\alpha'}G_{tt}\dot{t}\,. \tag{6.75}$$

This equation also explicitly demonstrates how, quite generally, the energy loss from a finite momentum endpoint does not depend on the energy contained in it, as the drain is caused by string worldsheet currents that do not know anything about the finite momentum except that it is there (as it changes the boundary conditions). Using $\xi = x$ parametrization and plugging (6.72) in (6.75) we get:

$$\frac{dE}{dx} = -\frac{|R|}{2\pi\alpha'}G_{xx}(z)\,. \tag{6.76}$$

In the case of AdS_5-Schwarzschild, we quickly arrive at (6.69). Of course, in order to find out how the energy loss depends on x, one must solve the null geodesic equation (6.73).

We can now easily apply this to the case of AdS_5 with Gauss-Bonnet higher derivative R^2 corrections, described in Section 3.4.3. In the AdS-GB background (3.59) formula

(6.76) immediately gives

$$\frac{dE_{GB}}{dx} = -\frac{\sqrt{\lambda}}{2\pi}\frac{1}{z^2}\frac{\sqrt{f_{GB}(z_*)}}{a}\,. \tag{6.77}$$

As we saw in Section 5.4, Gauss-Bonnet corrections had a significant effect on the energy loss and will be important in this context as well. We can also easily apply formula (6.76) to the non-conformal holographic model of Section 3.5, where the background is given by (3.68), so we have:

$$\frac{dE_{\mathrm{nCFT}}}{dx} = -\frac{\sqrt{h(r_*)}}{2\pi\alpha'}e^{2A_s(r)}\,, \tag{6.78}$$

where the subscript "s" denotes the string frame metric, which is now non-trivially related to the Einstein frame metric due to the running of the dilaton, as described in Section 3.5.6.

6.3.2 Shooting string limit

In this section we will, based on the finite endpoint momentum framework, develop a phenomenologically usable form of the instantaneous energy loss dE/dx, which we refer to as the "shooting strings" [36].

By phenomenologically usable, we mean dE/dx as given by (6.69), only expressed as a function of temperature T and distance x. Of course, we can numerically invert the solution of the null geodesic equation (6.70) (for given z_* and z_0) to obtain $z(x)$ and plug it in (6.69) to obtain dE/dx as a function of x. However, the issue here is that this would make the energy loss dependent on z_*, which at this point we do not know how to relate to some quantity in the boundary theory. Luckily, (6.70) has a particularly simple and universal form for small z_*:

$$x_{\mathrm{geo}}(z) = z_H^2\left[\left(\frac{1}{z}-\frac{1}{z_0}\right)+\mathcal{O}\left(\frac{z_*^4}{10z^5},\frac{z_*^4}{10z_0^5}\right)\right]\,. \tag{6.79}$$

The reason we are interested in this expansion is phenomenological: from (6.69) we see that if we start at z close to the boundary, the energy loss will be large, which means that the jets dual to these endpoints will be quenched quickly and hence won't be observable. Therefore, for observable jets, we need to start rather close to the horizon, and for $z_* < z$ we see that the expansion (6.79) is strongly convergent, resulting in an interesting novel universal form for energy loss:

$$\frac{dE}{dx} = -\frac{\pi}{2}\sqrt{\lambda}T^2\left(\frac{1}{\tilde{z}_0} + \pi T x\right)^2 , \tag{6.80}$$

where $\tilde{z}_0 \equiv \pi T z_0 \in [0, 1]$. With initial z_0 being close to the horizon, the endpoint is being "fired" upwards, which is the reason why we refer to this limit of small z_* and large z_0 as the "shooting string" limit (see Fig. 6.7 for illustration).

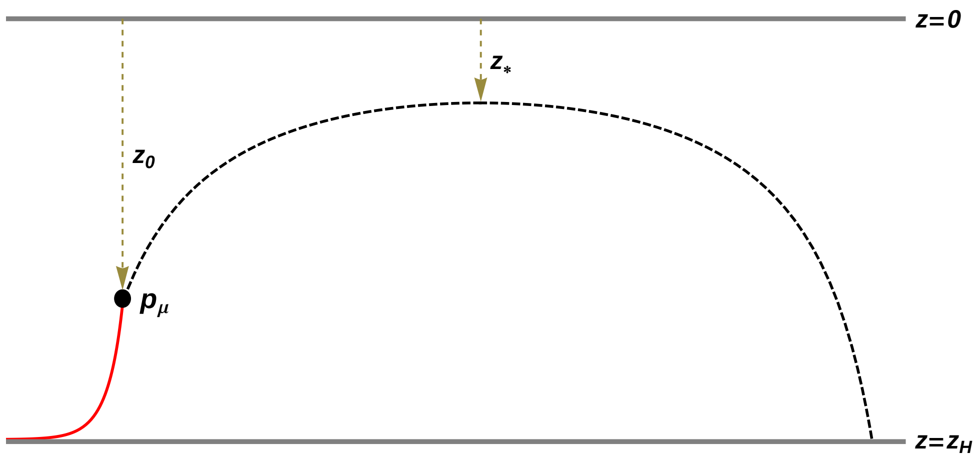

Figure 6.7: *Illustration of the shooting string. The finite momentum endpoint starts at some initial radial coordinate z_0 moving on an "upward" null geodesic parametrized by its point of closest approach to the boundary, z_*.*

The form (6.80) of energy loss has interesting physical regimes: at small x, it looks like a pure $\sim T^2$ energy loss, similar to the pQCD elastic energy loss (eq. (2.2)); for intermediate x, it looks like $\sim xT^3$ with a path dependence (but not the energy dependence) similar to the pQCD radiative energy loss (eqns. (2.28) and (2.29)); and, finally, for large x, it has a novel $\sim x^2T^4$ behavior. The size of $\tilde{z}_0$ (i.e. how much above the horizon the endpoint starts) dictates at what x each of these regimes becomes relevant. This is an interesting (and a very specific) generalization of the simpler "abc" models of energy loss [313], where $dE/dx \propto E^a x^b T^c$.

We should also note that the $\propto x^2$ path length dependence of the energy loss (6.80), according to several studies [308, 309], seems to be needed in order to achieve a simultaneous fit of v_2 and central R_{AA} at high p_T with the data (as discussed in Section 5.3). To our knowledge, (6.80) is the first clear derivation of this path length dependence in the case of light quarks.

Another motivation for considering endpoints that start close to the horizon comes from the bulk perspective. One generally envisions an effective model of a heavy ion collision by considering collisions of shock waves in AdS that have finite transverse extent and are sourced by some distribution of matter (see e.g. [321–323]). The horizon forms around that matter and thus the location of rare energetic string formation is more naturally near the horizon, rather than in the middle of the bulk.

Although this, together with the phenomenological justification appearing above (6.80), may to some extent support the assumption of considering z_0 close to z_H, the limit of small z_* was chosen mainly because of its simplicity: (6.79) is strongly convergent, leading to a z_*-independent expression of the energy loss for already moderately small z_*. Also, in the first attempts to confront the finite momentum with the data, we will often simply choose $\tilde{z}_0 = 1$; however, some perhaps more realistic distribution of both z_* and z_0 may be more appropriate and is left for future work.

Let us now take the shooting string limit in the case of Gauss-Bonnet energy loss, eq. (6.77). Null geodesics in the AdS-GB geometry look very similar to the ones in AdS_5-Schwarzschild (6.48), we only need to replace $f(z)$ by $f_{GB}(z)$ (eq. (5.18)). We could now take the shooting string limit by sending $z_* \to 0$ and then, for a given λ_{GB}, numerically integrate the null geodesic equation (5.18) and invert to obtain $z(x)$, which can then be plugged in (6.77) to get dE/dx as a function of x and T. However, since according to (3.58), λ_{GB} is constrained to be small, all these expressions are suitable for a perturbative expansion in λ_{GB}, allowing for a more practical analytic expression. To do this, we will expand the null geodesic (5.18) in λ_{GB} up to some order n and neglect all terms higher than $1/z^2$, as they are $\mathcal{O}(z^4)$ subleading. Of course, we will be able to check how accurate this is by comparing with the full numerical solution. We define a polynomial in λ_{GB}:

$$P_n(\lambda_{GB}) \equiv \frac{2}{z_H^2} \lim_{z\to 0} z^2 \left(\frac{dx_{\text{geo,(n)}}}{dz}\right)_{z_*=0}, \tag{6.81}$$

where n denotes the order of expansion in λ_{GB}. In this case, we can easily solve the geodesic equation:

$$z_n(x,\lambda_{GB}) = \frac{z_H^2 z_0 P_n(\lambda_{GB})}{z_H^2 P_n(\lambda_{GB}) - 2xz_0}. \tag{6.82}$$

This can be plugged in (6.77) to get explicitly the form of dE/dx for a given order n, yielding an expression quite similar to (6.80):

$$\frac{dE_{GB}}{dx} = -\sqrt{\lambda}\, T^2 F_n(\lambda_{GB}) \left(\frac{G_n(\lambda_{GB})}{\tilde{z}_0} + \pi T x\right)^2. \tag{6.83}$$

The functions F_n and G_n are functions of λ_{GB} only and do not have a particularly illuminating explicit form, even for small n. For λ_{GB} as large as $-7/36$, by comparing to the all-order numerical result, we found that it is enough to go to $n = 5$ order in expansion. In Fig. 6.8 we compare this energy loss to the energy loss without the Gauss-Bonnet term (6.80), where we can see that, at a maximally negative λ_{GB}, the energy loss with Gauss-Bonnet corrections can be up to two times smaller. This will, as we will soon see, have quite noticeable consequences for R_{AA}.

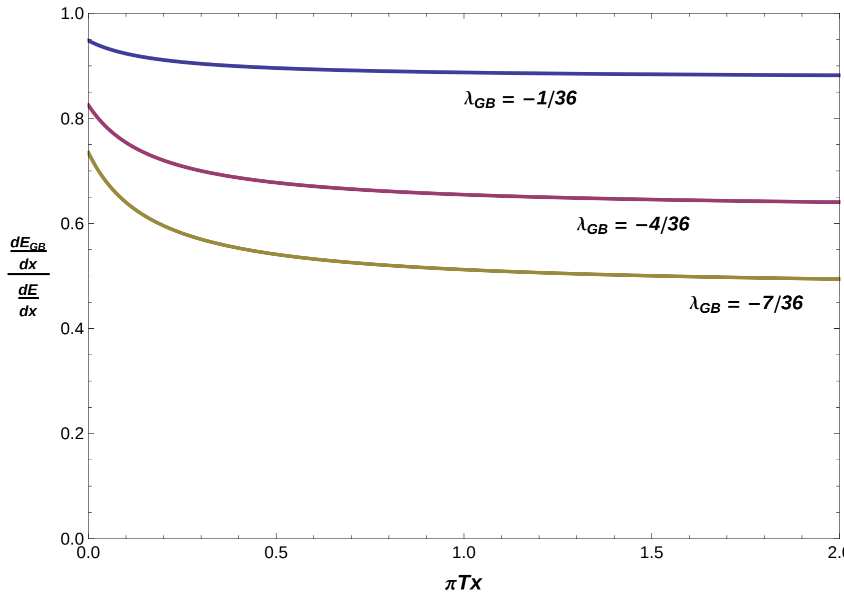

Figure 6.8: *Ratio of the instantaneous energy loss in pure AdS (6.80) and the energy loss with the Gauss-Bonnet corrections (6.83) as a function of x, for $\tilde{z}_0 = 1$ and for several different values of λ_{GB}.*

6.3.3 R_{AA} from shooting strings

As we saw in Section 5.4, the model of light quark energy loss based on falling strings severely underpredicts the LHC pion suppression data. Even though it had the right qualitative structure, the energy loss was simply too strong (which is a generic feature, already obvious from the maximum stopping distance bound), and coming close to the data required setting $\lambda \sim 0.01$ (see Fig. 5.7), which takes us far away from the supergravity approximation. In Section 6.2.1, we saw how finite endpoint momentum allows the falling string to travel about 20% farther (eq. (6.51)) and from Section 5.4 we know how sensitive the energy loss observables are to this. Furthermore, in this framework, we also have a precise and unambiguous expression for energy loss, which was missing in the case of falling strings. For these reasons, in this section we follow [36] and use the proposed shooting string formula for energy loss (6.80) (and (6.83)) to compute the nuclear modification factor R_{AA} for pions at RHIC and LHC.

As before, we will use the model of the expanding plasma with Glauber initial conditions from Sections 1.3 and 1.4[5]. In addition to this, we will also follow the prescription of [261], and in order to account for roughly three times more degrees of freedom in $\mathcal{N} = 4$ SYM than in QCD, relate the temperatures of these two theories through the requirement that they give the same energy density $\epsilon \propto T^4$:

$$T_{\text{SYM}} = 3^{-1/4}\, T_{\text{QCD}}\,. \tag{6.84}$$

As we can see from (6.80), this effect will slightly reduce the energy loss.

The results are shown in Fig. 6.9, where we used the pure AdS energy loss (6.80) and chose (as in the rest of the plots in the chapter) $\tilde{z}_0 = 1$. There we see that, first of all, qualitatively, our R_{AA} calculations seem to match the data well. In fact, the rise of R_{AA} with increasing p_T could have been expected, as the energy loss from finite endpoint momentum strings (6.75) is, quite generally, independent of energy, and according to the pocket formula (1.72), we have $R_{AA} \sim (1-\epsilon)^{n_Q - 1}$. To obtain a satisfactory quantitative fit, with a reasonable choice of parameters, we needed to choose $\lambda = 3$ at RHIC; however, using the same parameters and λ at the LHC shows that the data is severely underpredicted. Lowering λ to 1 for LHC data is not enough: one seems to need a rather small $\lambda = 0.25$ to obtain a satisfactory fit. Of course, with that λ, RHIC is then severely overpredicted. This is precisely the "surprising transparency" of the LHC [313], where the effects of temperature increase from RHIC to LHC affect the R_{AA} much more than

[5]In obtaining the pion R_{AA}, we need to use the fragmentation functions, which are evaluated at some energy (virtuality) scale Q (see Section 1.4.2). The finite momentum and its simple analytical formulas allow us to express the virtuality of the endpoint, $Q^2 \equiv p_0^2 - p_x^2$, simply as $Q^2 = E^2 \tilde{z}_*^4/(1-\tilde{z}_*^4)$, i.e. it is proportional to the endpoint's energy squared. This energy, and hence virtuality as well, decreases even during the "ascending" phase in the geodesic trajectory, in a unique way given by (6.69) and (6.70). However, at finite N, one should bear in mind that even bulk constructions can be off-shell; thus some N-suppressed contribution to virtuality may be significant compared to the rather suppressed classical expression just given. For this reason, we will use the usual prescription of $Q = p_T$, and note that, due to a, for our purposes, rather low sensitivity of the fragmentation functions to the Q^2-evolution, we do not expect that a choice of a different prescription would affect our results significantly.

the competing increase of the production spectra (Fig. 1.13).

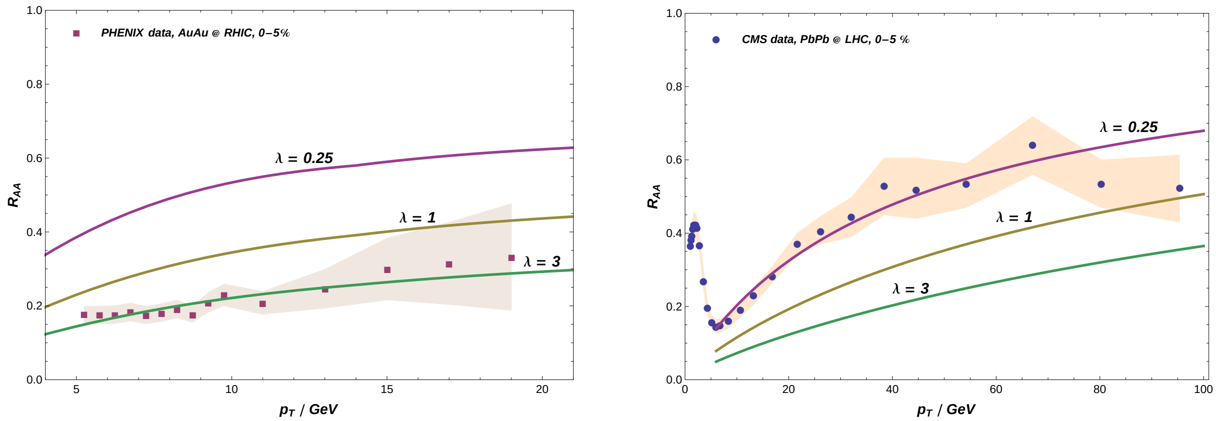

Figure 6.9: *Nuclear modification factor R_{AA} from shooting strings (6.80) at RHIC and LHC. Our calculations are compared to the suppression data from the PHENIX [309] and the CMS [84] collaborations for 0-5% centrality class. In different curves we only change the 't Hooft coupling λ, while they all share the same impact factor of b =3 fm, the freezout temperature of T_{fo} =170 MeV, the formation time of τ_0 =1 fm/c, and the initial $\tilde{z}_0$ =1.*

As we see in Fig. 6.9, we are quite close to the LHC data for $\lambda = 1$, and in the previous section we have seen that the Gauss-Bonnet corrections (6.83) can significantly reduce the energy loss (Fig. 6.8). This, expectedly, has noticeable consequences for R_{AA}: in Fig. 6.10 we see that it results in a higher R_{AA} that comes very close to the data for $\lambda = 1$. Now, recall that in the presence of the Gauss-Bonnet term, the ratio of the shear viscosity to entropy density, η/s, increases for negative values of λ_{GB} (eq. (3.64)). In fact, for a maximally negative λ_{GB}, the viscosity can be increased up to about $1.8/(4\pi)$, which is, together with our selected value of the formation time $\tau_0 = 1$ fm/c, in the ballpark of the parameters used in some of the most recent hydrodynamic simulations for the LHC [324] to describe the elliptic flow data of light hadrons.

Now that we have the central R_{AA} data well matched for a reasonable choice of parameters both at RHIC and LHC (separately), we can inspect what happens in the non-central case. In that case, we will compute the elliptic flow parameter using the approximate for-

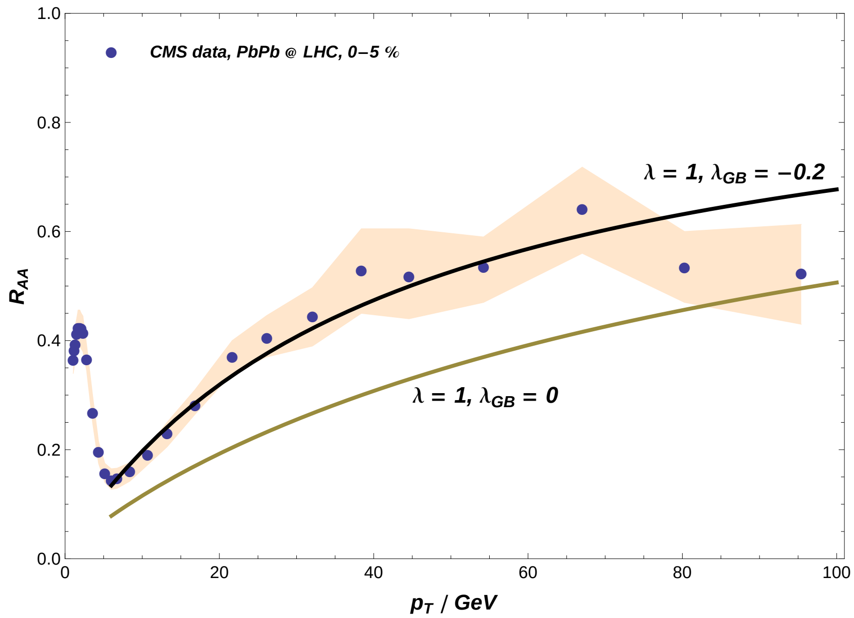

Figure 6.10: *Nuclear modification factor R_{AA} at the LHC for $\lambda = 1$, with and without the higher derivative Gauss-Bonnet corrections. All other parameters are the same as in Fig. 6.9.*

mula that immediately follows from the definition of v_2, eq. (1.21):

$$v_2 \approx \frac{1}{2} \frac{R_{AA}^{\text{in}} - R_{AA}^{\text{out}}}{R_{AA}^{\text{in}} + R_{AA}^{\text{out}}}\,, \tag{6.85}$$

where "in" and "out" corresponds to R_{AA} calculated considering only the particles being emitted in the $\phi = 0$ and $\phi = \pi/2$ directions (see Fig. 1.5). In Fig. 6.11 we see that in the case of RHIC, the splitting we predict for in and out R_{AA}'s in non-central collisions is not big enough, which is probably due to the (too) simple blast wave (1.61) we are using to model the transverse expansion of the plasma. We see a similar result in the case of LHC as well, where a too small in-out splitting results in v_2 that seems be somewhat below the data for the $\lambda = 1$ case with the Gauss-Bonnet corrections, which also matched the central R_{AA} data.

Finally, we should note that in all these calculations, we have considered pions coming

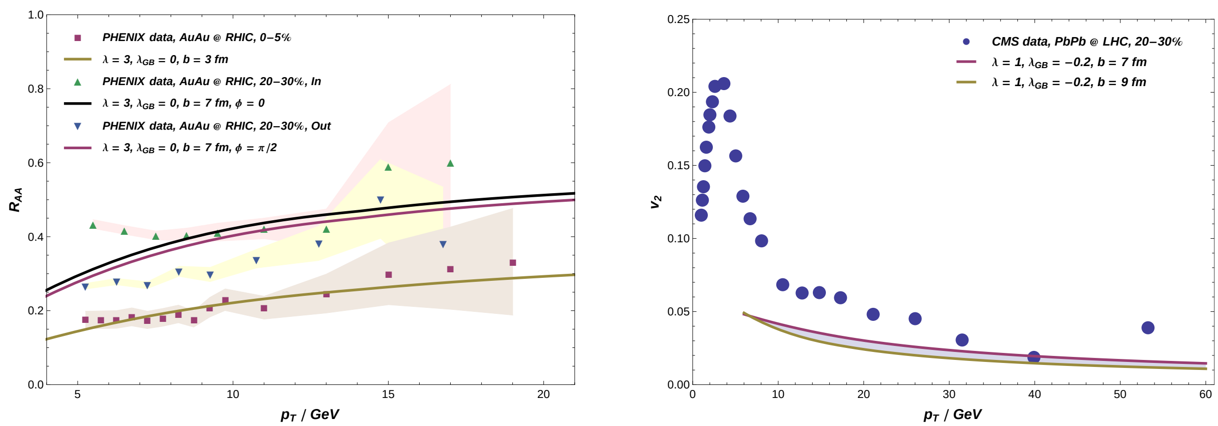

Figure 6.11: *Nuclear modification factor at RHIC in non-central collisions (left plot) and the elliptic flow parameter at the LHC (right plot). The experimental data for both RHIC [309] and LHC [75] are for the 20-30% centrality class. In the left plot we compare the R_{AA} in central collisions as well as the in and out R_{AA} in non-central collisions to our calculations for b =3 fm and b =7 fm, respectively. In the right plot, the band corresponds to the v_2 calculations for b between 7 and 9 fm. All the other parameters in these plots are the same as in Fig. 6.9.*

only from quarks, i.e. we have neglected the gluon contribution. One may worry that this is not justified, considering that the pp production spectrum for gluons is not negligible (Fig. 1.13). From the pQCD perspective, although at the pure partonic level, gluons dominate the spectrum up to very high p_T, after quenching (gluon quenching being enhanced by the 9/4 coming from the ratio of Casimirs) and then fragmentation to pions (which is softer, with $p_\pi \approx 0.5 p_g$), pion R_{AA} at moderate to high p_T is dominated by the quark jets. This has been shown explicitly in [198] and [313].

Although, at this point, we do not have a reliable way to incorporate gluons in the finite momentum picture, one may recall the "doubled" strings of [25] (discussed in Section 5.1.1), where the effect of doubling effectively leads to energy loss of gluons being two times higher than the energy loss of light quarks, which is close to the 9/4 factor from the ratio of Casimirs. In the context of finite momentum, we could perhaps envision this doubled string with a kink at the point where the string folds over, which has a finite momentum.

Since the energy flow is given only by the radial location of the finite momentum, due to the doubling of the string, the energy flow is now doubled compared to the case of a “single” string describing the light quarks. Although it is premature to say that the energy loss of gluons in this picture is simply two times the energy loss of the quarks, we could still entertain this idea and compute the pion R_{AA} in this way, and compare it to the R_{AA} calculated only from quarks, which is what we have been doing so far. This has been done in Fig. 6.12, where we see that the full pion R_{AA} $(q + g \to \pi)$ is somewhat below the $q \to \pi$ R_{AA}, but still rather close. In the case of CUJET [198], the pion R_{AA} was even better approximated by quarks, since, due to the dynamical medium effects in DGLV, the difference between quarks and gluons is somewhat more complex than the simple ratio of Casimirs.

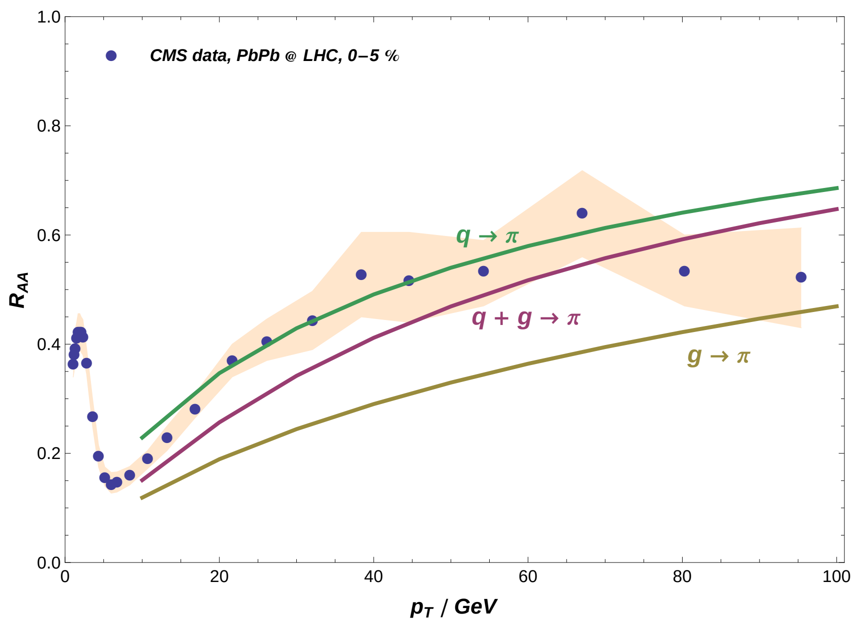

Figure 6.12: *Comparison of the pion R_{AA} at the LHC computed neglecting the gluon contribution, and including it through usage of a simple factor of 2 in the energy loss. This was done for $\lambda = 0.25$ and $\lambda_{GB} = 0$, and all the other parameters were the same as in Fig. 6.9.*

6.3.4 RHIC vs. LHC and the temperature sensitivity

It is clear that the choice of $\lambda = 1$, including the higher derivative corrections with $\lambda_{GB} = -0.2$ (which give $\eta/s = 1.8/(4\pi)$), that matches the LHC central R_{AA} data (black curve in Fig. 6.10) will result in a significant overprediction of the central RHIC data; $\lambda = 1$ with $\lambda_{GB} = -0.2$ at RHIC approximately corresponds to the $\lambda = 0.25$ case with $\lambda_{GB} = 0$, i.e. the purple curve in Fig. 6.9. Hence the simultaneous fit of the RHIC and the LHC central R_{AA} data remains a challenge in our simple constructions presented here. But we would like to point to a possible phenomenological effect that can be partially responsible for this discrepancy: the effective temperature uncertainties. Note that our energy loss formula (6.80) has a strong sensitivity to the temperature, $dE/dx \sim \sqrt{\lambda}T^3$ or even $\sqrt{\lambda}T^4$. Hence, even a small change in the temperature, $T \to \kappa T$, can have the same effect as a large change in the coupling, $\lambda \to \kappa^6\lambda$ or $\kappa^8\lambda$. For the same reasons, if we were too generous with the overall scale of the temperature we assumed in (1.65) by some small factor, this will effectively increase the coupling, and result in a fit of the LHC data for even "better" values of the coupling than in Fig. 6.10.

We cannot offer at the moment a concrete physical reason that would justify the possibility of temperature uncertainties, but we can speculate based on some very general arguments. From the perspective of the temperature formula (1.65) we see that one would expect the LHC to be roughly 30% hotter than RHIC, based on the ratio of the multiplicities. However, if the initial formation time τ_0 in the two cases is different, then the jet effectively feels a cooler or a hotter medium, according to the temperature formula (1.65) we are using. This is precisely what was suggested in [324], where the authors used a larger formation time at the LHC than at RHIC where $\tau_0 = 0.6$ fm/c [325], based on the requirements of the hydrodynamic simulations to fit the low p_T elliptic flow data. We see the effect of this in the left plot of Fig. 6.13, where changing τ_0 from 1 fm/c (blue) to

0.6 fm/c (red) for the case of $\lambda = 1$ and $\lambda_{GB} = -0.2$ (which fits the central LHC data) leads to a significant decrease in R_{AA}.

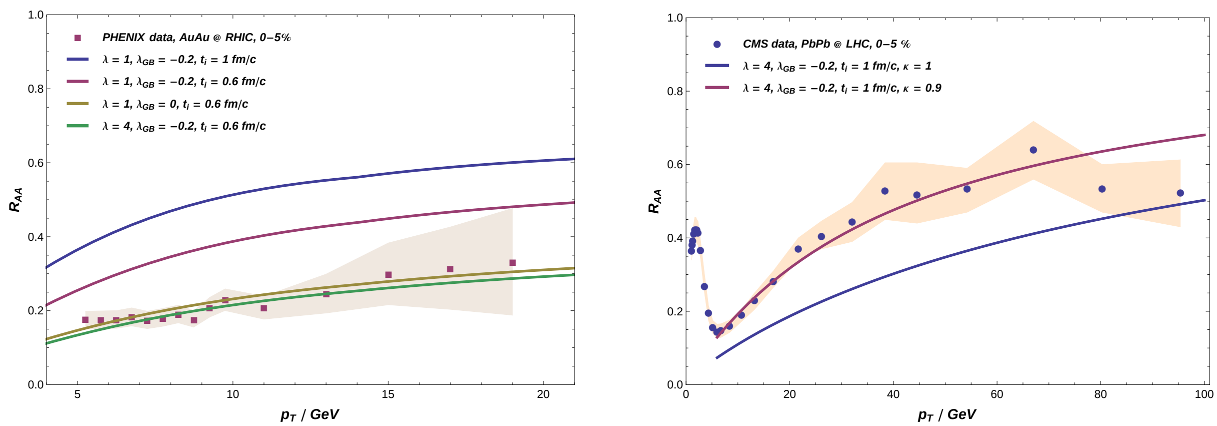

Figure 6.13: *Left: Nuclear modification factor at RHIC in central collisions for different choices of the 't Hooft coupling λ, dimensionless λ_{GB} and the formation time τ_0. Right: Nuclear modification factor at the LHC in central collisions with and without the temperature adjustment $T \to \kappa T$.*

Additionally, if we allow η/s to decrease (relative to LHC, where the temperature range is higher), which means increasing λ_{GB}, we can approach the RHIC data even more (yellow curve). We should note that this is just an illustration of the effect of the decrease of η/s on R_{AA}, as the same hydrodynamic calculations of [325] and [324] suggest that this decrease is not so strong. If we want to keep the same η/s at RHIC as it was at the LHC (meaning keeping $\lambda_{GB} = -0.2$) then we can get close to the data by increasing the coupling approximately 4 times (green curve). If we keep these parameters of the green curve and pass onto LHC (right plot of Fig (6.13)), where we set $\tau_0 = 1$ fm/c, we see that the curve is below the data (blue curve), but lowering the overall LHC temperature by only about 10% we are able to approach the data (red curve).

Another reason for seeing this surprising transparency of the LHC in our case may be the fact that we are working in a conformal theory where the coupling does not run. Hence, considering holographic duals of non-conformal field theories (as in Section 3.5), where the coupling gets an effective temperature running, may further reduce the RHIC-LHC splitting. In order to check this, we need to take the shooting string limit of (6.78), which is in this case fully numerical: one of the immediate observations is that the running of the dilaton moderately increases the energy loss at lower temperatures relative to the conformal limit, so we may expect this to affect the R_{AA} at RHIC more than at the LHC. In Fig. 6.14 we see that this is indeed so, and the non-conformal effects do bring down the RHIC R_{AA}, but this effect is not strong enough to resolve the problem entirely.

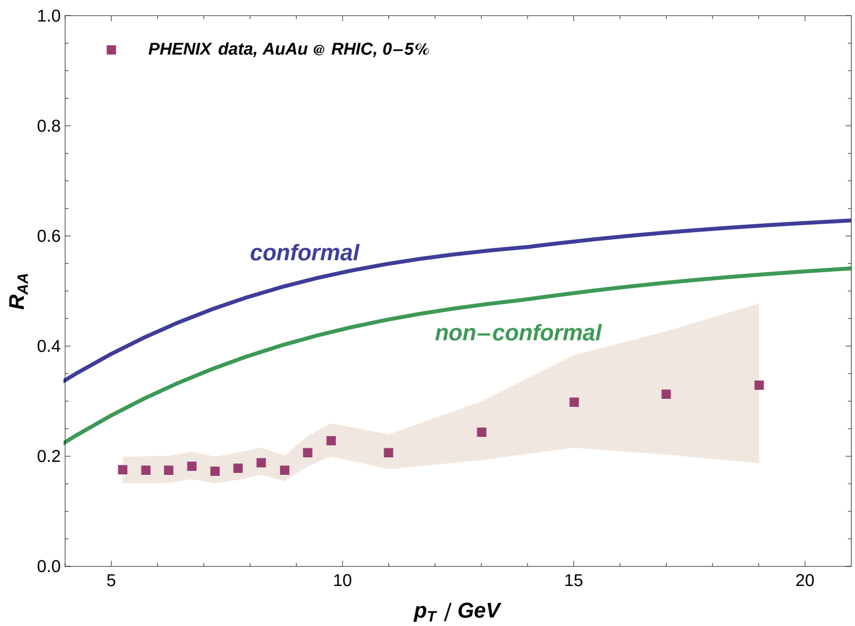

Figure 6.14: *Comparison of the shooting string R_{AA} at RHIC in the conformal and non-conformal plasma. In the conformal case, we used $\lambda = 0.25$ and $\lambda_{GB} = 0$, which fits the LHC (Fig. 6.9), while in the non-conformal case, we chose the effective coupling so that the LHC is fitted and then, keeping all the parameters fixed, calculated the R_{AA} at RHIC.*

The main message of this section is that, so far, every inclusion of some realistic effect on the gravity side (higher derivative corrections, non-conformal effects, etc.) brings us closer and closer to the data. Perhaps a consistent theoretical inclusion of all these effects at the same time could close the RHIC-LHC gap almost entirely.

Chapter 7

Conclusions

The AdS/CFT correspondence and its applications constitute a highly important and exciting theoretical endeavor, by allowing us to cast complex and generally intractable problems in strongly coupled physics into simpler calculations in classical gravity. We hope that this thesis and the work presented in it successfully illustrated this: in particular, we have used the gauge/gravity duality to gain a unique analytic insight into novel, non-equilibrium physics in strongly coupled gauge theories, inaccessible with conventional lattice or perturbative QCD techniques.

On our exciting journey, we have seen many appealing geometrical representations of various field theory phenomena: energetic quarks are represented by classical strings and their energy loss by the flux of the momentum down the string; mesons are fluctuations of D-branes; thermalization is dual to string endpoints falling into a black hole; energy density in the field theory is given by graviton fluctuations; momentum fluctuations of a heavy quark are caused by Hawking radiation originating from a horizon forming on the string worldsheet; and many other.

Apart from these intriguing qualitative pictures, holography can provide more quantitative results, including scalings of various quantities as well as, in some cases, definite numerical predictions. This includes an analytic derivation of an unexpectedly small (3/4) reduction of the entropy density in a strongly coupled plasma relative to the free gas limit, approximately observed in lattice QCD; calculation of the shear viscosity to entropy density ratio of $\eta/s = 1/(4\pi)$, applicable to a wide variety of strongly coupled systems, and a value of which was needed to explain the near perfect fluid flow observed at RHIC; a strong drag force on heavy quarks, consistent with the large heavy quark jet quenching observed at RHIC, and a natural emergence of the conical Mach cones possibly observed at RHIC; calculation of the jet quenching parameter and the stopping distance of light quarks in a strongly coupled plasma.

In this thesis we continued along this path and extended it, through quantitative studies of jet quenching in gauge/gravity duality, with special emphasis on light quarks. By constraining and confronting these calculations with the heavy ion experimental data from RHIC and LHC, our ultimate goal was to gain a better understanding of the strongly coupled quark-gluon plasma.

7.1 Summary and conclusions, chapter by chapter

The first prerequisite in applying the gauge/gravity duality to some physical system is to understand its properties. This has been addressed in Chapter 1. There we have seen that, at high enough temperatures and densities, we expect to see a phase transition from a gas of hadrons into a quark-gluon plasma, a soup of asymptotically free quarks and gluons. These extreme conditions are achievable in ultra-relativistic heavy ion collisions at RHIC and LHC, where the observation of a large elliptic flow v_2 indicated that the medium produced was a strongly coupled, near-perfect fluid, which quickly reaches the local thermal equilibrium. Another strong signal of the quark-gluon plasma formation is jet quenching, the attenuation (or disappearance) of hadrons originating from a parton that lost energy while traveling through the hot and dense medium. This is most clearly observed in the nuclear suppression factor R_{AA}, the observable of our central interest. We also presented a simple model of an expanding plasma with Glauber initial conditions that we will use in our calculations of R_{AA}.

Now that we understand some basic features of the medium, we go on to the description of the jet quenching in the standard approach of perturbative QCD, before studying it holographically. This was the subject of Chapter 2, where we have seen how the dominant mechanism of energy loss is the medium-induced gluon radiation. Among several available energy loss models, we focused on the DGLV model, where the radiative energy loss is given as an opacity expansion. With the goal of handling the realistic, "mesoscopic" case (relevant to conditions at RHIC and LHC), when the opacity is a moderately small number, we have developed a numerical code [135], based on importance sampling Monte Carlo algorithm, that allows us to compute the radiated gluon distribution at arbitrary orders in opacity. By computing the radiated gluon spectrum up to ninth order in opacity, we found that, at large gluon transverse momentum $k_\perp = xE$ (E being the energy of the jet), the gluon distribution $xdN/dxdk_\perp^2$ displays somewhat "softer" power tails ($\sim 1/k_\perp^3$), indicating the importance of keeping the (sometimes neglected) $k_\perp$ kinematic bounds finite when obtaining xdN/dx spectra. Comparison to the BDMPS formula for energy loss, where one assumes multiple soft scatterings (MSS) and neglects the finite kinematic bounds, showed that the predicted scaling of xdN/dx in BDMPS was broken at finite opacity, as well as that the radiated gluon spectrum depends in detail on the screening mass μ and the mean free path λ, and not only through a simple combination of $\hat{q} = \mu/\lambda$. Finally, by comparing the DGLV $k_\perp$-spectrum of radiated gluons (at fixed x) to the MSS limit of BDMPS/ASW, we saw how the finite opacity n nicely interpolates between the "thin" ($n = 1$) plasma approximation at large $k_\perp$ and the "thick" (MSS, $n = \infty$) approximation at low $k_\perp$.

After gaining some basic understanding of the medium and the probes we are interested in from the point of view of QCD, we start turning towards their holographic description in Chapter 3. There we saw how the AdS/CFT correspondence naturally arises as a duality between $\mathcal{N} = 4$ SYM gauge theory living on the worldvolume of N coincident D3-branes and a string theory on the AdS_5 spacetime sourced by those branes. Among many interesting aspects of the correspondence, we saw how, in order to study the theory at a finite temperature T, one needs to introduce a black hole horizon at a radial location $r_H \propto 1/T$, and that the introduction of quarks of mass M to SYM is dual to the introduction of an additional D7-brane to the geometry, which spans from the boundary $z = 0$ to $z_M \sim 1/M$. Noting the obvious differences between $\mathcal{N} = 4$ SYM and QCD, we have also considered a "bottom-up" gravity model, constructed so that its dual is a non-conformal field theory that shares some properties of QCD at finite temperature, and constrained so that it reproduces the lattice gauge theory data for thermodynamics and Polyakov loops.

Now that we have laid down all the relevant holographic tools we will need, we start with their application in Chapter 4 to study the energy loss of heavy quarks. There we saw how heavy quarks are modeled by trailing strings, where one of the endpoints, attached to the bottom of its D7-brane, is moving uniformly in one direction, while the rest of the string trails behind it. This led to a simple expression for the drag force (or energy loss) the heavy quark feels in a strongly coupled plasma. Motivated by the "heavy quark puzzle", the apparent strong jet quenching of heavy quarks observed at RHIC, we set to study how the relative relationship between the energy losses of charm and bottom quarks gets modified in the non-conformal holographic model of Chapter 3, where the QCD trace anomaly is explicitly taken into account. This is based on our work in [203] and [279]. We have found that indeed the ratio of charm and bottom quark energy losses is strongly modified in the temperature range close to T_c (and even comes rather close to unity), while at higher energies and temperatures it approaches the conformal limit, where it is given by the inverse ratio of the respective quark masses. However, computation of the heavy quark R_{AA} in an expanding plasma revealed that the discrepancy between charm and bottom quarks in this observable is still rather large and, in particular, that the charm quark is still significantly more suppressed than the bottom. Furthermore, we found that in passing from RHIC to the hotter LHC, the heavy quark R_{AA} changed very little, due to the competing decrease in the steepness of the production spectra. Extrapolating the zero-temperature positions of charm and bottom flavor D-branes to finite temperatures, we found that, at modestly high temperatures, the horizon seems to approach the bottom of the charm D-brane. Although a more rigorous theoretical treatment is needed to confirm these results, this nevertheless points to an interesting possibility that the charm quark might effectively become light, and this "hybrid" case may even be the key in reducing the gap between the charm and bottom R_{AA}.

After heavy quarks, we turn our attention to light quarks, which constitute the central part of this thesis. This starts in Chapter 5, where we study the energy loss and the stopping distance of light quarks using the model of falling strings, where the endpoints of the string are able to fall towards the horizon, as the D7-brane now fills the entire available geometry. We presented a simple analytical derivation [35] of the well known result for the maximum stopping distance of light quarks, $\Delta x \propto E^{1/3}$, that was previously reachable only through a combination of scaling arguments and numerical simulations. This method was shown to be easily extendable to other backgrounds, and an application to the case of AdS_5 geometry with Gauss-Bonnet quadratic curvature corrections quickly revealed the increase of the stopping distance, which was also verified numerically. Motivated by the lack of a well defined method for computing the instantaneous energy loss of light quarks, we have derived, by analyzing transformations of spacetime momentum fluxes on the classical string worldsheet, a general formula for instantaneous energy loss in non-stationary string configurations [33]. Application of this formula to the case of falling strings reveals that the energy loss does not display a well-pronounced Bragg peak at late times, as previously believed. More importantly, the energy loss at intermediate times, although susceptible to the initial conditions and "jet" definitions, had a seemingly linear path length dependence, similar to the standard result in pQCD. We also provided an analytical proof of this [36]. Finally, based on this result, we developed a phenomenological model of light quark energy loss [34], and used it to compute the R_{AA}. Comparison of our calculations with the light hadron suppression data at the LHC showed that, although R_{AA} had the right qualitative structure, the magnitude was too small, even after the Gauss-Bonnet higher derivative corrections were included. This indicated that the predicted jet quenching was simply too strong and that we may need more radical ideas to bring the holographic calculations close to the data without leaving the regime of validity of the supergravity approximation.

The last Chapter 6 represents perhaps our most original contribution. Partly motivated by the aforementioned inability to come close to the data, in [35] we considered a novel idea that classical strings can have finite momentum at their endpoints. We demonstrated how the finite momentum was needed in order to obtain an energy conserving description of the special yo-yo type string configurations in gauges where the worldsheet mapping was non-degenerate and one-to-one. Although it may seem that adding this extra boundary condition could additionally complicate the already complex classical string dynamics, it turns out it actually simplifies it: we found that the finite momentum endpoints exactly follow null geodesics in a general, curved spacetime. We also took the first steps to show that these ideas can be extended to the fermionic sector of the classical string: we showed that it is possible to generalize the Green-Schwarz superstring action in the light-cone gauge in flat space to include the finite endpoint momentum, while preserving all the supercharges. We then found that adding the finite momentum to the endpoints increases their stopping distance by about 20% with respect to the previous treatments with the falling strings. In other words, quark jets dual to these strings are less quenched, signaling a potentially better match with the experimental data. We have also demonstrated how one can numerically generate the string solutions with finite endpoint momentum, in cases when both of the endpoints are above the horizon and when one is behind it.

From the phenomenological perspective, the introduction of finite endpoint momentum leads to a perhaps more realistic description of energetic quarks as the endpoints themselves, with the string between them representing the color field they generate. In this way, one also obtains a clear distinction between the energy in the hard probe and energy contained in the color fields surrounding it, hence offering an unambiguous definition of the instantaneous jet energy loss that was missing in the previous treatments of the falling strings: the energy loss is simply identified with the flux of the energy from the endpoint into the bulk of the string. This energy loss is shown to have a strikingly simple form: it is independent of the energy stored in the endpoint, the details of the initial conditions and even the bulk shape of the string. It is essentially only a function of the radial location of the endpoint, hence allowing for a straightforward application to more general gravity duals. We finally describe the phenomenological implementation of these ideas from our [36], where, by assuming that the endpoints start close to the horizon (the "shooting string" limit), we arrived at a simple and phenomenologically usable novel formula for energy loss of light quarks. This formula nicely interpolates between the linear and the novel quadratic path length dependencies. Application of this shooting string formula (including the higher derivative corrections), showed, independently, a very good match with the central R_{AA} data for light hadrons at RHIC and LHC for reasonable choice of parameters, something that was not possible before with falling strings. We saw how a consistent simultaneous match of both the RHIC and the LHC data remains challenging, but we argued that the temperature sensitivity of our formula coupled with the uncertainties in the formation time of the plasma and the shear viscosity may enable us to reconcile these differences. We have also shown how the inclusion of non-conformal effects, which provide an effective temperature running of the coupling, provides an additional reduction of this RHIC-LHC splitting.

7.2 Prospects and outlook

Introduction of the finite endpoint momentum has opened doors to many possible future research avenues. On the formal side, there are several developments that seem natural. For instance, one may consider a doubled string with a finite energy on its folding point, or even strings with several double backs. An interesting generalization of these ideas is the consideration of finite energy and momentum on the worldvolume of D-branes and whether a better understanding of such localized momentum can help with the quantization of branes. Another interesting question is whether the supersymmetric generalization of the bosonic string with finite momentum endpoints holds in more general spacetimes and gauges, and whether one can still realize the κ-symmetry. Also, the investigation of the effects of finite g_s-corrections to the dynamics of finite endpoint momentum strings hanging from D-branes may lead to an effective mass for the endpoints and have interesting consequences for energy loss.

On the phenomenological side, perhaps the first immediate goal could be the application of the finite endpoint momentum framework to the case of heavy quarks and the effect this would have on the suppression of non-photonic electrons. Closely related to this is an investigation of a more unified treatment of both heavy and light quarks (and gluons) that this framework offers, which is not only theoretically appealing, but it may also allow for a more consistent treatment of the possibly "hybrid" case of the charm quark energy loss. Another important question that is at the basis of any energy loss calculation is that of the relevant initial conditions; that is, in what initial state should one prepare a string whose dual description is relevant for describing energetic jets in a realistic quark-gluon plasma? We have mentioned before how a consistent theoretical framework that can account simultaneously for the dependence of various hard probe observables on beam energy and centrality may still be missing, and perhaps finite endpoint momentum can help here as well. Maybe considering more phenomenological versions of the shooting string energy loss of the form $dE/dx \propto a(b+\pi T x)^2$ may provide a combination of path length dependencies that can help achieve a simultaneous match of the high-p_T v_2 and central R_{AA} data. Also, more realistic non-conformal models of the plasma and more realistic distributions of the shooting string initial conditions may help in reconciling the gap in the simultaneous match of the central RHIC and LHC data, as already signaled by some of our first attempts.

In conclusion, there are several interesting puzzles raised by the experimental data accumulated by RHIC and LHC, whose consistent theoretical description still seems to be challenging. Realistic holographic modeling of the medium and the relevant strongly coupled processes should be the key in inspecting to what extent the strongly coupled physics plays a role in them. We are now in a position to address these and other issues with the AdS/CFT correspondence better than ever before: we have powerful theoretical tools at hand and plethora of experimental data with high discriminative power. All this represents exciting opportunities for the ongoing program of applications of AdS/CFT to QCD, and will surely generate new theoretical ideas and interesting physics.

Bibliography

[1] G. 't Hooft, "Dimensional reduction in quantum gravity", gr-qc/9310026.

[2] L. Susskind, "The World as a hologram", *J.Math.Phys.* **36** (1995) 6377–6396, [hep-th/9409089].

[3] J. M. Maldacena, "The Large N limit of superconformal field theories and supergravity", *Adv.Theor.Math.Phys.* **2** (1998) 231–252, [hep-th/9711200].

[4] S. Gubser, I. R. Klebanov, and A. M. Polyakov, "Gauge theory correlators from noncritical string theory", *Phys.Lett.* **B428** (1998) 105–114, [hep-th/9802109].

[5] E. Witten, "Anti-de Sitter space and holography", *Adv.Theor.Math.Phys.* **2** (1998) 253–291, [hep-th/9802150].

[6] M. Gyulassy and L. McLerran, "New forms of QCD matter discovered at RHIC", *Nucl.Phys.* **A750** (2005) 30–63, [nucl-th/0405013].

[7] **PHENIX** Collaboration, K. Adcox *et. al.*, "Formation of dense partonic matter in relativistic nucleus-nucleus collisions at RHIC: Experimental evaluation by the PHENIX collaboration", *Nucl.Phys.* **A757** (2005) 184–283, [nucl-ex/0410003].

[8] **STAR** Collaboration, J. Adams *et. al.*, "Experimental and theoretical challenges in the search for the quark gluon plasma: The STAR Collaboration's critical assessment of the evidence from RHIC collisions", *Nucl.Phys.* **A757** (2005) 102–183, [nucl-ex/0501009].

[9] B. Back, M. Baker, M. Ballintijn, D. Barton, B. Becker, *et. al.*, "The PHOBOS perspective on discoveries at RHIC", *Nucl.Phys.* **A757** (2005) 28–101, [nucl-ex/0410022].

[10] **BRAHMS** Collaboration, I. Arsene *et. al.*, "Quark gluon plasma and color glass condensate at RHIC? The Perspective from the BRAHMS experiment", *Nucl.Phys.* **A757** (2005) 1–27, [nucl-ex/0410020].

[11] M. Luzum and P. Romatschke, "Conformal Relativistic Viscous Hydrodynamics: Applications to RHIC results at s(NN)**(1/2) = 200-GeV", *Phys.Rev.* **C78** (2008) 034915, [arXiv:0804.4015].

[12] **PHENIX** Collaboration, K. Adcox *et. al.*, "Suppression of hadrons with large transverse momentum in central Au+Au collisions at $\sqrt{s_{NN}} = 130$-GeV", *Phys.Rev.Lett.* **88** (2002) 022301, [nucl-ex/0109003].

[13] **STAR** Collaboration, J. Adams *et. al.*, "Transverse momentum and collision energy dependence of high p(T) hadron suppression in Au+Au collisions at ultrarelativistic energies", *Phys.Rev.Lett.* **91** (2003) 172302, [nucl-ex/0305015].

[14] **BRAHMS** Collaboration, I. Arsene *et. al.*, "Transverse momentum spectra in Au+Au and d+Au collisions at s**(1/2) = 200-GeV and the pseudorapidity dependence of high p(T) suppression", *Phys.Rev.Lett.* **91** (2003) 072305, [nucl-ex/0307003].

[15] M. Gyulassy, I. Vitev, X.-N. Wang, and B.-W. Zhang, "Jet quenching and radiative energy loss in dense nuclear matter", nucl-th/0302077.

[16] R. Baier, D. Schiff, and B. Zakharov, "Energy loss in perturbative QCD", *Ann.Rev.Nucl.Part.Sci.* **50** (2000) 37–69, [hep-ph/0002198].

[17] A. Majumder and M. Van Leeuwen, "The Theory and Phenomenology of Perturbative QCD Based Jet Quenching", *Prog.Part.Nucl.Phys.* **A66** (2011) 41–92, [arXiv:1002.2206].

[18] D. d'Enterria, "Jet quenching", arXiv:0902.2011.

[19] A. Karch and E. Katz, "Adding flavor to AdS / CFT", *JHEP* **0206** (2002) 043, [hep-th/0205236].

[20] S. Gubser, I. R. Klebanov, and A. Peet, "Entropy and temperature of black 3-branes", *Phys.Rev.* **D54** (1996) 3915–3919, [hep-th/9602135].

[21] E. Witten, "Anti-de Sitter space, thermal phase transition, and confinement in gauge theories", *Adv.Theor.Math.Phys.* **2** (1998) 505–532, [hep-th/9803131].

[22] S. S. Gubser, "Drag force in AdS/CFT", *Phys.Rev.* **D74** (2006) 126005, [hep-th/0605182].

[23] C. Herzog, A. Karch, P. Kovtun, C. Kozcaz, and L. Yaffe, "Energy loss of a heavy quark moving through N=4 supersymmetric Yang-Mills plasma", *JHEP* **0607** (2006) 013, [hep-th/0605158].

[24] P. M. Chesler, K. Jensen, and A. Karch, "Jets in strongly-coupled N = 4 super Yang-Mills theory", *Phys. Rev.* **D79** (2009) 025021, [arXiv:0804.3110].

[25] S. S. Gubser, D. R. Gulotta, S. S. Pufu, and F. D. Rocha, "Gluon energy loss in the gauge-string duality", *JHEP* **0810** (2008) 052, [arXiv:0803.1470].

[26] O. DeWolfe, S. S. Gubser, C. Rosen, and D. Teaney, "Heavy ions and string theory", *Prog.Part.Nucl.Phys.* **75** (2014) 86–132, [arXiv:1304.7794].

[27] I. R. Klebanov and M. J. Strassler, "Supergravity and a confining gauge theory: Duality cascades and chi SB resolution of naked singularities", *JHEP* **0008** (2000) 052, [hep-th/0007191].

[28] T. Sakai and S. Sugimoto, "Low energy hadron physics in holographic QCD", *Prog.Theor.Phys.* **113** (2005) 843–882, [hep-th/0412141].

[29] U. Gursoy and E. Kiritsis, "Exploring improved holographic theories for QCD: Part I", *JHEP* **0802** (2008) 032, [arXiv:0707.1324].

[30] U. Gursoy, E. Kiritsis, and F. Nitti, "Exploring improved holographic theories for QCD: Part II", *JHEP* **0802** (2008) 019, [arXiv:0707.1349].

[31] S. S. Gubser and A. Nellore, "Mimicking the QCD equation of state with a dual black hole", *Phys.Rev.* **D78** (2008) 086007, [arXiv:0804.0434].

[32] S. S. Gubser, A. Nellore, S. S. Pufu, and F. D. Rocha, "Thermodynamics and bulk viscosity of approximate black hole duals to finite temperature quantum chromodynamics", *Phys.Rev.Lett.* **101** (2008) 131601, [arXiv:0804.1950].

[33] A. Ficnar, "AdS/CFT Energy Loss in Time-Dependent String Configurations", *Phys.Rev.* **D86** (2012) 046010, [arXiv:1201.1780].

[34] A. Ficnar, J. Noronha, and M. Gyulassy, "Falling Strings and Light Quark Jet Quenching at LHC", *Nucl. Phys.* **A910-911** (2013) 252–255, [arXiv:1208.0305].

[35] A. Ficnar and S. S. Gubser, "Finite momentum at string endpoints", *Phys.Rev.* **D89** (2014) 026002, [arXiv:1306.6648].

[36] A. Ficnar, S. S. Gubser, and M. Gyulassy, "Shooting String Holography of Jet Quenching at RHIC and LHC", arXiv:1311.6160.

[37] M. Gell-Mann, "A Schematic Model of Baryons and Mesons", *Phys.Lett.* **8** (1964) 214–215.

[38] G. Zweig, "An SU(3) model for strong interaction symmetry and its breaking", *CERN-TH-401* (1964).

[39] M. Han and Y. Nambu, "Three Triplet Model with Double SU(3) Symmetry", *Phys.Rev.* **139** (1965) B1006–B1010.

[40] M. Gell-Mann and Y. Ne'eman, *The Eightfold Way.* Westview Press, 2000.

[41] V. Barnes, P. Connolly, D. Crennell, B. Culwick, W. Delaney, *et. al.*, "Observation of a Hyperon with Strangeness -3", *Phys.Rev.Lett.* **12** (1964) 204–206.

[42] M. Breidenbach, J. I. Friedman, H. W. Kendall, E. D. Bloom, D. Coward, *et. al.*, "Observed Behavior of Highly Inelastic electron-Proton Scattering", *Phys.Rev.Lett.* **23** (1969) 935–939.

[43] E. D. Bloom, D. Coward, H. DeStaebler, J. Drees, G. Miller, *et. al.*, "High-Energy Inelastic e p Scattering at 6-Degrees and 10-Degrees", *Phys.Rev.Lett.* **23** (1969) 930–934.

[44] **TASSO** Collaboration, R. Brandelik *et. al.*, "Evidence for Planar Events in e+ e- Annihilation at High-Energies", *Phys.Lett.* **B86** (1979) 243.

[45] C. Chang, K. Chen, D. Fox, A. Kotlewski, P. F. Kunz, *et. al.*, "Observed Deviations from Scale Invariance in High-Energy Muon Scattering", *Phys.Rev.Lett.* **35** (1975) 901.

[46] J. Christenson, G. Hicks, L. Lederman, P. Limon, B. Pope, *et. al.*, "Observation of massive muon pairs in hadron collisions", *Phys.Rev.Lett.* **25** (1970) 1523–1526.

[47] D. Gross and F. Wilczek, "Asymptotically Free Gauge Theories. 1", *Phys.Rev.* **D8** (1973) 3633–3652.

[48] H. D. Politzer, "Reliable Perturbative Results for Strong Interactions?", *Phys.Rev.Lett.* **30** (1973) 1346–1349.

[49] G. 't Hooft, "Unpublished", .

[50] H. Leutwyler, "On the foundations of chiral perturbation theory", *Annals Phys.* **235** (1994) 165–203, [hep-ph/9311274].

[51] Y. Nambu, "Strings, Monopoles and Gauge Fields", *Phys.Rev.* **D10** (1974) 4262.

[52] M. A. Shifman, A. Vainshtein, and V. I. Zakharov, "QCD and Resonance Physics. Sum Rules", *Nucl.Phys.* **B147** (1979) 385–447.

[53] A. Irving and R. Worden, "Regge Phenomenology", *Phys.Rept.* **34** (1977) 117–231.

[54] A. Chodos, R. Jaffe, K. Johnson, C. B. Thorn, and V. Weisskopf, "A New Extended Model of Hadrons", *Phys.Rev.* **D9** (1974) 3471–3495.

[55] A. Chodos, R. Jaffe, K. Johnson, and C. B. Thorn, "Baryon Structure in the Bag Theory", *Phys.Rev.* **D10** (1974) 2599.

[56] T. A. DeGrand, R. Jaffe, K. Johnson, and J. Kiskis, "Masses and Other Parameters of the Light Hadrons", *Phys.Rev.* **D12** (1975) 2060.

[57] F. Karsch, "Lattice QCD at high temperature and density", *Lect.Notes Phys.* **583** (2002) 209–249, [hep-lat/0106019].

[58] K. G. Wilson, "Confinement of Quarks", *Phys.Rev.* **D10** (1974) 2445–2459.

[59] F. Karsch, E. Laermann, and A. Peikert, "The Pressure in two flavor, (2+1)-flavor and three flavor QCD", *Phys.Lett.* **B478** (2000) 447–455, [hep-lat/0002003].

[60] F. Karsch, E. Laermann, and A. Peikert, "Quark mass and flavor dependence of the QCD phase transition", *Nucl.Phys.* **B605** (2001) 579–599, [hep-lat/0012023].

[61] S. Borsanyi, G. Endrodi, Z. Fodor, A. Jakovac, S. D. Katz, *et. al.*, "The QCD equation of state with dynamical quarks", *JHEP* **1011** (2010) 077, [arXiv:1007.2580].

[62] A. Bazavov, T. Bhattacharya, M. Cheng, N. Christ, C. DeTar, *et. al.*, "Equation of state and QCD transition at finite temperature", *Phys.Rev.* **D80** (2009) 014504, [arXiv:0903.4379].

[63] M. Cheng, S. Ejiri, P. Hegde, F. Karsch, O. Kaczmarek, *et. al.*, "Equation of State for physical quark masses", *Phys.Rev.* **D81** (2010) 054504, [arXiv:0911.2215].

[64] P. Hasenfratz and F. Karsch, "Chemical Potential on the Lattice", *Phys.Lett.* **B125** (1983) 308.

[65] "How Low Can RHIC Go?". http://www.bnl.gov/newsroom/news.php?a=21870.

[66] "Report of the workshop on BeV/nucleon collisions of heavy ions – how and why". Bear Mountain, New York, Nov. 29 – Dec. 1, 1974 (BNL-AUI, 1975).

[67] "A new state of matter created at CERN". http://newstate-matter.web.cern.ch/newstate-matter/Experiments.html.

[68] **PHOBOS** Collaboration, B. Back *et. al.*, "Charged-particle pseudorapidity distributions in Au+Au collisions at $s(NN)^{1/2} = 62.4$-GeV", *Phys.Rev.* **C74** (2006) 021901, [nucl-ex/0509034].

[69] **ALICE** Collaboration, K. Aamodt *et. al.*, "Charged-particle multiplicity density at mid-rapidity in central Pb-Pb collisions at $\sqrt{s_{NN}} = 2.76$ TeV", *Phys.Rev.Lett.* **105** (2010) 252301, [arXiv:1011.3916].

[70] J. Bjorken, "Highly Relativistic Nucleus-Nucleus Collisions: The Central Rapidity Region", *Phys.Rev.* **D27** (1983) 140–151.

[71] **PHENIX Collaboration** Collaboration, S. Adler *et. al.*, "Identified charged particle spectra and yields in Au+Au collisions at S(NN)**1/2 = 200-GeV", *Phys.Rev.* **C69** (2004) 034909, [nucl-ex/0307022].

[72] B. Muller, "Investigation of Hot QCD Matter: Theoretical Aspects", arXiv:1309.7616.

[73] **ALICE** Collaboration, K. Aamodt *et. al.*, "Elliptic flow of charged particles in Pb-Pb collisions at 2.76 TeV", *Phys.Rev.Lett.* **105** (2010) 252302, [arXiv:1011.3914].

[74] **ATLAS** Collaboration, G. Aad *et. al.*, "Measurement of the azimuthal anisotropy for charged particle production in $\sqrt{s_{NN}} = 2.76$ TeV lead-lead collisions with the ATLAS detector", *Phys.Rev.* **C86** (2012) 014907, [arXiv:1203.3087].

[75] **CMS** Collaboration, S. Chatrchyan *et. al.*, "Azimuthal anisotropy of charged particles at high transverse momenta in PbPb collisions at $\sqrt{s_{NN}} = 2.76$ TeV", *Phys.Rev.Lett.* **109** (2012) 022301, [arXiv:1204.1850].

[76] **STAR** Collaboration, J. Adams *et. al.*, "Azimuthal anisotropy in Au+Au collisions at s(NN)**(1/2) = 200-GeV", *Phys.Rev.* **C72** (2005) 014904, [nucl-ex/0409033].

[77] **STAR** Collaboration, B. Abelev *et. al.*, "Centrality dependence of charged hadron and strange hadron elliptic flow from s(NN)**(1/2) = 200-GeV Au + Au collisions", *Phys.Rev.* **C77** (2008) 054901, [arXiv:0801.3466].

[78] P. B. Arnold, G. D. Moore, and L. G. Yaffe, "Transport coefficients in high temperature gauge theories. 1. Leading log results", *JHEP* **0011** (2000) 001, [hep-ph/0010177].

[79] C. Gale, S. Jeon, and B. Schenke, "Hydrodynamic Modeling of Heavy-Ion Collisions", *Int.J.Mod.Phys.* **A28** (2013) 1340011, [arXiv:1301.5893].

[80] J. Bjorken, "Energy Loss of Energetic Partons in Quark - Gluon Plasma: Possible Extinction of High p(t) Jets in Hadron - Hadron Collisions", .

[81] J. C. Collins, D. E. Soper, and G. F. Sterman, "Factorization of Hard Processes in QCD", *Adv.Ser.Direct.High Energy Phys.* **5** (1988) 1–91, [hep-ph/0409313].

[82] N. Armesto, "Nuclear shadowing", *J.Phys.* **G32** (2006) R367–R394, [hep-ph/0604108].

[83] **ALICE** Collaboration, K. Aamodt *et. al.*, "Suppression of Charged Particle Production at Large Transverse Momentum in Central Pb–Pb Collisions at $\sqrt{s_{NN}} = 2.76$ TeV", *Phys.Lett.* **B696** (2011) 30–39, [arXiv:1012.1004].

[84] **CMS** Collaboration, S. Chatrchyan *et. al.*, "Study of high-pT charged particle suppression in PbPb compared to *pp* collisions at $\sqrt{s_{NN}} = 2.76$ TeV", *Eur.Phys.J.* **C72** (2012) 1945, [arXiv:1202.2554].

[85] **PHENIX** Collaboration, A. Adare *et. al.*, "Suppression pattern of neutral pions at high transverse momentum in Au + Au collisions at s(NN)**(1/2) = 200-GeV and constraints on medium transport coefficients", *Phys.Rev.Lett.* **101** (2008) 232301, [arXiv:0801.4020].

[86] J. Cronin, H. J. Frisch, M. Shochet, J. Boymond, R. Mermod, *et. al.*, "Production of Hadrons with Large Transverse Momentum at 200-GeV, 300-GeV, and 400-GeV", *Phys.Rev.* **D11** (1975) 3105.

[87] **PHENIX** Collaboration, S. Adler *et. al.*, "Absence of suppression in particle production at large transverse momentum in S(NN)**(1/2) = 200-GeV d + Au collisions", *Phys.Rev.Lett.* **91** (2003) 072303, [nucl-ex/0306021].

[88] **STAR** Collaboration, J. Adams *et. al.*, "Evidence from d + Au measurements for final state suppression of high p(T) hadrons in Au+Au collisions at RHIC", *Phys.Rev.Lett.* **91** (2003) 072304, [nucl-ex/0306024].

[89] **PHENIX** Collaboration, S. Adler *et. al.*, "Centrality dependence of direct photon production in s(NN)**(1/ 2) = 200-GeV Au + Au collisions", *Phys.Rev.Lett.* **94** (2005) 232301, [nucl-ex/0503003].

[90] **PHENIX** Collaboration, S. Adler *et. al.*, "Common suppression pattern of eta and pi0 mesons at high transverse momentum in Au+Au collisions at S(NN)**(1/2) = 200-GeV", *Phys.Rev.Lett.* **96** (2006) 202301, [nucl-ex/0601037].

[91] **PHENIX** Collaboration, S. Adler *et. al.*, "High p_T charged hadron suppression in Au + Au collisions at $\sqrt{s}_{NN} = 200$ GeV", *Phys.Rev.* **C69** (2004) 034910, [nucl-ex/0308006].

[92] H. Stoecker, "Collective flow signals the quark gluon plasma", *Nucl.Phys.* **A750** (2005) 121–147, [nucl-th/0406018].

[93] T. Matsui and H. Satz, "J/ψ Suppression by Quark-Gluon Plasma Formation", *Phys.Lett.* **B178** (1986) 416.

[94] P. Koch, B. Muller, and J. Rafelski, "Strangeness in Relativistic Heavy Ion Collisions", *Phys.Rept.* **142** (1986) 167–262.

[95] L. McLerran, "The CGC and the Glasma: Two Lectures at the Yukawa Insitute", *Prog.Theor.Phys.Suppl.* **187** (2011) 17–30, [arXiv:1011.3204].

[96] **H1 and ZEUS** Collaboration, F. Aaron *et. al.*, "Combined Measurement and QCD Analysis of the Inclusive e+- p Scattering Cross Sections at HERA", *JHEP* **1001** (2010) 109, [arXiv:0911.0884].

[97] L. D. McLerran and R. Venugopalan, "Computing quark and gluon distribution functions for very large nuclei", *Phys.Rev.* **D49** (1994) 2233–2241, [hep-ph/9309289].

[98] L. D. McLerran and R. Venugopalan, "Gluon distribution functions for very large nuclei at small transverse momentum", *Phys.Rev.* **D49** (1994) 3352–3355, [hep-ph/9311205].

[99] E. Iancu, A. Leonidov, and L. D. McLerran, "Nonlinear gluon evolution in the color glass condensate. 1.", *Nucl.Phys.* **A692** (2001) 583–645, [hep-ph/0011241].

[100] J. Jalilian-Marian, A. Kovner, A. Leonidov, and H. Weigert, "The Wilson renormalization group for low x physics: Towards the high density regime", *Phys.Rev.* **D59** (1998) 014014, [hep-ph/9706377].

[101] J. Jalilian-Marian, A. Kovner, A. Leonidov, and H. Weigert, "The BFKL equation from the Wilson renormalization group", *Nucl.Phys.* **B504** (1997) 415–431, [hep-ph/9701284].

[102] J. Jalilian-Marian, A. Kovner, L. D. McLerran, and H. Weigert, "The Intrinsic glue distribution at very small x", *Phys.Rev.* **D55** (1997) 5414–5428, [hep-ph/9606337].

[103] Y. V. Kovchegov, "NonAbelian Weizsacker-Williams field and a two-dimensional effective color charge density for a very large nucleus", *Phys.Rev.* **D54** (1996) 5463–5469, [hep-ph/9605446].

[104] E. Iancu and L. D. McLerran, "Saturation and universality in QCD at small x", *Phys.Lett.* **B510** (2001) 145–154, [hep-ph/0103032].

[105] L. D. McLerran, "The Color glass condensate and small x physics: Four lectures", *Lect.Notes Phys.* **583** (2002) 291–334, [hep-ph/0104285].

[106] T. Lappi, "Production of gluons in the classical field model for heavy ion collisions", *Phys.Rev.* **C67** (2003) 054903, [hep-ph/0303076].

[107] A. Kovner, L. D. McLerran, and H. Weigert, "Gluon production from nonAbelian Weizsacker-Williams fields in nucleus-nucleus collisions", *Phys.Rev.* **D52** (1995) 6231–6237, [hep-ph/9502289].

[108] A. Kovner, L. D. McLerran, and H. Weigert, "Gluon production at high transverse momentum in the McLerran-Venugopalan model of nuclear structure functions", *Phys.Rev.* **D52** (1995) 3809–3814, [hep-ph/9505320].

[109] A. Krasnitz and R. Venugopalan, "Nonperturbative computation of gluon minijet production in nuclear collisions at very high-energies", *Nucl.Phys.* **B557** (1999) 237, [hep-ph/9809433].

[110] A. Krasnitz and R. Venugopalan, "The Initial energy density of gluons produced in very high-energy nuclear collisions", *Phys.Rev.Lett.* **84** (2000) 4309–4312, [hep-ph/9909203].

[111] T. Lappi and L. McLerran, "Some features of the glasma", *Nucl.Phys.* **A772** (2006) 200–212, [hep-ph/0602189].

[112] V. Greco, C. Ko, and P. Levai, "Parton coalescence and anti-proton / pion anomaly at RHIC", *Phys.Rev.Lett.* **90** (2003) 202302, [nucl-th/0301093].

[113] R. Fries, B. Muller, C. Nonaka, and S. Bass, "Hadronization in heavy ion collisions: Recombination and fragmentation of partons", *Phys.Rev.Lett.* **90** (2003) 202303, [nucl-th/0301087].

[114] A. Andronic, P. Braun-Munzinger, and J. Stachel, "Hadron production in central nucleus-nucleus collisions at chemical freeze-out", *Nucl.Phys.* **A772** (2006) 167–199, [nucl-th/0511071].

[115] F. Cooper and G. Frye, "Comment on the Single Particle Distribution in the Hydrodynamic and Statistical Thermodynamic Models of Multiparticle Production", *Phys.Rev.* **D10** (1974) 186.

[116] R. Glauber and G. Matthiae, “High-energy scattering of protons by nuclei”, *Nucl.Phys.* **B21** (1970) 135–157.

[117] M. L. Miller, K. Reygers, S. J. Sanders, and P. Steinberg, “Glauber modeling in high energy nuclear collisions”, *Ann.Rev.Nucl.Part.Sci.* **57** (2007) 205–243, [nucl-ex/0701025].

[118] R. Vogt, *Ultrarelativistic heavy-ion collisions.* Elsevier, 2007.

[119] R. D. Woods and D. S. Saxon, “Diffuse Surface Optical Model for Nucleon-Nuclei Scattering”, *Phys.Rev.* **95** (1954) 577–578.

[120] W.-T. Deng, X.-N. Wang, and R. Xu, “Hadron production in p+p, p+Pb, and Pb+Pb collisions with the HIJING 2.0 model at energies available at the CERN Large Hadron Collider”, *Phys.Rev.* **C83** (2011) 014915, [arXiv:1008.1841].

[121] M. Gyulassy, I. Vitev, X.-N. Wang, and P. Huovinen, “Transverse expansion and high p(T) azimuthal asymmetry at RHIC”, *Phys.Lett.* **B526** (2002) 301–308, [nucl-th/0109063].

[122] B. Betz and M. Gyulassy, “Azimuthal Jet Tomography of Quark Gluon Plasmas at RHIC and LHC”, arXiv:1305.6458.

[123] M. Luzum and P. Romatschke, “Viscous Hydrodynamic Predictions for Nuclear Collisions at the LHC”, *Phys.Rev.Lett.* **103** (2009) 262302, [arXiv:0901.4588].

[124] H. Song and U. W. Heinz, “Multiplicity scaling in ideal and viscous hydrodynamics”, *Phys.Rev.* **C78** (2008) 024902, [arXiv:0805.1756].

[125] C. Shen, U. Heinz, P. Huovinen, and H. Song, “Systematic parameter study of hadron spectra and elliptic flow from viscous hydrodynamic simulations of Au+Au collisions at $\sqrt{s_{NN}} = 200$ GeV”, *Phys.Rev.* **C82** (2010) 054904, [arXiv:1010.1856].

[126] T. Renk, H. Holopainen, U. Heinz, and C. Shen, “A Systematic comparison of jet quenching in different fluid-dynamical models”, *Phys.Rev.* **C83** (2011) 014910, [arXiv:1010.1635].

[127] X.-N. Wang, “Private communication”.

[128] M. Cacciari, P. Nason, and R. Vogt, "QCD predictions for charm and bottom production at RHIC", *Phys.Rev.Lett.* **95** (2005) 122001, [hep-ph/0502203].

[129] V. Gribov and L. Lipatov, "Deep inelastic e p scattering in perturbation theory", *Sov.J.Nucl.Phys.* **15** (1972) 438–450.

[130] G. Altarelli and G. Parisi, "Asymptotic Freedom in Parton Language", *Nucl.Phys.* **B126** (1977) 298.

[131] Y. L. Dokshitzer, "Calculation of the Structure Functions for Deep Inelastic Scattering and e+ e- Annihilation by Perturbation Theory in Quantum Chromodynamics.", *Sov.Phys.JETP* **46** (1977) 641–653.

[132] B. A. Kniehl, G. Kramer, and B. Potter, "Fragmentation functions for pions, kaons, and protons at next-to-leading order", *Nucl.Phys.* **B582** (2000) 514–536, [hep-ph/0010289].

[133] C. Peterson, D. Schlatter, I. Schmitt, and P. M. Zerwas, "Scaling Violations in Inclusive e+ e- Annihilation Spectra", *Phys.Rev.* **D27** (1983) 105.

[134] M. Djordjevic, M. Gyulassy, R. Vogt, and S. Wicks, "Influence of bottom quark jet quenching on single electron tomography of Au + Au", *Phys.Lett.* **B632** (2006) 81–86, [nucl-th/0507019].

[135] A. Buzzatti, A. Ficnar, and M. Gyulassy, "Radiative energy loss at intermediate opacity", *Unpublished*.

[136] M. H. Thoma and M. Gyulassy, "Quark Damping and Energy Loss in the High Temperature QCD", *Nucl.Phys.* **B351** (1991) 491–506.

[137] E. Braaten and M. H. Thoma, "Energy loss of a heavy quark in the quark - gluon plasma", *Phys.Rev.* **D44** (1991) 2625–2630.

[138] E. Braaten and M. H. Thoma, "Energy loss of a heavy fermion in a hot plasma", *Phys.Rev.* **D44** (1991) 1298–1310.

[139] S. Peigne and A. Peshier, "Collisional energy loss of a fast heavy quark in a quark-gluon plasma", *Phys.Rev.* **D77** (2008) 114017, [arXiv:0802.4364].

[140] M. Djordjevic and U. Heinz, “Radiative heavy quark energy loss in a dynamical QCD medium”, *Phys.Rev.* **C77** (2008) 024905, [arXiv:0705.3439].

[141] R. D. Field, *Applications of perturbative QCD*. Addison-Wesley, 1989.

[142] M. Gyulassy, P. Levai, and I. Vitev, “Reaction operator approach to nonAbelian energy loss”, *Nucl.Phys.* **B594** (2001) 371–419, [nucl-th/0006010].

[143] Y. L. Dokshitzer and D. Kharzeev, “Heavy quark colorimetry of QCD matter”, *Phys.Lett.* **B519** (2001) 199–206, [hep-ph/0106202].

[144] M. Gyulassy and X.-n. Wang, “Multiple collisions and induced gluon Bremsstrahlung in QCD”, *Nucl.Phys.* **B420** (1994) 583–614, [nucl-th/9306003].

[145] X.-N. Wang, M. Gyulassy, and M. Plumer, “The LPM effect in QCD and radiative energy loss in a quark gluon plasma”, *Phys.Rev.* **D51** (1995) 3436–3446, [hep-ph/9408344].

[146] J. Gunion and G. Bertsch, “Hadronization by Color Bremsstrahlung”, *Phys.Rev.* **D25** (1982) 746.

[147] N. Armesto, B. Cole, C. Gale, W. A. Horowitz, P. Jacobs, *et. al.*, “Comparison of Jet Quenching Formalisms for a Quark-Gluon Plasma ’Brick’”, *Phys.Rev.* **C86** (2012) 064904, [arXiv:1106.1106].

[148] S. A. Bass, C. Gale, A. Majumder, C. Nonaka, G.-Y. Qin, *et. al.*, “Systematic Comparison of Jet Energy-Loss Schemes in a realistic hydrodynamic medium”, *Phys.Rev.* **C79** (2009) 024901, [arXiv:0808.0908].

[149] R. Baier, Y. L. Dokshitzer, A. H. Mueller, S. Peigne, and D. Schiff, “Radiative energy loss of high-energy quarks and gluons in a finite volume quark - gluon plasma”, *Nucl.Phys.* **B483** (1997) 291–320, [hep-ph/9607355].

[150] R. Baier, Y. L. Dokshitzer, A. H. Mueller, S. Peigne, and D. Schiff, “The Landau-Pomeranchuk-Migdal effect in QED”, *Nucl.Phys.* **B478** (1996) 577–597, [hep-ph/9604327].

[151] R. Baier, Y. L. Dokshitzer, A. H. Mueller, S. Peigne, and D. Schiff, “Radiative energy loss and p(T) broadening of high-energy partons in nuclei”, *Nucl.Phys.* **B484** (1997) 265–282, [hep-ph/9608322].

[152] R. Baier, Y. L. Dokshitzer, A. H. Mueller, and D. Schiff, "Radiative energy loss of high-energy partons traversing an expanding QCD plasma", *Phys.Rev.* **C58** (1998) 1706–1713, [hep-ph/9803473].

[153] R. Baier, Y. L. Dokshitzer, A. H. Mueller, and D. Schiff, "Angular dependence of the radiative gluon spectrum and the energy loss of hard jets in QCD media", *Phys.Rev.* **C60** (1999) 064902, [hep-ph/9907267].

[154] R. Baier, Y. L. Dokshitzer, A. H. Mueller, and D. Schiff, "On the angular dependence of the radiative gluon spectrum", *Phys.Rev.* **C64** (2001) 057902, [hep-ph/0105062].

[155] R. Baier, Y. L. Dokshitzer, A. H. Mueller, and D. Schiff, "Quenching of hadron spectra in media", *JHEP* **0109** (2001) 033, [hep-ph/0106347].

[156] R. Baier, Y. L. Dokshitzer, A. H. Mueller, and D. Schiff, "Medium induced radiative energy loss: Equivalence between the BDMPS and Zakharov formalisms", *Nucl.Phys.* **B531** (1998) 403–425, [hep-ph/9804212].

[157] R. Baier, Y. L. Dokshitzer, S. Peigne, and D. Schiff, "Induced gluon radiation in a QCD medium", *Phys.Lett.* **B345** (1995) 277–286, [hep-ph/9411409].

[158] B. Zakharov, "Fully quantum treatment of the Landau-Pomeranchuk-Migdal effect in QED and QCD", *JETP Lett.* **63** (1996) 952–957, [hep-ph/9607440].

[159] B. Zakharov, "Landau-Pomeranchuk-Migdal effect for finite size targets", *Pisma Zh.Eksp.Teor.Fiz.* **64** (1996) 737, [hep-ph/9612431].

[160] B. Zakharov, "Radiative energy loss of high-energy quarks in finite size nuclear matter and quark - gluon plasma", *JETP Lett.* **65** (1997) 615–620, [hep-ph/9704255].

[161] B. Zakharov, "Coherent final state interaction in jet production in nucleus-nucleus collisions", *JETP Lett.* **76** (2002) 201–205, [hep-ph/0207206].

[162] B. Zakharov, "Transverse spectra of radiation processes in-medium", *JETP Lett.* **70** (1999) 176–182, [hep-ph/9906536].

[163] B. Zakharov, "Light cone path integral approach to the Landau-Pomeranchuk-Migdal effect", *Phys.Atom.Nucl.* **61** (1998) 838–854, [hep-ph/9807540].

[164] N. Armesto, C. A. Salgado, and U. A. Wiedemann, "Medium induced gluon radiation off massive quarks fills the dead cone", *Phys.Rev.* **D69** (2004) 114003, [hep-ph/0312106].

[165] U. A. Wiedemann, "Gluon radiation off hard quarks in a nuclear environment: Opacity expansion", *Nucl.Phys.* **B588** (2000) 303–344, [hep-ph/0005129].

[166] A. Kovner and U. A. Wiedemann, "Eikonal evolution and gluon radiation", *Phys.Rev.* **D64** (2001) 114002, [hep-ph/0106240].

[167] U. A. Wiedemann, "Transverse dynamics of hard partons in nuclear media and the QCD dipole", *Nucl.Phys.* **B582** (2000) 409–450, [hep-ph/0003021].

[168] U. A. Wiedemann, "Jet quenching versus jet enhancement: A Quantitative study of the BDMPS-Z gluon radiation spectrum", *Nucl.Phys.* **A690** (2001) 731–751, [hep-ph/0008241].

[169] C. A. Salgado and U. A. Wiedemann, "Calculating quenching weights", *Phys.Rev.* **D68** (2003) 014008, [hep-ph/0302184].

[170] C. A. Salgado and U. A. Wiedemann, "A Dynamical scaling law for jet tomography", *Phys.Rev.Lett.* **89** (2002) 092303, [hep-ph/0204221].

[171] M. Gyulassy, P. Levai, and I. Vitev, "Jet quenching in thin plasmas", *Nucl.Phys.* **A661** (1999) 637–640, [hep-ph/9907343].

[172] M. Gyulassy, P. Levai, and I. Vitev, "Jet quenching in thin quark gluon plasmas. 1. Formalism", *Nucl.Phys.* **B571** (2000) 197–233, [hep-ph/9907461].

[173] M. Gyulassy, P. Levai, and I. Vitev, "NonAbelian energy loss at finite opacity", *Phys.Rev.Lett.* **85** (2000) 5535–5538, [nucl-th/0005032].

[174] M. Gyulassy, P. Levai, and I. Vitev, "Jet tomography of Au+Au reactions including multigluon fluctuations", *Phys.Lett.* **B538** (2002) 282–288, [nucl-th/0112071].

[175] M. Gyulassy, P. Levai, and I. Vitev, “Reaction operator approach to multiple elastic scatterings”, *Phys.Rev.* **D66** (2002) 014005, [nucl-th/0201078].

[176] I. Vitev and M. Gyulassy, “High p_T tomography of d + Au and Au+Au at SPS, RHIC, and LHC”, *Phys.Rev.Lett.* **89** (2002) 252301, [hep-ph/0209161].

[177] M. Djordjevic and M. Gyulassy, “Heavy quark radiative energy loss in QCD matter”, *Nucl.Phys.* **A733** (2004) 265–298, [nucl-th/0310076].

[178] X.-N. Wang and X.-f. Guo, “Multiple parton scattering in nuclei: Parton energy loss”, *Nucl.Phys.* **A696** (2001) 788–832, [hep-ph/0102230].

[179] X.-f. Guo and X.-N. Wang, “Multiple scattering, parton energy loss and modified fragmentation functions in deeply inelastic e A scattering”, *Phys.Rev.Lett.* **85** (2000) 3591–3594, [hep-ph/0005044].

[180] X.-N. Wang, “Dynamical screening and radiative parton energy loss in a quark gluon plasma”, *Phys.Lett.* **B485** (2000) 157–161, [nucl-th/0003033].

[181] E. Wang and X.-N. Wang, “Parton energy loss with detailed balance”, *Phys.Rev.Lett.* **87** (2001) 142301, [nucl-th/0106043].

[182] J. A. Osborne, E. Wang, and X.-N. Wang, “Evolution of parton fragmentation functions at finite temperature”, *Phys.Rev.* **D67** (2003) 094022, [hep-ph/0212131].

[183] B.-W. Zhang, E. Wang, and X.-N. Wang, “Heavy quark energy loss in nuclear medium”, *Phys.Rev.Lett.* **93** (2004) 072301, [nucl-th/0309040].

[184] B.-W. Zhang and X.-N. Wang, “Multiple parton scattering in nuclei: Beyond helicity amplitude approximation”, *Nucl.Phys.* **A720** (2003) 429–451, [hep-ph/0301195].

[185] A. Majumder, R. Fries, and B. Muller, “Photon bremsstrahlung and diffusive broadening of a hard jet”, *Phys.Rev.* **C77** (2008) 065209, [arXiv:0711.2475].

[186] A. Majumder, E. Wang, and X.-N. Wang, “Modified dihadron fragmentation functions in hot and nuclear matter”, *Phys.Rev.Lett.* **99** (2007) 152301, [nucl-th/0412061].

[187] A. Majumder and B. Muller, “Higher twist jet broadening and classical propagation”, *Phys.Rev.* **C77** (2008) 054903, [arXiv:0705.1147].

[188] P. B. Arnold, G. D. Moore, and L. G. Yaffe, “Transport coefficients in high temperature gauge theories. 2. Beyond leading log”, *JHEP* **0305** (2003) 051, [hep-ph/0302165].

[189] P. B. Arnold, G. D. Moore, and L. G. Yaffe, “Photon and gluon emission in relativistic plasmas”, *JHEP* **0206** (2002) 030, [hep-ph/0204343].

[190] S. Turbide, C. Gale, S. Jeon, and G. D. Moore, “Energy loss of leading hadrons and direct photon production in evolving quark-gluon plasma”, *Phys.Rev.* **C72** (2005) 014906, [hep-ph/0502248].

[191] S. Jeon and G. D. Moore, “Energy loss of leading partons in a thermal QCD medium”, *Phys.Rev.* **C71** (2005) 034901, [hep-ph/0309332].

[192] P. B. Arnold, G. D. Moore, and L. G. Yaffe, “Effective kinetic theory for high temperature gauge theories”, *JHEP* **0301** (2003) 030, [hep-ph/0209353].

[193] M. Djordjevic and M. Gyulassy, “The Ter-Mikayelian effect on QCD radiative energy loss”, *Phys.Rev.* **C68** (2003) 034914, [nucl-th/0305062].

[194] S. Wicks, W. Horowitz, M. Djordjevic, and M. Gyulassy, “Elastic, inelastic, and path length fluctuations in jet tomography”, *Nucl.Phys.* **A784** (2007) 426–442, [nucl-th/0512076].

[195] A. Buzzatti and M. Gyulassy, “Jet Flavor Tomography of Quark Gluon Plasmas at RHIC and LHC”, *Phys.Rev.Lett.* **108** (2012) 022301, [arXiv:1106.3061].

[196] A. Buzzatti and M. Gyulassy, “An overview of the CUJET model: Jet Flavor Tomography applied at RHIC and LHC”, arXiv:1207.6020.

[197] A. Buzzatti and M. Gyulassy, “A running coupling explanation of the surprising transparency of the QGP at LHC”, *Nucl.Phys.A904-905* **2013** (2013) 779c–782c, [arXiv:1210.6417].

[198] J. Xu, A. Buzzatti, and M. Gyulassy, “Azimuthal Jet Flavor Tomography with CUJET2.0 of Nuclear Collisions at RHIC and LHC”, arXiv:1402.2956.

[199] J. E. Gentle, *Random Number Generation and Monte Carlo Methods.* Springer, 2005.

[200] S. Wicks, "Up to and beyond ninth order in opacity: Radiative energy loss with GLV", arXiv:0804.4704.

[201] W. Horowitz and B. Cole, "Systematic theoretical uncertainties in jet quenching due to gluon kinematics", *Phys.Rev.* **C81** (2010) 024909, [arXiv:0910.1823].

[202] P. B. Arnold, "Simple Formula for High-Energy Gluon Bremsstrahlung in a Finite, Expanding Medium", *Phys.Rev.* **D79** (2009) 065025, [arXiv:0808.2767].

[203] A. Ficnar, J. Noronha, and M. Gyulassy, "Non-conformal Holography of Heavy Quark Quenching", *Nucl.Phys.* **A855** (2011) 372–375, [arXiv:1012.0116].

[204] G. 't Hooft, "A Planar Diagram Theory for Strong Interactions", *Nucl.Phys.* **B72** (1974) 461.

[205] B. Zwiebach, *A First Course in String Theory.* Cambridge University Press, 2005.

[206] E. Kiritsis, *String Theory in a Nutshell.* Princeton University Press, 2007.

[207] M. B. Green, J. Schwarz, and E. Witten, *Superstring Theory. Vol. 1: Introduction.* Cambridge University Press, 1987.

[208] F. Gliozzi, J. Scherk, and D. I. Olive, "Supersymmetry, Supergravity Theories and the Dual Spinor Model", *Nucl.Phys.* **B122** (1977) 253–290.

[209] F. Gliozzi, J. Scherk, and D. I. Olive, "Supergravity and the Spinor Dual Model", *Phys.Lett.* **B65** (1976) 282.

[210] J. H. Schwarz, "Superstring Theory", *Phys.Rept.* **89** (1982) 223–322.

[211] M. B. Green and J. H. Schwarz, "Supersymmetrical String Theories", *Phys.Lett.* **B109** (1982) 444–448.

[212] J. H. Schwarz, "Covariant Field Equations of Chiral N=2 D=10 Supergravity", *Nucl.Phys.* **B226** (1983) 269.

[213] J. H. Schwarz and P. C. West, "Symmetries and Transformations of Chiral N=2 D=10 Supergravity", *Phys.Lett.* **B126** (1983) 301.

[214] C. V. Johnson, *D-Branes.* Cambridge University Press, 2003.

[215] J. Polchinski, "Tasi lectures on D-branes", hep-th/9611050.

[216] J. Polchinski, "Dirichlet Branes and Ramond-Ramond charges", *Phys.Rev.Lett.* **75** (1995) 4724–4727, [hep-th/9510017].

[217] R. Leigh, "Dirac-Born-Infeld Action from Dirichlet Sigma Model", *Mod.Phys.Lett.* **A4** (1989) 2767.

[218] A. A. Tseytlin, "Born-Infeld action, supersymmetry and string theory", hep-th/9908105.

[219] E. Witten, "Bound states of strings and p-branes", *Nucl.Phys.* **B460** (1996) 335–350, [hep-th/9510135].

[220] L. Brink, J. H. Schwarz, and J. Scherk, "Supersymmetric Yang-Mills Theories", *Nucl.Phys.* **B121** (1977) 77.

[221] M. F. Sohnius and P. C. West, "Conformal Invariance in N=4 Supersymmetric Yang-Mills Theory", *Phys.Lett.* **B100** (1981) 245.

[222] S. Mandelstam, "Light Cone Superspace and the Ultraviolet Finiteness of the N=4 Model", *Nucl.Phys.* **B213** (1983) 149–168.

[223] P. S. Howe, K. Stelle, and P. Townsend, "Miraculous Ultraviolet Cancellations in Supersymmetry Made Manifest", *Nucl.Phys.* **B236** (1984) 125.

[224] O. Aharony, S. S. Gubser, J. M. Maldacena, H. Ooguri, and Y. Oz, "Large N field theories, string theory and gravity", *Phys.Rept.* **323** (2000) 183–386, [hep-th/9905111].

[225] J. Casalderrey-Solana, H. Liu, D. Mateos, K. Rajagopal, and U. A. Wiedemann, "Gauge/String Duality, Hot QCD and Heavy Ion Collisions", arXiv:1101.0618.

[226] S. S. Gubser, I. R. Klebanov, and A. A. Tseytlin, "String theory and classical absorption by three-branes", *Nucl.Phys.* **B499** (1997) 217–240, [hep-th/9703040].

[227] P. Breitenlohner and D. Z. Freedman, "Positive Energy in anti-De Sitter Backgrounds and Gauged Extended Supergravity", *Phys.Lett.* **B115** (1982) 197.

[228] P. Breitenlohner and D. Z. Freedman, “Stability in Gauged Extended Supergravity”, *Annals Phys.* **144** (1982) 249.

[229] V. Balasubramanian, P. Kraus, A. E. Lawrence, and S. P. Trivedi, “Holographic probes of anti-de Sitter space-times”, *Phys.Rev.* **D59** (1999) 104021, [hep-th/9808017].

[230] V. Balasubramanian, P. Kraus, and A. E. Lawrence, “Bulk versus boundary dynamics in anti-de Sitter space-time”, *Phys.Rev.* **D59** (1999) 046003, [hep-th/9805171].

[231] L. Susskind and E. Witten, “The Holographic bound in anti-de Sitter space”, hep-th/9805114.

[232] A. W. Peet and J. Polchinski, “UV / IR relations in AdS dynamics”, *Phys.Rev.* **D59** (1999) 065011, [hep-th/9809022].

[233] G. Gibbons and S. Hawking, “Action Integrals and Partition Functions in Quantum Gravity”, *Phys.Rev.* **D15** (1977) 2752–2756.

[234] B. Bringoltz and M. Teper, “The Pressure of the SU(N) lattice gauge theory at large-N”, *Phys.Lett.* **B628** (2005) 113–124, [hep-lat/0506034].

[235] J. Erdmenger, N. Evans, I. Kirsch, and E. Threlfall, “Mesons in Gauge/Gravity Duals - A Review”, *Eur.Phys.J.* **A35** (2008) 81–133, [arXiv:0711.4467].

[236] A. Karch and A. O’Bannon, “Chiral transition of N=4 super Yang-Mills with flavor on a 3-sphere”, *Phys.Rev.* **D74** (2006) 085033, [hep-th/0605120].

[237] J. Babington, J. Erdmenger, N. J. Evans, Z. Guralnik, and I. Kirsch, “Chiral symmetry breaking and pions in nonsupersymmetric gauge / gravity duals”, *Phys.Rev.* **D69** (2004) 066007, [hep-th/0306018].

[238] L. D. Landau and E. M. Lifshitz, *Statistical Physics, Parts 1 and 2*. Butterworth-Heinemann, 1975.

[239] D. T. Son and A. O. Starinets, “Minkowski space correlators in AdS / CFT correspondence: Recipe and applications”, *JHEP* **0209** (2002) 042, [hep-th/0205051].

[240] G. Policastro, D. T. Son, and A. O. Starinets, "The Shear viscosity of strongly coupled N=4 supersymmetric Yang-Mills plasma", *Phys.Rev.Lett.* **87** (2001) 081601, [hep-th/0104066].

[241] N. Iqbal and H. Liu, "Universality of the hydrodynamic limit in AdS/CFT and the membrane paradigm", *Phys.Rev.* **D79** (2009) 025023, [arXiv:0809.3808].

[242] P. Kovtun, D. Son, and A. Starinets, "Viscosity in strongly interacting quantum field theories from black hole physics", *Phys.Rev.Lett.* **94** (2005) 111601, [hep-th/0405231].

[243] J. M. Maldacena, "Wilson loops in large N field theories", *Phys.Rev.Lett.* **80** (1998) 4859–4862, [hep-th/9803002].

[244] S.-J. Rey and J.-T. Yee, "Macroscopic strings as heavy quarks in large N gauge theory and anti-de Sitter supergravity", *Eur.Phys.J.* **C22** (2001) 379–394, [hep-th/9803001].

[245] S.-J. Rey, S. Theisen, and J.-T. Yee, "Wilson-Polyakov loop at finite temperature in large N gauge theory and anti-de Sitter supergravity", *Nucl.Phys.* **B527** (1998) 171–186, [hep-th/9803135].

[246] A. Brandhuber, N. Itzhaki, J. Sonnenschein, and S. Yankielowicz, "Wilson loops in the large N limit at finite temperature", *Phys.Lett.* **B434** (1998) 36–40, [hep-th/9803137].

[247] H. Liu, K. Rajagopal, and U. A. Wiedemann, "Calculating the jet quenching parameter from AdS/CFT", *Phys.Rev.Lett.* **97** (2006) 182301, [hep-ph/0605178].

[248] S.-x. Chu, D. Hou, and H.-c. Ren, "The Subleading Term of the Strong Coupling Expansion of the Heavy-Quark Potential in a N=4 Super Yang-Mills Vacuum", *JHEP* **0908** (2009) 004, [arXiv:0905.1874].

[249] V. Forini, "Quark-antiquark potential in AdS at one loop", *JHEP* **1011** (2010) 079, [arXiv:1009.3939].

[250] Z.-q. Zhang, D.-f. Hou, and H.-c. Ren, "The finite 't Hooft coupling correction on jet quenching parameter in a $\mathcal{N} = 4$ Super Yang-Mills Plasma", *JHEP* **1301** (2013) 032, [arXiv:1210.5187].

[251] S. S. Gubser, I. R. Klebanov, and A. A. Tseytlin, "Coupling constant dependence in the thermodynamics of N=4 supersymmetric Yang-Mills theory", *Nucl.Phys.* **B534** (1998) 202–222, [hep-th/9805156].

[252] T. Banks and M. B. Green, "Nonperturbative effects in AdS in five-dimensions x S**5 string theory and d = 4 SUSY Yang-Mills", *JHEP* **9805** (1998) 002, [hep-th/9804170].

[253] A. Buchel, J. T. Liu, and A. O. Starinets, "Coupling constant dependence of the shear viscosity in N=4 supersymmetric Yang-Mills theory", *Nucl.Phys.* **B707** (2005) 56–68, [hep-th/0406264].

[254] A. Buchel, "Resolving disagreement for eta/s in a CFT plasma at finite coupling", *Nucl.Phys.* **B803** (2008) 166–170, [arXiv:0805.2683].

[255] N. Armesto, J. D. Edelstein, and J. Mas, "Jet quenching at finite 't Hooft coupling and chemical potential from AdS/CFT", *JHEP* **0609** (2006) 039, [hep-ph/0606245].

[256] S. Forste, D. Ghoshal, and S. Theisen, "Stringy corrections to the Wilson loop in N=4 superYang-Mills theory", *JHEP* **9908** (1999) 013, [hep-th/9903042].

[257] B. Zwiebach, "Curvature Squared Terms and String Theories", *Phys.Lett.* **B156** (1985) 315.

[258] M. Brigante, H. Liu, R. C. Myers, S. Shenker, and S. Yaida, "Viscosity Bound Violation in Higher Derivative Gravity", *Phys.Rev.* **D77** (2008) 126006, [arXiv:0712.0805].

[259] D. M. Hofman and J. Maldacena, "Conformal collider physics: Energy and charge correlations", *JHEP* **0805** (2008) 012, [arXiv:0803.1467].

[260] R.-G. Cai, "Gauss-Bonnet black holes in AdS spaces", *Phys.Rev.* **D65** (2002) 084014, [hep-th/0109133].

[261] S. S. Gubser, "Comparing the drag force on heavy quarks in N=4 super-Yang-Mills theory and QCD", *Phys.Rev.* **D76** (2007) 126003, [hep-th/0611272].

[262] T. Sakai and S. Sugimoto, "More on a holographic dual of QCD", *Prog.Theor.Phys.* **114** (2005) 1083–1118, [hep-th/0507073].

[263] R. Casero, C. Nunez, and A. Paredes, "Towards the string dual of N=1 SQCD-like theories", *Phys.Rev.* **D73** (2006) 086005, [hep-th/0602027].

[264] P. Ouyang, "Holomorphic D7 branes and flavored N=1 gauge theories", *Nucl.Phys.* **B699** (2004) 207–225, [hep-th/0311084].

[265] M. Mia, K. Dasgupta, C. Gale, and S. Jeon, "Five Easy Pieces: The Dynamics of Quarks in Strongly Coupled Plasmas", *Nucl.Phys.* **B839** (2010) 187–293, [arXiv:0902.1540].

[266] U. Gursoy, E. Kiritsis, L. Mazzanti, and F. Nitti, "Deconfinement and Gluon Plasma Dynamics in Improved Holographic QCD", *Phys.Rev.Lett.* **101** (2008) 181601, [arXiv:0804.0899].

[267] U. Gursoy, E. Kiritsis, L. Mazzanti, and F. Nitti, "Holography and Thermodynamics of 5D Dilaton-gravity", *JHEP* **0905** (2009) 033, [arXiv:0812.0792].

[268] E. Kiritsis, "Dissecting the string theory dual of QCD", *Fortsch.Phys.* **57** (2009) 396–417, [arXiv:0901.1772].

[269] U. Gursoy, E. Kiritsis, L. Mazzanti, and F. Nitti, "Improved Holographic Yang-Mills at Finite Temperature: Comparison with Data", *Nucl.Phys.* **B820** (2009) 148–177, [arXiv:0903.2859].

[270] U. Gursoy, E. Kiritsis, G. Michalogiorgakis, and F. Nitti, "Thermal Transport and Drag Force in Improved Holographic QCD", *JHEP* **0912** (2009) 056, [arXiv:0906.1890].

[271] U. Gursoy, E. Kiritsis, L. Mazzanti, and F. Nitti, "Langevin diffusion of heavy quarks in non-conformal holographic backgrounds", *JHEP* **1012** (2010) 088, [arXiv:1006.3261].

[272] S. S. Gubser, S. S. Pufu, and F. D. Rocha, "Bulk viscosity of strongly coupled plasmas with holographic duals", *JHEP* **0808** (2008) 085, [arXiv:0806.0407].

[273] H. Chamblin and H. Reall, "Dynamic dilatonic domain walls", *Nucl.Phys.* **B562** (1999) 133–157, [hep-th/9903225].

[274] R. M. Wald, *General Relativity.* University Of Chicago Press, 1984.

[275] J. Alanen, K. Kajantie, and V. Suur-Uski, "A gauge/gravity duality model for gauge theory thermodynamics", *Phys.Rev.* **D80** (2009) 126008, [arXiv:0911.2114].

[276] J. Noronha, "Connecting Polyakov Loops to the Thermodynamics of SU(N(c)) Gauge Theories Using the Gauge-String Duality", *Phys.Rev.* **D81** (2010) 045011, [arXiv:0910.1261].

[277] S. M. Carroll, *Spacetime and Geometry: An Introduction to General Relativity.* Addison Wesley, 2004.

[278] V. Balasubramanian and P. Kraus, "A Stress tensor for Anti-de Sitter gravity", *Commun.Math.Phys.* **208** (1999) 413–428, [hep-th/9902121].

[279] A. Ficnar, J. Noronha, and M. Gyulassy, "Jet Quenching in Non-Conformal Holography", *J.Phys.* **G38** (2011) 124176, [arXiv:1106.6303].

[280] G. W. Semenoff and K. Zarembo, "Holographic Schwinger Effect", *Phys.Rev.Lett.* **107** (2011) 171601, [arXiv:1109.2920].

[281] J. Casalderrey-Solana and D. Teaney, "Transverse Momentum Broadening of a Fast Quark in a N=4 Yang Mills Plasma", *JHEP* **0704** (2007) 039, [hep-th/0701123].

[282] G. Giecold, E. Iancu, and A. Mueller, "Stochastic trailing string and Langevin dynamics from AdS/CFT", *JHEP* **0907** (2009) 033, [arXiv:0903.1840].

[283] W. Horowitz and M. Gyulassy, "Heavy quark jet tomography of Pb + Pb at LHC: AdS/CFT drag or pQCD energy loss?", *Phys.Lett.* **B666** (2008) 320–323, [arXiv:0706.2336].

[284] J. Noronha, M. Gyulassy, and G. Torrieri, "Conformal Holography of Bulk Elliptic Flow and Heavy Quark Quenching in Relativistic Heavy Ion Collisions", *Phys.Rev.* **C82** (2010) 054903, [arXiv:1009.2286].

[285] M. Chernicoff and A. Guijosa, "Acceleration, Energy Loss and Screening in Strongly-Coupled Gauge Theories", *JHEP* **0806** (2008) 005, [arXiv:0803.3070].

[286] J. Casalderrey-Solana and D. Teaney, "Heavy quark diffusion in strongly coupled N=4 Yang-Mills", *Phys.Rev.* **D74** (2006) 085012, [hep-ph/0605199].

[287] S. S. Gubser, "Momentum fluctuations of heavy quarks in the gauge-string duality", *Nucl.Phys.* **B790** (2008) 175–199, [hep-th/0612143].

[288] J. J. Friess, S. S. Gubser, G. Michalogiorgakis, and S. S. Pufu, "The Stress tensor of a quark moving through N=4 thermal plasma", *Phys.Rev.* **D75** (2007) 106003, [hep-th/0607022].

[289] S. S. Gubser, S. S. Pufu, and A. Yarom, "Energy disturbances due to a moving quark from gauge-string duality", *JHEP* **0709** (2007) 108, [arXiv:0706.0213].

[290] P. M. Chesler and L. G. Yaffe, "The Wake of a quark moving through a strongly-coupled plasma", *Phys.Rev.Lett.* **99** (2007) 152001, [arXiv:0706.0368].

[291] A. Guijosa and J. F. Pedraza, "Early-Time Energy Loss in a Strongly-Coupled SYM Plasma", *JHEP* **1105** (2011) 108, [arXiv:1102.4893].

[292] A. Mikhailov, "Nonlinear waves in AdS / CFT correspondence", hep-th/0305196.

[293] C. P. Herzog, "Energy Loss of Heavy Quarks from Asymptotically AdS Geometries", *JHEP* **0609** (2006) 032, [hep-th/0605191].

[294] R. A. Janik and R. B. Peschanski, "Asymptotic perfect fluid dynamics as a consequence of Ads/CFT", *Phys.Rev.* **D73** (2006) 045013, [hep-th/0512162].

[295] G. Giecold, "Heavy quark in an expanding plasma in AdS/CFT", *JHEP* **0906** (2009) 002, [arXiv:0904.1874].

[296] E. Caceres and A. Guijosa, "Drag force in charged N=4 SYM plasma", *JHEP* **0611** (2006) 077, [hep-th/0605235].

[297] **PHENIX** Collaboration, A. Adare *et. al.*, "Energy Loss and Flow of Heavy Quarks in Au+Au Collisions at s(NN)**(1/2) = 200-GeV", *Phys.Rev.Lett.* **98** (2007) 172301, [nucl-ex/0611018].

[298] **STAR** Collaboration, J. Bielcik, "Centrality dependence of heavy flavor production from single electron measurement in s(NN)**(1/2) = 200-GeV Au + Au collisions", *Nucl.Phys.* **A774** (2006) 697–700, [nucl-ex/0511005].

[299] **ALICE** Collaboration, B. Abelev *et. al.*, "Suppression of high transverse momentum D mesons in central Pb-Pb collisions at $\sqrt{s_{NN}} = 2.76$ TeV", *JHEP* **1209** (2012) 112, [arXiv:1203.2160].

[300] P. M. Chesler, K. Jensen, A. Karch, and L. G. Yaffe, "Light quark energy loss in strongly-coupled N = 4 supersymmetric Yang-Mills plasma", *Phys.Rev.* **D79** (2009) 125015, [arXiv:0810.1985].

[301] P. K. Kovtun and A. O. Starinets, "Quasinormal modes and holography", *Phys.Rev.* **D72** (2005) 086009, [hep-th/0506184].

[302] Y. Hatta, E. Iancu, and A. H. Mueller, "Jet evolution in the N=4 SYM plasma at strong coupling", *JHEP* **05** (2008) 037, [arXiv:0803.2481].

[303] C. Athanasiou, P. M. Chesler, H. Liu, D. Nickel, and K. Rajagopal, "Synchrotron radiation in strongly coupled conformal field theories", *Phys.Rev.* **D81** (2010) 126001, [arXiv:1001.3880].

[304] V. E. Hubeny, "Relativistic Beaming in AdS/CFT", arXiv:1011.1270.

[305] P. Arnold and D. Vaman, "Jet quenching in hot strongly coupled gauge theories revisited: 3-point correlators with gauge-gravity duality", *JHEP* **1010** (2010) 099, [arXiv:1008.4023].

[306] P. Arnold and D. Vaman, "Jet quenching in hot strongly coupled gauge theories simplified", *JHEP* **1104** (2011) 027, [arXiv:1101.2689].

[307] B. Betz and M. Gyulassy, "Constraints on the Path-Length Dependence of Jet Quenching in Nuclear Collisions at RHIC and LHC", arXiv:1404.6378.

[308] C. Marquet and T. Renk, "Jet quenching in the strongly-interacting quark-gluon plasma", *Phys.Lett.* **B685** (2010) 270–276, [arXiv:0908.0880].

[309] **PHENIX** Collaboration, A. Adare *et. al.*, "Neutral pion production with respect to centrality and reaction plane in Au+Au collisions at $\sqrt{s_{NN}}$=200 GeV", arXiv:1208.2254.

[310] Y. Hatta, E. Iancu, and A. Mueller, "Deep inelastic scattering off a N=4 SYM plasma at strong coupling", *JHEP* **0801** (2008) 063, [arXiv:0710.5297].

[311] F. Dominguez, C. Marquet, A. Mueller, B. Wu, and B.-W. Xiao, "Comparing energy loss and p-perpendicular - broadening in perturbative QCD with strong coupling N = 4 SYM theory", *Nucl.Phys.* **A811** (2008) 197–222, [arXiv:0803.3234].

[312] P. M. Chesler and K. Rajagopal, "Jet quenching in strongly coupled plasma", arXiv:1402.6756.

[313] W. Horowitz and M. Gyulassy, "The Surprising Transparency of the sQGP at LHC", *Nucl.Phys.* **A872** (2011) 265–285, [arXiv:1104.4958].

[314] J. Casalderrey-Solana, D. C. Gulhan, J. G. Milhano, D. Pablos, and K. Rajagopal, "A Hybrid Strong/Weak Coupling Approach to Jet Quenching", arXiv:1405.3864.

[315] W. A. Bardeen, I. Bars, A. J. Hanson, and R. D. Peccei, "A Study of the Longitudinal Kink Modes of the String", *Phys. Rev.* **D13** (1976) 2364–2382.

[316] X. Artru, "Classical String Phenomenology. 1. How Strings Work", *Phys. Rept.* **97** (1983) 147.

[317] L. Wulff, "The type II superstring to order θ^4", *JHEP* **1307** (2013) 123, [arXiv:1304.6422].

[318] M. B. Green and J. H. Schwarz, "Covariant Description of Superstrings", *Phys.Lett.* **B136** (1984) 367–370.

[319] M. B. Green and J. H. Schwarz, "Properties of the Covariant Formulation of Superstring Theories", *Nucl.Phys.* **B243** (1984) 285.

[320] J. P. Boyd, *Chebyshev and Fourier Spectral Methods.* Dover Publications, Inc., 2000.

[321] P. M. Chesler and L. G. Yaffe, "Horizon formation and far-from-equilibrium isotropization in supersymmetric Yang-Mills plasma", *Phys.Rev.Lett.* **102** (2009) 211601, [arXiv:0812.2053].

[322] S. S. Gubser, S. S. Pufu, and A. Yarom, "Entropy production in collisions of gravitational shock waves and of heavy ions", *Phys.Rev.* **D78** (2008) 066014, [arXiv:0805.1551].

[323] M. P. Heller, D. Mateos, W. van der Schee, and D. Trancanelli, "Strong Coupling Isotropization of Non-Abelian Plasmas Simplified", *Phys.Rev.Lett.* **108** (2012) 191601, [arXiv:1202.0981].

[324] H. Song, S. Bass, and U. W. Heinz, "Spectra and elliptic flow for identified hadrons in 2.76 A TeV Pb+Pb collisions", arXiv:1311.0157.

[325] H. Song, S. A. Bass, U. Heinz, T. Hirano, and C. Shen, "Hadron spectra and elliptic flow for 200 A GeV Au+Au collisions from viscous hydrodynamics coupled to a Boltzmann cascade", *Phys.Rev.* **C83** (2011) 054910, [arXiv:1101.4638].

[326] P. Romatschke, "New Developments in Relativistic Viscous Hydrodynamics", *Int.J.Mod.Phys.* **E19** (2010) 1–53, [arXiv:0902.3663].

[327] G. Gibbons and K.-i. Maeda, "Black Holes and Membranes in Higher Dimensional Theories with Dilaton Fields", *Nucl.Phys.* **B298** (1988) 741.

[328] D. Garfinkle, G. T. Horowitz, and A. Strominger, "Charged black holes in string theory", *Phys.Rev.* **D43** (1991) 3140.

[329] G. T. Horowitz and A. Strominger, "Black strings and P-branes", *Nucl.Phys.* **B360** (1991) 197–209.

Appendix A

Some basic results from statistical physics and hydrodynamics

In this appendix we will derive and summarize some elementary results in statistical physics and discuss the basics of hydrodynamics, both of which will be used at different points in this thesis.

A.1 Some basic results from statistical physics

In this section we will be primarily interested in the energy density and pressure of an ideal gas of (massless) fermions and bosons.

We start with the volume density of particles with momentum k and degeneracy g,

$$dn = \frac{d^3k}{(2\pi)^3} g f(k) \,, \tag{A.1}$$

where $f(k)$ is the Bose-Einstein or Fermi-Dirac distribution,

$$f(k) = \frac{1}{e^{k\beta} \pm 1}\,, \tag{A.2}$$

where $\beta = 1/T$ and where we have assumed that the particles are massless and that the chemical potential is zero. Integrating this, we obtain

$$n_{\mathrm{BE}} = g\frac{\zeta(3)}{\pi^2}T^3\,, \qquad n_{\mathrm{FD}} = g\frac{3\zeta(3)}{4\pi^2}T^3\,, \tag{A.3}$$

where $\zeta(3) \approx 1.202$. Similarly, the energy density $d\varepsilon = kdn$ is then

$$\varepsilon_{\mathrm{BE}} = g\frac{\pi^2}{30}T^4\,, \qquad \varepsilon_{\mathrm{FD}} = g\frac{7\pi^2}{240}T^4\,. \tag{A.4}$$

For gluons, the degeneracy comes from the two transverse polarizations and the color degeneracy, $g_g = 2(N_c^2 - 1) = 16$, while for N_f massless quarks and antiquarks, the spin degeneracy gives a factor of 2, inclusion of both particles and anti-particles another factor of 2, and together with color degeneracy, one arrives at $g_q = 12N_f$. Therefore, for a quark-gluon plasma we have:

$$\begin{aligned} \varepsilon_{\mathrm{QGP}} &= \frac{\pi^2}{60}(32 + 21N_f)T^4\,, \\ n_{\mathrm{QGP}} &= \frac{\zeta(3)}{\pi^2}(16 + 9N_f)T^3\,. \end{aligned} \tag{A.5}$$

Again, note that we have neglected the chemical potential μ, which would result in additional terms in (A.5) (more details on this are available in e.g. [118]).

A.2 Basics of hydrodynamics

In this section we will briefly describe some basic concepts in relativistic hydrodynamics and define some quantities that we will need at various points in the thesis. This is not meant to be by any means a review of hydrodynamics; a good exaple of those, with special emphasis on applications to heavy ion physics, can be found in [326] and [79].

In general, hydrodynamics is an effective theory of an underlying interacting quantum field theory, that is valid in the limit of small frequencies and large wavelengths. Hydrodynamic fields are expectation values of quantum operators, and it is therefore a classical theory, whose equations of motion consist of the conservation of energy and the momentum and the conservation of various transport currents J_μ:

$$\partial^\mu T_{\mu\nu} = 0\,, \qquad \partial^\mu J_\mu = 0\,. \tag{A.6}$$

where $T_{\mu\nu}$ is the energy-momentum tensor. We define the perfect (or ideal) fluid as the fluid that looks isotropic in the local rest frame. This means that the energy-momentum tensor in that frame must have the following form:

$$T^{\mu\nu}_{\text{id,lrf}} = \text{diag}(\varepsilon, P, P, P)\,, \tag{A.7}$$

where the coefficients ε and P are called the energy density and pressure, respectively. We also define the four-velocity $u^\mu = dx^\mu/d\tau$, which is, since it has three independent components, constrained by $u^2 = u^\mu u_\mu = 1$. In a general Lorentz frame, we can build $T^{\mu\nu}_{\text{id}}$ out of available scalars (ε, P), vectors (u^μ) and tensors (the metric $g_{\mu\nu}$), and demand it to be symmetric and give back (A.7) in the local rest frame:

$$T^{\mu\nu}_{\text{id}} = (\varepsilon + P)u^\mu u^\nu - Pg^{\mu\nu}\,. \tag{A.8}$$

In the perfect fluid case, one neglects all the dissipative (viscous) effects, which we can add through the viscous stress tensor $\Pi^{\mu\nu}$:

$$T_{\mu\nu} = T^{\mathrm{id}}_{\mu\nu} + \Pi_{\mu\nu}\,. \tag{A.9}$$

More generally, we can look at this as the gradient expansion in four-velocities u^μ, so that the ideal energy-momentum tensor contains no velocity gradients, which are all contained in $\Pi^{\mu\nu}$. If we are interested in the dynamics of the system at length and time scales greater than those set by the gradients in $\Pi^{\mu\nu}$, we may neglect that piece completely, and in this limit we go back to the ideal fluid. The applicability of the ideal hydrodynamics is determined by the isotropization scale τ_{iso}, when $T_{\mu\nu}$ becomes diagonal in the rest frame (eq. (A.7)), and the thermalization scale τ_{eq}, when there is no more entropy produced. For a conformal fluid, the trace of the energy momentum tensor must vanish, $T^\mu_\mu = 0$, which, from (A.8) implies that $\varepsilon = 3P$, the simplest equation of state. In general, the equation of state is not that simple and is provided by e.g. lattice QCD calculations (Fig. 1.2). The equation of state, together with a set of initial conditions for the distribution of the energy density ε (for example, Glauber or CGC) constitutes main inputs to a hydrodynamic calculation.

Allowing for the first order gradients in $\Pi^{\mu\nu}$ introduces first dissipative effects to the ideal fluid and this limit is hence called the first order dissipative hydrodynamics. The form of the first-order $\Pi^{\mu\nu}$ is constrained by covariance to be

$$\Pi^{\mu\nu} = -\eta(\varepsilon)\sigma^{\mu\nu} - \zeta(\varepsilon)\Delta^{\mu\nu}\nabla\cdot u\,, \tag{A.10}$$

where ∇_μ is the covariant derivative, $\Delta_{\mu\nu}$ is the transverse projector and $\sigma^{\mu\nu}$ is a specific (traceless) combination of these, exact form of which is not important for our discussion (more about this in [326]). In (A.10), η and ζ are the shear and bulk viscosities, respectively. Again, for a conformal system, $\Pi^{\mu}{}_{\mu} = 0$ and hence $\zeta = 0$, but η does not need to vanish (as $\sigma^{\mu\nu}$ is traceless). In addition to the constitutive relations (A.6), one now also needs additional thermodynamic relations, and in all these equations of motion, η and ζ appear divided by the entropy density s, which is the reason why we usually see combinations of η/s (and ζ/s) reported as parameters in various hydrodynamic calculations.

Appendix B

More on the AdS/CFT correspondence

In this appendix we will discuss other interesting and more technical aspects of the AdS/CFT correspondence, that will also be used at various points in the thesis. In particular, in Section B.1 we will describe in detail the supergravity solution for black p-branes, insights from which are important to understand the emergence of $AdS_5 \times S^5$ as the near-horizon geometry of a stack of D3-branes. In Section B.2 we discuss in detail the geometry of Anti-de Sitter space, important for understanding its boundedness, as well as some more advanced constructions.

B.1 Black p-branes and D-branes

In Section 3.2.1 we discuss how the AdS/CFT correspondence arises from looking at the stack of coincident D3-branes in type IIB string theory in the low energy ($\alpha' \to 0$) limit, from two different points of view. In Section 3.1.2 we note how the low energy limit of that string theory is the type IIB supergravity, so in this section we will look for the black hole solutions in that theory, as those will prove to be directly related to the geometry sourced by D-branes. More on this topic can be found in e.g. [206, 224].

We will be looking for a classical black hole solution to 10D supergravity that also carries electric charge with respect to the Ramond-Ramond (RR) $(p+1)$-form A_{p+1}, a massless antisymmetric tensor field available in supergravity. In general, in type IIB supergravity, p must be odd, and we should keep in mind that we will eventually set this to $p=3$. Therefore, in addition to the dilaton Φ and the string frame metric $G^{(s)}_{\mu\nu}$, we will also include $F_{p+2}=dA_{p+1}$ to the low energy action (3.6):

$$S=\frac{1}{(2\pi)^7\alpha'^4}\int d^{10}x\sqrt{-G^{(s)}}\left[e^{-2\Phi}\left(R+4\left(\nabla\Phi\right)^2\right)-\frac{2}{(8-p)!}F^2_{p+2}\right]. \tag{B.1}$$

In this theory we look for a p-dimensional electric source of charge $=N$ that is flat in p dimensions:

$$ds^2=ds^2_{10-p}+e^{\alpha}\sum_{i=1}^{p}dx^i dx^i\,, \tag{B.2}$$

where ds^2_{10-p} must then be of Lorentzian signature and spherically symmetric in the sense that $\int_{S^{8-p}}\star F_{p+2}=N$, i.e. the RR source is at the origin and the $(8-p)$-dimensional sphere surrounds it. We will call this solution a p-brane, which is for now completely unrelated to D-branes of the full string theory: we are simply looking for a charged black hole that extends in p flat dimensions.

The solution of the equations of motion for ansatz (B.2) is [327–329]:

$$ds^2=-\frac{f_+(\rho)}{\sqrt{f_-(\rho)}}dt^2+\sqrt{f_-(\rho)}\sum_{i=1}^{p}dx^i dx^i+\frac{f_-(\rho)^{-\frac{1}{2}-\frac{5-p}{7-p}}}{f_+(\rho)}d\rho^2+\rho^2 f_-(\rho)^{\frac{1}{2}-\frac{5-p}{7-p}}d\Omega^2_{8-p}\,, \tag{B.3}$$

where

$$f_\pm(\rho)=1-\left(\frac{r_\pm}{\rho}\right)^{7-p}\,, \tag{B.4}$$

where ρ is the radial coordinate of the $(8-p)$-dimensional sphere and $r_\pm$ are two constants of motion which, as usual when solving for a black hole, can be related to the (ADM) mass of the black hole and its charge N:

$$M = \frac{(8-p)r_+^{7-p} - r_-^{7-p}}{(7-p)(2\pi)^7 d_p l_P^8}, \qquad N = \frac{(r_+r_-)^{\frac{7-p}{2}}}{d_p g_s l_s^{7-p}} \,. \tag{B.5}$$

Here g_s is the asymptotic string coupling constant (defined through (B.6) below), $l_P = g_s^{1/4} l_s$ is the 10-dimensional Planck length and $d_p = 2^{5-p}\pi^{\frac{5-p}{2}}\Gamma(\frac{7-p}{2})$. The solution for the dilaton is

$$e^{2\Phi} = g_s^2 f_-(\rho)^{\frac{p-3}{2}} \,. \tag{B.6}$$

Note that in the case of $p = 3$, the dilaton is constant.

The previous solution was given in the so-called string frame, where the Ricci scalar in the action (B.1) has the $e^{-2\Phi}$ factor in front. In order to get the standard Einstein-Hilbert form (i.e. without the dilaton factor), we define the Einstein frame metric as $G_{\mu\nu} \equiv e^{-\Phi/2} G^{(s)}_{\mu\nu}$ (also discussed in Section 3.5.6). As we can see from (B.3), the Einstein frame metric has a horizon at $\rho = r_+$ and, for $p \leq 6$, also a curvature singularity at $\rho = r_-$, and hence we need $r_+ > r_-$ to cover it. Due to relations (B.5), this condition of covering the singularity with the horizon, i.e. $r_+ \geq r_-$, translates into an inequality[1] between the mass and the charge of the black hole:

$$M \geq \frac{N}{(2\pi)^p g_s l_s^{p+1}} \,, \tag{B.7}$$

where in the case of equality we call the solution an extremal p-brane, while in the case of ">" we have a non-extremal black p-brane. They are called black because there is an event horizon for $r_+ > r_-$ and in the extremal limit, its area vanishes.

[1]This is also equivalent to the BPS bound in 10-dimensional supersymmetry.

Let us now focus on the extremal case $r_+ = r_-$ outside the horizon, in which case we define a new radial coordinate

$$r^{7-p} = \rho^{7-p} - r_+^{7-p}\,, \tag{B.8}$$

so that the horizon is now at $r = 0$. Plugging this in (B.3) we get explicitly

$$ds^2 = \frac{1}{\sqrt{H(r)}}\left(-dt^2 + \sum_{i=1}^{p} dx^i dx^i\right) + \sqrt{H(r)}\left(dr^2 + r^2 d\Omega_{8-p}^2\right)\,, \tag{B.9}$$

where $H(r)$ is a harmonic function in $9-p$ dimensions (i.e. a solution of $\Delta_{(9-p)}H_{(9-p)} \propto Q\delta^{(9-p)}(x^i)$):

$$H(r) \equiv \frac{1}{f_+(r)} = 1 + \frac{r_+^{7-p}}{r^{7-p}}, \qquad r_+^{7-p} \equiv d_p g_s N l_s^{7-p}\,. \tag{B.10}$$

Solutions (B.9) and (B.10) will be important when we start constructing the AdS/CFT correspondence, since, for $p = 3$, the near-horizon ($r \to 0$) limit of this geometry is precisely $AdS_5 \times S^5$. Also, since this solution is a solution of classical supergravity, this means that, from the string theoretical point of view, it is valid when the curvature of the p-brane geometry r_+ is small compared to the stringy scale $\sqrt{\alpha'}$ so that we can neglect the stringy corrections (which will be true in the low energy, $\alpha' \to 0$, limit).

The crucial connection was made by Polchinski [216], who realized that D-branes give in fact the full string theoretical description of p-branes, as it turns out that D-branes act as sources of RR charges (for N Dp-branes, we get N units of RR charge). This also means that our extremal p-brane solution (B.9) is in fact equivalent to the geometry sourced by Dp-branes. We discuss more about D-branes in Section 3.1.3.

B.2 Structure of Anti-de Sitter space

In this section we will discuss some important properties of Anti-de Sitter space; although perhaps a bit too extensive for our purposes, it is nevertheless needed for understanding the details of the AdS geometry. More on the geometry of AdS space can be found in [206].

We will be using Penrose diagrams, which preserve the causal and topological structure of the space, but have "infinities" at a finite distance in the diagram. The way to achieve this is to define a coordinate transformation that brings these infinities to a finite distance and then drop the conformal factor, as it does not affect the null geodesics (since $ds^2 = 0$), and hence preserve the causal structure of the space. For these reasons, this procedure is sometimes called the conformal compactification.

Let us do this first with the Minkowski space, $\mathbb{R}^{1,p}$, where we assume $p \geq 2$ (if $p = 1$, the treatment is only slightly different). The metric in spherical coordinates is

$$ds^2 = -dt^2 + dr^2 + r^2 d\Omega_{p-1}^2 \,. \tag{B.11}$$

Let us now perform a series of coordinate transformations:

$$u_\pm = t \pm r, \quad u_\pm = \tan \tilde{u}_\pm, \quad \tilde{u}_\pm = (\tau \pm \theta)/2 \,, \tag{B.12}$$

i.e. we first pass to the lightcone coordinates, then "compactify" them, and then disentangle them again. Here $\theta \geq 0$, since $r \geq 0$. The metric (B.11) becomes:

$$ds^2 = \frac{1}{4\cos^2 \tilde{u}_+ \cos^2 \tilde{u}_-} \left[-d\tau^2 + d\theta^2 + \sin^2 \theta d\Omega_{p-1}^2 \right] \,. \tag{B.13}$$

Dropping the conformal factor, we have a simple triangular Penrose diagram (for a fixed angle on the $(p-1)$-sphere), see Fig. B.1.

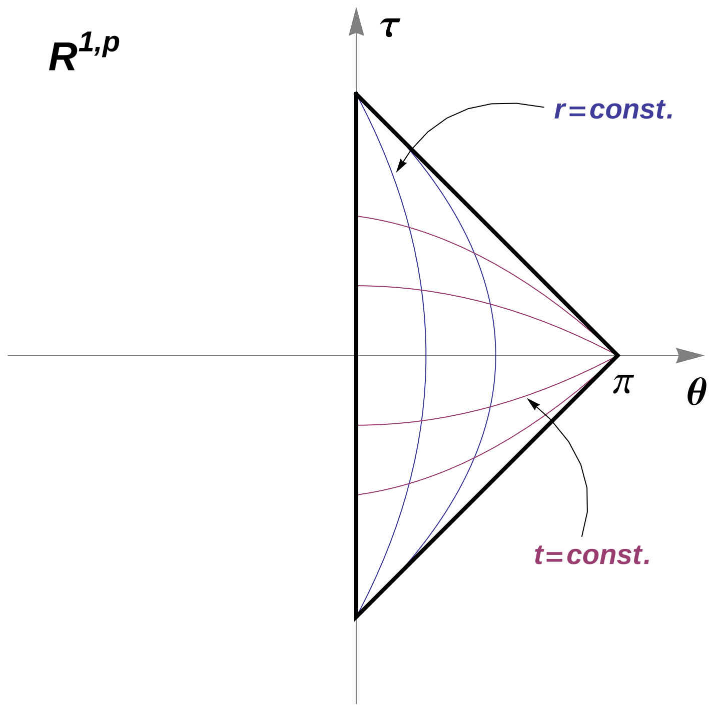

Figure B.1: *Penrose diagram of a conformally compactified Minkowski space* $\mathbb{R}^{1,p}$.

We can now analytically continue this geometry outside of this triangle, so that $-\infty < \tau < \infty$ (and $0 \leq \theta \leq \pi$). This maximally extended space is called the Einstein static universe and has the geometry of $\mathbb{R} \times S^p$, with $\theta = 0$ and $\theta = \pi$ corresponding to the north and south poles of S^p.

The previous analysis is not only a warm-up, but will also prove useful in the analysis of the AdS space, which we will now define. In general, a curved d-dimensional space can be defined by specifying its embedding in a (simpler) $(d+1)$-dimensional space; e.g. a 2-dimensional surface of the sphere can be defined in flat 3D space by equation $X_1^2 + X_2^2 + X_3^2 = R^2$. In a similar way we can define the Anti-de Sitter space, a space of Lorentzian signature and a constant, negative curvature. AdS_{p+2} can be defined as a hyperboloid of some radius L,

$$X_0^2 + X_{p+2}^2 - \sum_{i=1}^{p+1} X_i^2 = L^2\,, \tag{B.14}$$

in a flat $(p+3)$-dimensional space of metric

$$ds^2 = -dX_0^2 + \sum_{i=1}^{p+1} dX_i^2 - dX_{p+2}^2\,. \tag{B.15}$$

From here we see that this space has an $SO(2,p+1)$ isometry and is maximally symmetric (i.e. homogeneous and isotropic). The solution for this embedding is given by

$$\begin{aligned} X_0 &= L\cosh\rho\cos\tau\,, \\ X_{p+2} &= L\cosh\rho\sin\tau\,, \\ X_i &= L\sinh\rho\,\Omega_i\,, \quad i = 1, ..., p+1\,. \end{aligned} \tag{B.16}$$

Plugging these in (B.15) we get

$$ds^2 = L^2\left[-\cosh(\rho)^2 d\tau^2 + d\rho^2 + \sinh(\rho)^2 d\Omega^2\right]\,, \tag{B.17}$$

where we need to take $\rho \geq 0$ and $0 \leq \tau \leq 2\pi$ to cover the hyperboloid once. However, we have a physical problem, originating from the periodicity of τ: the geometry (B.17) close to $\rho = 0$ looks like $S^1 \times \mathbb{R}^{p+1}$, with S^1 representing closed timelike (τ) curves. To avoid this problem, we can simply unwrap the τ circle and take $-\infty < \tau < \infty$, which defines a universal covering of the hyperboloid. Coordinates (B.17), defined in this way, are called the global coordinates of AdS_{p+2}.

Now we can compactify the ρ direction in order to study the causal structure of AdS

space by defining θ as

$$\tan\theta = \sinh\rho\,, \tag{B.18}$$

where $0 \leq \theta \leq \pi/2$ since $\rho \geq 0$. Plugging this in (B.17) we arrive at

$$ds^2 = \frac{L^2}{\cos(\theta)^2}\left[-d\tau^2 + d\theta^2 + \sin(\theta)^2 d\Omega^2\right]\,. \tag{B.19}$$

This is, up to a conformal factor, the same metric as (B.13), i.e. the metric of the Einstein static universe, however the difference now is that θ is constrained to be $\theta \leq \pi/2$, instead of $\theta \leq \pi$, which means that AdS_{p+2} can be conformally mapped into one half of the Einstein static universe. Furthermore, since this geometry is actually $\mathbb{R}\times S^{p+1}$, $\theta = \pi/2$ is the great circle: at fixed τ, the space is hence a $(p+1)$-dimensional hemisphere (shaded region in Fig. B.2) and the equator at $\theta = \pi/2$ is the boundary of the space, that has the topology of S^p, as we can see from (B.19)[2].

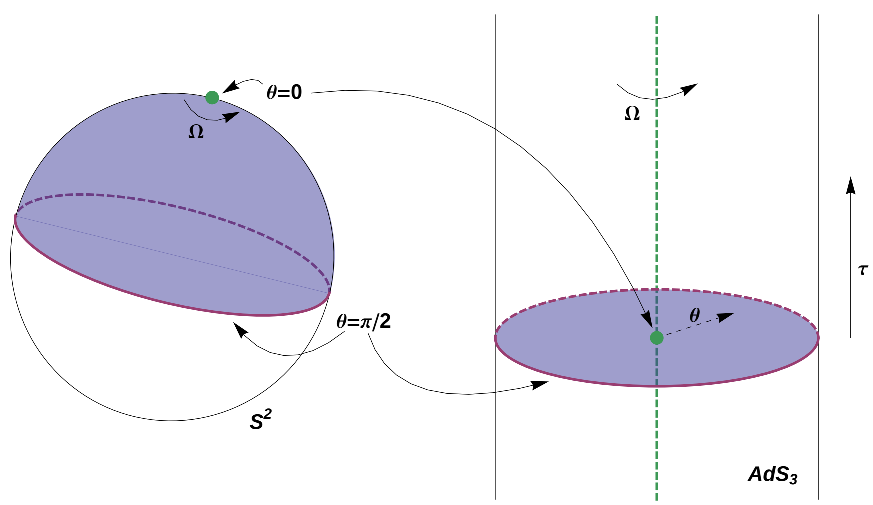

Figure B.2: *Conformal equivalence of one half of Einstein static universe and the global AdS.*

[2]More generally, if a space can be conformally compactified into some region that has the same boundary structure as one half of the Einstein static universe, the spacetime is called asymptotically AdS.

Therefore, AdS_{p+2} is a bounded space and the boundary (of a conformally compactified AdS) has the geometry of $\mathbb{R} \times S^p$, which is the same as the geometry of a conformally compactified $(p+1)$-dimensional Minkowski space $\mathbb{R}^{p+1}$; this is important for the construction of the AdS/CFT correspondence, as it will turn out that, in some sense, the flat gauge theory "lives" on the boundary of AdS. Also, for this reason, it should be possible to find the coordinate system on AdS, where the boundary looks like the usual, flat Minkowski space. These are precisely the Poincaré coordinates $(r, t, \vec{x})$ where $r > 0$ and $(t, \vec{x}) \in \mathbb{R}^{p+1}$, which provide the solution to the embedding equation (B.14) if:

$$\begin{aligned}
X^0 &= \frac{L}{2r}\left[1 + \frac{r^2}{L^2}\left(L^2 + \vec{x}^2 - t^2\right)\right] , \\
X^i &= r x_i \, , \quad i = 1, ..., p \, , \\
X^{p+1} &= \frac{L}{2r}\left[1 - \frac{r^2}{L^2}\left(L^2 - \vec{x}^2 + t^2\right)\right] , \\
X^{p+2} &= r t \, .
\end{aligned} \tag{B.20}$$

Plugging these in (B.15) we get the familiar set of coordinates:

$$ds^2 = \frac{r^2}{L^2}\left(-dt^2 + d\vec{x}^2\right) + \frac{L^2}{r^2} dr^2 \, , \tag{B.21}$$

with the boundary at $r \to \infty$. Another useful set of coordinates is achieved by defining

$$z \equiv \frac{L^2}{r} \, , \tag{B.22}$$

in which case the metric (B.21) becomes a $(p+2)$-dimensional Minkowski space with a simple "warp" factor:

$$ds^2 = \frac{L^2}{z^2}\left(-dt^2 + d\vec{x}^2 + dz^2\right) \, . \tag{B.23}$$

That is, every "z-slice" of the AdS space in these coordinates is conformally symmetric (up to a warp factor) to $\mathbb{R}^{p+1}$, which is also the geometry of the boundary (which is now at $z = 0$). Finally, an important thing to note is that because $z > 0$ (and $r > 0$), this set of coordinates covers only one half of the hyperboloid, which is called the Poincaré patch.